UNIVERSITY OF SOUTHAMPTON

FACULTY OF NATURAL SCIENCES

CHEMISTRY

Volume 1 of 1

Combinatorial Synthesis and High Throughput Screening of Perovskite Electrocatalysts

by

Fiona Kate Rogers

Thesis for the degree of Doctor of Philosophy

September 2016

UNIVERSITY OF SOUTHAMPTON

ABSTRACT

FACULTY OF NATURAL SCIENCES

Chemistry

Thesis for the degree of Doctor of Philosophy

COMBINATORIAL SYNTHESIS AND HIGH-THROUGHPUT SCREENING OF PEROVSKITE ELECTROCATALYSTS

Fiona Kate Rogers

Compositionally graduated films of a $SrTi_{1-x}Fe_xO_{3-y}$ (STFO) perovskite electrocatalyst were successfully prepared by High Throughput Physical Vapour Deposition (HT-PVD). X-ray diffraction measurements confirmed a cubic perovskite structure for all values of x as well as an increase in the cubic lattice parameter with increasing x from 0.392 ± 0.001 nm for $SrTiO_3$ to 0.386 ± 0.001 nm for $SrFeO_3$ in accordance with Vegard's Law. A Raman mode corresponding to an O-stretching vibration was observed which is disallowed by symmetry in the cubic structure and suggests a localised lattice distortion. The films were highly resistive, $< 7 \times 10^{-8}$ S cm^{-1}, at low x but conductivity increased with increasing x before reaching a plateau at 0.041 S cm^{-1} for $x > 0.75$.

High electrocatalytic activity towards the oxygen evolution reaction (OER), characterised by over-potentials below 0.2 V, was found for STFO electrode compositions with $x > 0.5$. The high OER activity was however found to correlate with low electrode stability, consistent with the participation of lattice oxygen in the OER mechanism. This was supported by the observed redox electrochemistry which showed evidence of reversible oxygen intercalation. An optimal electrode composition of $SrTi_{0.5}Fe_{0.5}O_{3-y}$ is recommended as OER activity showed no significant increase for higher Fe content whilst electrode stability decreases. Low electrocatalytic activity towards the oxygen reduction reaction (ORR) was observed for all compositions. The ORR did not occur until after surface reduction of the films suggesting that the surface reduction is required for the creation of active surface sites.

The STFO perovskite system was also investigated on Fe doped STO (110) surfaces. A series of reconstructed surfaces were prepared and characterised by low energy electron diffraction (LEED) in agreement with the literature. X-ray photo-electron spectroscopy (XPS) and low energy ion scattering spectroscopy (LEISS) confirmed that Fe doping was successful in incorporation of Fe into the perovskite structure. Fe incorporation was observed to improve the ORR electrocatalytic activity of the surface however no OER electrocatalytic activity was observed

Table of Contents

Acknowledgements

I would like to thank my supervisor Prof. Brian Hayden for his guidance and support throughout the preparation of this work. I always felt a lot better about the work after a meeting with Brian!

Thanks are also owed to the many members of the group, past and present, who have supported me throughout my PhD candidature. In particular Fiona McBride who helped me to set-up the electrochemical transfer system as well as with the endless repairs which were required in the beginning! She also provided many helpful discussions, a lot of knowledge about surface science and a very handy extra pair of hands when it came to the electrochemical transfers. I also wish to thank Jin Yao for preparing the electrochemical arrays for the high-throughput electrochemistry and for taking the profilometry measurements of the thin film thickness. Thanks also to Sandy Kerr for his help with the PVD system and generally his company when we were working on the chamber together.

I am extremely grateful for the help I received from the mechanical workshop without which I wouldn't have got very far! I would especially like to thank Alan for always being willing to make time for me and my various UHV problems and for being so sympathetic!

Finally a special thanks to my family and to Paul for putting up with me throughout these last four years.

Abbreviations

4PP	Four point probe
AEM	Alkaline exchange membrane
AES	Atomic emission spectroscopy
AFC	Alkaline fuel cell
DFT	Density functional theory
DMFC	Direct methanol fuel cell
EDX	Energy dispersive x-ray spectroscopy
EELS	Electron energy loss spectroscopy
HER	Hydrogen evolution reaction
HOR	Hydrogen oxidation reaction
HPRR	Hydrogen peroxide reduction reaction
HT-PVD	High-Throughput Physical Vapour Deposition
LEED	Low energy electron diffraction
LEISS	Low energy ion scattering spectroscopy
OER	Oxygen evolution reaction
ORR	Oxygen reduction reaction
PEFC	Polymer electrolyte fuel cell
PEM	Polymer electrolyte membrane
PLD	Pulsed lased deposition
RHEED	Reflection high energy electron diffraction
SOFC	Solid oxide fuel cell
SFO	$SrFeO_{3-y}$
STFO	$SrTi_{1-x}Fe_xO_{3-y}$

STM	Scanning tunnelling microscopy
STO	$SrTiO_3$
TSP	Titanium sublimation pump
UHV	Ultra-high vacuum
UPS	Ultraviolet photoelectron spectroscopy
XPS	Photoelectron Spectroscopy
XRD	X-ray diffraction

Chapter 1: Introduction

1.1 Sustainable Energy Sources

Despite attempts to improve our energy efficiency within the current energy infrastructure, it is widely accepted that new sustainable energy sources will be required to meet our future energy demands. In 2014 renewable sources, including biofuels, biomass, geothermal, hydropower solar and wind, were estimated to account for 9.1% of global electricity generation which is an increase of 0.6% compared to 2013 [1]. In the UK, 19.1% of electricity was generated from renewable sources for 2014, over half of this from wind power, and renewable sources supplied 7% of total energy consumption when heat and fuel for transport was included [2]. The UK is committed to raise this figure to 15% of total energy supply from renewable sources as part of the EU energy directive which seeks to meet 20% of all energy requirements through renewable sources by 2020 [3]. At least 164 countries worldwide are now committed to renewable energy targets [4].

One of many problems faced in improving the global energy infrastructure is the intermittent nature of renewable energy sources such as solar, wind and hydropower. Research and investment in efficient energy conversion and storage technologies is a necessity so that surplus energy can be held in reserve for times when supply cannot meet demand [5]. Electrochemical devices can provide a solution via the conversion of electrical energy into chemical energy which can be stored, for example by driving the electrochemical production of fuels such as hydrogen which can be converted back into electrical energy when required [6, 7].

1.2 Electrochemical Energy Conversion and Storage

Currently the most widespread use of electrochemistry to convert and store electrical energy is in rechargeable batteries, including Li-ion, which are used for portable devices such as mobile phones and laptops [8, 9]. These devices are capable of converting electrical energy into a chemical form, storing the chemical energy and then converting it back into electrical energy as required. Whilst highly effective on this small scale, research to scale up such devices for transport and large static applications suitable for the conversion and storage of renewable energy is ongoing as higher energy density, lower cost and an improvement in safety is required [8, 10, 11]. Metal-air batteries are a key area of interest for these applications as they provide a higher theoretical energy density [12], this will be discussed further in **Section 1.6**.

An alternative to battery technology is the storage of energy in the form of hydrogen achieved by the electrolysis of water [13, 14]. The electrical energy is used to drive the non-spontaneous water splitting reaction and is converted into chemical energy in the form of hydrogen and oxygen gases. The energy may then be stored and converted back into electrical energy when required via the spontaneous recombination reaction which is a clean process producing only water, heat and energy [6]. Clearly for this process to be viable the energy conversions must take place with high efficiency to avoid energy losses.

The efficiency of an electrochemical cell is determined according to **Equation** 1-1 [15] where V_{cell} is the measured cell voltage and ΔE is the difference in the equilibrium potential of the anode and cathode reactions.

$$Efficiency\ (\%) = \frac{V_{cell}}{\Delta E}\ x\ 100\%$$

Equation 1-1

The cell voltage will differ from ΔE due to voltage losses in the cell according to **Equation** 1-2 [15]. The η_a and η_c terms represent the over-potentials for the anode and cathode reactions which are dependent on the electrode materials used. The IR term represents the ohmic voltage loss due to resistance in the cell components. High efficiency is therefore obtained by selection of appropriate electrode materials to minimise the over-potentials for the electrode reactions coupled with innovation in cell design to avoid resistance.

$$V_{cell} = \Delta E - \eta_a - \eta_c - IR$$

Equation 1-2

1.3 Water electrolysis cells

Water electrolysis cells use electrical energy to drive the non-spontaneous water splitting reaction shown in **Equation** 1-3 by application of a potential across the two electrodes of the cell [16]. Typical designs for water electrolysis cells operating under acidic and alkaline conditions are shown in **Figure 1-1**. The electrolyte component of the cell allows the migration of ions from one electrode to the other whilst the electrons pass through an external circuit. Some form of porous separator is also required which allows the ions to pass through but prevents recombination of the product gases, in some cell designs the electrolyte itself may act as this separator. The electrolyte material may be either acidic, allowing the passage of protons, or alkaline, allowing the passage of hydroxide ions.

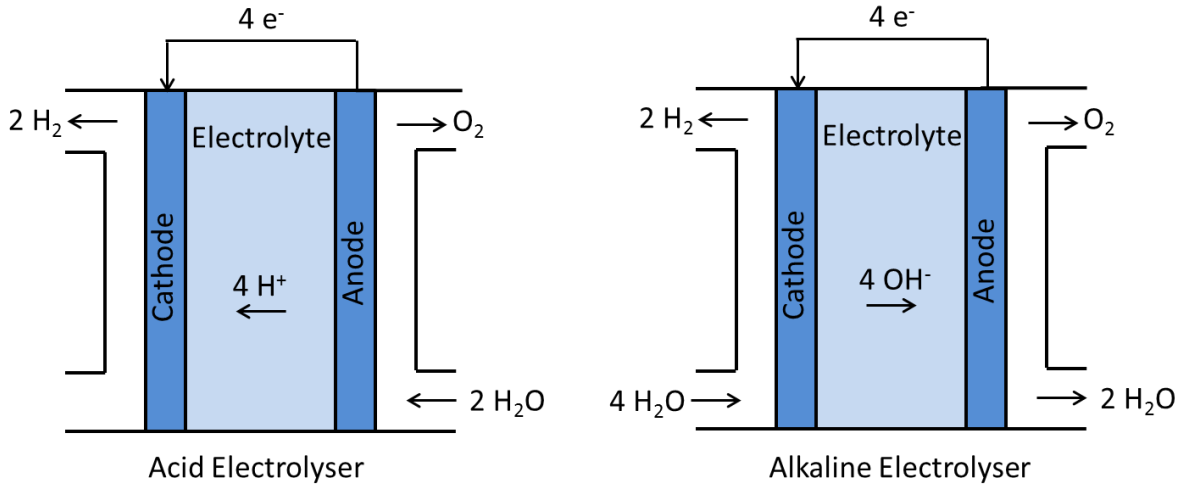

Figure 1-1: Schematic of a typical water electrolysis cells operating under acidic conditions (left) and alkaline conditions (right).

$$2\,H_2O_{(l)} \rightarrow 2H_{2\,(g)} + O_{2\,(g)}$$

Equation 1-3

For an acidic electrolyser water is fed to the anode of the cell where oxygen is evolved according to Equation 1-4 [16]. The protons produced by this reaction pass through the electrolyte to the cathode whilst the electrons pass through the external circuit. The protons and electrons recombine at the cathode to evolve hydrogen according to **Equation** 1-5 [16].

$$2\,H_2O \rightarrow O_2 + 4\,H^+ + 4\,e^-$$

Equation 1-4

$$2H^+ + 2\,e^- \rightarrow\ H_2$$

Equation 1-5

For an alkaline electrolyser, water is fed to the cell cathode and hydroxide ions are produced during hydrogen evolution as shown by **Equation** 1-6 [16]. These ions are transported through the electrolyte to the anode where oxygen is evolved according to **Equation** 1-7 [16].

$$H_2O + 2e^- \rightarrow\ H_2 + 2OH^-$$

Equation 1-6

$$4\,OH^- \rightarrow\ O_2\ + 2\,H_2O + 4\,e^-$$

Equation 1-7

Alkaline electrolysers are generally preferable due to the better kinetics of the oxygen evolution reaction (OER) in alkaline electrolyte on non-precious metal catalysts [17, 18].

1.3.1 Alkaline Electrolysers

Commercial electrochemical hydrogen production plants mainly use alkaline electrolysis cells with a liquid KOH electrolyte [19]. This cell design requires a porous separator designed to prevent mixing of the product gases whilst allowing transport of water and hydroxide ions between the electrodes. The porous separator does not however completely prevent the mixing of the product gases [19] leading to relatively low energy efficiency of around 60% [20] and a risk of creating an explosive H_2/O_2 mixture [19]. This cell design also suffers from low current densities due to large ohmic losses from the resistance of the liquid electrolyte and the porous separator [19].

1.3.2 Polymer Electolyte Electrolysers

The efficiency of electrolysers may be improved by replacement of the liquid electrolyte with a polymer electrolyte membrane which acts as a more efficient separator preventing the mixing of the product gases [19]. Whilst stable proton conducting membranes such as Nafion are a well-established technology, the development of similar hydroxide ion conducting membranes has proved challenging [20]. The uptake of the acid electrolyser has been limited by the high cost of both the membrane and the precious metal catalysts used at the anode and cathode [20]. A further drawback is that ultra-pure distilled water is required for the operation of polymer electrolyte membranes [21] as contaminants may block the conducting membrane or active sites on the electrodes.

1.3.3 Solid Oxide Electrolysers

Solid oxide electrolysers contain a solid metal oxide electrolyte which is non-porous resulting in very low mixing of the product gases and very high efficiency. Ion transport through the oxide electrolyte requires high operation temperatures in some cases reaching 1000 °C [21]. Major issues with this technology therefore lie in obtaining cost-effective materials which are able to withstand this high temperature.

1.4 H_2/O_2 Fuel cells

A fuel cell converts chemical energy via a spontaneous redox reaction into electrical energy. A schematic of a typical cell design showing the key components is shown in **Figure 1-2**. The overall cell reaction for a H_2/O_2 fuel cell is shown in **Equation** 1-8, the only product is water [16]. Fuel cells differ from batteries in that the fuel source is stored externally from the cell. As such, they do not require charging and are limited instead by the size of fuel tank available. As well as their use alongside electrolysis cells for the storage and conversion of energy obtained from renewable sources, fuel cells can also act as a primary source of electrical energy if there is a suitable clean chemical fuel source such as hydrogen or methanol available.

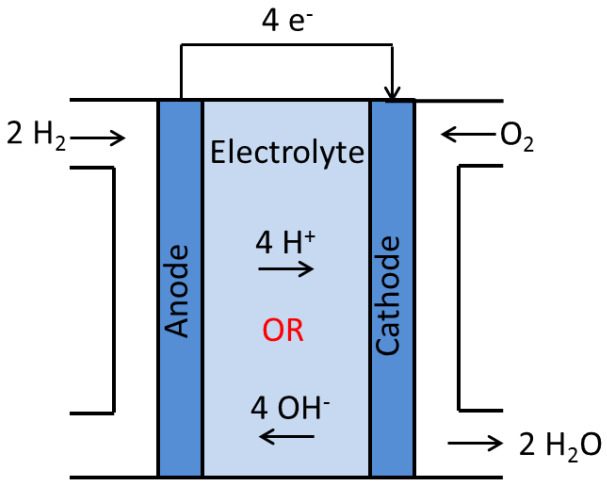

Figure 1-2: Schematic of a typical H_2/O_2 fuel cell.

$$2\,H_{2\,(g)} + O_{2\,(g)} \rightarrow 2H_2O_{(l)}$$

Equation 1-8

One of the key elements in the cell design is the operating pH. For a cell operating under acidic conditions the hydrogen fuel is oxidised at the fuel cell anode, according to **Equation** 1-9 [16], to produce protons which pass through the electrolyte to the cathode. The electrons generated from the anode reaction pass through an external circuit to the cathode producing electrical energy. At the cathode the protons and electrons combine with oxygen to form water as shown by **Equation** 1-10 [16].

$$H_2 \rightarrow 2H^+ + 2\,e^-$$

Equation 1-9

$$O_2 + 4\,H^+ + 4\,e^- \rightarrow 2\,H_2O$$

Equation 1-10

Alternatively in a cell operated in alkaline conditions, oxygen is reduced at the cathode according to **Equation** 1-11 and the hydroxide ions act as the mobile charge carriers which pass though the electrolyte to the anode to combine with hydrogen according to **Equation** 1-12 [17].

$$O_2 + 2\,H_2O + 4\,e^- \rightarrow 4\,OH^-$$

Equation 1-11

$$H_2 + 2OH^- \rightarrow 2H_2O + 2e^-$$

Equation 1-12

Whilst the kinetics of the hydrogen oxidation reaction (HOR) are fast, the kinetically slow cathodic oxygen reduction reaction is the major source of efficiency loss for a H_2/O_2 fuel cell [22]. One significant advantage of cells operating under alkaline conditions is that the ORR kinetics are improved in strongly alkaline media compared to acidic media [15, 23].

A variety of different types of fuel cell are currently in development with the major variations between them being the electrolyte material (which can be liquid or solid) and operating temperature. There will also be differences in the power output and the choice of the fuel cell will depend on the application.

1.4.1 Alkaline Fuel Cells (AFCs)

AFCs typically use 35-40% liquid KOH as the electrolyte, where a liquid electrolyte is used a porous separator is required to prevent direct mixing of the inlet gases [15, 17]. AFCs have been successfully employed in large static applications but their efficiency combined with their low operating temperatures (50-120 °C) should also make these cells suitable for transport applications. The development of these cells for transport and portable applications has however been limited both by the hazardous liquid electrolyte and by the poor tolerance of the cell to impurities such as CO_2. CO_2 from the gas feeds reacts with the KOH electrolyte to form carbonates in the electrode pores, degrading the electrolyte and blocking the pores of the electrodes [17].

1.4.2 Polymer Electrolyte Fuel Cells (PEFCs)

In a similar way to the analogous electrolyser technology the efficiency of fuel cells can be improved by replacement of the porous separator and liquid electrolyte with a solid polymer membrane [15]. This also improves the resistance to CO_2 impurities since although the cationic groups on the membrane will carbonate, it is already a solid and there are no mobile cations which can form pore-blocking precipitates. Additionally since the membrane supports the two catalyst layers the design is much more compact which is ideal for transport applications. Since the development of stable AEMs has lagged behind PEM technology, a large amount of research and development has focussed on PEM Fuel Cells despite the poorer ORR kinetics in acidic media which leads to the requirement of expensive noble metal catalysts.

1.4.3 Solid Oxide Fuel Cells (SOFCs)

In this cell design a ceramic solid oxide electrolyte separates the two electrodes. In the usual set up oxygen is reduced at the air electrode and the oxide ions migrate through the solid electrolyte to react with the fuel. Alternatively a proton conducting solid electrolyte can be used, in this case hydrogen is reduced at the fuel electrode to form protons which can go on to react with oxygen at the air electrode to form water [24]. SOFCs operate at higher temperatures, typically 500-1000 °C [25, 26], this higher temperature increases the resilience of the cell to gas feed impurities and means that CO can also be oxidised at the anode according to **Equation** 1-13 [27].

$$CO + O^{2-} \rightarrow CO_2 + 2e^-$$

Equation 1-13

A key issue in the development of SOFCs is the difficulty in selecting materials for the electrodes and electrolyte which will be compatible at the high temperatures required both for their operation and in the preparation of the cell. Reactions between the electrode and electrolyte materials must be avoided and the materials must also have similar thermal expansion [25].

1.5 Regenerative Fuel Cells

The development of bi-functional electrode materials which can catalyse both the water splitting and re-combination reactions allows for both the conversion of electrical energy into storable chemical energy and the reverse process to be achieved using a single electrochemical cell, thus reducing costs. Such a device is termed a regenerative fuel cell [6].

1.5.1 Alkaline water electrolysis/AFC system

The coupling of the alkaline water electrolysis system with the alkaline fuel cell system is possible by switching the polarity of the cell. The hydrogen electrode must be able to support both the HOR and HER whilst the oxygen electrode must be capable of supporting both the ORR and OER. In addition to the electrocatalytic requirements both electrodes must be able to withstand potentials required for both reactions.

Neither requirement is particularly problematic at the hydrogen electrodes since both reactions have good kinetics and the potentials required are not extreme. The oxygen electrode can be problematic however as both reactions are kinetically slow and oxygen evolution requires harsh oxidising potentials. Mixed transition metal oxides have proved to be the most promising option for this application with examples including $LaCoO_3$ and $Na_xPt_3O_4$.

1.5.2 PEM/PEFC system

The compact design and increased safety of this system arising from the replacement of liquid electrolyte with a solid polymer membrane allows for use in transport applications. This type of system could therefore be used for local hydrogen generation in fuel cell vehicles [15, 19].

It is possible to circumvent the stability issues of the electrodes in this system by keeping the polarity of the cell the same in both the electrolysis and fuel cell modes whilst the inlet/outlet of reactants and products is changed. In this case both oxidation reactions, the OER and HOR, occur at the same electrode whilst the other electrode is used to catalyse the reduction reactions, the ORR and HER [28]. Pt-based catalysts are suitable for both reduction reactions whilst IrO_2 or RuO_2 which are active for the OER are also capable of catalysing the HOR which has fast kinetics [16].

1.5.3 Solid oxide system

The high temperature solid oxide electrolysers and fuel cells can also be coupled to create a regenerative system. The kinetics of the reactions are improved by the high temperature which provides some of the energy required for the reactions. The same problems with finding materials compatible with the high-temperature environment which occur in each of the individual systems also apply to the hybrid system.

1.6 Metal-air batteries

Metal-air batteries generate electricity from the redox reaction between a metal anode and oxygen from the air which is brought in to the cell through the open-structured cathode, also known as the air electrode [8], this is shown schematically in **Figure 1-3**. Metal-air batteries have higher theoretical energy densities than other common battery technologies such as lithium-ion and nickel-metal hydride batteries [11, 29]. This high energy density is partly due to the cathode fuel, oxygen, being supplied from the air and so not being contained in the cell but high energy density is also achieved by the selection of anode metals with a high density of valence electrons to atomic nuclei such as Li, Zn, Al and Mg.

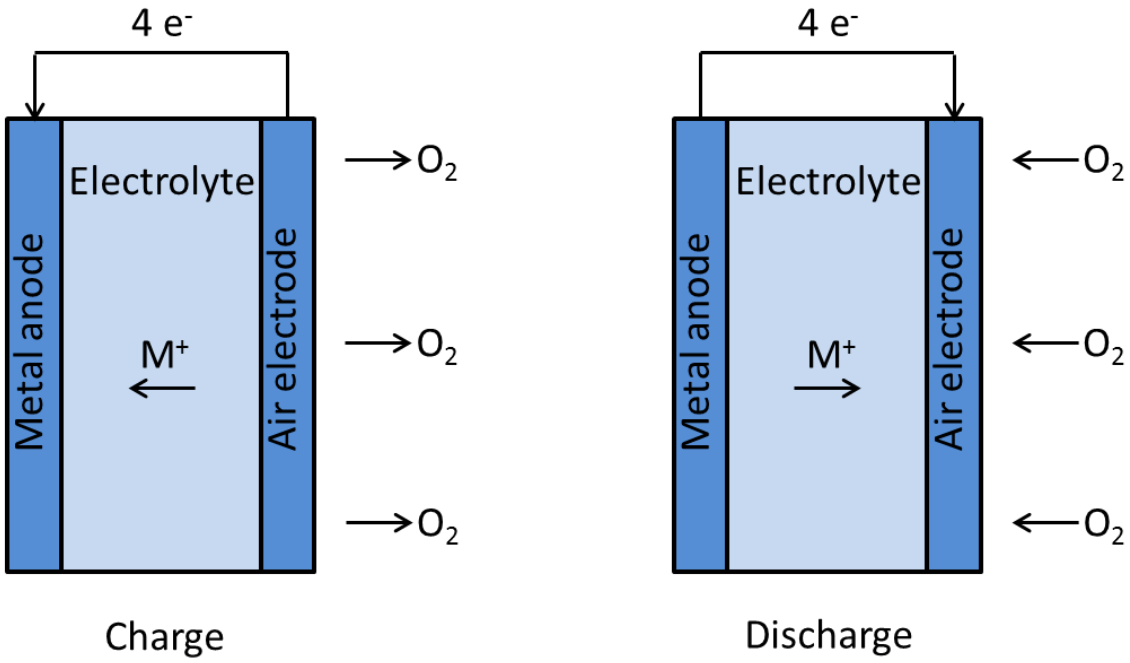

Figure 1-3: Schematic diagram showing the design of a metal-air battery showing charging (left) and discharge (right).

As with other hydrogen-cycle technologies, metal air batteries also rely on the kinetically slow ORR as the cathode reaction and in the same way transition metal oxide electrocatalysts have been considered as possible substitutes for expensive noble metal catalysts. An additional challenge for metal-air batteries lies in the desire for a rechargeable battery. If a bi-functional cathode material can be found which supports both the ORR and OER the electrode reactions can be effectively reversed to replenish the metal anode and allow for charging of the battery with electrical input. Since perovskites are capable of catalysing both the ORR and OER in alkali they have been of interest for this purpose.

1.7 Electrocatalysis

The electrochemical reactions which are essential to the function of fuel cells, battery devices and electrolysis cells are very strongly dependent on the surface composition and atomic arrangement of the electrode materials employed [22]. The study of new electro-catalysts by surface sensitive techniques is therefore vital to the development of this technology which could provide clean and sustainable energy for the future and which is currently hindered by the high cost of noble metal based catalysts.

Of key concern when developing a new electrocatalyst is the *overpotential* of the reaction at the electrode surface, that is to say the difference between the measured electrode potential and the equilibrium potential of the reaction [15]. This will have an effect on the working voltage of the cell which has a theoretical value of 1.23 V based on the equilibrium potentials of the HOR and ORR [30, 31]. No working H_2/O_2 fuel cell has so far achieved this potential and 85 % of this loss in efficiency has been attributed to the slow rate of the ORR [22].

Also of importance is the *current density* which describes the amount of current produced per unit area of the catalyst at a fixed potential [15]. The ultimate goal of electrocatalysis is to obtain a high current density as close as possible to the equilibrium potential.

In order to find active electrocatalysts many attempts have been made at rationalising the observed activity of electrocatalytic materials and identifying an activity descriptor which is an easily measured chemical or electronic property of the material which can be used to aid in the design of an ideal electrocatalyst. The Sabatier principle states that an active catalyst material must be able to bind the reactant in order to aid in the formation of reaction intermediates but must not bind it so strongly that products cannot be released from the surface. This leads to a volcano-shaped relationship between the electrocatalytic activity and the strength of the surface-reactant bonding. A suitable activity descriptor provides a good indicator of this bonding strength and a volcano-shaped plot as shown in **Figure 1-4** should be expected. The rate determining step may change from one branch of the volcano to the other from a reaction step involving bond formation on the left side to one involving bond breaking on the right side.

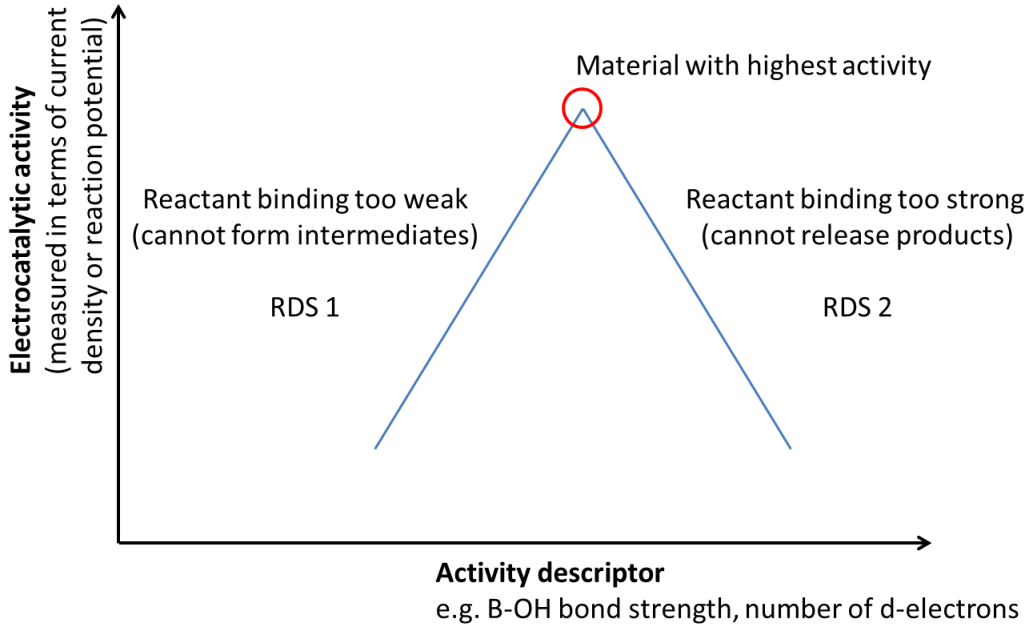

Figure 1-4: Schematic of a volcano plot showing the expected dependence of electrocatalytic activity on a suitable descriptor. On the left hand branch of the plot the interaction between the electrocatalyst and the reactant is too low and the formation of reaction intermediates and products is not favoured. On the right hand branch the interaction between the electrocatalyst and the reactant is too high and the release of the reaction product from the surface is not favoured. The most active material is found at the top of the volcano where these two factors are balanced. The rate determining step may differ for the two branches.

1.8 Hydrogen Electrocatalysis

Whilst it has already been discussed that major limitations on fuel cell and electrolyser technologies lie with the slow kinetics of the ORR and OER, effective catalysis of the HOR and HER still presents many challenges. In order for electrochemical devices to function efficiently fast HOR kinetics are required and electrode materials must therefore be carefully chosen to provide good catalysis combined with sufficient stability towards the often harsh pH, temperature and potential of the working environment.

So far, the best catalyst which has been identified for both the HOR and the HER is Pt and the uptake of fuel cell and electrolyser technology has been limited by the high cost of Pt and other noble metal based catalysts. In addition Pt is also susceptible to poisoning by CO which blocks active sites on the electrode surface reducing catalytic efficiency and decreasing the lifetime of the fuel cell. Alloying Pt with cheaper metals such as Ru has the effect of decreasing cost and also reducing the affinity of CO to the catalyst thus extending the lifetime of the catalyst [32]. Another approach to reducing Pt usage has been dispersal on high surface area support materials, however both techniques still rely on Pt, an ever more scarce and expensive commodity.

1.9 Oxygen Electrocatalysis

Both the ORR and OER are complex multi-step reactions involving various oxygen containing intermediates. The activation energy for the formation of the intermediates is lowered by interaction with metal atoms particularly when the metal atoms are able to change valence state to bond with the oxygen atoms. The requirements for the electrode materials which support the two reactions are therefore broadly similar. The material must be able to bind oxygen in order to stabilise the intermediates in the reaction but must not form stable oxides which would not allow the oxygen to be released [33]. Additionally the material must be stable at the oxidising potentials at which the ORR and OER occur. The most active materials for the ORR are Pt alloys whereas the OER occurs on oxidised metal surfaces and whilst PtO_2 is an active OER catalyst it is surpassed by RuO_2 and IrO_2 [30, 34]. One reason for this is the high conductivity of RuO_2 and IrO_2 compared to the relatively insulating PtO_2. Pt, Ru and Ir based materials are however not favoured for commercial electrochemical devices due to their low abundance and high cost [35].

Currently the best ORR catalysts are also Pt based and even these have over-potentials of >400 mV for the production of a useful amount of current [36]. Attempts to reduce the cost of Pt loading again include the introduction of high surface area carbon supports and alloying with other metals. Pt alloys with transition metals such as Cr, Fe and Mn have shown improved ORR activity and are capable of reducing the overpotential by up to 25 mV [37, 38]. Unfortunately these alloys are often not stable and leach in acid electrolyte which is particularly problematic in PEM fuel cells where they can block sites in the membrane and increase the cell resistance causing a loss of voltage (IR drop) [15].

As discussed earlier, the kinetics of the ORR are much slower than those for the HOR and other anode reactions. Since the kinetics of the ORR are improved in alkaline conditions it is realistic to consider alternatives to Pt catalysts at the cathode of alkaline fuel cells. Transition metal oxides are promising as ORR/OER catalysts since they are resistant to high pH and the highly oxidising environment at the cathode.

1.10 Oxide Electrocatalysts for the ORR/OER

Transition metal oxides provide several advantages over metal surfaces for catalysis of the ORR as well as the OER. Firstly, metal oxides are the thermodynamically stable state of most metals at potentials required for the ORR and OER. Additionally oxide surfaces have redox and acid/base functionality which aids electron transfer and therefore electrocatalysis. Finally, metal oxides are much cheaper and more abundant than noble metal catalysts. Whilst many oxides have shown promise as ORR/OER catalysts due to their low over-potentials, which are comparable to Pt catalysts, the reported current densities have been low since catalysis is kinetically limited on the oxide surface by poor electron transport [35]. The development of better oxide-based electrocatalysts is therefore linked to the reduction in the band gap of oxide materials and the improvement of the electronic conductivity at the surface.

One method for improving the conductivity of oxide catalysts is the synthesis of composite materials with conductive carbon [39, 40] . Synthesis methods which produce nano-particles which can be supported on conductive carbon are also widely employed which have the additional benefit of increasing the surface area of the electrocatalysts and as such improving their mass activity [41-43].

The inherent conductivity of the oxide catalysts can be improved by introducing oxygen defects into the material since these defects encourage the movement of oxide ions and electrons. Liu *et al.* [44] used a sputtering method to prepare transition metal oxides with oxygen defects for use as cathodes for Direct Methanol Fuel Cells (DMFCs). The materials showed ORR activity in acid electrolyte in the order $ZrO_{2-x} > CoO_{4-x} > TiO_{2-x} = SnO_{2-x} > NbO_{5-x}$, where x indicates the number of oxygen defects. The oxides were also found to be selective for the ORR with no crossover for the methanol oxidation reaction which is an unfavourable characteristic of traditional Pt catalysts.

A further approach to the development of electronically conducting oxide electrocatalysts focuses on oxides with crystal structures containing multiple metal ions such as those with the spinel structure, $A[B_2]O_4$, and the perovskite structure, ABO_3, which have also been investigated for their OER and ORR activity [45-53]. These materials can support multiple metal cations at the A and B sites as well as oxygen vacancies which encourage redox activity. This has the effect of improving the mobility of electrons and oxide ions through the structure and as such improves the electronic and ionic conductivity.

The significance of the introduction of redox activity into ORR/OER electrocatalysts extends beyond the improvement of electronic conductivity and there is evidence to support the involvement of redox reactions in the ORR and OER mechanisms. One example of this is in manganese oxides which have shown promise as ORR electrocatalysts in alkaline media [41, 54-56]. Cao *et al.* [54] studied various different MnO_2 catalysts and identified a link between the Mn^{3+}/Mn^{4+} redox couple and ORR activity. They used linear voltammetry to observe that oxygen reduction current increased with increasing electroreduction of the film and proposed that the ORR mechanism required the presence of Mn^{3+} which is then able to donate an electron to oxygen resulting in the oxidation of Mn^{3+} to Mn^{4+}.

1.11 Scope of this thesis

Two different experimental approaches have been employed in this work, firstly the high-throughput synthesis, characterisation and screening of thin films samples and secondly a surface science study. For the surface science study a single crystal sample was required to provide a well-ordered surface for characterisation. The sourcing of such a sample meant that the choice of a perovskite to study was limited to those based on $SrTiO_3$ (STO) which is widely available as a single crystal substrate.

STO is an insulator with a band gap of 3.2 eV [57] and as such was not expected to show electrocatalytic activity. The conductivity can however be improved by the addition of a dopant and for this work Fe was chosen. $SrTi_{1-x}Fe_xO_{3-y}$ (STFO) is a relatively widely studied material and crucially adopts the cubic perovskite structure across the solid solution from $SrTiO_3$ (STO) where x = 0 to $SrFeO_{3-y}$ (SFO) where x = 1 [58-60]. The Fe dopant was however mainly selected with regard to the electronic structure of the formally Fe^{4+} ions. The Fe^{4+} ions adopt a high spin d^4 electronic structure which has been linked to high OER [46] and ORR [61] activity. STFO materials also have interesting redox properties since Fe is also able to adopt the Fe^{3+} oxidation state which creates oxygen vacancies in the lattice. The degree of oxygen deficiency in the lattice is represented by y.

Following the discussion of the experimental approaches in Chapter 2 this thesis is structured as follows. Chapters 3-6 relate to the high-throughput synthesis, characterisation and screening of STFO thin film electrocatalysts. In Chapter 3 the high-throughput synthesis of STFO is discussed with regards to the bulk composition, surface composition and conductivity of the materials obtained. The crystal structure of the materials and a discussion of possible distortions to the cubic perovskite structure is discussed in Chapter 4. In Chapter 5 the redox electrochemistry of STFO is considered whilst Chapter 6 focusses on the electrocatalytic activity. Finally in Chapter 7 the results of the surface science study on Fe doped STO surfaces are discussed.

Chapter 2: Experimental Methods

This chapter contains information and background theory relating to the experimental instrumentation and methods used in this work for the preparation of samples and subsequent characterisation and electrochemical screening. Whilst this provides a general overview to the work more detailed information on experimental procedures is included in subsequent chapters.

Two different methods were applied to the investigation of the activity of STFO transition metal oxide electrocatalysts which exhibit the perovskite crystal structure. The main focus of the work was the high-thoughput synthesis, characterisation and screening of STFO electrocatalyst libraries. The aim of this approach was to investigate a large portion of the compositional map and identify trends in activity which could then be related to composition, electronic structure or crystal structure. In addition to this a complementary surface science study using a single crystal sample was designed in order to investigate the mechanism of electrocatalysis on the perovskite surface by correlation of observed electrocatalytic activity with surface structure.

2.1 High-throughput physical vapour deposition (HT-PVD)

2.1.1 Comparison with other methods

2.1.1.1 Solid-state synthesis

Perovskite materials can be synthesised by a variety of high temperature solid state reactions [47, 62-65]. This usually follows a procedure of mixing the salts of the metals in stoichiomethric proportions either mechanically or by a method of co-precipitation, followed by some regime of pressing into pellet form and heat treatments sometimes above 1200 ° C for as long as 70 h. In bulk synthesis the reactants are stable and so there is a high kinetic barrier to combining them. It is therefore difficult to control and the resulting material may not be thoroughly mixed. This method is also time consuming and each composition must be prepared individually so that large scale exploration of the compositional map is not practical.

2.1.1.2 Thin film synthesis

The preparation of thin film samples under ultra-high vacuum (UHV) and controlled gas atmospheres allows for deposition of contaminant free films. Pulsed Laser Deposition (PLD) is a widely used technique for the preparation of thin films of material in a controlled manner. In order to prepare perovskite thin films a target material must first be prepared by a solid state method similar to those described above. This is then laser ablated to form a plasma which deposits the perovskite onto the substrate. This method is again time consuming for preparation of a single composition but the components are mixed in the plasma so the kinetic barrier to combining them is lower so there is more control over the homogeneity of the product. This method has been used to epitaxially grow thin films of perovskite onto $SrTiO_3$ single crystals [66-68].

2.1.1.3 High-throughput thin film synthesis

As discussed above, the preparation of films of individual composition by methods such as PLD can be time consuming rendering large scale exploration of the compositional map impractical. In order to screen large compositional ranges for electrocatalytic materials the thin film materials must be prepared using high-throughput methods.

One way to produce films containing multiple compositions is to use “fast-sequential” methods in which the material is built up layer-by-layer by deposition from a series of sources controlled by masks or moving shutters [69-71]. In order to achieve adequate mixing of the elements using this method, the sample requires annealing following the deposition [70]. Alternatively there are some techniques which allow for the creation of a compositional gradient by deposition of the elements in parallel [72-74]. These “parallel” methods are simpler since only one layer is required with no changing of masks or annealing as the elements are intimately mixed during deposition. Depending on the method, however, they may produce a more limited range of compositions.

HT-PVD [74] is a parallel technique which has previously been employed to prepare complex oxides including those with the perovskite structure [75-78]. Using this technique elements are deposited simultaneously using multiple off-axis sources, the kinetic barrier to mixing is low allowing highly controlled atomic mixing of the elements. The deposition is controlled both by deposition rate and by a wedge system which is capable of producing composition gradients across the substrates. This gives preparation of a large portion of the compositional map for the perovskite materials of interest on a single substrate under identical conditions. This method combined with high throughput electrochemical techniques allows for fast screening of materials with a range of composition and is ideal for studying solid solutions of perovskites to determine the optimal compositions for electrocatalytic activity.

2.1.2 HT-PVD chamber design

The HT-PVD deposition chamber used for this work was held at a base-pressure below 1 x 10^{-8} mbar with pumping via a cryo-pump alongside a turbo-molecular pump backed by an oil-free rotary pump. Gases can be inlet into the chamber either in molecular form or as an atomic plasma generated using a plasma source (Oxford Applied Research).

Samples are loaded into the chamber for deposition via a sample transfer line which is also held under ultra-high vacuum conditions and connects the chamber to a XPS analysis chamber, a RF sputter-deposition chamber and a further PVD deposition chamber as well as the sample load-lock. The load lock can be isolated and vented to atmospheric pressure to allow for the loading of new samples to the system without disruption of the ultrahigh vacuum conditions in the rest of the system.

A schematic of the deposition chamber is shown in **Figure 2-1**. The chamber is able to accommodate up to six sources for the deposition of metallic elements. Three of these sources are Knudsen cells (K-cell, DCA HTKS) for which the evaporation of the source material is achieved by heating and the rate can be controlled by variation of the temperature of the source. In the chamber configuration used in this work one of these sources was removed to allow for mounting of the plasma source, as shown. The remaining three sources are electron-beam evaporators (e-guns, Temescal) for which evaporation is achieved by bombardment of the source material with an electron beam and can be controlled by the power of the electron beam. These sources are employed for materials with a high melting point. The rate of the deposition from the e-beam sources can be measured using quartz crystal microbalances positioned above the sources.

The off-axis position of the deposition sources creates a graduated deposition profile which can be enhanced by the use of moveable shutters. The shutters are moved inwards to create a steeper deposition profile or outwards for a more gradual profile, the function of the wedge shutters has been described in detail by Guerin and Hayden [74].

In order to overcome the geometrical limitations of the chamber an angled wedge shutter can be used to alter the deposition profile and give the effect of deposition from a different position in the chamber, controlled by the angle of the wedge. Angled wedge shutters were used to control the deposition profile of the Sr and Ti sources, as shown on **Figure 2-1**. A 60° angled wedge shutter was used on the Ti source to give a deposition profile consistent with the Ti source being positioned opposite to the Fe source, as shown by the arrow. This gave the desired linear variation of the Ti and Fe concentration along the tie line. A 45 ° angled wedge shutter was used on the Sr source to alter the deposition profile such that it could be varied in the direction perpendicular to that of the Ti-Fe concentration, as shown by the arrow. Ti (pellets, 99.995%, Testbourne) and Fe (granules, 99.95%, Testbourne) were deposited from electron-beam evaporators. The Sr (pieces, 99.9%, Testbourne) deposition was achieved from a Knudsen cell.

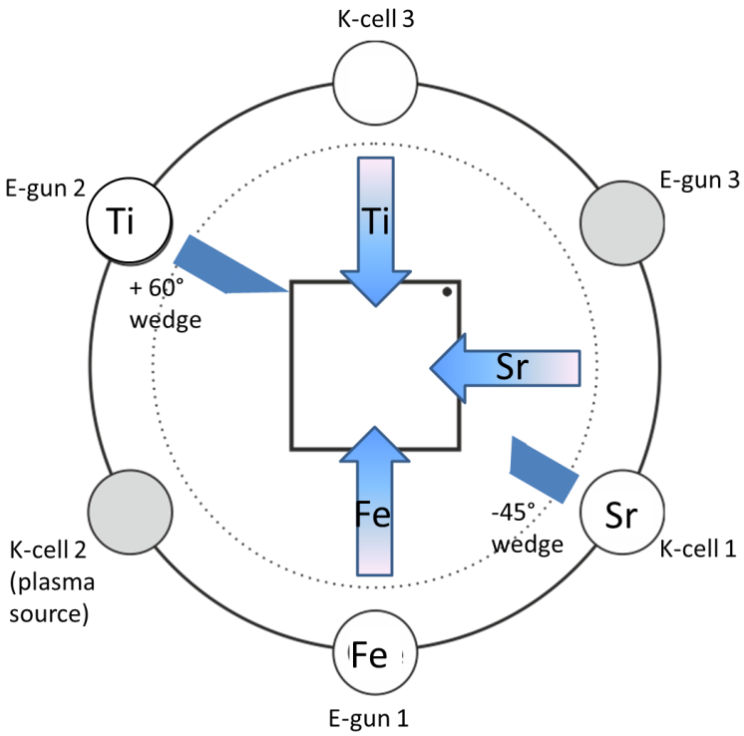

Figure 2-1: Schematic of the HT-PVD deposition chamber.

Uniform films can also be deposited by moving the shutters outwards to create as small as possible gradient in the deposition profile and rotating the sample to nullify the effects of the off-axis source positions on the deposition profile.

The thin films were deposited onto 35 x 35 mm substrates of Si and SiN for characterisation, the techniques used are summarised in **Table 2-1**. For electrochemical measurements the films were deposited onto electrochemical arrays, shown schematically in **Figure 2-2**. The arrays consist of 100 ITO electrode pads and tracks connecting to external contact pads with a layer of SiO_2 to prevent contact of the ITO tracks with the electrolyte. A deposition mask such as that shown on the right of **Figure 2-2** was used to limit the film deposition to the area of the electrode pads, the windows of the mask are slightly larger than the electrode pads to ensure that all the ITO is covered in the deposition. The ITO arrays were fabricated by Jin Yao.

Substrate	**Experimental Techniques**
Si	EDX, XPS, Raman
SiN	XRD, 4pp, Raman, EDX, XPS.
ITO chip	XRD, EDX, Electrochemistry.

Table 2-1: Summary of characterisation techniques.

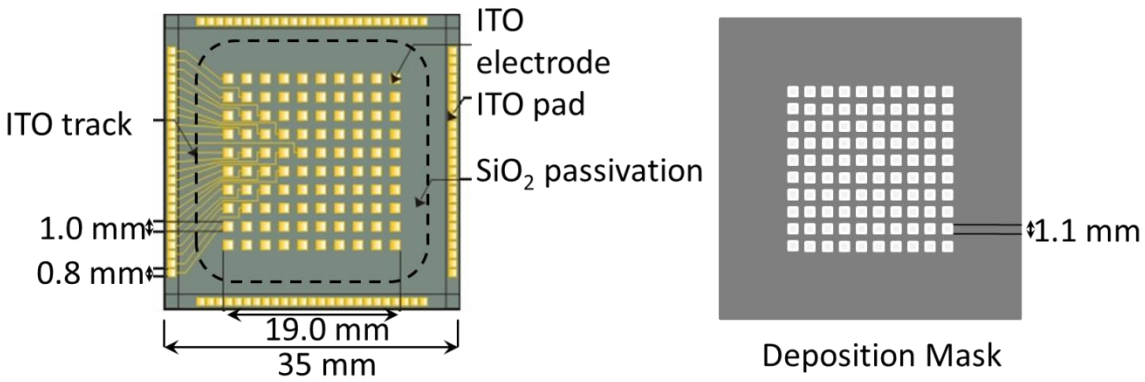

Figure 2-2: Schematic of electrochemical array shown alongside the deposition mask.

2.2 High-throughput characterisation methods

The thin film samples were characterised in high-throughput, in most cases data was taken at points corresponding to the 100 electrodes of the electrochemical array. The measurement points are shown for a continuous film in **Figure 2-3**. In most cases the instrumentation used for characterisation was equipped with an automated XY stage which allowed for mapping of the desired data points.

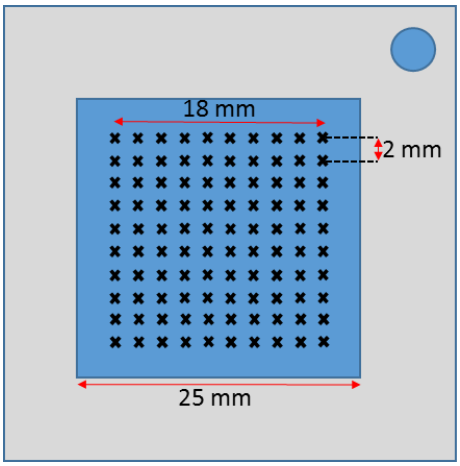

Figure 2-3: Schematic to show positions of measurement points on a continuous film.

2.2.1 Energy-dispersive x-ray spectroscopy (EDX)

Energy-dispersive x-ray spectroscopy (EDX) identifies elements present in a sample by measurement of their characteristic x-ray emission which arises from their unique atomic structures. An electron or x-ray beam is directed at the sample causing emission of a photoelectron. This leaves a hole in the inner shell which is filled by relaxation of an outer shell electron releasing energy in the form of an x-ray which is equal to the difference in the energy of the two shells. This is shown in **Figure 2-4**.

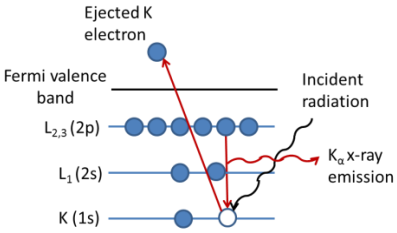

Figure 2-4: Schematic diagram of the x-ray emission arising from the relaxation of an outer shell electron into a hole created from photo-ionisation of the atom by ejection of a 1s electron.

The composition of the films was determined using an EDX micro-analyser (Oxford Inca 300) coupled with a scanning electron microscope (Jeol, JSM 5910) for surface imaging so that EDX measurements could be performed at specific known points on the sample, typically corresponding to the 100 discreet electrodes of the electrochemical array. The error in the compositions obtained from EDX measurements was estimated by taking 3 repeat measurements at the 4 corners of a thin film sample and was found to be around ± 2 at.% leading to an error in the determined x value, where x = Fe/(Ti+Fe), of ± 0.4.

2.2.2 Thickness measurements of STFO thin films

Measurement of the film thickness was undertaken by Jin Yao using a P16 Stylus Profiler (KLA Tencor).

2.2.3 X-ray photo-electron spectroscopy (XPS)

Photoelectron spectroscopy (XPS) was used to investigate the surface composition of the PVD deposited STFO thin films and the chemical state of the surface atoms which will both be of critical importance to the electrocatalytic activity.

In this technique the surface is bombarded with x-ray photons, of energy hν, ejecting core electrons from the surface atoms, as shown in **Figure 2-5**. Measurement of the kinetic energy, E_k, of these ejected electrons allows calculation of the binding energy of the electron, E_B, in accordance with the equation for the photo-electric effect shown in **Equation** 2-1, which also accounts for the work function of the spectrometer, W. The binding energy of the emitted photoelectron is the energy difference between the final electronic state following photo-ionisation and the initial electronic state. If no re-organisation occurs after photoemission then this equates simply to the orbital energy.

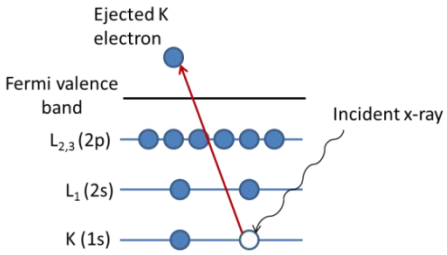

Figure 2-5: Schematic diagram showing photo-ionisation of an atom by emission of a 1s electron.

$$E_B = h\nu - E_k - W$$

Equation 2-1

The measurement of the XPS spectra were made under UHV conditions using a twin anode x-ray source (Al Kα and Mg Kα) and hemispherical analyser (VG clam) at constant analyser energy (CAE). For the STFO films with composition gradients an analyser energy of 50 eV was used and the analysis area was restricted to cover a radius of around 5 mm which would be the equivalent of 4 electrodes on the electrochemical chip. The sample stage could be moved to allow for analysis of compositions across the sample. For the uniform films of $SrTiO_3$ and $SrFeO_3$ a larger slit size could be used to increase the signal so a lower analyser energy of 20 eV was used to improve resolution.

2.2.3.1 Chemical state information

2.2.3.2 Initial State Effects

The initial electronic state of an atom can be altered by changes in oxidation state or chemical bonding and this will have an impact on the measured XPS binding energies [79]. If the change results in an increase in electron density on the atom, this will be observed as a lowering of the measured binding energies for the ejected photo-electron and vice versa. An increase in the oxidation state of a given element or chemical bonding to electronegative atoms would therefore both be expected to result in an increase in the binding energy of the ejected photo-electron when only initial state effects are considered. This is not always the case however as the energy of the final photo-ionised state must also be considered.

2.2.3.3 Final State Effects

The final electronic state is the (n-1)-electron state in which there is a core hole. Following photo-ionisation the remaining electrons re-organise to minimise the energy of the ionised atom by shielding the nuclear charge [79, 80]. The shielding can originate from the electrons on the photo-ionised atom or from electrons on the atoms surrounding the photo-ionised atom. The magnitude of the resulting reduction in the energy of the final state is known as the relaxation energy and results in a lowering of the measured binding energy. This relaxation energy will be different for atoms in different oxidation states and so this final state effect can disrupt the relationship between oxidation state and binding energy.

2.2.3.4 Spin-orbit coupling

Another effect of the final electronic state is the splitting of XPS peaks by spin-orbit coupling as observed for the Ti 2p XPS spectrum shown in **Figure 2-6**. Following photo-ionisation, the remaining electron in the core-level orbital can exist in either of two energetically equivalent final states i.e. spin up or spin down (s = ½, s = -½) as shown in **Figure 2-7**. A magnetic interaction between the spin of the electron (described by the quantum number s) and the orbital angular momentum (described by the quantum number l) leads to a splitting of the states and a consequent splitting of the peak in the XPS spectrum.

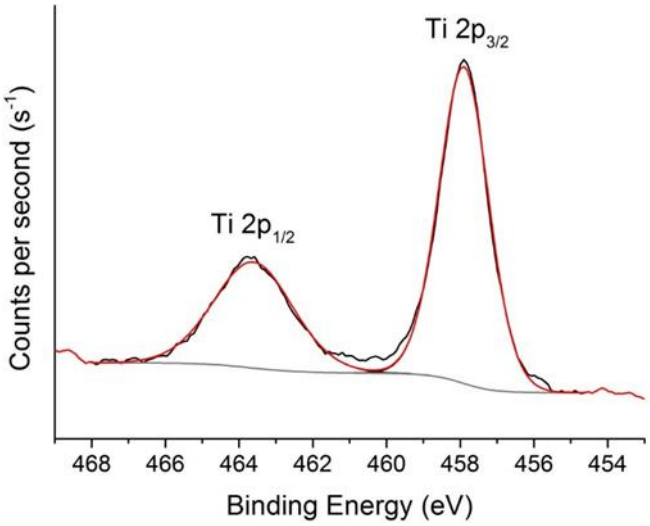

Figure 2-6: Ti 2p XPS spectrum for a uniform film of STO deposited by PVD at 650 °C under a 500 W oxygen plasma. The peak is split into a doublet by the effects of spin-orbit coupling. The peaks are labelled according to the quantum number j of the state.

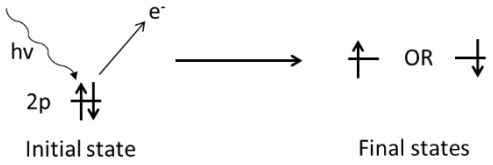

Figure 2-7: Effect of photo-ionisation on the spin state of the remaining electron.

The relative intensities of the doublet peaks are different for each sub-shell and are determined by the ratio of 2j+1 for each state where the total angular momentum quantum number, j, is equal to l + s. These are given in **Table** 2-2.

Subshell	j	Area ratio
s	-1/2, 1/2	No splitting
p	1/2, 3/2	1 : 2
d	3/2, 5/2	2 : 3
f	5/2, 7/2	3 : 4

Table 2-2: j quantum numbers and area ratios for doublet peaks for each sub-shell.

2.2.3.5 Peak fitting routine

Casa XPS was used for the fitting of XPS spectra. The peak fitting parameters included the appropriate area ratios for doublet peaks as indicated in **Table** 2-2 as well as appropriate constraints on the FWHM of the peaks. Fitting parameters are indicated in the discussion of the spectra.

2.2.3.6 Quantification of XPS spectra

Quantification of XPS spectra is possible using peak areas combined with relative sensitivity factors for the elements which are used to calibrate the measured signal by comparison with the signal obtained from the pure element. **Equation** 2-2 shows how the concentration of an element, A, in a compound may be calculated for the measured intensities of XPS signals for each element in the film, denoted by I, and the relative sensitivity factors for each element, denoted by I^{∞} [81]. The technique is however very surface sensitive with an analysis depth of 2-10 nm [82] in the case of thin films the formation of surface layers upon exposure to atmosphere or during annealing processes may mean that this surface composition is not representative of the bulk.

$$[A](atomic\ \%) = \frac{I_A/I_A^{\infty}}{\Sigma\, I/I^{\infty}}$$

Equation 2-2

Calculations based on the peak intensities of XPS spectra are subject to quite large degrees of error, up to 15-20%, due to the inaccuracy in the estimation of the peak intensity from the peak-fitted XPS spectrum [83].

2.2.4 X-ray diffraction

Identification of the crystal phases present in the sample was undertaken using XRD (Bruker D8). Powder diffraction patterns are usually represented as intensity versus the diffraction angle, 2θ. Each peak in the intensity represents diffraction from a particular lattice plane and the position of the peaks is determined by the spacing in the crystal lattice. Crystalline phases give sharp diffraction peaks whereas amorphous phases give broad backgrounds. The peak positions and relative intensities of the peaks provide a fingerprint for a particular crystalline phase. Phase identification is achieved by comparison of the pattern with known standards in a database such as the International Centre for Diffraction Data (ICDD) Powder Diffraction File (PDF). Further information can be obtained from the diffraction pattern including the unit cell parameters which are obtained from the peak positions and any distortions to the crystal lattice can therefore also be observed. Crystalline materials with unit cells of high symmetry such as cubic perovskites give simple well defined patterns in XRD.

Data was taken as an average of three measurements except for $SrTiO_3$ and $SrFeO_3$ data which is an average of 16 points across the uniform films. A major source of error in the measurement can be poor alignment of the sample which leads to uncertainty in the two theta peak position.

2.2.5 Raman Spectroscopy

Raman spectra were measured using a Raman microscope (Horiba Xplora) fitted with a 532 nm laser. The sample is illuminated with a laser beam, most of this radiation will be elastically scattered and is filtered out of the signal using a monochromator, inelastically scattered radiation which has been shifted in energy due to interaction with the sample is sent to a detector. The energy shifts in this radiation give information about the rotational and vibrational states and ultimately the bonding environments in the material.

Inelastic scattering resulting from photons interacting with electron density in the bonds of the material is known as Raman scattering. In order for Raman scattering to be observable there must be a change in the polarizability for a particular bond vibration or rotation [84]. For high symmetry crystal structures all Raman lines may be symmetry forbidden as is the case for undistorted cubic perovskites.

Raman spectroscopy can ultimately be employed for phase identification by matching the observed line positions to predictions from theory or to previously obtained results. The observation of additional un-predicted lines in the Raman spectra can also give an indication of lattice distortions.

2.2.6 Electrical Conductivity measurements

The conductivity of the STFO thin films was calculated from the sheet resistance, measured with a Model 280DI Four-Point Probe Mapping System (Four Dimensions) which uses the Van der Pauw 4-point probe method [85]. In this method a current is applied through the two outer probe tips and the voltage loss due to the sample resistance is measured across the two inner probe tips as shown in **Figure 2-8**. The probe used had a tip-pressure >60 g and the tip spacing, s, was 1 mm. The conductivity was calculated taking into account film thickness, obtained from profilometry measurements.

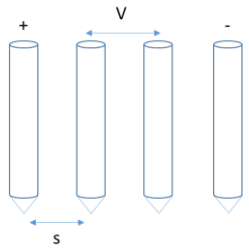

Figure 2-8: Probe arrangement for four-point probe measurements.

2.3 High-throughput electrochemical screening

The high-throughput electrochemical measurements were made using a three-compartment electrochemical cell specifically designed to accommodate the high-throughput electrochemical array [86]. An annotated photograph of the set-up is shown in **Figure 2-9**.

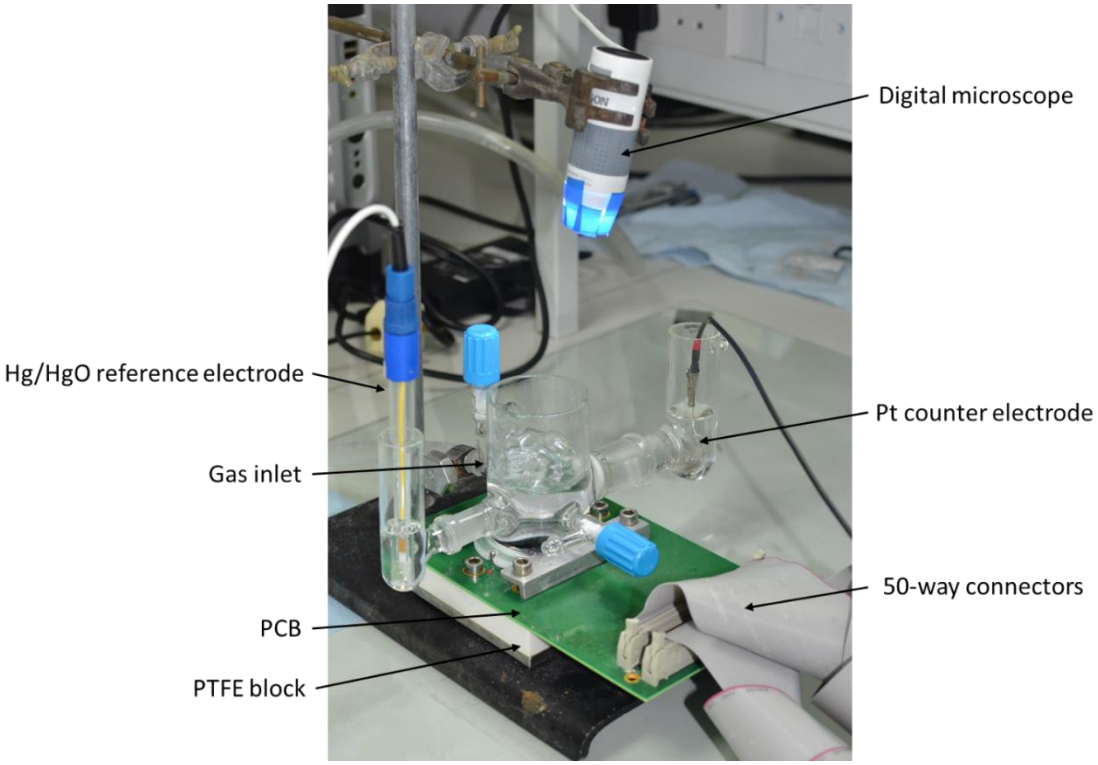

Figure 2-9: Set-up for electrochemical measurements showing three-compartment electrochemical cell.

The array is placed into a PTFE block as shown in **Figure 2-10** and an Au gasket is used to ensure electrical contact between the external pads of the array and the printed circuit board, PCB, which is placed over the array and secured in place as shown in **Figure 2-11**. The PCB connects the external contact pads of the array to a 100-channel potentiostat via two 50-way cables visible in **Figure 2-9**. The three-compartment glass electrochemical cell can then be attached to the PCB using a rubber gasket to ensure the electrolyte solution does not leak into the electrical connections. A Pt mesh was used as a counter electrode inside a compartment separated from the main cell by a glass sinter. A Hg/HgO reference electrode was mounted inside a luggin capillary to reduce the effects of IR drop.

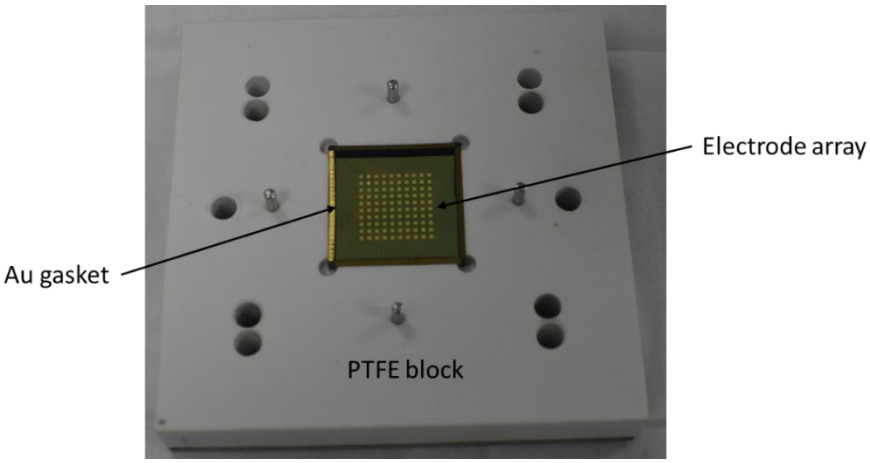

Figure 2-10: Electrode array in PTFE block with Au gasket.

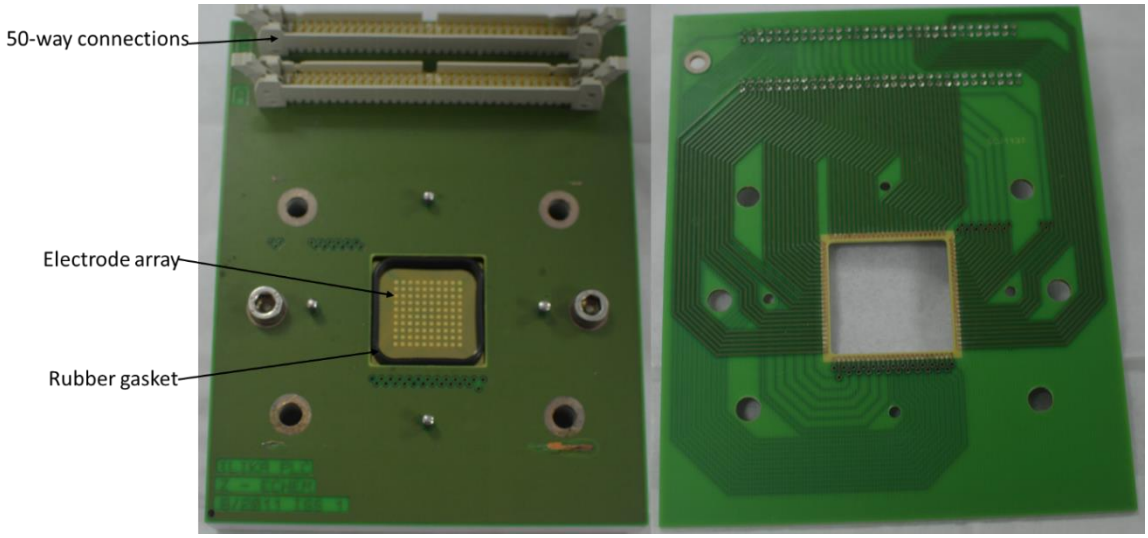

Figure 2-11: Printed circuit board, shown in contact with the electrochemical array and on the reverse with gold contacts and tracks visible.

A digital microscope mounted over the array cell allowed for photographs and videos of the electrode array to be taken during the electrochemical experiments, an example of which is shown in **Figure 2-12**. In this way any visual changes to the film caused by redox reactions or film degradation could be observed.

Figure 2-12: Photograph of electrode array taken during electrochemical experiments.

2.4 Data Analysis – Paradise

The analysis of high-throughput datasets was achieved in this work by the use of specialist software developed by Ilika Technologies. The software allows for the convenient determination of key parameters such as peak positions, peak intensity and integrated peak areas for each measurement position. The software also includes functions for the smoothing and background subtraction of the data-sets. Specific parameters used in the analysis of data will be included alongside data-sets.

2.5 Surface science methods

Ultra-high vacuum (UHV) conditions allow for the study of well characterised surfaces as the surface can be kept contaminant free. In fact, for a pressure of $1x10^{-10}$ mbar, it has been calculated that in the worst case scenario in which every atom which approaches the surface sticks, only a few percent of a monolayer of contaminant atoms will be present after one hour [87]. UHV also allows for the use of electron probing techniques such as XPS and LEED which are not possible under atmospheric conditions due to the scattering of electrons by gas molecules. The development of UHV analysis techniques has allowed catalytic processes including electrocatalytic reactions to be studied in atomic detail on well-defined surfaces. Studies on single crystal surfaces under UHV conditions provide insight into the activity of surface sites enabling us to relate catalytic activity to geometric as well as electronic effects, deepening our understanding of the surface reaction mechanisms. Single crystal studies are widely used to complement data obtained from computational methods since the well-defined single crystal surface can be conveniently modelled. In this way a wide range of surfaces can be screened for catalytic activity using the computational methods and a select number are then prepared and tested electrochemically to confirm the results.

2.5.1 The Electrochemical Transfer System

The experiments were performed in a UHV system with base pressure < 5 x10^{-10} mbar, a schematic of which is shown in **Figure 2-13**. The UHV electrochemical transfer system comprises two chambers, a surface science chamber equipped with LEED optics and an XPS system and an isolatable electrochemical chamber. The chamber is pumped by two turbo-molecular pumps, one associated with each chamber, backed by a rotary pump.

The single crystal sample was mounted onto a manipulator arm which allows transfer from the surface science chamber directly to the electrochemical chamber with no exposure to atmosphere. The surface science chamber remains under UHV conditions whilst the electrochemical chamber is vented to atmospheric pressure with Ar during the electrochemical experiments.

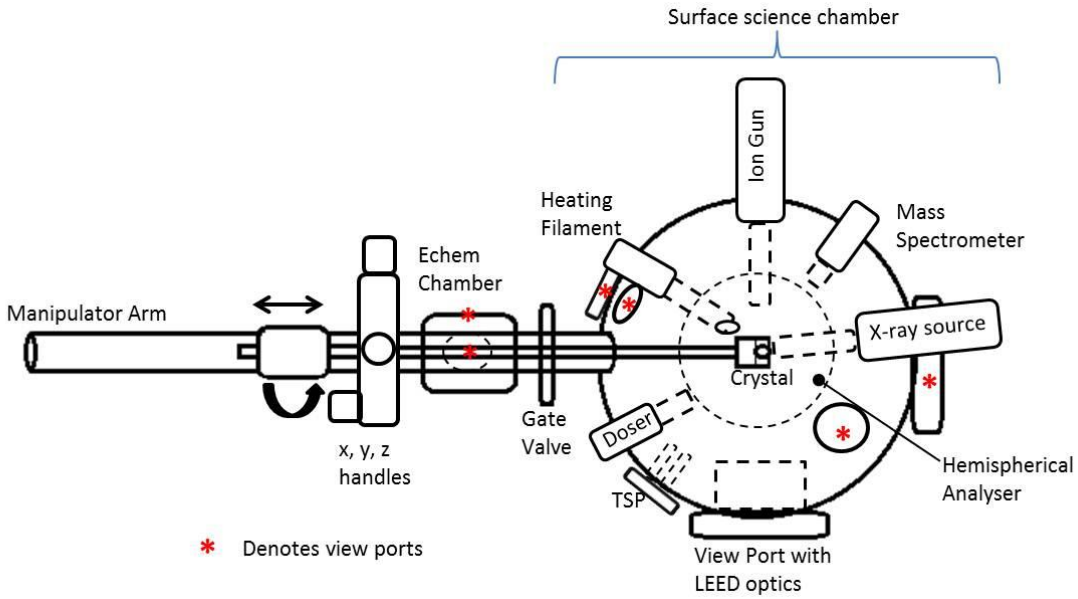

Figure 2-13: Schematic diagram of the transfer system.

2.5.1.1 Mounting of the STO single crystal

A 0.5 wt.% Nb doped $SrTiO_3$ single crystals with (110) orientation (± 0.2 °) was purchased from Pi-Kem Ltd. for use in the perovskite surface science electrochemical transfer studies. $SrTiO_3$ is one of the few perovskite materials available commercially as single crystals. It has the ideal cubic structure and is made conductive by low level Nb doping which renders it suitable for study by LEED and XPS. The as received (110) crystal has been mounted onto the transfer arm in a Ta boat as shown in **Figure 2-14**. A hole in the side of the crystal allowed for insertion of c-type thermocouple wire for monitoring of the crystal temperature during annealing processes.

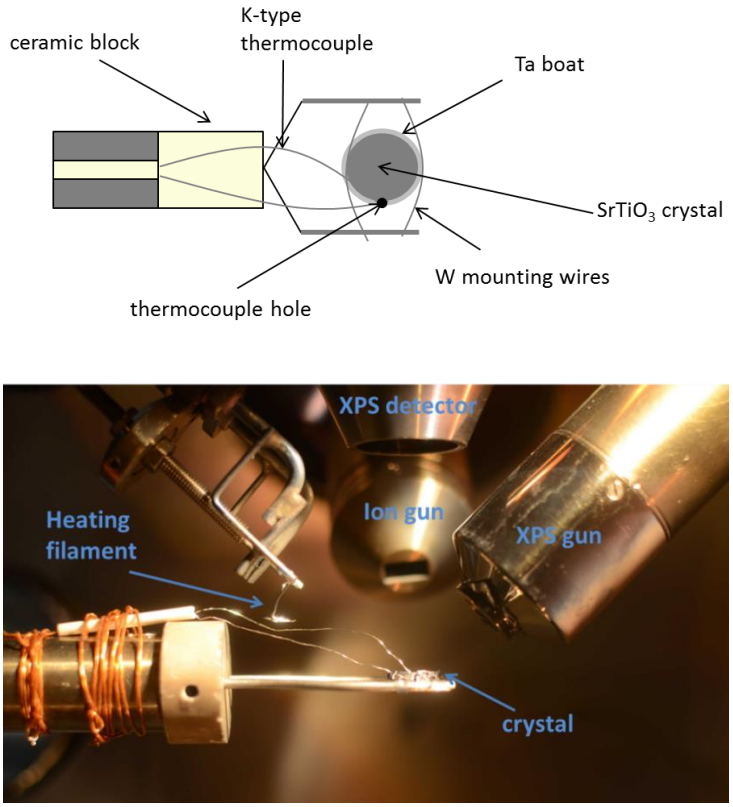

Figure 2-14: Schematic of the crystal mount (top) and view of crystal mounted inside the chamber (bottom).

2.5.2 Preparation of STO (110) surfaces

Several methods may be employed to remove surface contaminants and obtain a well-ordered surface. One such method of achieving this is by cleaving a sample, perhaps a long bar, in situ in order to create a new contaminant free surface. This method can be difficult to employ reproducibly and there is a tendency to create stepped surfaces. In addition there will clearly be a limit to the number of surfaces which can be cleaved from a single sample. Alternatively a single crystal sample which has been cut and polished to a high degree of accuracy can be cleaned in situ using annealing and ion bombardment techniques to create a contaminant free surface.

Annealing a sample removes surface contaminants by desorption but strongly bound adsorbates may not desorb at temperatures below the melting point of the sample and in this case ion bombardment may be used. Ar^+ ions are usually used to bombard the surface and remove layers of atoms. Clearly this method is destructive and the resulting surface whilst free of contaminant will be damaged. Since the contaminant may be less easily sputtered than the sample many layers may have to be removed and certain elements may be removed preferentially leaving holes in the sample surface and Ar atoms embedded. The sample will require subsequent annealing to restore order which could result in contaminants from the bulk diffusing to the surface. It is therefore common for many cycles of sputtering and annealing to be employed in order to create a clean and ordered surface.

Carbon impurities were removed from the surface of the STO (110) crystal by cycles of Ar^+ sputtering at 3 kV (2 mA emission current) and flash annealing at 875 K in 1 x 10^{-7} mbar O_2.

2.5.3 Preparation of STO(110)-Fe Surface Alloys

Fe was deposited onto the clean STO surface from a doser, the design of which is detailed in **Figure 2-15**. The Fe doser consisted of a hairpin tungsten filament (0.7 mm diameter, ≥99.95% purity) wrapped tightly with Fe wire (0.5 mm diameter, ≥99.998% purity) surrounded by a steel shield. Fe was dosed for 2 minutes at ca. 975 K onto the clean STO surface. A clean surface which had undergone Ar^+ sputtering (1 kV, 2mA, 0.3 µA drain current) was also treated with the same Fe dose. Although no difference was seen in the XPS spectra before and after the Ar^+ sputtering it was expected that the sputtering process would roughen the surface and improve the incorporation of Fe.

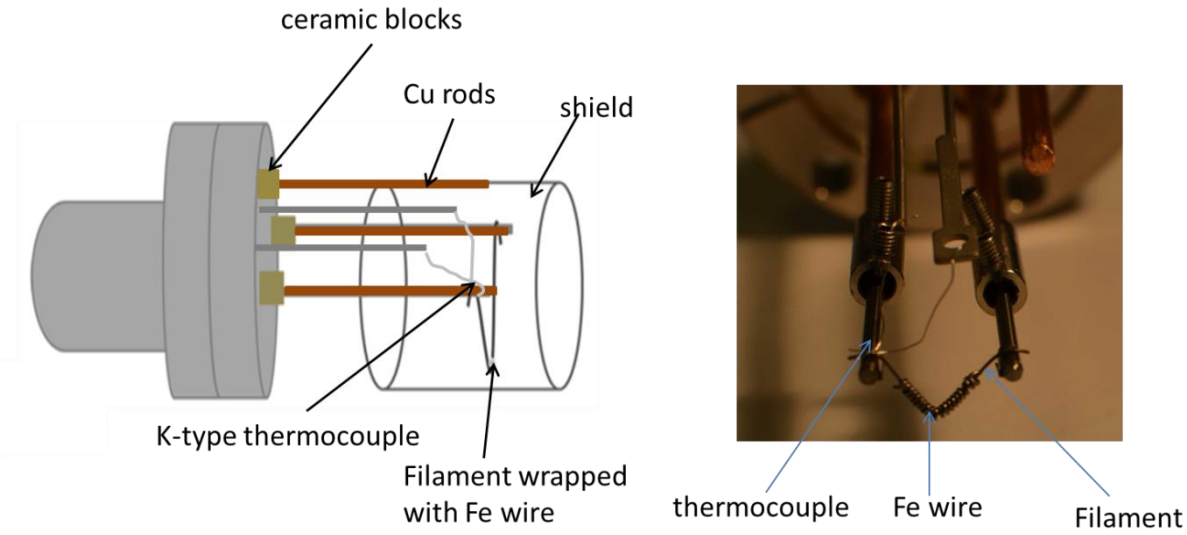

Figure 2-15: Schematic of Fe doser and labelled photograph.

2.5.4 XPS Characterisation of STO (110)-Fe Surface Alloys

Photoelectron spectroscopy (XPS) was used to investigate the surface composition of the Fe dosed $SrTiO_3$. The measurement of the XPS spectra were made under UHV conditions using a twin anode x-ray source (Al Kα and Mg Kα) and hemispherical analyser (VG clam) at a constant analyser energy (CAE) of 20 eV. Background theory relating to the XPS technique was discussed in **Section 2.2.3**.

Quantification of the amount of Fe dosed onto the STO surface requires a different method to that of the mixed alloy discussed in **Section 2.2.3.6** since the XPS technique is surface sensitive and a larger signal will be obtained for the top Fe layer compared to the underlying STO layer. The amount of Fe dosed on the STO surface was therefore estimated using a method devised by Briggs and Seah [82] for the calculation of the thickness of an overlayer of an adsorbate, A, on a substrate, B. This method attempts to account for the difference in the signal observed from the adsorbate layer relative to the underlying substrate by accounting for the inelastic mean free path of the electron through the adsorbate layer, λ_A. λ_A was calculated according to **Equation** 2-3 where E is the energy of the electrons above the Fermi level in eV obtained from the kinetic energy of the peak and a is the thickness of a monolayer of the adsorbate.

$$\lambda_A = \frac{532}{E^2} + 0.41(aE)^{1/2}$$

Equation 2-3

The thickness of the overlayer in nm, d_A, was then calculated according to inelastic mean free path of the electrons through the overlayer, A, calculated according to **Equation** 2-4 where θ is the angle of emission, I_A and I_B are the intensities of the peaks due to the adsorbate and substrate respectively and I_A^∞ and I_B^∞ are the relative sensitivity factors for A and B as discussed in Section 2.2.3.6.

$$d_A = -\lambda_A \cos\theta \; ln\left(\frac{I_A^\infty \times I_B}{(I_A \times I_B^\infty) + (I_A^\infty \times I_B)}\right)$$

Equation 2-4

In the prepared surfaces where Fe is incorporated into the STO by annealing processes the quantification method described in **Section 2.2.3.6** was used under the assumption that the Fe penetrated into the topmost layers. Since it is likely that the majority of the Fe will remain in the upper layers and will not be uniformly distributed up to the analysis depth this assumption introduces a large degree of error. The compositions given in the results section are therefore purely for comparison between the surfaces.

2.5.5 LEED Characterisation of STO(110)-Fe Surface Alloys

The structure of the prepared STO and Fe dosed STO surfaces was determined using LEED. In this technique a beam of low energy electrons is directed at the surface. The electron beam is scattered by the surface atoms and the diffraction is observed as spots on a phosphor screen. When an electron is scattered by an atom, the scattered electron will interfere with electrons scattered by adjacent atoms. If the electrons are in phase they interfere constructively according to Bragg's law shown in **Equation** 2-5 where nλ is an integral number of wavelengths and d is the interatomic spacing in the direction defined by the scattering angle θ.

$$n\lambda = 2dsin\theta$$

Equation 2-5

A retarding field analyser blocks inelastically scattered electrons from the detector which would result in a high background. Constructive interference of the elastically scattered electrons gives diffracted beams of electrons which, if the surface is sufficiently well ordered, are observed as clear spots on the screen. The diffraction pattern observed on the screen corresponds to the reciprocal lattice of the real space surface. Standard notation for LEED patterns of surface reconstructions [88] was used where STO (110)- (nxm) indicates a reconstruction of periodicity nxm relative to the periodicity of the underlying STO (110) surface.

The size of the unit cell of the perovskite lattice in real space was estimated for the surfaces by comparison with a LEED image taken on a W (100) surface using the same instrument and conditions. Crucially all of the analysed LEED patterns were obtained at the same beam energy of 100 eV. The unit cell of the W (100) surface is cubic with a lattice parameter, a, of 3.16 Å. The reciprocal lattice parameter a* was calculated according to **Equation** 2-6 and the relationship between this value and the distance measured between the spots on the LEED image was used to provide a conversion factor for determining the lattice parameters of the STO surfaces.

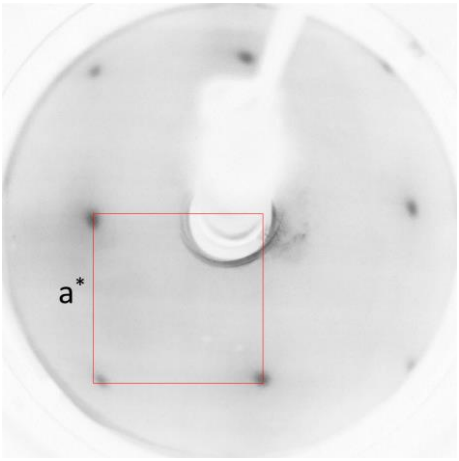

Figure 2-16: LEED image of the clean W (100) surface taken at 100 eV. Red box shows reciprocal unit cell where a^* is the reciprocal of the unit cell parameter, a.

$$a^* = \frac{2\pi}{a}$$

Equation 2-6

2.5.6 LEISS Characterisation of STO(110)-Fe Surface Alloys

Low Energy Ion Scattering Spectroscopy (LEISS) is capable of providing both compositional and structural information from the surface. LEISS is also very surface specific with the possibility of restricting the signal obtained to the top surface layer alone.

In a LEISS experiment a beam of ions, usually H^+, Ne^+ or Ar^+, is directed at the surface in a well-defined direction. A schematic of the scattering which takes place when an ion of mass M_1 and energy E_0 approaches a surface atom is shown in **Figure** 2-17. The energy of the scattered ion, E_1, may be determined by **Equation** 2-7 [87]. An incident ion of mass, M_1 and energy, E_0 striking a surface atom of mass M_2 will be scattered by an angle, θ_1. Since these values are fixed, measurement of the energy of the scattered ions, E_1, gives the mass of the surface atom, M_2, from which they have been scattered.

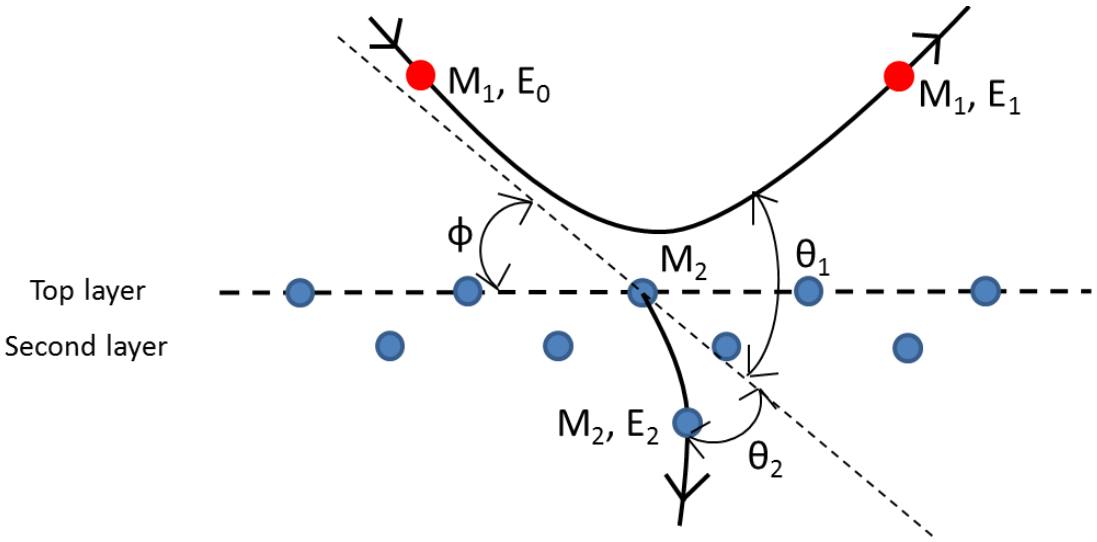

Figure 2-17: A schematic diagram showing the scattering of incident ion of mass M_1 and energy E_0 by a surface atom of mass, M_2

$$\frac{E_1}{E_0} = \frac{1}{(1+A)^2}\left[(\cos\theta_1) \pm (A^2 - sin^2\theta_1)^{1/2}\right]^2 \quad where\ A = {}^{M_2}/_{M_1}$$

Equation 2-7

LEISS has greater surface specificity than XPS and as such was used to confirm the surface cleanliness. A qualitative analysis of the surface, particularly in terms of the confirmation of the successful deposition of Fe was also possible. Whilst quantitative analysis is possible in LEISS there would be a high degree of error in such a calculation. Structural analysis is also possible for adsorbates on simple metal surfaces [89] by variation of the impact angle, ϕ, which changes the degree to which atoms in the topmost layer block scattering from atoms in lower layers and can allow identification of the relative positions of the atoms. Such an analysis would be very complicated for a mixed oxide due to the number of different atoms present.

2.5.7 Electrochemical Screening of STO(110)-Fe Surface Alloys

In order to evaluate the electrocatalytic activity of the prepared STO and Fe-dosed STO surfaces the prepared crystal was transferred to the electrochemical chamber which was then isolated from the surface science chamber and filled to atmospheric pressure with high purity argon. The electrochemical cell was then attached and filled with 0.1 M KOH electrolyte.

Figure 2-18 (left) shows the electrochemical cell which contains a Pd/H reference electrode, a Pt foil counter electrode and a Pt working electrode. The cell attaches via a set of bellows beneath the electrochemical chamber which allow movement of the cell towards the crystal. Electrochemical contact is achieved by forming a meniscus of electrolyte just above the opening of the cell and approaching close to the crystal. **Figure 2-18** (right) shows the view of the crystal within the chamber with the top of the electrochemical cell visible at the bottom of the window.

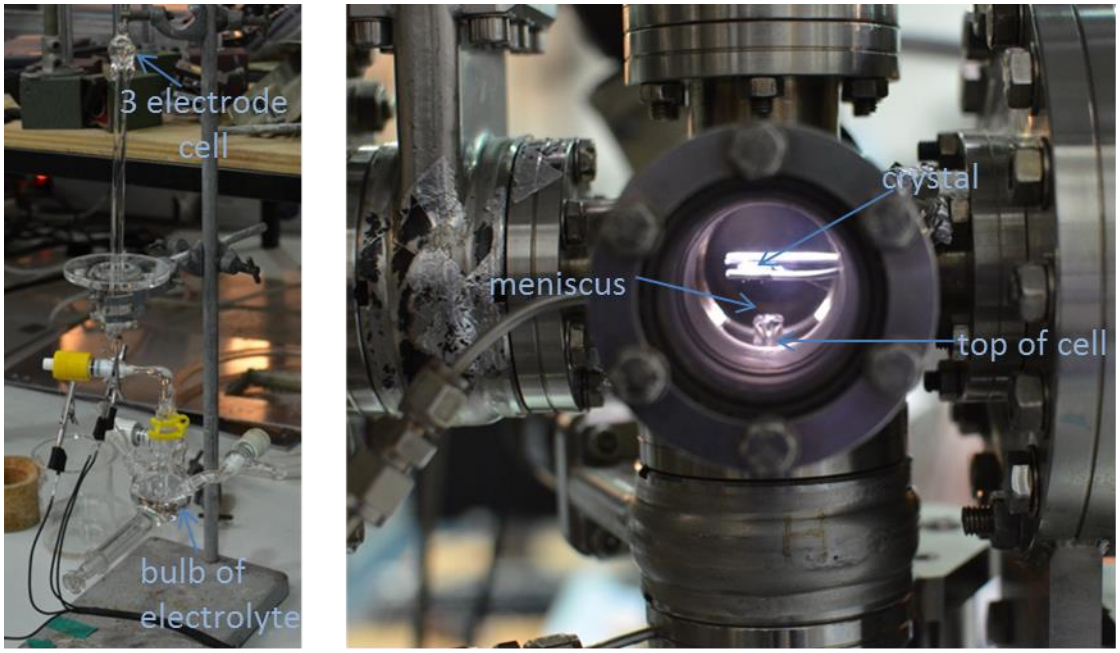

Figure 2-18: Left – the electrochemical cell set up on the bench. Right - electrochemical chamber showing the crystal with the top of the electrochemical cell visible.

Cyclic voltammetry experiments were performed using a portable potentiostat (PG 581, Uniscan). The Pd/H reference electrode was charged by cycling at negative potentials, typically by application of -0.7 V to -0.9 V for 10 minutes. The Pt wire electrode was used to verify that the potential of the Pd/H reference was 0.05 V_{RHE} both before and after electrochemical testing of the crystal surface. The electrolyte was 0.1 M KOH made using KOH pellets (Fischer, ≥95%) and ultra-pure water (18.2 MΩ, ELGA).

Chapter 3: High-throughput synthesis of perovskite libraries

3.1 Introduction

3.1.1 The perovskite crystal structure

The ABO_3 perovskite crystal structure is shown from two views in **Figure 3-1**. The adoption of this structure is based largely on the relative sizes of the A and B site cations although clearly the charge of the cations must also balance. Due to the size restrictions of the perovskite crystal structure the A site cation is typically a large lanthanide or alkaline earth such as La, Ca or Sr whilst the B site cation is often a first row transition metal. The B-site transition metal ions, shown in blue, form corner sharing BO_6 octahedra whilst the large A-site counter cation, shown in green, sits in a 12-coordinate cuboctahedral site.

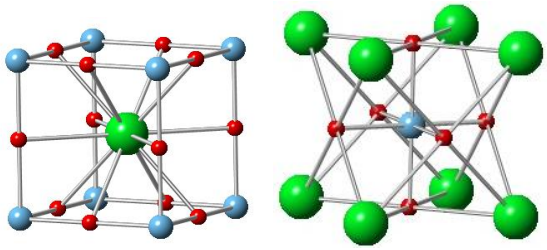

Figure 3-1: Schematic views of a cubic perovskite, ABO3, drawn using CrystalMaker. The "A" atom is shown in green, the "B" atom in blue and the oxygen atoms in red. On the left of the figure the 12-co-ordinate A-site cation is shown in the centre whilst on the right the octahedral B-site cation is shown in the centre.

3.1.2 Electrical properties of perovskites

Perovskite materials have been reported to have both high electronic and ionic conductivities and many including STFO have mixed conductivity. The electronic conductivity usually arises from electron-hopping between B-site cations of difference valence as shown in **Figure 3-2A**. This requires a B-site cation which is capable of adopting different oxidation states as is the case for many transition metals including Fe and Mn.

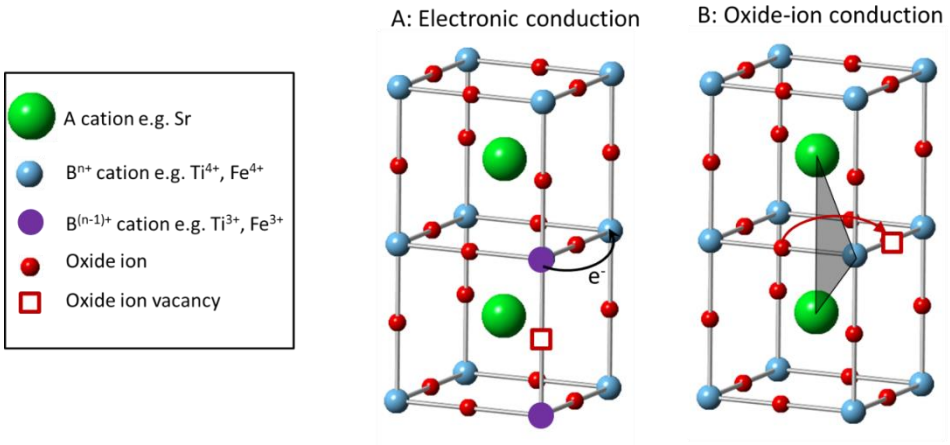

Figure 3-2: Schematic showing (A) electronic conduction and (B) oxide ion conduction through the perovskite lattice. Electronic conduction occurs by "electron hopping" between B site cations of different valencies. Oxide ion conduction requires movement of an oxide ion into a vacant site, the path of the oxide ion is shown by the red arrow and is restricted at the point shown by the shaded triangle.

Electronic conductivity depends upon the movement of charge carriers through a material and as such the general expression for conductivity, shown in **Equation** 3-1, shows the dependence upon the concentration of charge carrying electrons and holes, represented by n and p respectively, and their mobility through the solid, μ_e and μ_h. The final term, e, represents the charge of an electron. A material with high electronic conductivity requires a high concentration of charge carriers and a structure which permits their movement through the solid.

$$\sigma = n\,\mu_e\,e + p\,\mu_h\,e$$

Equation 3-1

Oxide ion conductivity arises in perovskite materials through the presence of mobile oxygen vacancies in the lattice. **Figure 3-2B** shows the movement of an oxide ion into a vacant site in the lattice, the shaded area shows the narrowest point which the ion must pass through to reach the vacant site. In most perovskites this area is smaller than the radius of the oxide ion and relaxation and thermal vibration of the ions is assumed to help the ion pass. Structural factors such as increasing the unit cell parameter, a, can therefore influence ionic conductivity. Distortions to the lattice usually disfavour oxide ion conduction since the oxide sites become inequivalent which increases the energy barrier to oxide ion conduction between the sites [90].

Large alkaline earth metals such as Sr or Ca can act as the A site cation in perovskites and substitution of these ions into the lattice is one way of improving the conductivity. Since these ions have a charge of +2, rather than +3 which is found in the La perovskites, there must be charge compensation either electronic, by an increase of the charge on the B ion from +3 to +4, or ionic, by the introduction of oxygen vacancies.

In the case of electronic charge compensation, partial substitution of a trivalent A site cation with a divalent cation would lead to B site cations in both the +3 and +4 oxidation states. The TM^{3+}/TM^{4+} couples can act as sites for electron (or hole) hopping for n (or p) type conductivity. A maximum number of these sites would be expected for 50% replacement of the trivalent ion leading to a 1:1 ratio of TM^{3+}/TM^{4+} if only electronic charge compensation occurs. This is roughly the situation for $La_{1-x}Sr_xMnO_3$ the oxidation state of the Mn ion increases from +3 to +4 with increasing Sr content, x. Experimentally the conductivity actually drops from $LaMnO_3$ to $La_{0.6}Sr_{0.4}MnO_3$ before increasing up to $SrMnO_3$ [62]. There is a structural transition between cubic $LaMnO_3$ and hexagonal $SrMnO_3$ since the increase in the proportion of smaller Mn^{4+} ions creates strain in the perovskite structure.

As mentioned above charge compensation can alternatively occur via the formation of oxygen vacancies. The charge compensation mechanism which occurs depends on the ability of the metal cation to donate an electron to the oxygen ligand. Later transition metals including Fe, Co and Ni are more electronegative and less able to donate electrons, this leads to weakly bound lattice oxygen and a tendency to form oxygen vacancies [91].

3.1.3 STFO perovskites

The perovskite libraries produced in this work are based on $SrTi_{1-x}Fe_xO_3$ (STFO) which forms a cubic perovskite structure across the compositional range from $SrTiO_3$ to $SrFeO_3$. For these materials the large Sr^{2+} cation occupies the A-site of the perovskite lattice whilst Ti and Fe cations share the B-site lattice positions in a ratio determined by x. The structure of these materials will be discussed further in **Chapter** 4**:**

In order to favour the formation of the perovskite crystal structure, materials must be synthesised with a 1:1 ratio of suitable A-site and B-site cations. For the STFO materials where both Ti and Fe can occupy the B-site lattice positions this means that the proportion of Sr atoms in the material should be equal to the total number of Ti and Fe atoms i.e. Sr at.% = Ti at.% +Fe at.%.

Figure 3-3 shows two methods for plotting the pseudo-ternary composition of the STFO perovskite materials to demonstrate this requirement. Firstly the variation in Sr, Ti and Fe content is shown with increasing x to demonstrate how the pseudo ternary Sr content of the film remains at 50 at.% whilst the Ti content decreases from 50 at.% at x = 0 ($SrTiO_3$) to 0 at.% at x = 1 ($SrFeO_3$) and the Fe content increases in a complementary fashion. The same relationship is shown by a ternary diagram in which the red-dashed line represents the $SrTi_{1-x}Fe_xO_{3-y}$ compositional tie line where Sr = 50 at.%.

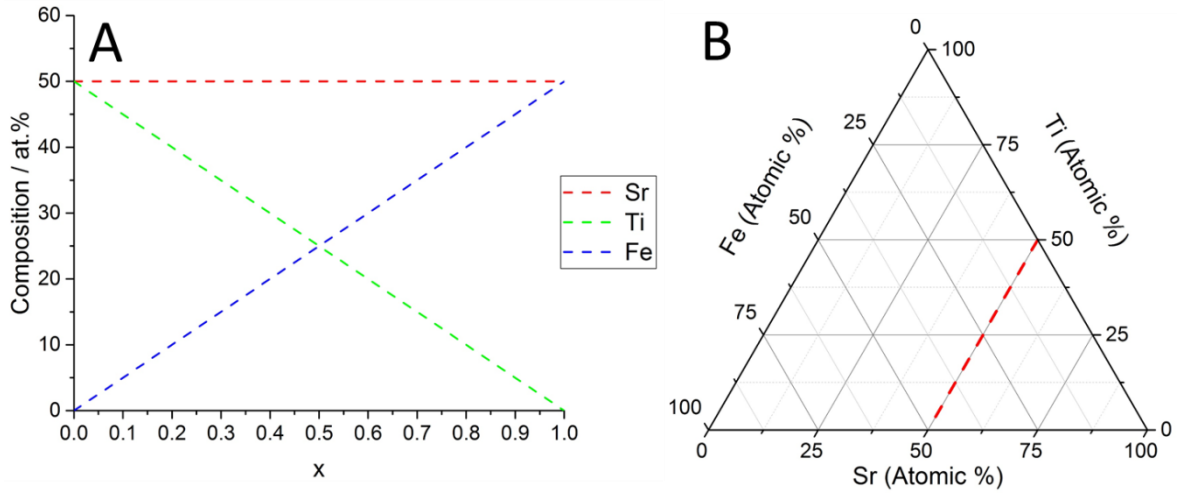

Figure 3-3: Two graphical representations of the pseudo-ternary composition of STFO perovskites. In (A) the variation in the proportion of Sr, Ti, and Fe atoms in at.% is shown with increasing x along the $SrTi_{1-x}Fe_xO_{3-y}$ compositional tie-line. In (B) the same information is plotted as a ternary diagram where the red dashed line represents the $SrTi_{1-x}Fe_xO_{3-y}$ compositional tie-line.

3.1.4 Oxygen-deficient STFO

In a fully oxidised $SrTi_{1-x}Fe_xO_3$ perovskite the Ti and Fe cations both have a formal +4 oxidation state. STFO is however also able to adopt the perovskite crystal structure with a proportion of Fe in the Fe^{3+} oxidation state. In these oxygen deficient $SrTi_{1-x}Fe_xO_{3-y}$ perovskites every two Fe^{3+} ions is charge balanced by the presence of an oxygen vacancy, the number of such vacancies is denoted by y. Fully reduced STFO perovskites in which all of the Fe adopts the formal Fe^{3+} oxidation state are also stable [92, 93], these materials are represented by the formula $SrTi_{1-x}Fe_xO_{3-0.5x}$.

In fact the oxygen deficient STFO perovskites form quite readily since the Fe^{3+} oxidation state has the favourable d^5 half-shell electronic configuration and is the preferred oxidation state for Fe, occurring in the main oxide Fe_2O_3. The Fe^{4+} oxidation state is by contrast not common and the adoption of this oxidation state in STFO is thought to rely on the high covalent character of the Fe-O bonding which results in charge transfer from the oxygen ligands leading to a predominately $d^5\underline{L}$ electronic ground state, where $\underline{L}$ represents a ligand hole [94]. This can be considered as the transfer of an electron from the oxygen ligand to Fe ion as shown in **Equation** 3-2.

$$Fe^{4+} - O^{2-} \leftrightarrow Fe^{3+} - O^{-}$$

Equation 3-2

The oxygen content of STFO perovskites has a significant impact on the observed properties and as such several studies have attempted to estimate the oxygen content of STFO perovskites synthesised under varying conditions. One method for determination of the oxygen content is the iodometric titration of the dissolved material using HI [92, 95, 96]. Mossbauer spectroscopy has also been used to determine the relative amounts of Fe^{4+} and Fe^{3+} in $SrTi_{1-x}Fe_xO_{3-y}$ by fitting of the spectra into components corresponding to Fe ions in distinct chemical environments [58, 95-97]. Agreement between oxygen contents determined using these two methods has been demonstrated [95, 96].

3.1.5 Electrical properties of STFO

Many studies have reported that the electronic conductivity of STFO improves with increasing Fe content [59, 65, 92]. This can be rationalised by the consideration of the electronic structures of the Ti^{4+} and Fe^{4+} cations. The Ti^{4+} cation has a closed shell d^0 electronic structure, this electronic structure is highly stable and the movement of electrons is not favoured. As a result STO is a wide band gap semi-conductor at room temperature [57] with an electronic band structure as shown in **Figure 3-4**. The Fermi-level (E_f) lies in the centre of the band gap and there are no available states for electron transfer.

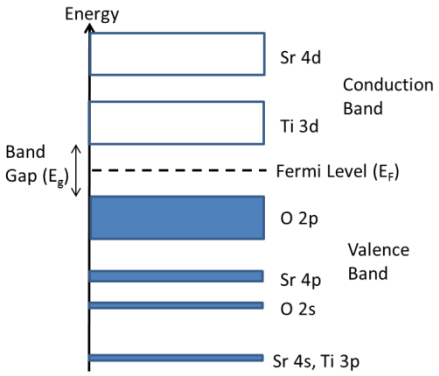

Figure 3-4: Electronic band structure of undoped $SrTiO_3$.

The Fe^{4+} cations in STFO have a d^4 electronic structure in which the d-orbital is split into lower energy, t_{2g}, and higher energy, e_g, orbitals by the effects of the oxygen ligand co-ordination, as shown in **Figure 3-5**, to give a $t_{2g}^3 e_g^1$ electronic structure.

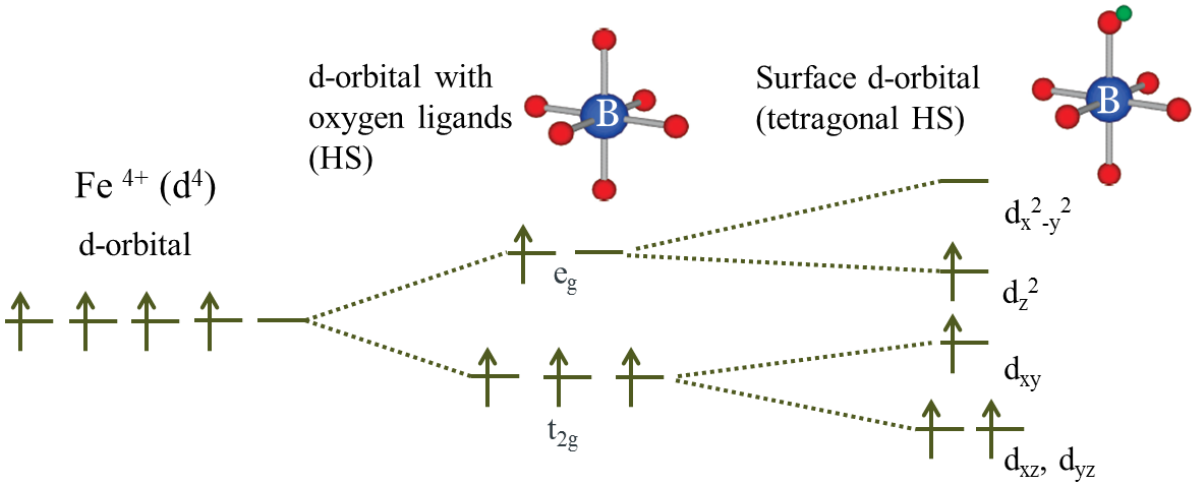

Figure 3-5: Electronic structure of the Fe^{4+} cation in the octahedral B-site of a perovskite lattice. The d-orbital is split into anti-bonding e_g and bonding t_{2g} orbitals by the effects of ligand field splitting. At the surface a tetragonal distortion splits the orbitals further.

As mentioned earlier the unusual Fe^{4+} oxidation state in STFO is stabilised by highly covalent Fe-O bonding which allows charge transfer from the oxygen ligands and an electronic ground state which is better described as $d^5\underline{L}$ rather than d^4. The electron transfer occurs through the overlap of the e_g electronic orbital of the Fe ion with the sp_σ orbital of the oxygen ligand. In terms of the electronic band structure this leads to the formation of a broad σ^* conduction band as shown in **Figure 3-6** for SFO. The band is partially filled and E_f lies within the band such that there are available electronic states close to E_f for electron transfer and metallic conductivity has been observed for SFO [98, 99].

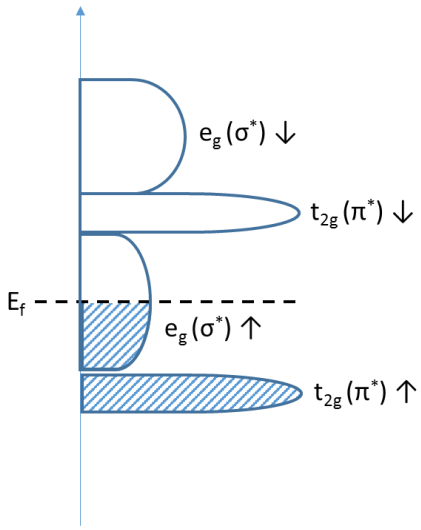

Figure 3-6: Schematic band diagram for SFO.

Consideration of the band structure of the mixed STFO system can be approached in two ways, either the effect of the addition of Fe to STO or conversely the addition of Ti to SFO. In the case of Fe addition to STO, calculations by Evarestov *et al.* [100] have identified two dopant regimes for the oxidised $SrTi_{1-x}Fe_xO_3$ material. At low dopant concentrations, $x < 0.03$, the valance d-electrons are localised at the Fe dopant centres whilst at dopant concentrations above $x = 0.03$ the electronic states are able to overlap and the d-electrons are delocalised. This leads to the formation of additional electronic bands in the band gap close to the Fermi level, providing states for electron transfer and explaining the increase in electronic conductivity [100, 101].

In the case where Ti is added to SFO the empty Ti 3d states would be expected to lie at higher energy leading to no overlap with the Fe 3d and O 2p states. The effect of the Ti ions would be to disrupt the conduction path through the Fe-O bonds. In terms of the band structure this decreases the overlap of the Fe 3d states which introduces a band gap.

3.1.6 STFO synthesis routes

The general synthesis methods for perovskite oxides were discussed in Section 2.1 but the methods used to synthesise STFO will be discussed here with a focus on the properties of the materials produced.

The synthesis of STFO perovskites has been achieved by high temperature solid state reactions using $SrCO_3$, TiO_2 and Fe_2O_3 powders as precursors [58, 65, 92, 102]. The powders are mechanically mixed and calcined in a furnace at high temperatures, typically 1200 °C for at least 10 h. Another commonly used method for preparation of STFO perovskites is a liquid-mix technique [59, 93, 103] in which Sr, Ti and Fe salts are mixed in citric acid solution with ethylene glycol to form a polymer precursor which must then also be calcined using similar temperatures and durations as for the simple mixed oxide method. This method should provide a more homogeneous material however due to the more intimate mixing of the elements.

The calcination using either method is usually under an air atmosphere and generally produces an oxygen deficient material with a proportion of the Fe ions in the Fe^{3+} oxidation state [59, 65, 93]. Preparation of the fully reduced $SrTi_{1-x}Fe_xO_{3-0.5x}$ perovskites has been achieved by calcination under Ar [93] or N_2 [92]. In order to produce fully oxidised STFO perovskites high pressure oxygen annealing, up to 60 MPa O_2 [58, 104] or heating with an oxidant such as $KClO_4$ [94] is required.

An alternative method for obtaining the oxidised material is electrochemical oxidation as first proposed by Wattiaux *et al.* [96] for the preparation of $SrFeO_3$. It was demonstrated that a highly oxygen deficient sample prepared using the methods described above with calcination in Ar could be oxidised by application of a potential of 1.3 V at room temperature for 60 h in 1 M KOH solution using a standard 3 electrode cell set-up. The oxygen content of the reduced perovskite precursor was confirmed as $SrFeO_{2.5}$ using both iodometric titration and Mossbauer spectroscopy.

The intercalation of oxygen into the perovskite lattice is an important property which has implications for the oxygen electrocatalytic activity. This will be discussed in more detail in Chapter 5 where results regarding the redox electrochemistry of the STFO materials prepared in this work will be presented.

STFO has previously been prepared as a thin film using pulsed laser deposition (PLD) [105, 106]. Since this method requires the preparation of a solid target using one of the methods described above prior to the ablation of the target in UHV for the deposition of the thin the studies are limited in the number of compositions which can be conveniently prepared. Jung and Tuller [106] deposited STFO perovskites with x = 0.35 and x = 0.5 by the PLD method with a substrate temperature of 700 °C and an oxygen pressure of 7 x 10^{-3} mbar which they increased post-deposition to 8-9 mbar to improve the oxidation of the film. They do not however investigate the oxygen content of the thin films produced by this method. Yu *et al.* [105] deposited STFO perovskites with x < 0.01 by PLD using a substrate temperature of 700 °C and an oxygen pressure of 0.1 mbar.

As discussed in **Section 2.1**, the HT-PVD method used in this work allows for a lower formation temperature of the perovskite phase by the use of atomic sources which gives intimate mixing of the elements. In addition an oxygen plasma source was used which provides a high oxygen chemical potential during the reaction and should aid in the formation of oxidised films.

3.2 Results

3.2.1 Pseudo-ternary composition

Data from SEM-EDX measurements was used to determine the composition of the STFO films deposited by PVD. The deposition was successfully optimised to produce thin film samples with compositions close to the STFO tie-line as shown in **Figure 3-7**. The samples will be termed "tie-line" samples.

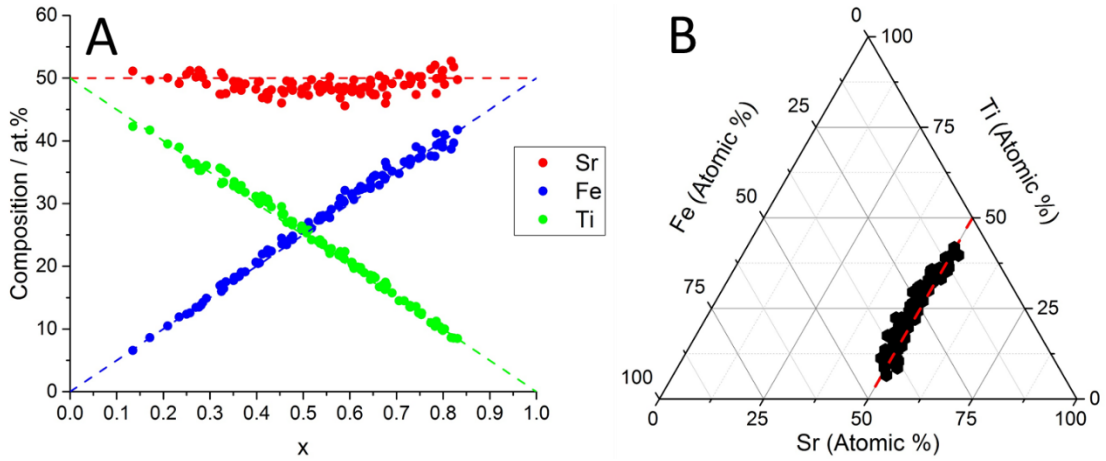

Figure 3-7: Two graphical representations of the pseudo-ternary composition of a STFO perovskite thin film deposited by PVD at 650 °C under an oxygen plasma source obtained by EDX. In (A) the variation in the proportion of Sr, Ti, and Fe atoms in at.% is shown with increasing x along the $SrTi_{1-x}Fe_xO_{3-y}$ compositional tie-line. In (B) the same information is plotted as a ternary diagram where the red dashed line represents the $SrTi_{1-x}Fe_xO_{3-y}$ compositional tie-line.

Samples were also obtained with a gradient in Sr composition as shown in **Figure 3-8**. The range of Sr compositions covered by these samples was found to be 38 at.% < Sr < 62 at.%. This should allow for investigation of the robustness of the perovskite structure to Sr deficiency and excess. These samples will be termed “Sr-graduated” to distinguish them from samples deposited with tie-line compositions.

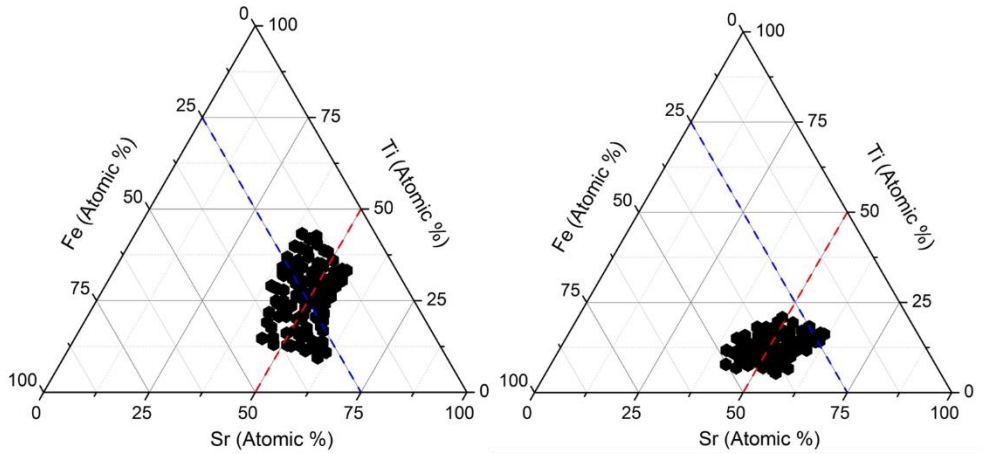

Figure 3-8: Ternary diagrams showing the pseudo-ternary composition of STFO perovskite thin films deposited by PVD at 650 °C under an oxygen plasma source obtained by EDX. The red-dashed line represents the $SrTi_{1-x}Fe_xO_{3-y}$ compositional tie-line. These samples were deposited with a gradient in Sr composition in addition to the Ti/Fe compositional gradient. The blue dashed line represents compositions with a constant Fe content of 25 at.%, this line will be used to investigate the effect of Sr content on the properties and electrochemistry of the materials.

3.2.2 Oxygen content

The STFO thin films were prepared under a beam of atomic oxygen from a plasma source and it was expected that this more reactive source of oxygen would aid the oxidation of the material and produce a near stoichiometric film. Further films were produced under molecular oxygen for comparison and these films were characterised both as deposited and following post deposition annealing in a tube furnace under a flow of O_2 at 650 °C for 6 h.

The error in EDX measurements is quite high, around ± 2 at.%, and the accuracy of the measurement may be affected by ambient and surface oxygen so this data cannot be relied upon to give an accurate value for the oxygen deficiency of the film but may provide information on the general trends in oxygen content with composition and variations due to preparation conditions. Since oxygen deficiency in the films is associated with the preferential adoption of the Fe^{3+} oxidation state rather than the Fe^{4+} oxidation state required for stoichiometry it would therefore be expected that for an oxygen-deficient film the oxygen content would decrease with increasing Fe content, as denoted by x.

Figure 3-9 shows the oxygen stoichiometry of the films plotted against the Fe content, denoted by x, for the sample deposited with composition close to the $SrTi_{1-x}Fe_xO_{3-y}$ tie-line. This sample shows oxygen stoichiometry close to or above the stoichiometric value of 3, shown by the black dashed line, for compositions across the film. This indicates that this film has a high level of oxidation with all B site cations in the +4 oxidation state and no oxygen defects i.e. y = 0. Most of the above stoichiometric oxygen compositions lie within the error range of the measurement as indicated by the error bars on the plot and the over-estimation is likely to be due to the presence of ambient and surface oxygen. However the presence of above stoichiometric levels of oxygen could be an indication of the presence of other oxide phases.

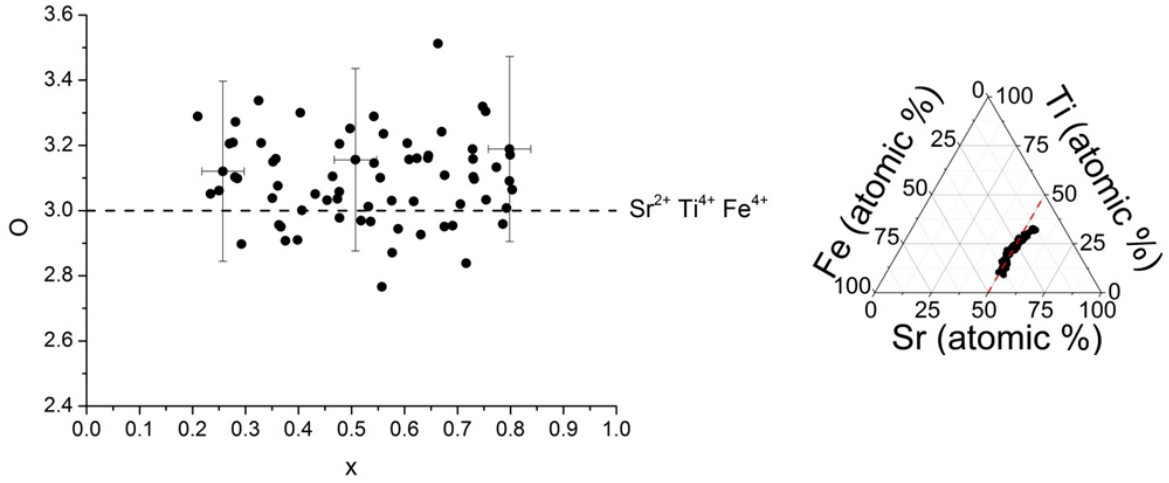

Figure 3-9: Variation of the oxygen stoichiometry with Fe content, denoted by x, for compositions across the $SrTi_{1-x}Fe_xO_{3-y}$ composition tie-line where Sr = 50 ± 2 at.%. All data taken from EDX measurements on STFO film deposited on SiN at 650 °C under atomic oxygen at compositions close to the tie-line composition as shown in the ternary plot on the right of the figure. Error bars show error in EDX measurements. Black dashed line shows oxygen content for stoichiometric $SrTi_{1-x}Fe_xO_3$.

For STFO materials away from the $SrTi_{1-x}Fe_xO_{3-y}$ compositional tie-line, i.e. where Sr ≠ Ti+Fe, the oxygen content will depend on the Sr/(Ti+Fe) ratio due to the difference in oxygen stoichiometry of the Sr A-site cation, which forms AO, and the Ti and Fe B site cations which form BO_2. The oxygen content would therefore be expected to decrease with increasing Sr content.

The oxygen content of the film deposited in atomic oxygen at 650 °C is shown as a colour map on the pseudo-ternary plot in **Figure 3-10**. The oxygen content is close to the value of 60 at.% expected for the stoichiometric perovskite for all compositions. There is a clear decrease in O content with increasing Sr content but no apparent trend with the Fe/Ti ratio.

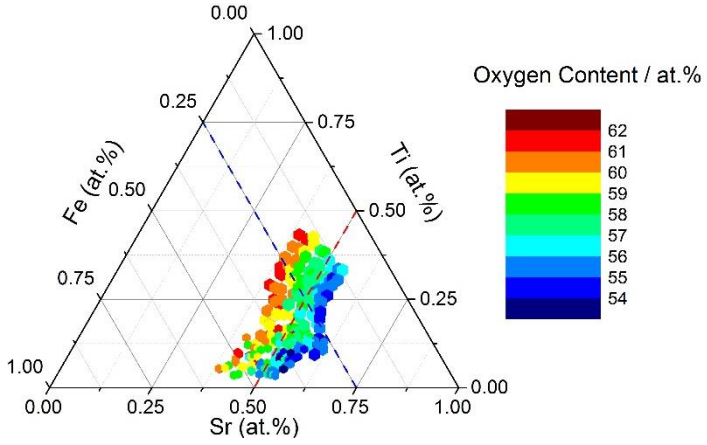

Figure 3-10: Ternary plot showing variation in oxygen content (at.%) obtained from SEM-EDX on Sr graduated STFO films deposited on SiN at 650 °C under atomic oxygen. The $SrTi_{1-x}Fe_xO_{3-y}$ composition tie-line, shown in red represents composition with Sr = 50 at.%. The $Sr_nTi_{0.75-n}Fe_{0.25}O_{3-y}$ tie-line shown in blue represents compositions with Fe = 25 at.%.

Figure 3-11 shows the oxygen stoichiometry of the films plotted against the Fe content for compositions along the $SrTi_{1-x}Fe_xO_{3-y}$ tie-line, shown by the red dashed line in **Figure 3-10**. The black dashed lines show the oxygen stoichiometry calculated at varying x for the cation oxidation states shown. There is a peak in the oxygen stoichiometry of the film at around x = 0.65 where it reaches a value of 3, the value expected for a film containing only B site cations in the +4 oxidation state. For all other values of x a stoichiometry below 3 is obtained, indicating the presence of some proportion of Fe^{3+} and possibly also Ti^{3+}.

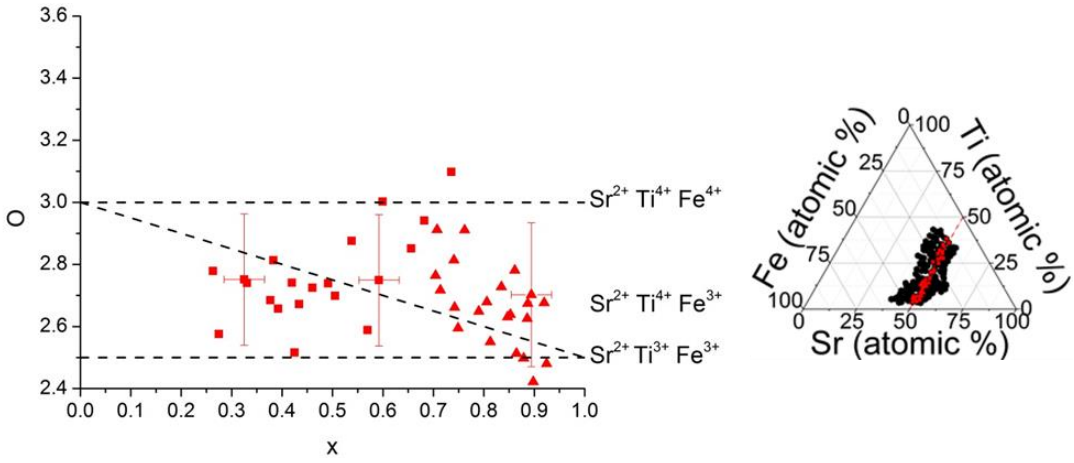

Figure 3-11: Variation of the oxygen stoichiometry with Fe content, denoted by x, for compositions across the $SrTi_{1-x}Fe_xO_{3-y}$ composition tie-line where Sr = 50 ± 2 at.%. All data taken from EDX measurements on STFO films deposited on SiN at 650 °C under atomic oxygen. Data taken from two samples with compositions shown by the ternary on the right of the figure, red squares show data from a sample with Fe content in the range 0.25 < x < 0.75 and red triangles show data from a sample with higher Fe content such that x > 0.7 where x = Fe/(Ti+Fe). Error bars show error in EDX measurements. Black dashed lines show oxygen contents calculated for the cation oxidation states shown.

There is a clear difference in the oxygen stoichiometry obtained for these films and that obtained for the film deposited with a small Sr range, close to the perovskite tie-line, for which data was shown in **Figure 3-9** and no oxygen deficiency was measured. Despite the use of the same temperature and oxygen plasma settings for the depositions a difference would not be unexpected since the introduction of the wedge shutter on the Sr source required the adjustment of deposition rates both by changing the Sr source temperature and the power of the e-beam evaporation of Ti and Fe. These results however cannot be considered to be conclusive in part due to the large degree of error expected in the measurement. Even in the case where the obtained oxygen content was considered to be accurate it cannot be definitely assigned to oxygen defects in the perovskite lattice as there is also the possibility of the formation of other oxide phases.

Figure 3-12 shows the decrease in oxygen content with pseudo-ternary Sr content along the $Sr_nTi_{0.75-n}Fe_{0.25}O_{3-y}$, shown by the blue dashed line in **Figure 3-10**, along this line the pseudo-ternary Fe content of the film is 25%. The black line shows the expected oxygen content for the cation oxidation states indicated. When the Sr content is <50% the oxygen content is slightly below the value for the stoichiometric film but as the level of Sr in the film increases the oxygen content deviates further from this stoichiometric value. This suggests that the film is oxygen deficient with the most likely source of the oxygen deficiency being the presence of Fe in the lower Fe^{3+} oxidation state rather than Fe^{4+}. At a Sr content of 50% the oxygen content of the films is close to that expected for a film with Fe exclusively in the Fe^{3+} oxidation state corresponding to a composition of $SrTi_{0.5}Fe_{0.5}O_{2.75}$. At higher Sr contents (Sr>50%) the oxygen contents continues to decrease below levels where it can be accounted for by a Fe^{3+} oxidation state, this could be explained by the presence of Ti^{3+}.

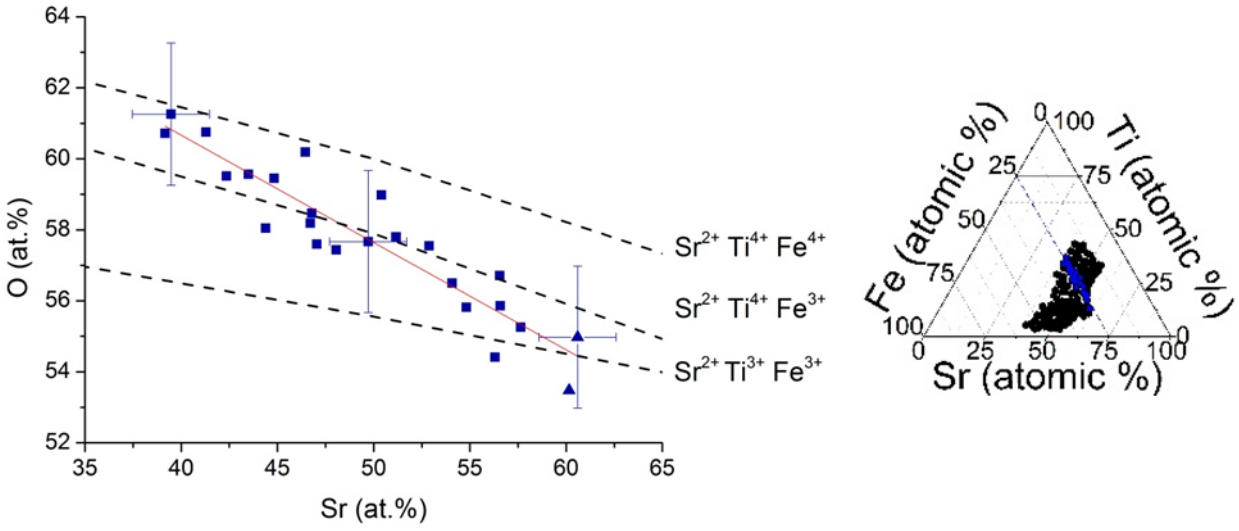

Figure 3-12: Variation in oxygen content in at.% with Sr content in at.% for compositions across the $Sr_nTi_{0.75-n}Fe_{0.25}O_{3-y}$ tie-line where Fe = 25 ± 2 at.%. All data taken from EDX measurements on STFO films deposited on SiN at 650 °C under atomic oxygen. Data taken from two samples, blue squares show data from a sample with Fe content in the range 0.25 < x < 0.75 and blue triangles show data from a sample with higher Fe content such that x > 0.7 where x = Fe/(Ti+Fe). Error bars show error in EDX measurements. Black dashed lines show oxygen contents calculated for the cation oxidation states shown.

Again these results must be treated carefully due to the known errors in the measurement but these results could provide an indication that the formation energy of the stoichiometric perovskite increases with increasing Sr content and consequentially oxygen deficient phases with lower formation energy are formed.

The oxygen stoichiometry obtained from EDX measurements of the STFO films prepared in molecular oxygen both as deposited and after annealing in a tube furnace at 650 °C under molecular oxygen is plotted in **Figure 3-13**. All of the points showed an oxygen stoichiometry above 3. The most likely cause for this higher than expected oxygen content would be the formation of an oxygen-rich impurity phase such as SrO_2 or $Sr(OH)_2$ although $SrCO_3$ is also a possibility. Data only available along the $SrTi_{1-x}Fe_xO_{3-y}$ tie-line so the effect of the Sr content on the oxygen content of these films cannot be assessed.

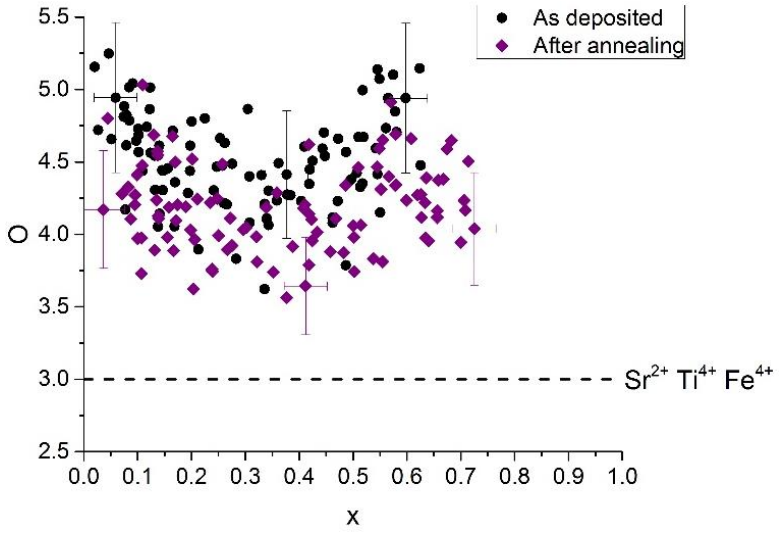

Figure 3-13: Variation of the oxygen stoichiometry with Fe content, denoted by x, for compositions across the $SrTi_{1-x}Fe_xO_{3-y}$ composition tie-line where Sr = 50 ± 2 at.%. Data taken from EDX measurements on an STFO film deposited on SiN at 650 °C under molecular oxygen.

The slight decrease in oxygen stoichiometry after annealing could be due to greater formation of the perovskite phase from the oxygen-rich impurity phases. This is consistent with evidence from XRD studies which will be discussed in **Section 4.2.2.4**.

3.2.3 Film Thickness

Profilometry was used to determine the thickness of the thin films. The variation in thickness of the films is expected to depend mainly on the deposition conditions and geometry of sources in the chamber. For the current work the increase in Fe content in the electrocatalyst film is offset by a decrease in Ti content and so no overall change in the amount of material deposited is expected in this direction and so no significant changes in thickness are expected. Any increase in Sr content however is not offset in this way and so the amount of material deposited and the thickness should increase with increasing Sr content. This is of course a simplistic view of the situation which does not take into account possible changes in film density.

Points were taken at each of the four corners of the films to estimate the variation in thickness across the films. **Figure 3-14** shows how the film thickness varies with composition across a film deposited under atomic oxygen. As expected there is a significant increase in the film thickness with increasing Sr content.

A thickness variation was also observed in the tie-line sample although this was much smaller. Whilst the profilometry measurements have quite a high degree of accuracy (± 1-2 nm), the method of taking points at the corners and interpolating the data will clearly introduce errors.

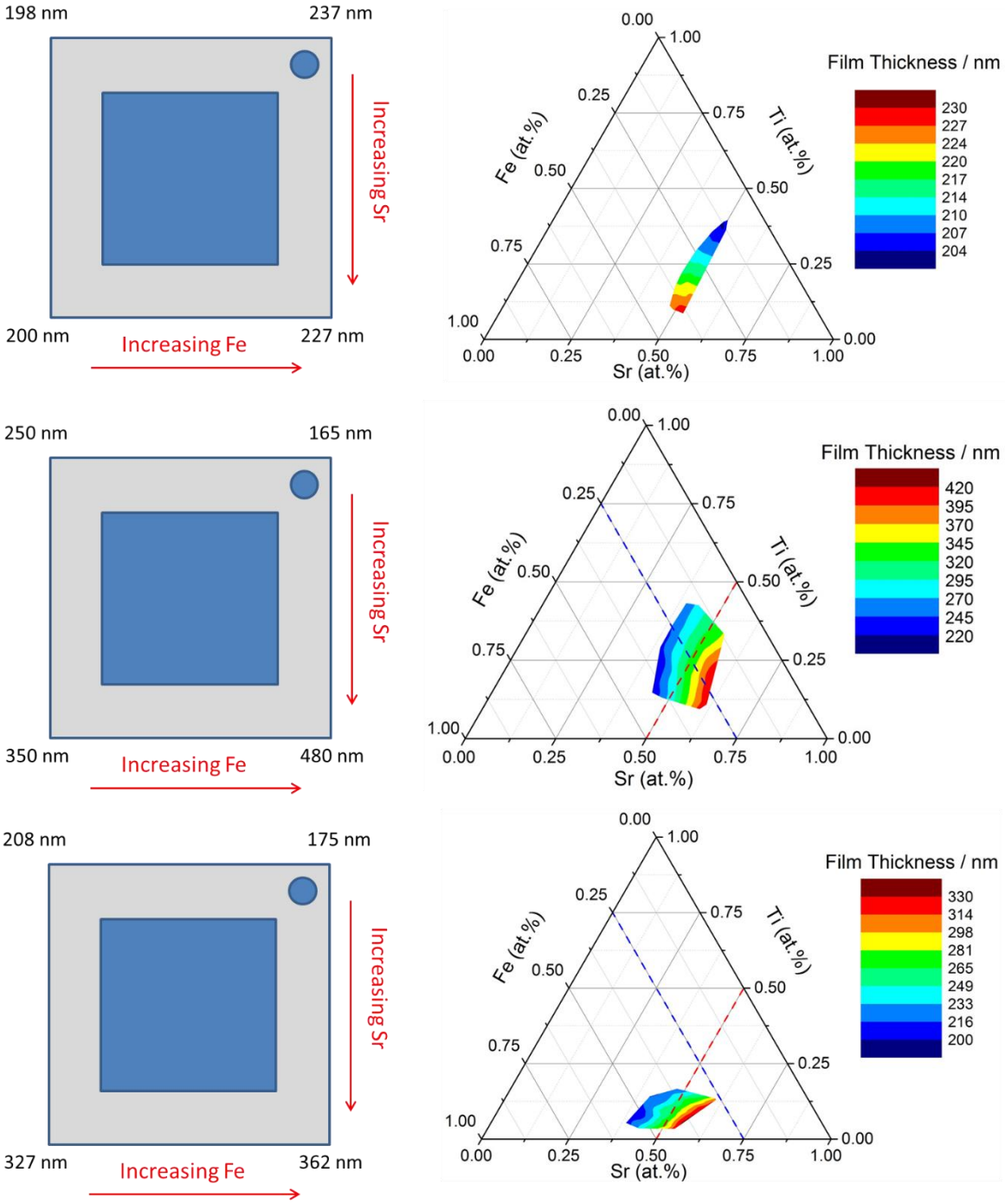

Figure 3-14: Thickness variations in $SrTi_{1-x}Fe_xO_{3-y}$ films deposited under atomic oxygen at 650 °C obtained from profilometry. Four points were taken at the corners of the film as shown and interpolated to cover the 19 x 19 mm area of 10x10 electrode array to give the thickness change in ternary space.

3.2.4 Conductivity measurements

The variation in conductivity over the sample is shown by the colour map in **Figure 3-15**. The points shown in grey indicate compositions where the sheet resistivity exceeded the measurement limit of 8 x 10^{-11} Ω which is indicative of conductivity lower than 7 x 10^{-8} S cm^{-1}. There does however seem to be a large jump between the first measurable conductivities which are of the order of 1 x 10^{-5} S cm^{-1} which could be an indication that a problem with the instrument or set-up caused the measurement limit of sheet resistance to be lower than reported.

Figure 3-15 shows the variation in conductivity of the STFO films across ternary compositional space. Measurable conductivities are observed generally above a pseudo-ternary Fe composition of 25%, which corresponds to the region on the right of the blue dotted line in the ternary diagram. The conductivities increase above this point with increasing Fe composition which is consistent with expectations based on the literature [59, 65, 92, 101]. The conductivity also had some dependence on Sr content and the highest conductivities were measured for films with high Fe and low Sr contents and it was at the low Fe, high Sr regions of the samples that resistivity measurements were over-scale of the instrument. This could be due to the presence of insulating Sr oxide or carbonate phases evidence of which was found in the XPS data and will be discussed in the next section.

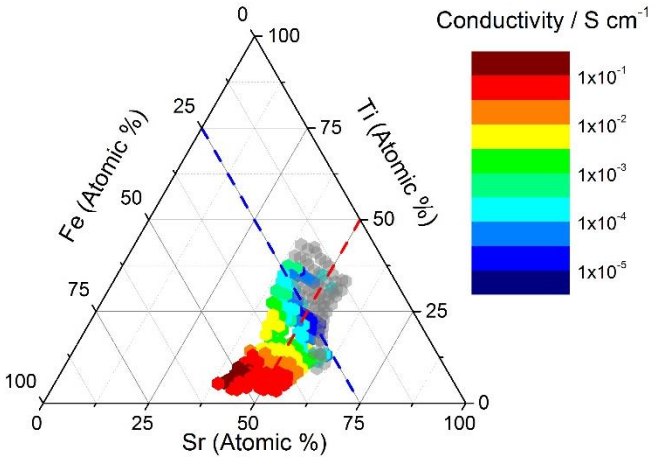

Figure 3-15: Ternary diagram with colour map showing the variation in conductivity across the $SrTi_{1-x}Fe_xO_{3-y}$ thin films deposited by PVD under atomic oxygen at 650 °C. The highest conductivities, shown in red, were measured at high Fe, low Sr compositions and decrease as Fe content decreases or Sr content increases. Data in grey shows compositions which gave sheet resistivities over-scale of the instrument limit.

Figure 3-16 shows the correlation between the conductivity of the film, determined using the Van-der Pauw four-point probe method, and the Fe content, x, for the STFO films as denoted by x.

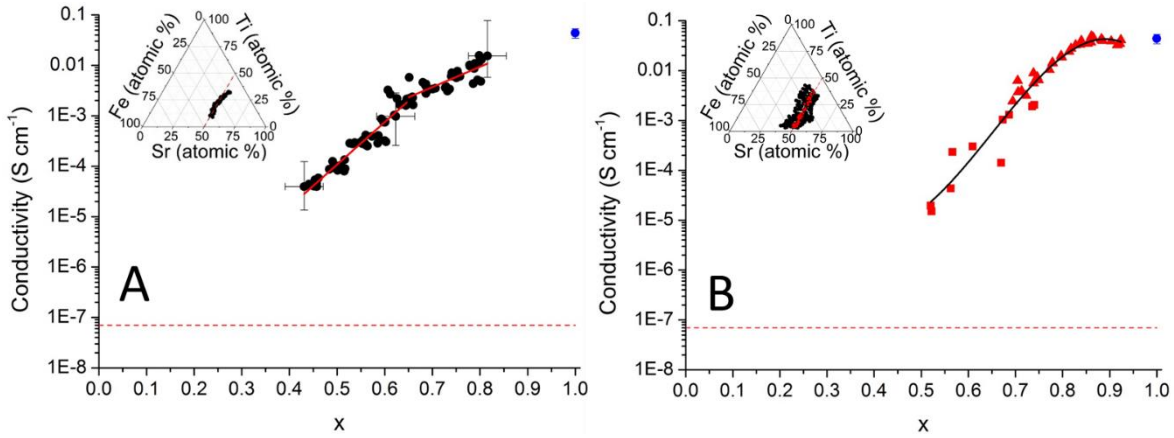

Figure 3-16: Variation in conductivity with Fe concentration, x, for $SrTi_{1-x}Fe_xO_{3-y}$ thin films. Data shown is from (A) tieline sample with Sr = 50 ± 5 at.%, shown by black dots, and (B) two Sr graduated samples with Sr shown by red dots and triangles, also shown is data from the uniform SFO film, shown by blue dot.

The conductivity of the SFO uniform film was 0.043 ± 0.009 S cm^{-1} which is lower than previous observations for stoichiometric $SrFeO_3$ which exceed 1 S cm^{-1} [98]. This is considered to be an indicator that the material is oxygen deficient, containing a proportion of Fe^{3+} ions for which electrons are localised. Takeda *et al.* [99] measured the conductivity of bulk samples of oxygen deficient $SrFeO_{3-y}$ and found that the electronic conductivity decreased with increasing oxygen vacancies. Conductivities of a similar order of magnitude as observed in this work for $SrFeO_{3-y}$ were measured for samples with y = 0.35. Given this it seems likely that the STFO materials deposited under the same conditions will also display some degree of oxygen deficiency.

The STFO films were highly resistive at compositions below x = 0.43, exceeding the measurement limit of 8 x 10^{-11} Ω in sheet resistance which equates to a conductivity lower than 7 x 10^{-8} S cm^{-1}. There was a large jump in conductivity at the x = 0.43 composition with conductivity on the order of 3 x 10^{-5} S cm^{-1} after which point the conductivity increased logarithmically before reaching a plateau at 0.041 ± 0.009 S cm^{-1} for x > 0.75. In the region where conductivity could be measured it was of a similar magnitude to a study of bulk STFO materials prepared under an air atmosphere by Da Silva *et al.* [101] as shown in **Figure 3-17**. Also shown on the figure is data from a study by Brixner *et al.* [92] which relates to bulk samples of the reduced $SrTi_{1-x}Fe_xO_{3-x/2}$ material which shows lower conductivity values due to the localisation of electrons at Fe^{3+} ions.

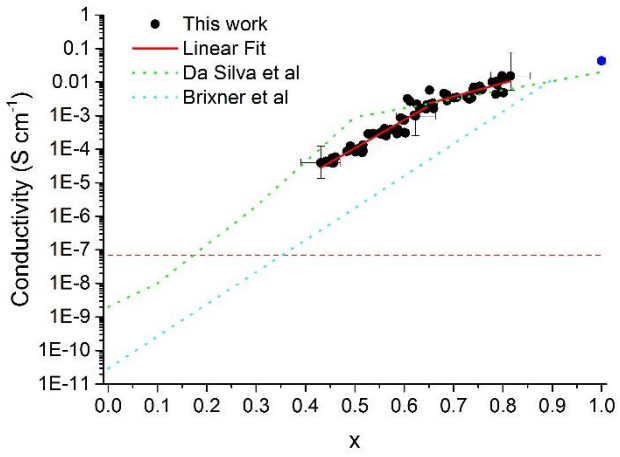

Figure 3-17: Comparison of conductivity measurements obtained in this work for a $SrTi_{1-x}Fe_xO_{3-y}$ perovskite thin film deposited by HT-PVD and literature results obtained for STFO materials.

In the Brixner *et al.* study [92] bulk samples of the oxygen deficient $SrTi_{1-x}Fe_xO_{3-x/2}$ system were prepared by high-temperature solid state methods with calcination under a N_2 atmosphere to favour the formation of the reduced perovskites with a predominant Fe^{3+} oxidation state. The increase in Fe content with increasing x was rationalised as due to trace amounts of Fe^{4+} in the lattice which introduce charge carrying holes, h, by the equilibrium shown in **Equation** 3-3 and so result in the observation of p-type conductivity. They also suggest that the conductivity may be improved by a larger overlap of the electronic states caused by a decreasing lattice size identified in x-ray diffraction studies on the materials.

$$Fe^{4+} \rightleftharpoons Fe^{3+} + h$$

Equation 3-3

Whilst some studies agree that materials in the STFO system have p-type conductivity [107], other studies have found that the conductivity changes with oxygen partial pressure from p-type at high oxygen partial pressure to n-type at low oxygen partial pressure and ionic conductivity in the intermediate region [59, 65]. The mechanism of conduction in these materials is complicated and depends highly on the degree of oxidation of the films. All of the studies discussed however report an increase in the conductivity with increasing Fe content, regardless of n-type, ionic or p-type behaviour which is consistent with the results presented here.

The high resistivity of the films observed below x = 0.43 does not seem consistent with the expectation of the formation of electronic bands at x = 0.03 which was predicted by Evarestov *et al.* [108] and should lead to significant electronic conductivity. In neither of the literature studies considered here is there a jump in the conductivity consistent with that which in this study would be required to bring the conductivity above the measurement limit at x = 0.43. It is of course possible that a problem with the instrument or set-up caused the measurement limit of sheet resistance to be lower than reported. Alternatively this could be caused by a structural effect and this possibility will be discussed more in the next chapter.

3.2.5 XPS measurements

The XPS system is integrated into the same UHV system as the PVD deposition chamber which should allow for the analysis of samples without exposure to atmosphere. This is desirable due to the surface sensitive nature of XPS which means that adsorbates on the surface restrict signal from the film. Unfortunately the XPS system was not operational during the period in which the thin films were deposited and the necessity of making other measurements on the films meant that the samples had to be removed from the system and re-introduced at a later time. As such when the samples were re-introduced into the UHV system, they were subjected to annealing for 30 mins at 200 °C prior to XPS measurement to remove adsorbed water from the surface of the samples.

This annealing process is not expected to remove more strongly bound surface adsorbates or possible surface phases such as carbonates which may form upon exposure to atmosphere. Annealing at a higher temperature to remove these would however risk changing the crystal structure or oxygen content of the films which decreases the applicability of the measurements. One advantage to the exposure of the films to atmosphere prior to measurement does exist in that it gives a more accurate picture of the state of the surface of the electrodes which will also be exposed to atmosphere prior to the electrochemical measurements. The results will also relate more closely to the other characterisation methods which were all applied after exposure of the samples to atmosphere.

XPS measurements were made on two STFO thin film samples deposited under atomic oxygen at 650 °C, one with composition close to the $SrTi_{1-x}Fe_xO_{3-y}$ tie-line similar to that shown by **Figure 3-18** and one which covered a larger region of compositional space. The measurement points and corresponding EDX compositions are shown in **Figure 3-18**. XPS spectra were also obtained for the uniform films of the binary oxides, $SrTiO_3$ and $SrFeO_3$, deposited under atomic oxygen by measurement of a point at the centre of the film.

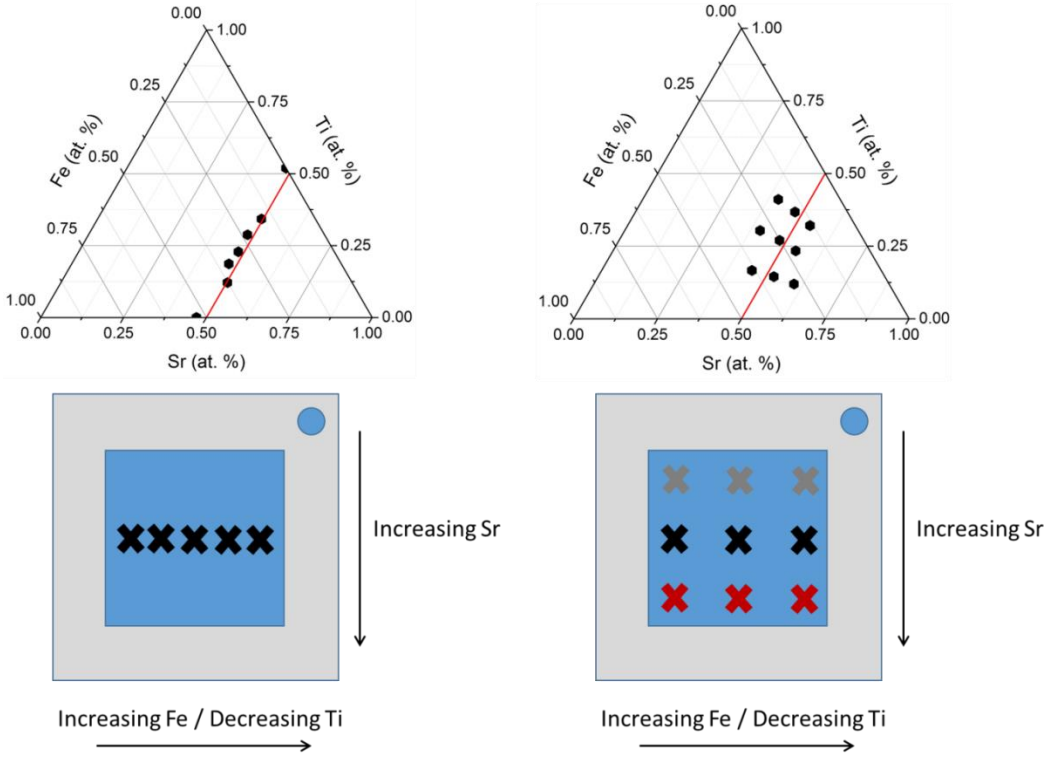

Figure 3-18: Ternary diagrams showing the composition of the XPS measurement points as obtained from SEM-EDX (top). Schematic diagram to show XPS measurement points. For samples deposited with compositions close to the $SrTi_{1-x}Fe_xO_{3-y}$ tie-line five points were taken at different Fe/Ti ratios as shown on the left. For samples covering a larger compositional space where the Sr content changed significantly, nine data points were taken in a 3x3 square as shown on the right. Points with Sr content, as measured by EDX, close to the tie-line i.e. Sr_{EDX} = 50 ± 2 at. % are shown by black crosses. Points with low Sr content i.e. Sr_{EDX} = 40 – 45 at. % are shown by the grey crosses. Points with high Sr content i.e. Sr_{EDX} = 54 – 60 % are shown by the red crosses.

3.2.5.1 C 1s

In order to remove the effects of charging for the semiconducting materials all spectra have been referenced to the C 1s peak at 285 eV which is due to adsorbed carbon. The C1s spectra measured for STFO compositions with varying x are shown in **Figure 3-19**. In addition to the peak due to C-C, fixed at 285 eV, a peak at 289 eV consistent with the presence of CO_3 was observed. A very minor additional C-O or C-OH component was also identified and is shown in green.

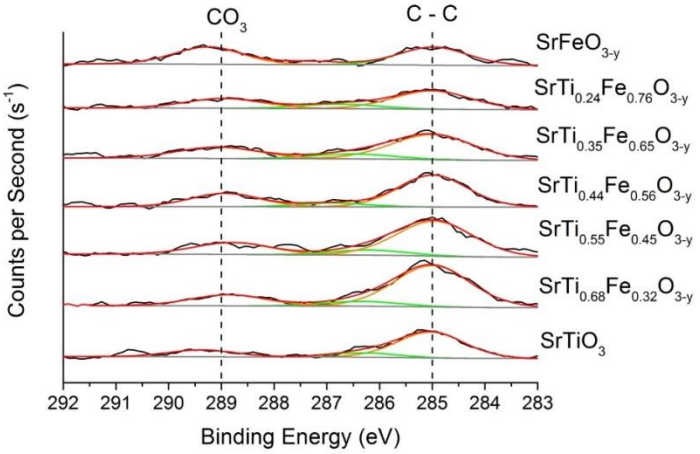

Figure 3-19: C 1s XPS spectra for $SrTi_{1-x}Fe_xO_3$ films deposited by PVD at 650 °C under a 500 W oxygen plasma. Peak at 285 eV is assigned to carbon adsorbed on the film surface whilst the peak at 289 eV is assigned to surface carbonates.

3.2.5.2 Sr 3d

The Sr 3d regions of the XPS spectra for compositions along the $SrTi_{1-x}Fe_xO_{3-y}$ compositional tie-line are shown in **Figure 3-20**. The peaks were fitted into two overlapping doublets with a $Sr_{5/2}$:$Sr_{3/2}$ spin-orbit splitting ratio of 2:3 and separation of 1.8eV. Several studies have reported the presence of two distinct environments for the Sr ion which are observed as two doublets in the Sr 3d spectrum of $SrTi_xFe_xO_{3-y}$ [102, 109-111]. The low binding energy component is assigned to Sr in the bulk perovskite lattice whereas angle resolved XPS experiments have confirmed that the high binding energy component represents surface Sr which is present in a distinct chemical environment [110-112].

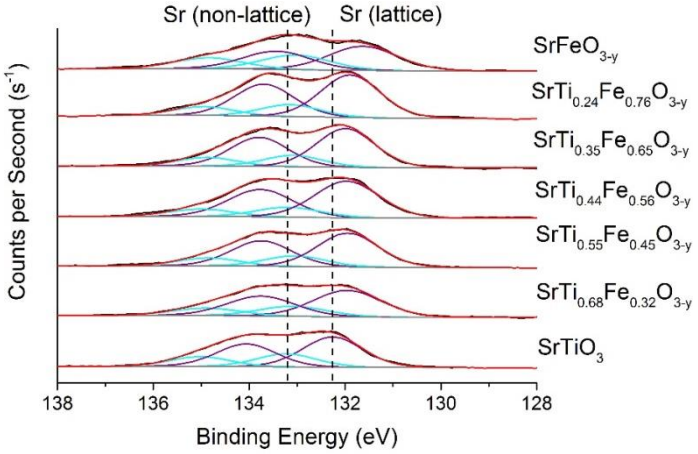

Figure 3-20: Sr 3d XPS spectra for $SrTi_{1-x}Fe_xO_3$ films deposited by PVD at 650 °C under a 500 W oxygen plasma. The doublet at low binding energy, shown by the purple line was assigned to Sr in the perovskite lattice. The doublet at high binding energy, shown by the light blue line was assigned to Sr not in the perovskite lattice which may be an impurity phase or a surface phase. Dotted lines show position of Sr $3d_{5/2}$ (lattice) and Sr $3d_{5/2}$ (non-lattice).

The doublet assigned to Sr in the bulk perovskite lattice shifts to lower binding energy with increasing Fe content. This shift is explained by inter-atomic effects caused by the addition of shielding conduction electrons to the lattice. A similar shift was seen in the Ti 2p and O 1s regions and will be discussed in **Section 3.2.5.7**.

The binding energy shift observed for surface atoms can be explained by the inter-atomic effects which cause a reduction in binding energy for an atom bound within a lattice. The atoms in the bulk are stabilised by the neighbouring atoms whilst the surface atoms which have fewer neighbouring atoms experience less of a stabilising effect and as such will experience a smaller shift to higher binding energy [113]. Many studies however attribute the high energy component to surface impurities such as $SrCO_3$, SrO and $Sr(OH)_2$ [102, 110, 111].

The effect of varying the Sr content is shown in **Figure 3-21** . The non-lattice component of the Sr 3d spectrum was increased relative to the lattice component with increasing Sr, this is particularly noticeable for the above stoichiometric $Sr_{1.1}(Ti_{0.5}Fe_{0.5})O_{3-y}$ composition. The FWHM of the peaks also increased as Sr content increased indicating that there may be other environments for the Sr cation which could not however be fit satisfactorily by the addition of another doublet.

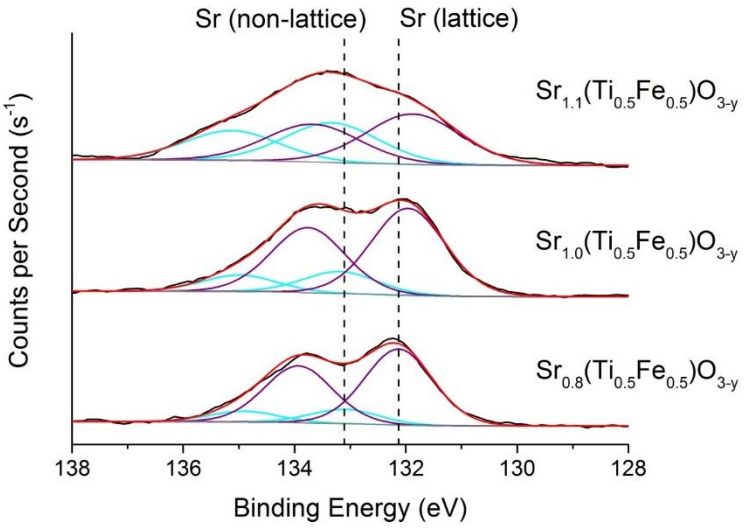

Figure 3-21: Sr 3d XPS spectra for $Sr_n(Ti_{0.5}Fe_{0.5})O_{3-y}$ films deposited by PVD at 650 °C under a 500 W oxygen plasma with varying Sr content. The doublet at low binding energy, shown by the purple line was assigned to Sr in the perovskite lattice. The doublet at high binding energy, shown by the light blue line was assigned to Sr in a surface phase.

There are two possible explanations for the increase in the non-lattice Sr component, either Sr is increasingly segregated to the surface at higher Sr contents or the higher binding energy component does not arise solely from Sr surface ions but includes ions in a separate phase. The observed increase in the FWHM of the peak supports the latter argument.

Where Sr is present in above stoichiometric amounts it is considered likely that the additional Sr will form SrO rock-salt structured layers which intersperse with layers of perovskite. The Sr atoms in these layers would sit in lower co-ordinate sites bonding to 9 oxygen ligands rather than the 12-co-ordinate sites in the perovskite structure. This will be discussed further in the next chapter.

3.2.5.3 O 1s

In a similar way to Sr 3d, XPS studies have identified at least two and in some cases three different chemical environments for the photoelectrons in $SrTi_{1-x}Fe_xO_{3-y}$, which appear in the XPS spectra as a lower binding energy component, assigned to oxygen in the bulk perovskite lattice, and a higher energy component which has been shown by angle resolved XPS studies to be a surface phase [112]. The surface phase is assigned to carbonates, hydroxides or both.

The data obtained for the $SrTi_{1-x}Fe_xO_{3-y}$ thin films, shown in **Figure 3-22**, clearly comprises of at least two components. A good fit was obtained with two components for the uniform $SrTiO_3$ film whilst the addition of a third component improved the fit for the Fe containing perovskites. The low binding energy component, shown by the purple line is assigned to oxygen in the perovskite lattice whilst the highest binding energy component shown by the light blue lines was assigned to surface carbonates including $SrCO_3$. The component shown in green is likely to correspond to another surface component such as hydroxides including $Sr(OH)_2$.

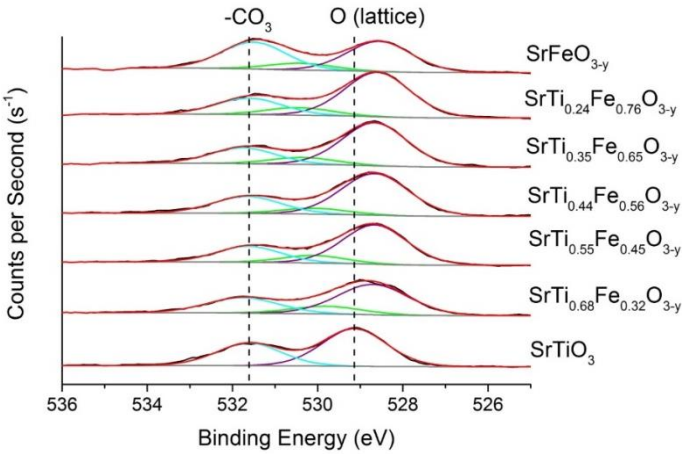

Figure 3-22: O 1s XPS spectra for $SrTi_{1-x}Fe_xO_3$ films deposited by PVD at 650 °C under a 500 W oxygen plasma. The component at higher binding energy, shown by the green line arises due to surface hydroxide and/or carbonates whilst the lower binding energy component, shown by the blue line arises due to oxygen in the perovskite lattice.

As was seen for the lattice component in the Sr 3d spectra, the O 1s lattice component also shifts to lower binding energy upon the addition of Fe to the $SrTiO_3$ lattice due to the effects of the addition of conduction electrons to the lattice which shield the nuclear charge.

The effect of increasing the Sr content on the O 1s XPS spectrum is shown in **Figure 3-23**. In a similar way to the Sr 3d spectrum there is an increase in non-lattice O components relative to the lattice component with increasing Sr content. An additional peak at high binding energy was required to fit the spectrum of the above stoichiometric $Sr_{1.1}(Ti_{0.5}Fe_{0.5})O_{3-y}$ composition which may arise due to O atoms in SrO rock-salt layers as discussed in **Section 3.2.5.2** above.

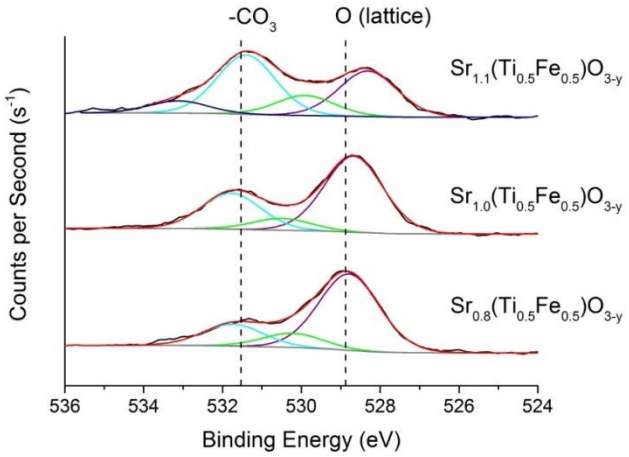

Figure 3-23: O 1s XPS spectra for $Sr_n(Ti_{0.5}Fe_{0.5})O_{3-y}$ films deposited by PVD at 650 °C under a 500 W oxygen plasma with varying Sr content. The component at higher binding energy, shown by the green line arises due to surface hydroxide and/or carbonates whilst the lower binding energy component, shown by the blue line arises due to oxygen in the perovskite lattice.

3.2.5.4 Ti 2p

The Ti 2p region of the XPS spectrum of $SrTiO_3$ is shown in **Figure 3-24**. The data for the Ti 2p region was fitted with a doublet with $2p_{3/2}$:$2p_{1/2}$ splitting ratio of 2:1. There was no evidence of the presence of Ti^{3+} which would be observed as a shoulder at low binding energy and so it is assumed all Ti is present in the Ti^{4+} oxidation state.

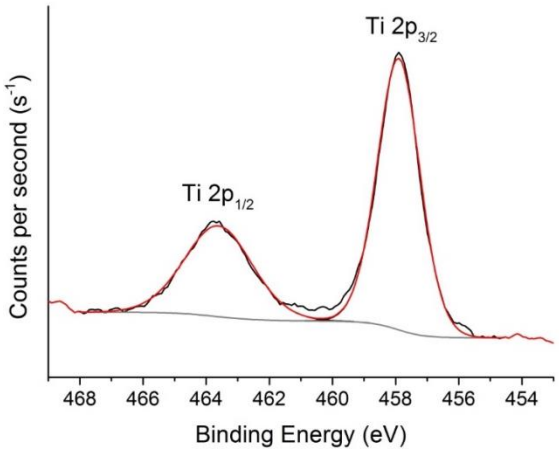

Figure 3-24: Ti 2p XPS spectrum for a uniform film of $SrTiO_3$ deposited by PVD at 650 °C under a 500 W oxygen plasma. The peak is split into a doublet by the effects of spin-orbit coupling. The peaks are labelled according to the quantum number j of the state. Coster-Kronig broadening is observed for the $2p_{1/2}$ peak causing a larger FWHM than for the $2p_{3/2}$ peak.

The $2p_{1/2}$ peak is broader than the $2p_{3/2}$ peak, the FWHM of the fitted peaks are 2.5 eV and 1.6 eV respectively. This has been observed previously for STO and other 3d-transition metal compounds [114-116] and is a result of Coster-Kronig decay of the core hole [116]. In a Coster-Kronig decay process, the core-hole is filled by an electron from a higher sub-shell of the same shell. The $2p_{1/2}$ core-hole can therefore be filled by an electron from the $2p_{3/2}$ sub-shell but there is no higher sub-shell to allow for the $2p_{3/2}$ core-hole to decay by a Coster-Kronig process. Since a Coster-Kronig process occurs between two sub-shells in the same shell it is faster and since the core-hole lifetime is inversely related to peak width, this results in a broader peak for the $2p_{1/2}$ sub-shell than for the $2p_{3/2}$ sub shell [116].

The Ti 2p XPS spectra for compositions along the $SrTi_{1-x}Fe_xO_{3-y}$ tie-line are shown in **Figure 3-25**. All the spectra can be fit by a single doublet assigned to Ti^{4+} with no evidence to support the presence of a lower oxidation state.

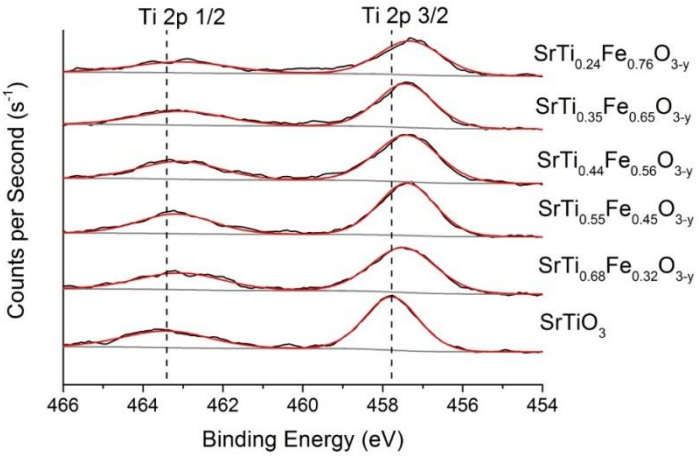

Figure 3-25: Ti 2p XPS spectra for $SrTi_{1-x}Fe_xO_3$ films deposited by PVD at 650 °C under a 500 W oxygen plasma.

Figure 3-26 shows the XPS spectra for STFO compositions with x = 0.5 and varying Sr contents. The peaks are fit in the same manner as for the tie-line compositions but an increase in the FWHM of the Ti $2p_{3/2}$ is observed with increasing Sr content from 1.66 for n = 0.8 to 1.71 for n = 1 and finally 1.94 for n = 1.1. This could be an indication that the number of distinct chemical environments for the Ti ions increases. There is no significant change in the binding energy position of the peaks.

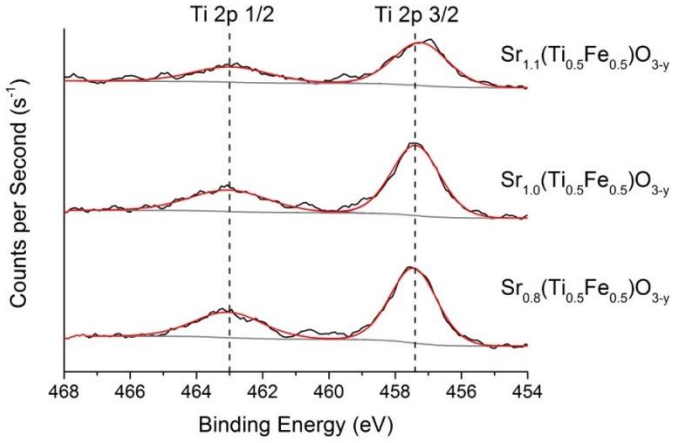

Figure 3-26: Ti 2p XPS spectra for $Sr_n(Ti_{0.5}Fe_{0.5})O_{3-y}$ films deposited by PVD at 650 °C under a 500 W oxygen plasma with varying Sr content.

3.2.5.5 Fe 2p

As discussed in **Section 3.1.4** the Fe ions is $SrFeO_{3-y}$ may exist in either the Fe^{3+} or Fe^{4+} formal oxidation states depending on the oxygen content of the material. Where Fe^{3+} is present there will be oxygen ion vacancies to balance the charge and the ground state electronic structure of the ion will be d^5.

Where Fe adopts the formal Fe^{4+} oxidation state there is significant covalent character to the Fe-O bonding and charge transfer occurs from the oxygen ligands to the Fe ion. The ground state is therefore dominated by a $d^5\underline{L}$ electronic structure, where $\underline{L}$ represents a ligand hole, rather than the d^4 configuration [94]. In this case no oxygen vacancies are required for charge balance and the charge fluctuation between the d^4 and $d^5\underline{L}$ states results in delocalised electrons which give rise to metallic conductivity in the material. The charge transfer from the oxygen ligands to the Fe^{4+} ion reduces the actual charge on the metal and so would be expected to reduce the chemical shift relative to the Fe^{3+} ion in the XPS spectra. Boquet *et al.* [94] compared spectra from fully oxidised $SrFeO_3$ with spectra from $LaFeO_3$ in which the Fe adopts the Fe^{3+} oxidation state and found only a small chemical shift of 0.5 eV whereas a shift of 2 eV was observed between $LaFeO_3$ and data from oxides containing Fe^{2+}.

Figure 3-27 shows the Fe 2p XPS spectrum obtained for the $SrFeO_{3-y}$ film which consists of a spin orbit doublet with broad asymmetric peaks. Previous XPS studies on STFO [102] and related materials [117, 118] have deconvoluted the spectra into two components assigned to Fe in the Fe^{3+} and Fe^{4+} oxidation states and used the ratio of intensity of the peaks to calculate the Fe^{3+}/Fe^{4+} ratio. This is then used to calculate the oxygen content of the material using the assumption that for every two Fe^{3+} ions there will be a charge compensating oxygen vacancy.

In fact the peak shape is not due to the presence of components from multiple oxidation states and is commonly seen for materials containing solely high spin Fe^{3+}. The biggest contribution to the peak shape is actually multiplet splitting arising from the presence of unpaired electrons in the valence band which undergo spin-orbit coupling with the 2p core hole following photo-ionisation. Additional effects of electrostatic interactions and crystal field interactions were included in calculations by Gupta and Sen [119] which first predicted the multiplet splitting of the Fe 2p peaks for free Fe^{3+} using the Hartree-Fock free-ion method. Various studies since have refined these predictions and shown how the multiplet peaks can be fit to XPS data obtained for various high spin Fe^{3+} compounds [120-122].

In **Figure 3-27** the Fe $2p_{3/2}$ peak has been fit according to an average multiplet splitting profile given by Biesinger *et al.* [122]. The profile was obtained from XPS spectra of various Fe^{3+} compounds measured using a monochromated x-ray source. The relative binding energies, intensities and FWHMs of the peaks were constrained to the values given. The peaks in black represent the Fe $2p_{3/2}$ mutiplets whilst the peak shown in purple represents surface ions which are shifted to higher binding energy either because of reduced co-ordination leading to lower electron density or because of a decrease in the crystal field energy. The green peaks are satellites due to the use of a non-monochromated x-ray source, these appear at binding energies 10 eV below the main peaks. The blue peak is assigned to a shake up satellite.

The data shows a good fit but is intended only to show that the peak shape is governed by mutiplet splitting rather than the ratio of Fe^{3+}/Fe^{4+} and as such the intensity ratios of peaks fitted to this data cannot be used to obtain this relationship. Such an analysis would only be possible using high-resolution data obtained from a monochromated x-ray source and requires the fitting of the individual multiplet components which have not been calculated for the Fe^{4+} ion.

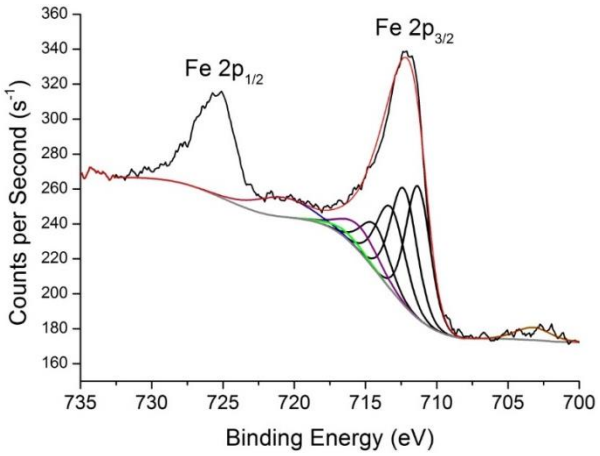

Figure 3-27: Fe 2p XPS spectrum of $SrFeO_{3-\gamma}$ film deposited by PVD at 650 °C under a 500 W oxygen plasma. The Fe $2p_{3/2}$ peak is fit according to splitting patterns given by Biesinger [122] for Fe^{3+} compounds which include multiplet splittings, shown in black, a peak due to surface Fe^{3+}, shown in purple and a shake-up satellite, shown in blue. Also included are satellites arising from the un-monochromated x-ray source which are positioned at binding energies 10 eV below the main peaks and are shown in green.

Alternative explanations have been proposed for the satellite in the Fe 2p XPS spectrum. Some studies suggest it appears due to charge transfer from the oxygen ligands screening the core-hole in the final state In this case the main peak is assigned to well screened final states, $\underline{c}d^5\underline{L}$ or $\underline{c}d^6\underline{L}$, where $\underline{c}$ denotes the core-hole following ionisation and the satellite peak is assigned to poorly screened $\underline{c}d^4$ and $\underline{c}d^5$ states.

Figure 3-28 shows how the Fe 2p spectra change over the $SrTi_{1-x}Fe_xO_{3-y}$ tie-line. The spectra show similar broad peaks due to the effects of mutiplet splitting. Unlike the Sr 3d, Ti 2p and O 1s XPS spectra the binding energy of the peak does not change with increasing Fe content in the lattice. No significant change in the shape or binding energy of the spectra was observed with increasing Sr content as shown in **Figure 3-29**.

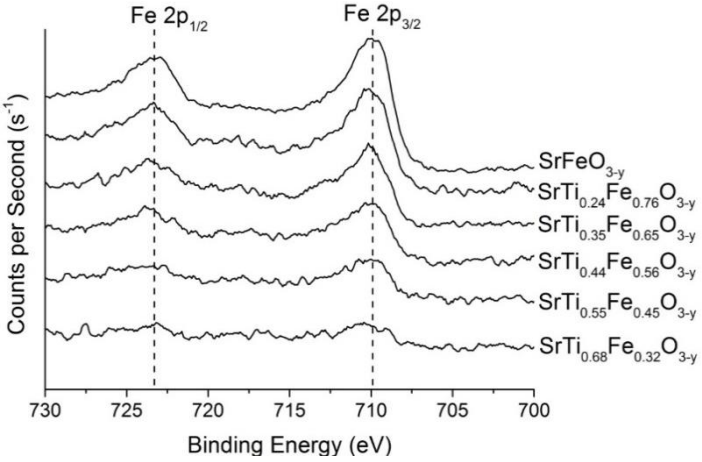

Figure 3-28: Fe 2p XPS spectra for $SrTi_{1-x}Fe_xO_3$ films deposited by PVD at 650 °C under a 500 W oxygen plasma.

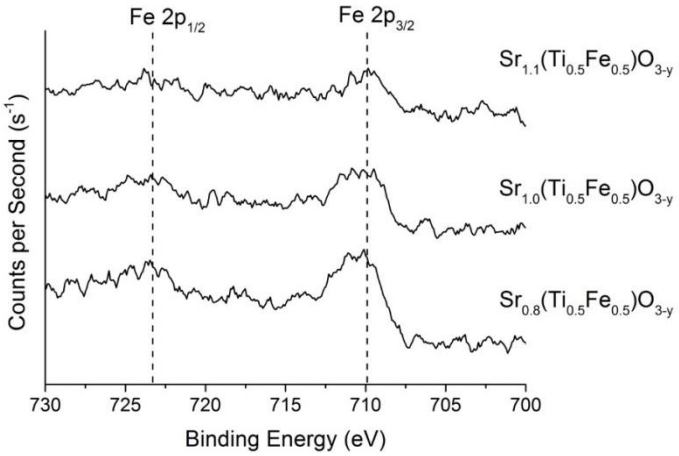

Figure 3-29: Fe 2p XPS spectra for $Sr_n(Ti_{0.5}Fe_{0.5})O_{3-y}$ films deposited by PVD at 650 °C under a 500 W oxygen plasma with varying Sr content.

3.2.5.6 Surface Composition

Since XPS is a surface sensitive technique with an analysis depth of 2-10 nm it can be used to identify any changes in composition which occur close to the sample surface. This is clearly highly relevant to the use of the materials as electrocatalysts since the surface will provide the active sites for catalysis. **Figure 3-30** shows the pseudo-ternary compositions of the STFO films prepared under atomic oxygen as obtained from the peak intensities of the XPS spectra taken in the Sr 3d, Ti 2p and Fe 2p regions combined with the corresponding relative sensitivity factors as given by Wagner *et al.* [81]. In all cases the surface composition obtained by XPS give higher Sr content than was measured for the bulk film by EDX.

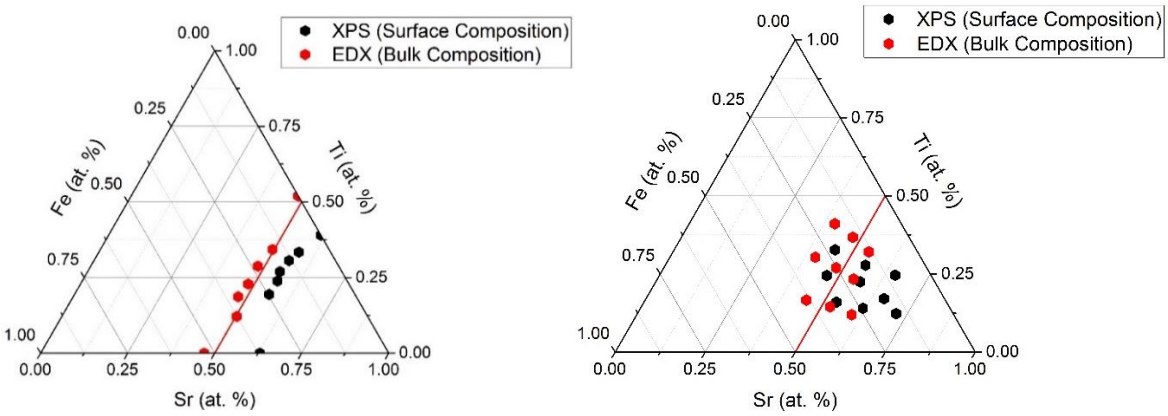

Figure 3-30: Ternary diagrams showing the surface compositions of the $SrTi_{1-x}Fe_xO_{3-y}$ thin films, deposited by PVD at 650 °C under atomic oxygen, obtained from the peak intensities of XPS spectra from the Sr 3d, Ti 2p and Fe 2p regions combined with the corresponding relative sensitivity factors as given by Wagner *et al.* [81]. The compositions obtained by EDX, which provides a bulk measurement, are shown in red. The surface compositions obtained from the XPS measurements are higher in Sr than the bulk EDX measurements and also give a higher Ti/Fe ratio.

Previous XPS studies of $SrTi_{1-x}Fe_xO_{3-y}$ materials have reported differences in the surface composition compared to the bulk, most notably the segregation of Sr at the surface which has been reported to form an insulating layer, having a detrimental impact on the conductivity and electrocatalytic activity [110, 111]. Studies of $SrTi_{1-x}Fe_xO_{3-y}$ thin films deposited by PLD have reported that the presence of this phase increased with increasing Fe content [110, 111]. Whilst Sr segregation has been observed for a variety of Sr containing perovskites [113, 123, 124] the driving force for the process is not known. It has been suggested that lattice strain arising from the high co-ordination number of the large Sr ion lies behind the effect. In this case the introduction of smaller Fe^{4+} ions which reduce the size of the perovskite lattice would be expected to increase the strain and so an increase in Sr segregation with increasing Fe content is readily explained [111].

The ratio of the A site Sr cation to the B-site Ti and Fe cations was calculated from the XPS data and plotted against Fe content, x, in **Figure 3-31**. The ratio was found to be higher than the expected value of 1 for all Fe contents, indicating some degree of Sr enrichment at the surface of the thin film. The level of Sr surface enrichment is roughly the same for all measured values of x although it is slightly higher for the binary oxides, $SrTiO_3$ and $SrFeO_3$. This could be due to the different deposition conditions for these films since the removal of the wedge shutters to produce a uniform film requires the adjustment of deposition rates.

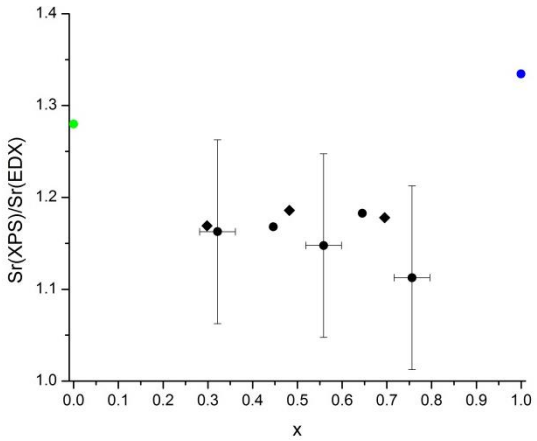

Figure 3-31: Variation in the degree of Sr surface enrichment with increasing Fe content, as denoted by x. The surface enrichment is determined by the ratio of the Sr content determined by XPS to the Sr content determined by EDX. Data shown by black dots correspond to measurements on the STFO film with compositions close to the $SrTi_{1-x}Fe_xO_{3-y}$ tie-line. The points shown by diamond markers correspond to measurements on the film deposited over a wider compositional range, although only points with Sr_{EDX} = 50 ± 2 at. % are shown. Data for $SrTiO_3$ and $SrFeO_3$ is shown by green and blue dots, respectively.

3.2.5.7 Changes in chemical state

It should be possible to identify changes in the chemical state of surface atoms by investigation of the XPS spectra since variation in the chemical environment including changes to oxidation state or lattice site will affect the binding energy of the emitted photo-electron. **Figure 3-32** shows the shift in the binding energy for the Sr 3d, Ti 2p and O 1s peaks in the XPS spectra of $SrTi_{1-x}Fe_xO_3$ and $SrFeO_3$ films relative to their position in the uniform $SrTiO_3$ film. Clearly data cannot be plotted in this way for Fe 2p since Fe is not present in $SrTiO_3$. The Fe 2p spectra did not show any significant shifts as shown in **Figure 3-28**, however since the peak structure was complicated and could not be de-convoluted this observation could be misleading.

The Sr 3d, Ti 2p and O 1s peaks in the XPS spectra of the Fe-containing films were all shifted to lower binding energy compared to their positions in the XPS spectra of $SrTiO_3$. This could be explained by a final state effect in which the addition of Fe adds delocalised conduction electrons to the lattice which screen the nuclear charge in $SrFeO_{3-y}$ reducing the energy of the final photo-ionised state and so lowering the energy difference between the initial and final states [94].

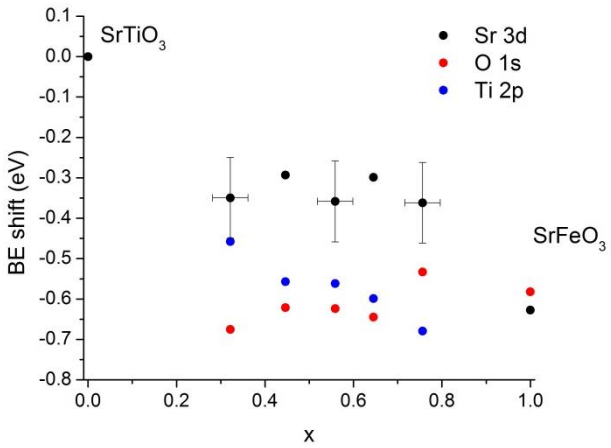

Figure 3-32: Binding energy shifts for Sr 3d (black), Ti 2p (blue) and O 1s (red) lines in XPS spectra for SrTi1-xFexO3 and SrFeO3 films deposited by PVD at 650 °C under a 500 W oxygen plasma relative to line position in SrTiO3 uniform film.

The trend in the binding energy shift is however clearly not linear with increasing Fe content and it is likely that a number of competing effects contribute to the observed trends in binding energy. A chemical shift is possible since Fe has higher electronegativity than Ti and would be expected to draw electron density away from the other metal atoms resulting in an increase in the binding energy. Another possible effect is a shift in the Fermi-level of the material with the addition of Fe since the binding energy is reported relative to the Fermi-level of the spectrometer which should be at the same energy as the sample if the system is properly grounded and any charging effects have been taken into account. The addition of Fe to the lattice would be expected to increase the electron density in the metal 3d states which would cause an upshift in the Fermi-level of the material and a shift of the peaks to higher binding energy.

A much clearer trend in the binding energy shift is observed with varying Sr content as shown in **Figure 3-33**. Since the materials become less electronically conductive with increasing Sr content, as discussed in **Section 3.2.4**, this shift to lower binding energy cannot be due to an increasing number of conduction electrons. This binding energy shift is likely to arise from changes in the chemical bonding due to changes in the crystal lattice structure which are likely to occur with increasing Sr content and will be discussed in detail in the next chapter.

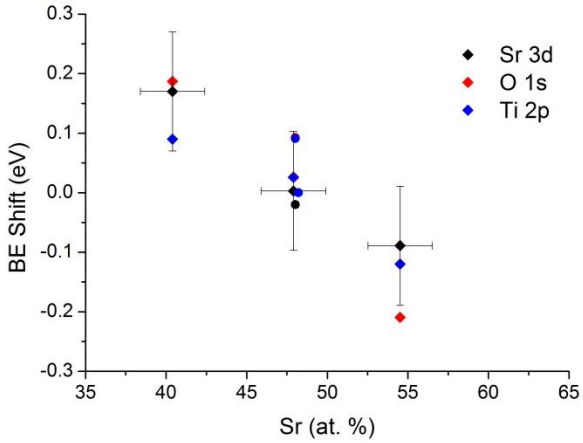

Figure 3-33: Binding energy shifts for Sr 3d (black), Ti 2p (blue) and O 1s (red) lines in XPS spectra for STFO films with varying Sr content deposited by PVD at 650 °C under a 500 W oxygen plasma relative to line position in $SrTi_{0.5}Fe_{0.5}O_3$ composition.

3.2.5.8 Bulk composition

Estimates of the "bulk" composition of the $SrTi_{1-x}Fe_xO_{3-y}$ films have been made based on the assignments made in the previous section using ratios of the intensities of the XPS spectra combined with the relative sensitivity factors determined by Wagner [81]. When the surface Sr component is subtracted from the calculation of the composition, the ternary composition shown in **Figure 3-34** is obtained. This composition lies closer to the compositional tie-line and as such is much closer to the composition obtained for the bulk film by EDX.

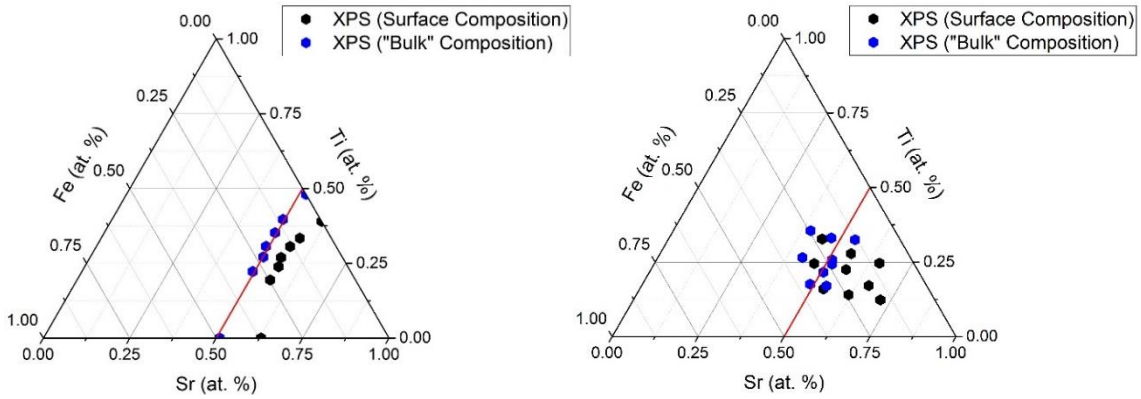

Figure 3-34: Ternary diagrams showing the bulk (blue) and surface (black) compositions of the $SrTi_{1-x}Fe_xO_{3-y}$ thin films, deposited by PVD at 650 °C under atomic oxygen, obtained from the peak intensities of XPS spectra from the Sr 3d, Ti 2p and Fe 2p regions combined with the corresponding relative sensitivity factors as given by Wagner. The bulk composition was obtained by removal of the component assigned to a surface Sr phase in the Sr 3d spectrum. Removal of the surface Sr component leads to a composition which lies on the Sr/(Ti+Fe) = 1 compositional tie-line.

Whilst the determination of the relative ratios of the metal cations in STFO has given consistent results the estimation of the oxygen content in this way is not considered appropriate due to errors in the determination of the integrated peak areas. Whilst a peak due to oxygen in the perovskite lattice was distinctly observable in the O 1s spectra presented in **Figure 3-22** the uncertainty in the surface state and number and identity of peaks due to oxygen adsorbates is likely to introduce a large degree of error. Such an analysis may have been possible if the films had not been removed from the UHV system following deposition before re-introduction for XPS measurements.

3.2.5.9 Effect of preparation conditions

Figure 3-35 shows data from the XPS and EDX measurements of the pseudo-ternary compositions of the STFO thin films deposited under molecular oxygen both as deposited (A) and after subsequent annealing in a tube furnace at 650 °C under O_2 (B). In both cases there was Sr surface enrichment. Various compositions for the Sr-rich surface layer have been suggested including $SrCO_3$, SrO and $Sr(OH)_2$ [102, 110, 111].

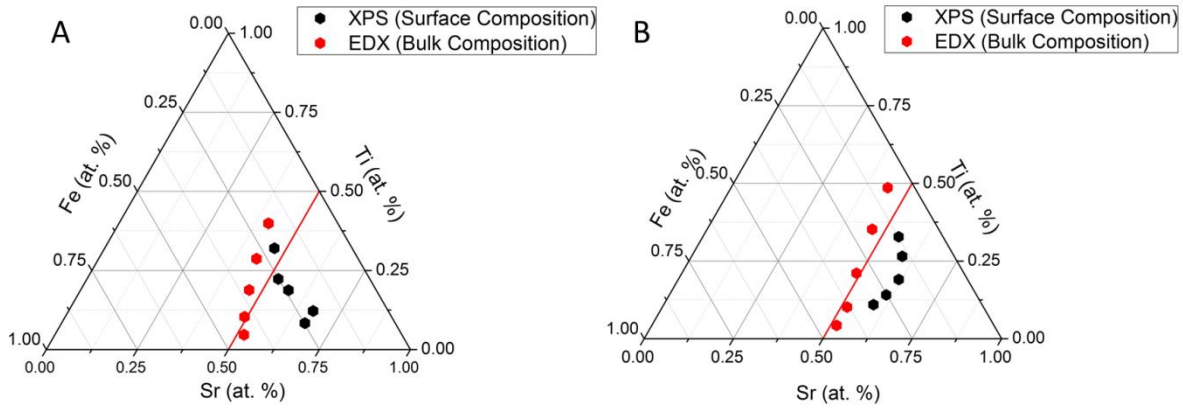

Figure 3-35: Ternary diagrams showing the surface compositions of the $SrTi_{1-x}Fe_xO_{3-y}$ thin films, deposited by PVD at 650 °C under molecular oxygen both as deposited (A) and after subsequent annealing in a tube furnace at 650 °C under O_2 (B). Data obtained from the peak intensities of XPS spectra from the Sr 3d, Ti 2p and Fe 2p regions combined with the corresponding relative sensitivity factors as given by Wagner *et al.* [81]. The compositions obtained by EDX, which provides a bulk measurement, are also shown in red. The surface compositions obtained from the XPS measurements are higher in Sr than the bulk EDX measurements.

The O 1s spectra of the films prepared under molecular oxygen showed an increase in the peak assigned to non-lattice components compared to the peak assigned to oxide ions in the perovskite lattice as shown in **Figure 3-36**. On the basis of this the peak assigned to non-lattice oxygen is assumed to not only be due to oxygen adsorbates but also include other non-perovskite oxide phases. The appearance of such phases in the films prepared under molecular oxygen is consistent with observations of higher than expected oxygen content in the EDX compositional studies discussed in **Section 3.2.2**. The decrease in the peak assigned to oxygen in the perovskite lattice is consistent with results from x-ray diffraction which will be discussed in the next chapter and which show that for high Fe contents there is a significant decrease in the perovskite crystalline phases in these samples.

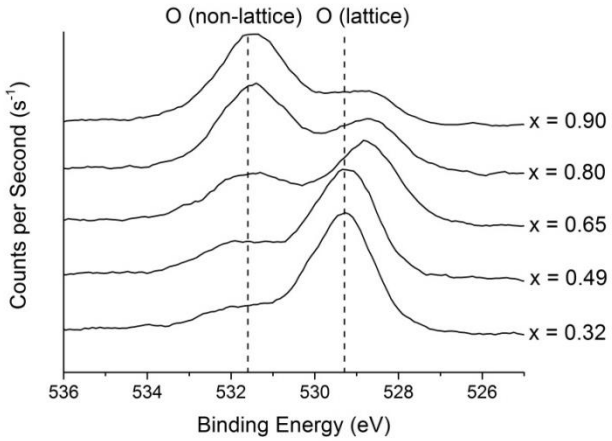

Figure 3-36: O 1s XPS spectra for $SrTi_{1-x}Fe_xO_3$ films deposited by PVD at 650 °C under molecular oxygen. The peak assigned to lattice oxygen decreases with increasing Fe content, x, whilst the peak assigned to non-lattice oxygen increases.

3.3 Conclusions

Compositionally graduated films with compositions across a large portion of the $SrTi_{1-x}Fe_xO_{3-y}$ compositional tie-line were successfully deposited using a HT-PVD method. The composition of the deposited films was determined using EDX and showed that the samples were within the compositional range $0.15 < x < 0.85$. Samples were also successfully deposited with a gradient in the Sr concentration such that the ratio of Sr to Ti and Fe in the film varied from $Sr_{0.6}(Ti, Fe)O_{3-y}$ to $Sr_{1.6}(Ti, Fe)O_{3-y}$. These samples should make it possible to assess the robustness of the perovskite structure to cation deficiency at the A and B sites, since the Sr-rich form should be considered as B-site deficient.

EDX measurements also gave a rough indication of the oxygen contents of the films although as discussed these are subject to a degree of error. For films deposited using the oxygen plasma source, the calculated oxygen stoichiometry was within the range expected for STFO adopting the perovskite structure which has an ideal oxygen stoichiometry of $SrTi_{1-x}Fe_xO_3$ but which may exhibit lower oxygen stoichiometry due to the formation of oxygen vacancies which would be charge compensated by a decrease in the oxidation state of the B-site cations from +4 to +3. The theoretical minimum would be expected to be $SrTi_{1-x}Fe_xO_{2.5}$ although one study has reported the preparation of $SrFeO_2$ by use of a hydride reducing agent [125].

Conductivity measurements on the oxygen plasma-prepared STFO thin film samples using the Van der Pauw 4-point probe method showed an increase in conductivity with increasing Fe content, x, consistent with previous studies of the bulk material [59, 65, 92, 101], before reaching a plateau at 0.041 ± 0.009 S cm^{-1} for $x > 0.75$. The conductivity of the SFO uniform film was 0.043 ± 0.009 S cm^{-1} which is lower than previous observations for stoichiometric $SrFeO_3$ which exceed 1 S cm^{-1} [98]. This is considered to be an indicator that the material is oxygen deficient, containing a proportion of Fe^{3+} ions for which electrons are localised. Given this it seems likely that the STFO materials deposited under the same conditions will also display some degree of oxygen deficiency.

The $SrTi_{1-x}Fe_xO_{3-y}$ films were highly resistive at compositions below $x = 0.43$, exceeding the measurement limit in sheet resistance leading to a conductivity lower than 7×10^{-8} S cm^{-1}. There was a large jump in conductivity at the $x = 0.43$ composition with conductivity on the order of 3×10^{-5} S cm^{-1}. It is not known whether this is a genuine effect caused by changes in the electronic or crystal structure at this point or whether it could be due to a problem with the instrument or set-up which led to the measurement limit lower than that reported by the manufacturer.

XPS measurements were used to determine the surface composition of the films and confirmed that there was a segregation of Sr to the surface which was consistent with previous studies of the material. The surface component was observed as a distinct doublet in the Sr 3d spectrum, the removal of this component from calculation of the film composition resulted in a composition close to that obtained from the bulk EDX measurements.

It was not possible to determine the oxidation state of the Fe cation from the XPS measurements due to the complex mutiplet splitting of the Fe 2p spectra. However a shift to lower binding energy in the Sr 3d, Ti 2p and O 1s XPS spectra provides evidence for the addition of conduction electrons to the lattice which are able to provide inter-atomic screening of the final photo-ionised state. This would be consistent with the adoption of the formal Fe^{4+} oxidation state which has a $t_{2g}^{3}e_{g}^{1}$ electronic configuration in which the e_g electronic state is delocalised.

Unfortunately no clear trend between the binding energy shift and x could be identified which could be due to conflicting effects which increase the binding energy such as shifts in the Fermi level, changes in the Madelung potential or the electronegativity of the Fe ion. However it could also arise due to differential charging due to an insulating surface layer or even insufficient conductivity of the film at lower Fe contents and as such it would be recommended that any future XPS studies on this material use an electron-gun to flood the sample with negative charge and prevent charging effects.

Chapter 4: Structural Characterisation of Electrocatalyst Libraries

4.1 Introduction

The perovskite crystal structure, ABO_3, is highly flexible and able to accommodate a large range of different metal cations at both A and B sites, vacancies at both the cationic and anionic sites and even intergrowth phases with different crystal structures. The result of this is a highly tuneable structure which is able to exhibit a diverse range of desirable properties including ferro-electricity [76], high temperature superconductivity [126] , piezo-electric [78] and dielectric behaviour [127, 128].

To aid in the design of functional materials attempts must be made to understand how changes to the crystal structure caused by these modifications affect the observed properties. Unfortunately identification of such relationships is not simple in part due to the robustness of the perovskite crystal structure which remains near-cubic with the result that lattice distortions are not always identifiable from x-ray diffraction data. This has led to some confusion in the literature in cases where properties are assigned as due to electronic structure without consideration of possible lattice distortions or ordered phases. In particular for $SrTi_{1-x}Fe_xO_{3-y}$ (STFO) much of the literature is focussed on how the addition of Fe affects the electronic structure whilst complicated discussions of the effect of the known oxygen deficiency and the possibility of a vacancy-ordered structure analogous to those observed for $SrFeO_3$ are largely avoided.

Of additional concern is the possibility of the formation of phase mixtures since the different non-stoichiometric crystalline polymorphs often have similar formation energies and so where there is non-stoichiometry the existence of a single phase of long-range crystalline order may not be realistic.

An obstacle in the characterisation of the STFO materials prepared in this work is the uncertainty in the oxygen content which has been estimated from EDX and XPS data. Despite this, clear trends in the data in particular from Raman and XRD measurements can be related to the data obtained in the electrochemical experiments to give a strong suggestion of the structure-activity relationships at work, especially when they are considered in the context of the existing literature.

4.1.1 The perovskite crystal structure

The perovskite crystal structure, shown from two views in **Figure 4-1**, was briefly introduced in the previous chapter. In this chapter the structure will be considered in more detail with a particular focus on the distortions to the crystal structure which can occur based on the relative sizes of the metal cations.

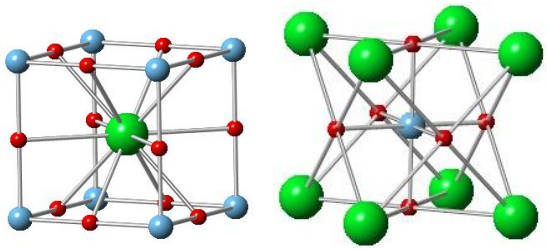

Figure 4-1: Schematic views of a cubic perovskite, ABO_3, drawn using CrystalMaker. The "A" atom is shown in green, the "B" atom in blue and the oxygen atoms in red. On the left of the figure the 12-co-ordinate A-site cation is shown in the centre whilst on the right the octahedral B-site cation is shown in the centre.

The stability of the perovskite crystal structure containing cations, A and B, has been described by the Goldschmitt tolerance factor, t, defined in **Equation** 4-1, where r_A, r_B and r_O are the ionic radii of the A-site cation, the B-site cation and the oxygen ion respectively. A stable perovskite crystal structure has a Goldschmitt tolerance factor of $0.77 < t < 1$ [90].

$$t = \frac{r_A + r_o}{\sqrt{2}\,(r_B + r_O)}$$

Equation 4-1

A perfect cubic perovskite has t = 1, this occurs when the ionic radius of the A site cation is equivalent in size to the oxygen ion (1.40 Å). When t deviates from 1 distortions in the lattice occur resulting in the adoption of one of the crystal structures shown in **Figure 4-2**. For structures with t > 1 the hexagonal crystal structure becomes stable due a reduction in the B – O –B bond angle which results in a tilting of the BO_6 octahedra. For T < 1 tetragonal and orthorhombic distortions to the lattice occur [90].

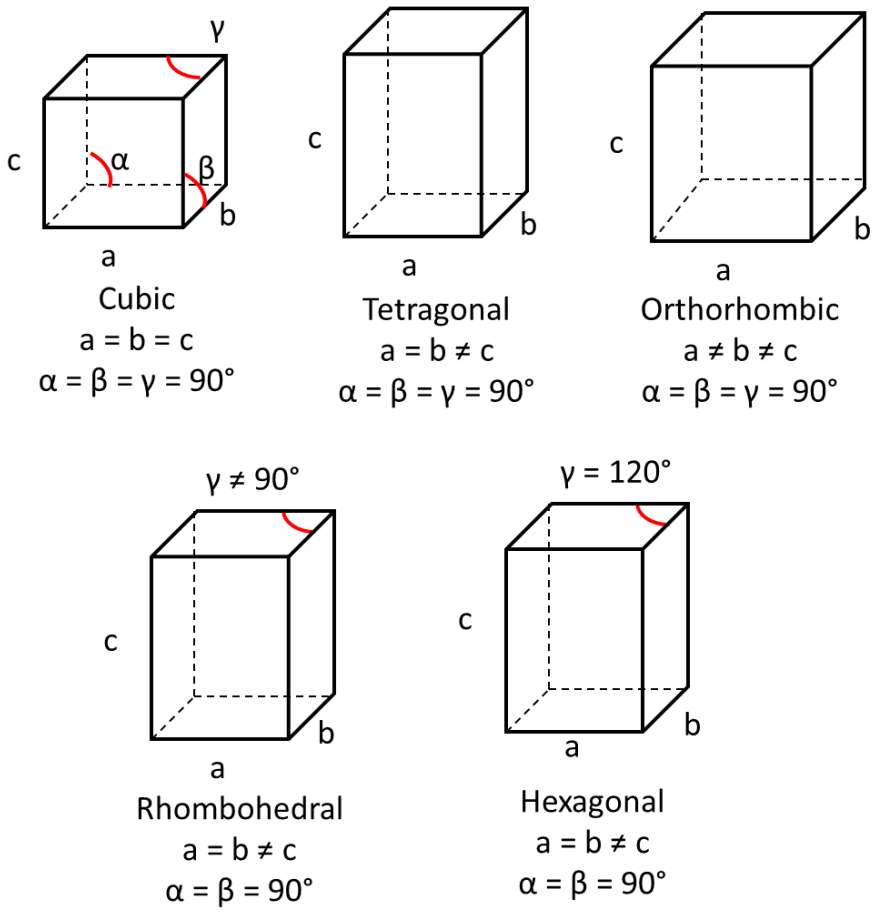

Figure 4-2: Unit cells for the cubic, tetragonal, orthorhombic, rhombohedral and hexagonal crystal lattice systems.

4.1.2 STFO crystal structure

Studies of bulk STFO have confirmed a cubic perovskite structure across the compositional range from $SrTiO_3$ to $SrFeO_3$ [58-60]. Sr^{2+} ions occupy the A-site of the lattice whilst Ti^{4+} and Fe^{4+} ions occupy the B-sites. The stability of these materials could be predicted by calculation of the Goldschmitt tolerance factors using Equation 4-1 and values for the atomic radii of the ions of Sr^{2+} = 1.44 Å, Ti^{4+} = 0.605 Å, Fe^{4+} = 0.585 Å and O^{2-} = 1.40 Å. A value of t = 1 is obtained for $SrTiO_3$ indicating a perfect cubic perovskite structure whilst a slightly larger value of 1.01 is obtained for $SrFeO_3$ due to the smaller size of the Fe^{4+} ion.

The above relates to the fully oxidised material and more significant distortions to the cubic crystal structure would be expected for oxygen deficient materials. Oxygen deficient STFO materials form readily due to the preference of Fe to form the Fe^{3+} oxidation state which has the favourable half-shell d^5 electronic configuration rather than the Fe^{4+} oxidation state which is required for the stoichiometric material.

Whilst the lattice is able to accommodate oxygen vacancies whilst retaining a near cubic structure the larger size of the Fe^{3+} ion causes orthorhombic and tetragonal distortions of the lattice [93]. These observed distortions are consistent with the calculated Goldschmitt tolerance factor of t = 0.98 for the fully reduced $SrFeO_{2.5}$ material.

The Goldschmitt tolerance factor provides an indication of the thermodynamic properties of the perovskite and materials which deviate from the ideal value of 1 would be expected to have higher formation energies. The replacement of Ti^{4+} cations with Fe^{4+} or Fe^{3+} ions in the $SrTiO_3$ lattice as x increases along the $SrTi_{1-x}Fe_xO_{3-y}$ tie line would be expected to cause an increase in the formation energy of the material as neither ion matches the size requirements of the lattice as well as the Ti^{4+} ion.

An increase in formation energy of STFO with increasing Fe dopant content has been observed in experimental studies [59, 93]. In particular Schulze-Küppers *et al.* [93] monitored the formation of the cubic perovskite using x-ray diffraction for several compositions between x = 0 to x = 1. They reported that for STO (x = 0) the cubic perovskite phase could be obtained at 800 °C whilst for STFO with x = 0.25 and x = 0.35 the pure cubic phase could only be obtained by increasing the temperature above 1000 °C. The preparation of a cubic perovskite for STFO with x = 0.5 required a formation temperature of 1100 °C and for x = 0.75, 1200 °C was required. Below these temperatures the materials displayed a mixture of oxygen-deficient orthorhombic, tetragonal and cubic phases. The single cubic phase for SFO could not be obtained using these methods even at a temperature of 1200 °C.

The STFO materials in this work were synthesised using HT-PVD methods and the energy barrier to formation of the perovskite phase is lowered by the atomic mixing of the elements achieved by using atomic sources and an oxygen plasma source. As such much lower temperatures have been required to obtain the cubic perovskite crystal structure. However since the materials were deposited under identical conditions across a compositional range on a single substrate the formation of a variety of crystalline phases depending on the Fe content could be expected.

4.1.3 Ordered superstructures

In addition to the distortions to the lattice discussed above, the ordering of cations or oxygen vacancies in the extended perovskite structure can also have a major effect on the properties of the materials.

4.1.3.1 Cation-ordered structures

The extended perovskite crystal structure can be considered to consist of layers of alternating AO and BO_2 planes as shown in **Figure 4-3**. A key consideration when thinking about the structure of the STFO materials is the ordering of the Ti and Fe cations at the B site. Cation ordering is possible at either the A or B site of perovskite materials where there is a large enough difference in the charge, size or electronegativity of the ions occupying the site [129]. This leads to the formation of layered structures where the A or B site cations separate into distinct planes.

An example of this cation ordering is shown in **Figure 4-3** for a perovskite with two B site cations present in equal concentration, $A_2(B1)(B2)O_6$ which may also be written as $(A(B1)O_3)(A(B2)O_3)$ to emphasise the layered structure. This type of structure is often termed a double perovskite. Other layered structures are also possible depending on the ratio of the B1 and B2 cations. These structures may be described by $(A(B1)O_3)_1(A(B2)O_3)_n$ where n indicates the number of $A(B2)O_3$ planes which alternate with the $A(B1)O_3$ planes.

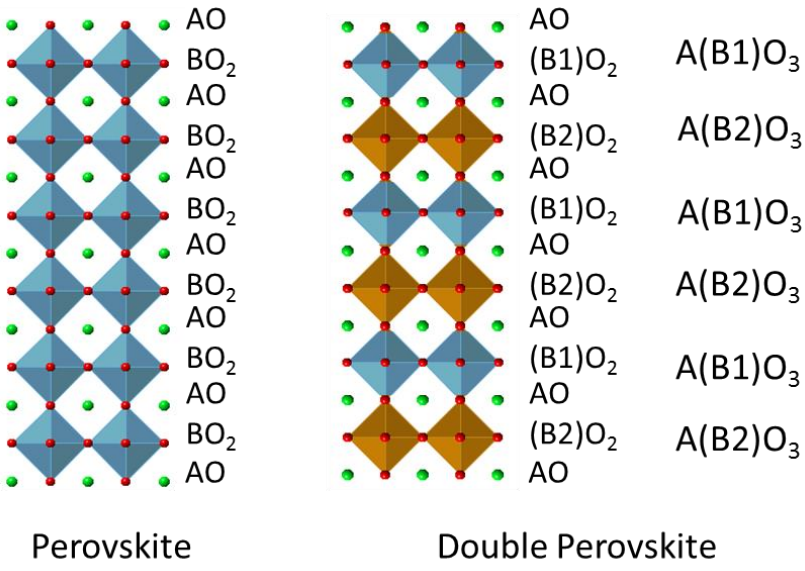

Figure 4-3: Schematic of perovskite crystal structure showing layers of AO and BO2 planes and double perovskite structure showing alternating layers of B1 and B2 polyhedra.

Cation ordering may not be expected for STFO since the Ti^{4+} and Fe^{4+} ions present in the stoichiometric material have equal charge and are of similar size. In this case a random distribution of Fe and Ti cations throughout the structure could be envisaged. However Fe does have greater electronegativity and a preference for the Fe^{3+} oxidation state which leads to the formation of oxygen vacancies in Fe containing perovskites. Consequentially layered perovskite structures may therefore become the most stable configuration for oxygen deficient materials where layers of $SrTiO_3$ alternate with layers of $SrFeO_{3-y}$.

4.1.3.2 Vacancy-ordered structures

Whilst reduced $SrTiO_3$ shows a solid solution with no ordering of oxygen-vacancies, $SrFeO_{3-y}$ has been reported [130] to form three distinct oxygen vacancy ordered phases described by the formula $Sr_nFe_nO_{3n-1}$ (n = 2, 4, 8) as depicted in **Figure 4-4**. The structure with n = ∞ represents the stoichiometric $SrFeO_3$ material which has cubic symmetry and all Fe ions present as octahedral Fe^{4+}. Whilst the formation of oxygen vacancies should donate electrons to the lattice and lead to n-type conductivity, the ordering of such vacancies has a negative impact on the conductivity as the electrons are trapped at certain sites thus reducing their mobility.

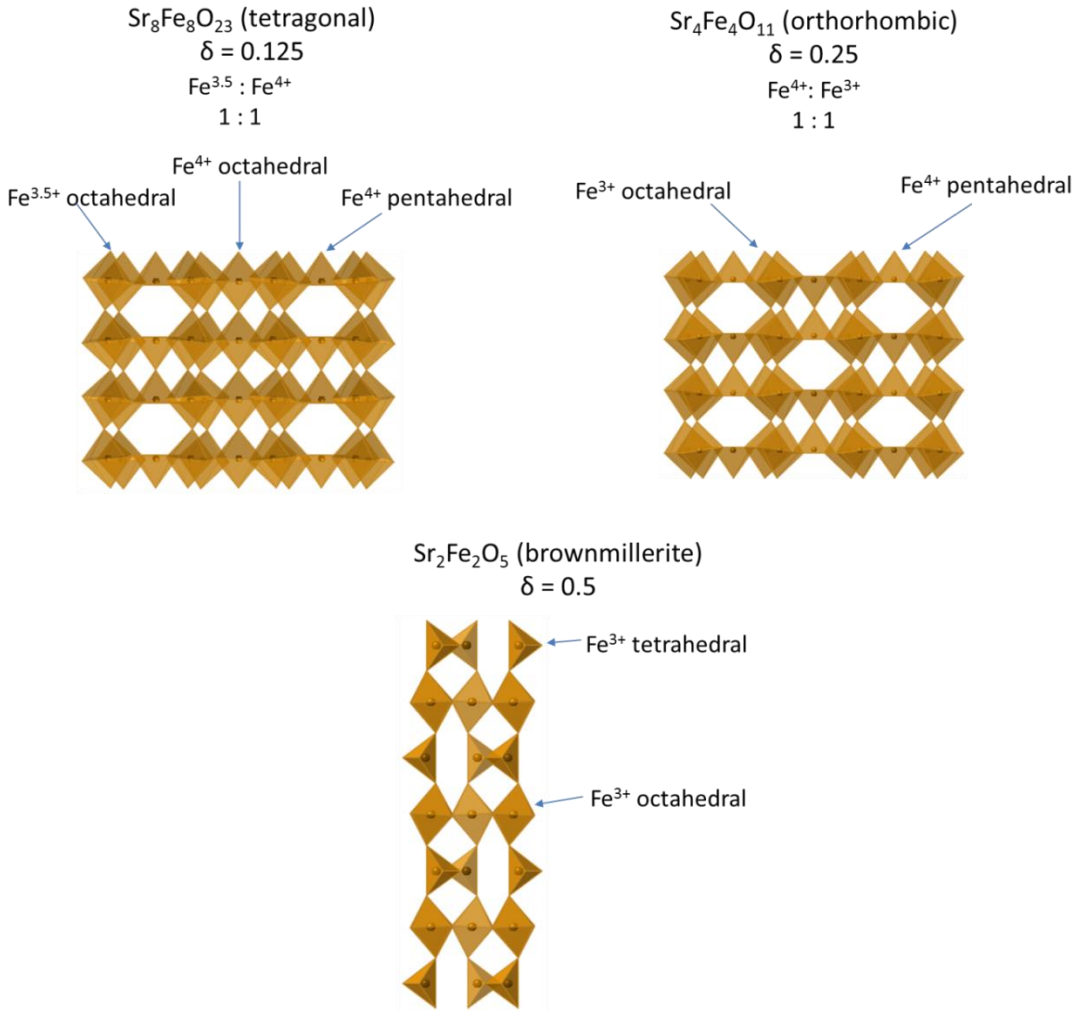

Figure 4-4: Schematic of oxygen vacancy ordered structures of $SrFeO_{3-\delta}$ where δ = 0.125, 0.25 and 0.5.

The presence of more than one layer of Fe ions leads to a larger range of possible oxygen vacancy patterns as shown in **Figure 4-5** [131].

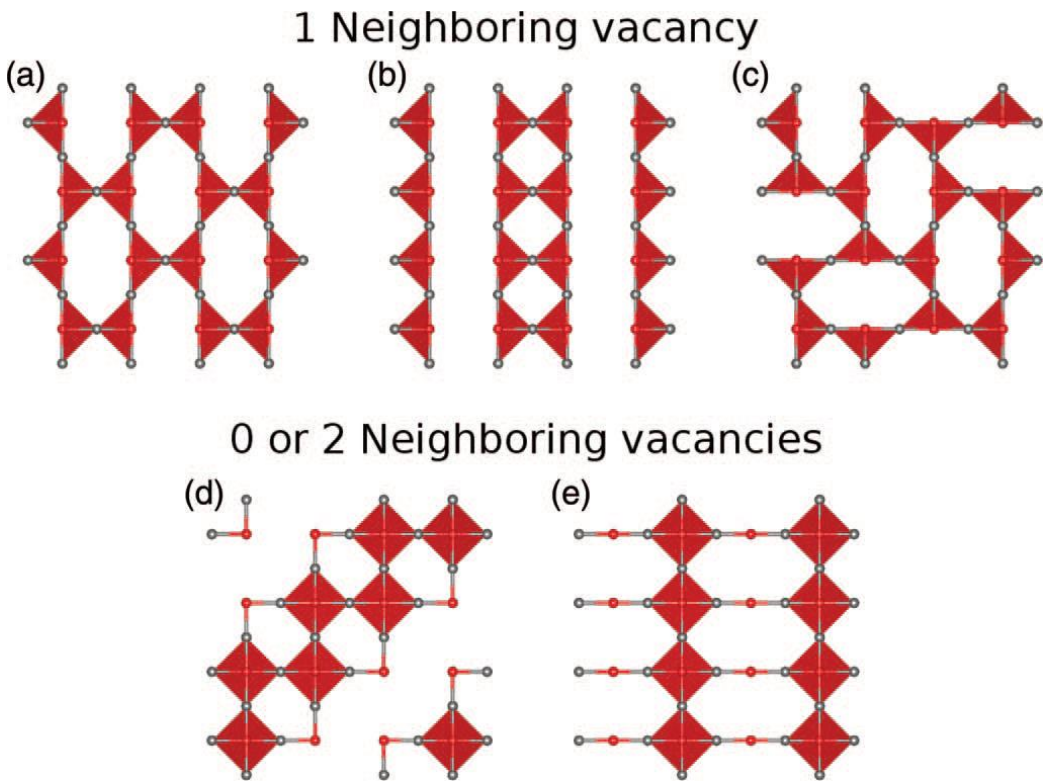

Figure 4-5: Schematic showing possible oxygen vacancy ordering patterns.

4.1.3.3 STFO ordered superstructures

Figure 4-6 shows schematic diagrams of three cation-ordered $(SrTiO_3)_1(SrFeO_{3-y})_n$ structures. For x < 0.5 structures with n < 1 are possible in which $SrTiO_3$ planes alternate with a $SrFeO_{3-y}$ planes e.g. the structure with n = 0.5, x = 0.33 consists of two $SrTiO_3$ planes alternating with a $SrFeO_3$ plane. In all of these structures the planes of Fe^{4+} ions are separated by at least one plane of Ti^{4+} ions.

For x > 0.5 however Fe ions would need to insert into the $SrTiO_3$ layers creating a new type of oxygen lattice site, Fe-Fe axial eventually leading to the n = 2 structure at x = 0.66 which consists of two $SrFeO_3$ planes alternating with a $SrTiO_3$ plane. At higher Fe contents ordered structures with more $SrFeO_3$ planes alternating with a $SrTiO_3$ plane could be formed. The key point about the x = 0.66 (n = 2) composition is the introduction of the Fe-Fe(axial) oxygen sites not present at lower Fe contents.

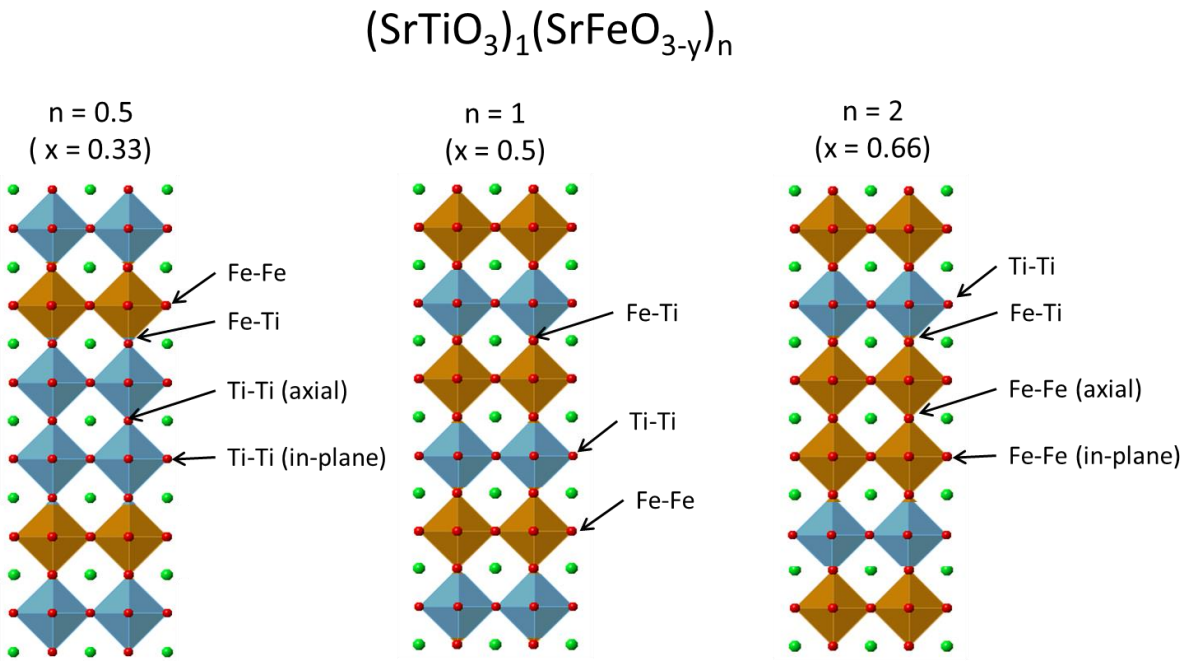

Figure 4-6: Schematic showing ordering of B site Ti and Fe cations in $SrTi1\text{-}xFe_xO_{3-y}$ to form $(SrTiO_3)_1(SrFeO_{3-y})_n$ superstructures where n represents the number of $SrFeO_3$ layers alternating with $SrTiO_3$ layers. The B site Ti and Fe cations are represented by blue and brown tetrahedra, respectively.

Berger *et al.* [131] investigated such $(SrTiO_3)_1(SrFeO_{3-y})_n$ structures for n = 1, the double perovskite structure, and n = 2, where two layers of $SrTiO_3$ alternate with one layer of $SrFeO_{3-y}$. The stoichiometric, y = 0, structures are shown above in **Figure 4-6**, the different chemical environments for the oxygen ions in the structure are indicated by arrows. Density functional theory calculations on the structures predicted a decrease in band-gap with increasing n. They also investigated the stability of oxygen vacancies and confirmed the expectation that oxygen vacancies are most stable at the Fe-Fe sites, followed by the Fe-Ti sites and lastly the Ti-Ti sites. They also suggested that a larger range of oxygen vacancy ordered structures are possible for the n=2 structure which has a double layer of $SrFeO_{3-y}$ and therefore contains axial Fe-Fe sites not present in the n=1 structure.

4.1.4 Inter-growth structures

The perovskite structure is also able to tolerate intergrowth structures of different phases. The Ruddlesden-Popper series with compositions $A_nB_{n-1}O_{3n+1}$ consist of layers of perovskite interspersed with layers of rock salt structure, A_2O_2 as shown schematically in **Figure 4-7**. The $Sr_nTi_{n-1}O_{3n+1}$ series is known and studies on this system have shown a decrease in stability with increasing n [132]. Structures of this type should be possible for the STFO electrocatalyst films for compositions with Sr > Ti + Fe.

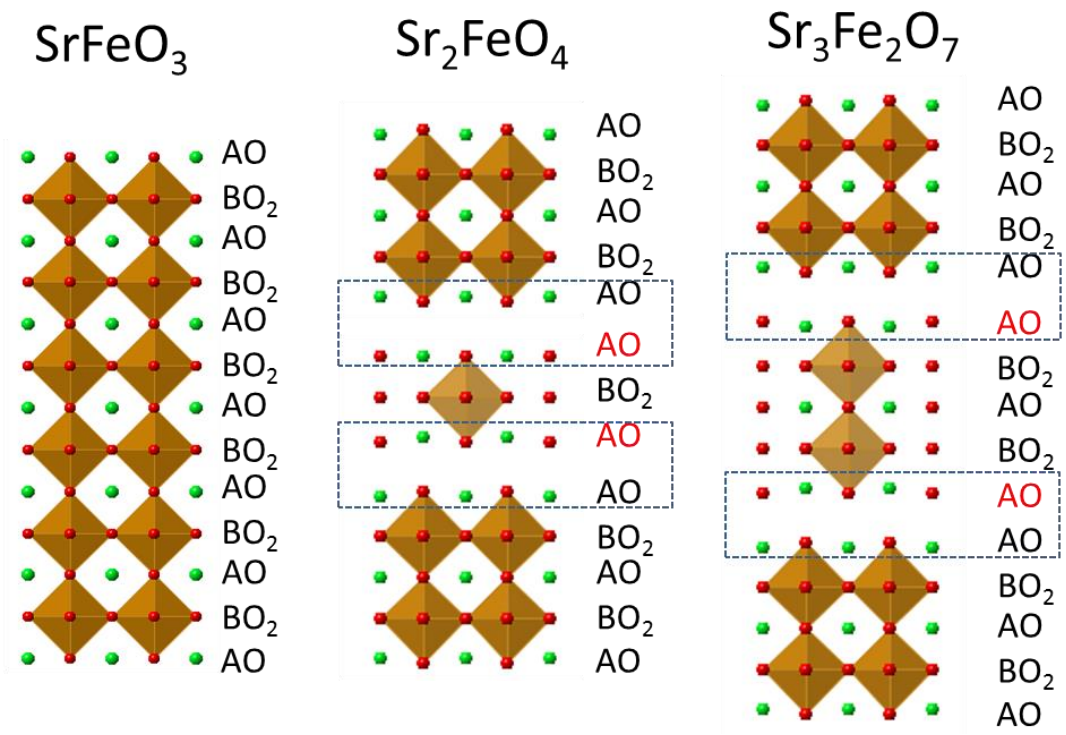

Figure 4-7: Schematic of crystal structures of $SrFeO_3$, Sr_2FeO_4 and $Sr_3Fe_2O_7$ highlighting the rock-salt inter-growth layer which is interspersed with layers of the perovskite structure in Sr_2FeO_4 and $Sr_3Fe_2O_7$.

Whilst the perovskite crystal structure is unable to accept interstitial oxygen, the Ruddlesden-Popper structured material can accept interstitial oxygen into the rock-salt structured layers [133]. This provides an additional mechanism for the diffusion of oxygen through the lattice.

4.2 Results

4.2.1 Visual inspection of films

The first evidence to support the presence of distinct crystalline phases in the STFO samples comes from a visual inspection of the films. **Figure 4-8** shows a photograph of a STFO film deposited with compositions close to the $SrTi_{1-x}Fe_xO_{3-y}$ tie line alongside a ternary diagram showing the composition of the samples as determined by EDX.

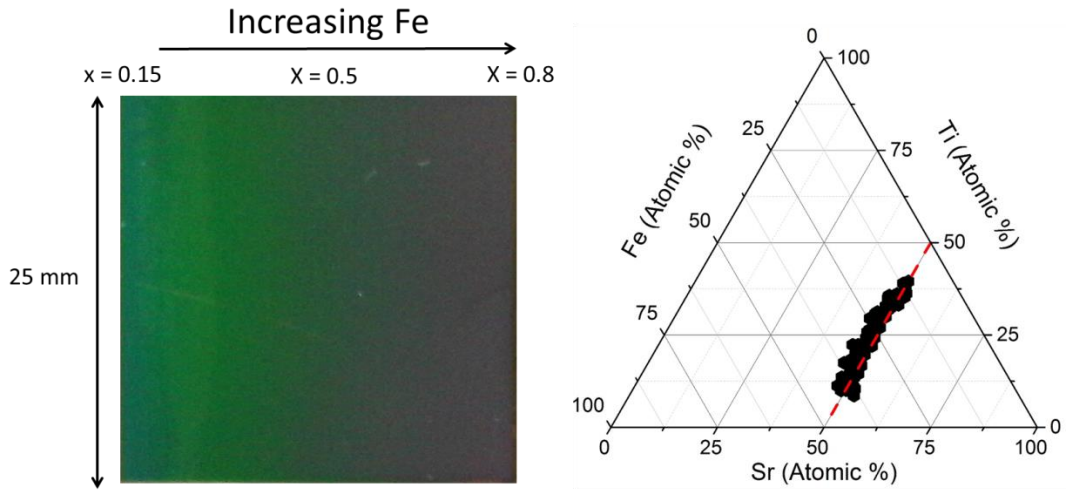

Figure 4-8: Photograph of STFO thin film on SiN substrates showing a colour change with increasing Fe content alongside ternary diagram showing composition of sample.

The sample shows a clear change in colour upon addition of the Fe dopant and at higher Fe content, above x = 0.5, the film appears much darker and more metallic having a similar appearance to the uniform $SrFeO_3$ film shown in **Figure 4-9**. This is consistent with the changing electronic structure of the materials which are expected to show a decreased band-gap and increasing metallic behaviour as Fe content is increased. However it should be noted that the change in colour is not gradual over the film, occurring sharply at compositions close to x = 0.5. This sharp change seems more likely to arise from a change in the crystal structure.

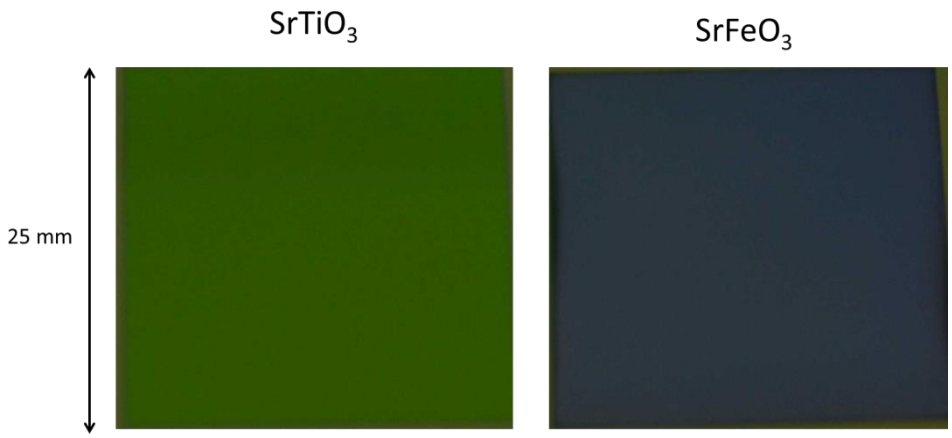

Figure 4-9: Photographs of uniform films of $SrTiO_3$ and $SrFeO_3$ deposited under atomic oxygen at 650 °C on a SiN substrate. Film thickness = 200 nm.

Changes in the colour of the STFO films with increasing Sr content are also observed. Photographs of STFO sample deposited with a larger range of Sr compositions are shown alongside ternary diagrams showing the sample composition as obtained by EDX in **Figure 4-10.**

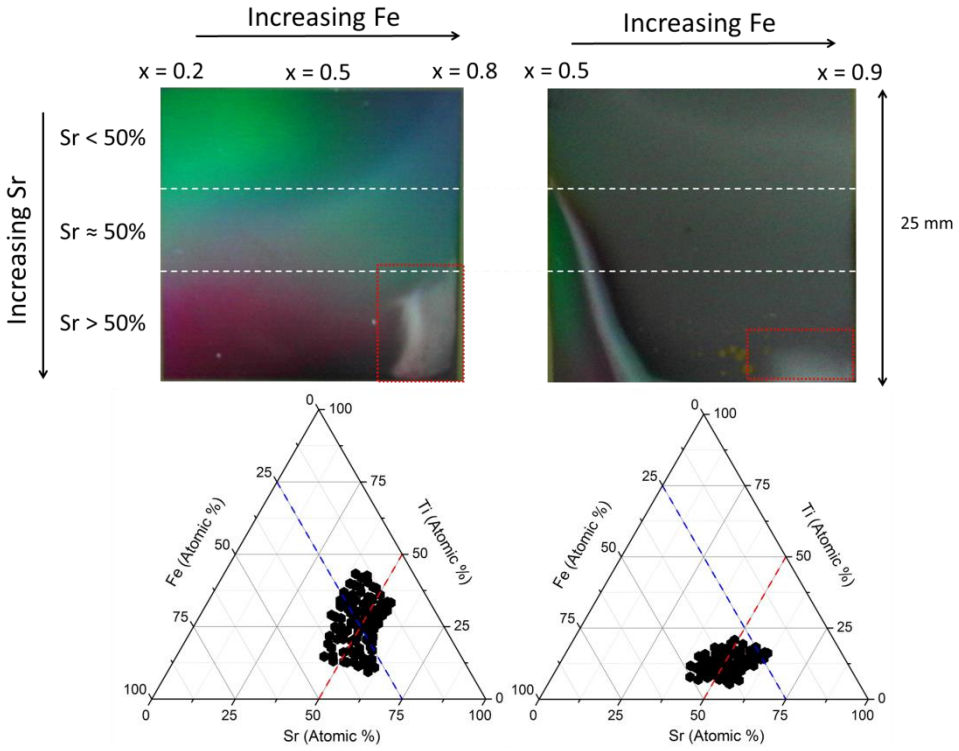

Figure 4-10: Photographs of a STFO thin film deposited under atomic oxygen at 650 °C on a SiN substrate.

Changes in the colour of the film are expected with varying thickness and it should be noted that the thickness of the film increases with increasing Sr content which could be a factor in the colour variation seen in this direction. The colour changes could however be indicative of changes in the electronic or crystal structure of the material. Evidence for this could be found in the observation that the sample with compositions in the range $0.2 < x < 0.8$ shows a colour change as the Sr content and thickness increases whilst the sample with higher Fe content, with compositional range $0.5 < x < 0.9$ which shows the same increase in thickness shows a largely uniform colour for x values above around 0.6. This higher Fe content film has a metallic appearance similar to that observed for the binary SFO film shown in **Figure 4-9**.

The sample can roughly be split into three regions by Sr content as shown by the white dotted lines. At the top of the film the Sr content is below the 50% required for a stoichiometric ABO_3 perovskite structure. In this region the film shows a colour change at x = 0.5 as was seen for the tie-line sample in **Figure 4-8** which is again consistent with the changing electronic structure of the materials which are expected to show a decreased band-gap and increasing metallic behaviour.

As the Sr content of the film approaches 50% however no colour change is observed with changing Ti/Fe ratio indicating the presence of a single phase. This is interesting since it would be expected that the film would have a similar appearance to the tie-line sample at this point. This could be evidence that the different deposition conditions required to deposit the film over a larger range of Sr compositions has had an effect on the properties of the material. The most likely reason for this would be a difference in the oxygen content of the two samples, however much more evidence would be required to confirm this theory.

Above 50% Sr there is another change in the colour of the film which could be due to the formation of a new phase or combination of phases. One possibility for an additional phase here would be the Ruddlesden-Popper structures in which the excess Sr is ordered into SrO rock-salt layers as discussed in section 4.1.4. Additionally at higher Fe contents there appears to be the formation of a white surface oxide, highlighted by the red-box in the photographs, which could be evidence of Sr surface segregation or could be a distinct phase.

4.2.2 X-ray Diffraction

4.2.2.1 $SrTiO_3$ and $SrFeO_3$

X-ray diffraction data for uniform films of $SrTiO_3$ and $SrFeO_3$, prepared at 650 °C under atomic oxygen is shown in **Figure 4-11** and **Figure 4-12**. In both cases a cubic perovskite structure was observed with no other crystalline phases present. The lattice constant for $SrTiO_3$ was calculated to be 0.392 ± 0.01 nm which is larger than the value of 0.3907 ± 0.0001 nm [59, 60, 93, 102] reported by other researchers. The lattice constant for $SrFeO_{3-y}$ was calculated as 0.386 ± 0.001 nm, which is consistent with the reported value of 0.3860 ± 0.0001 nm [101, 102, 134].

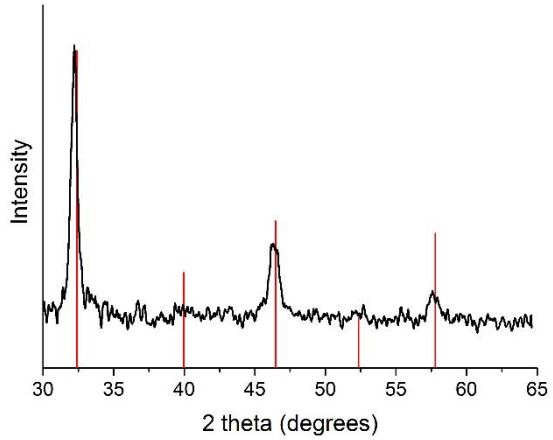

Figure 4-11: X-ray diffraction pattern for a $SrTiO_3$ film deposited by PVD at 650 °C under a 500 W oxygen plasma. PDF card #01-079-0174 ($SrTiO_3$) is shown by the red bars.

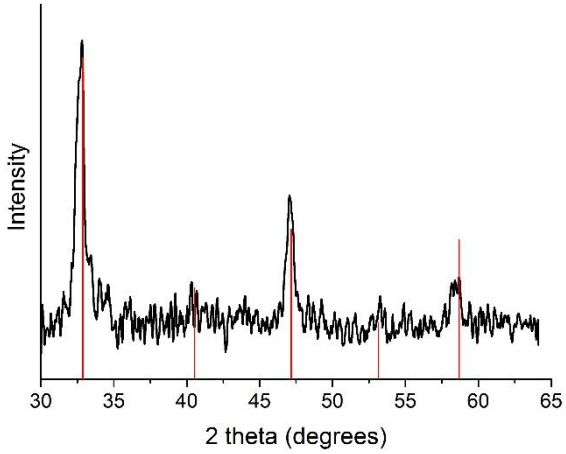

Figure 4-12 X-ray diffraction pattern for a $SrFeO_3$ film deposited by PVD at 650 °C under a 500 W oxygen plasma. PDF card #01-070-5775 ($SrFeO_3$) is shown by the red bars.

4.2.2.2 $SrTi_xFe_{1-x}O_3$

XRD data from the STFO films, prepared at 650 °C under atomic oxygen, confirmed a cubic perovskite structure across the $SrTi_{1-x}Fe_xO_{3-y}$ tie line as shown in **Figure 4-13**, this is consistent with previous studies of the bulk material [58-60]. As the Fe content of the samples increases, there is a shift in the 2 theta position of the peaks due to the contraction of the crystal lattice caused by the replacement of Ti^{4+} ions (r = 0.605 Å) with smaller Fe^{4+} ions (r = 0.585 Å).

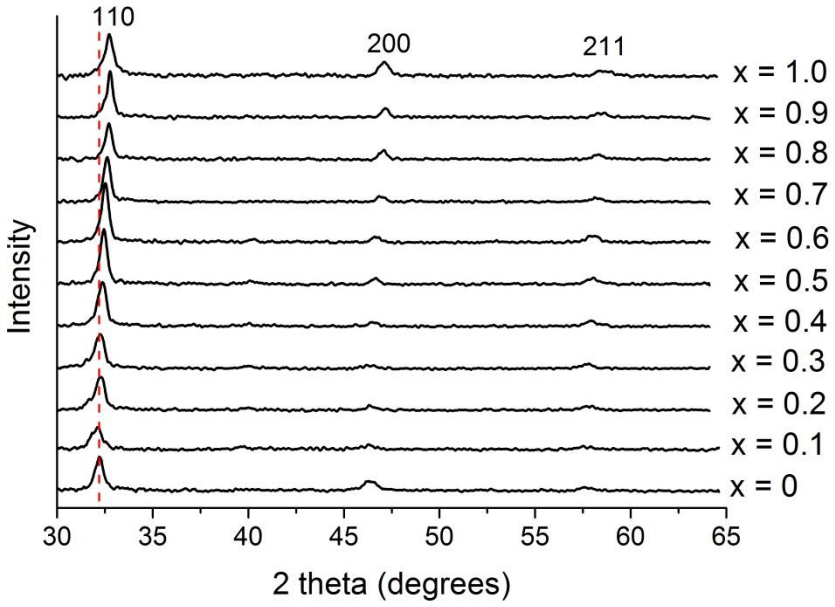

Figure 4-13: X-ray diffraction patterns for a STFO film deposited at 650 °C under atomic oxygen. Red dashed line indicates the position of the (110) reflection for STO.

The observation of a cubic perovskite structure along the $SrTi_{1-x}Fe_xO_{3-y}$ tie line suggests an undistorted structure with no ordered superstructure apparent. However the perovskite lattice is very robust and all of the structures discussed in **Section 4.1.3** can occur with retention of a near-cubic structure and as such may not be identifiable from x-ray diffraction data. An example of a possible cation-ordered and vacancy ordered structure for $SrTi_{0.5}Fe_{0.5}O_{2.75}$ is shown in **Figure 4-14**.

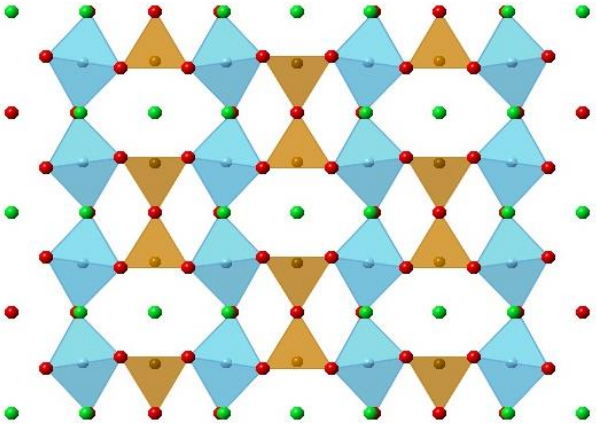

Figure 4-14: Schematic showing ordering of B site Ti and Fe cations in $SrTi_{0.5}Fe_{0.5}O_{3-y}$ to form a $(SrTiO_3)$ $(SrFeO_{3-y})$ superstructure where oxygen deficient $SrFeO_{3-y}$ layers alternate with $SrTiO_3$ layers. The B site Ti and Fe cations are represented by blue and brown polyhedra, respectively.

A calculated XRD spectrum for this structure is shown in **Figure 4-15** alongside the calculated spectrum for $SrFeO_3$. The XRD spectrum for the cation-ordered oxygen-deficient structure does not differ significantly from that expected for the perovskite structure. The slight doublet structure which appears in the peaks is likely to be lost in instrumental broadening unless very high resolution data is available.

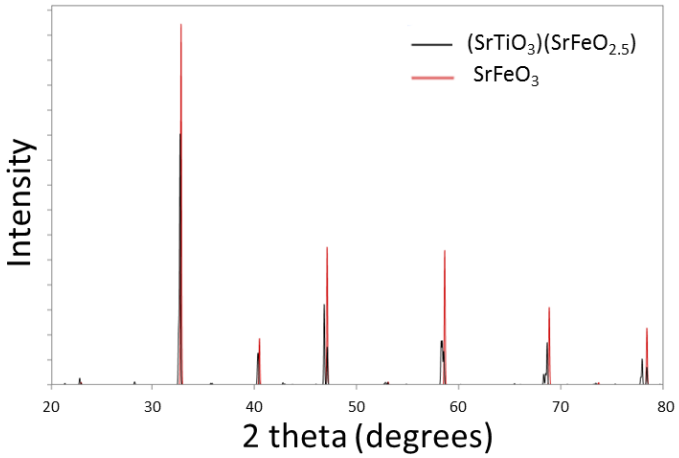

Figure 4-15: XRD spectrum for $(SrTiO_3)$ $(SrFeO_{3-y})$ calculated from the crystal structure using CrystalDiffract software. The calculated spectrum for $SrFeO_3$ is shown in red to demonstrate the similarity between the two spectra.

The cubic perovskite structure is observed over a large range of compositions on the STFO thin films as shown by **Figure 4-16A** which shows the intensity of the (110) reflection. It is somewhat unusual that the (110) peak shows a maximum at higher Fe contents when it has generally been assumed that the increase in Fe content would increase the formation energy of the lattice due to the poorer fit of the Fe cation in either oxidation state into the B-site of the perovskite lattice when compared to Ti^{4+}. This may be an indication that the PVD method employing the reactive oxygen plasma source is highly effective at synthesis of the Fe-rich phases, which are difficult to prepare thermodynamically, via the provision of a different formation path with a low kinetic barrier to mixing of the elements.

Figure 4-16B shows the variation in the two theta peak position of the (110) reflection with film composition in ternary space and confirms that there is little variation with Sr content whilst there is a gradual shift to lower 2 theta with increasing Fe content due to contraction of the crystal lattice as described earlier.

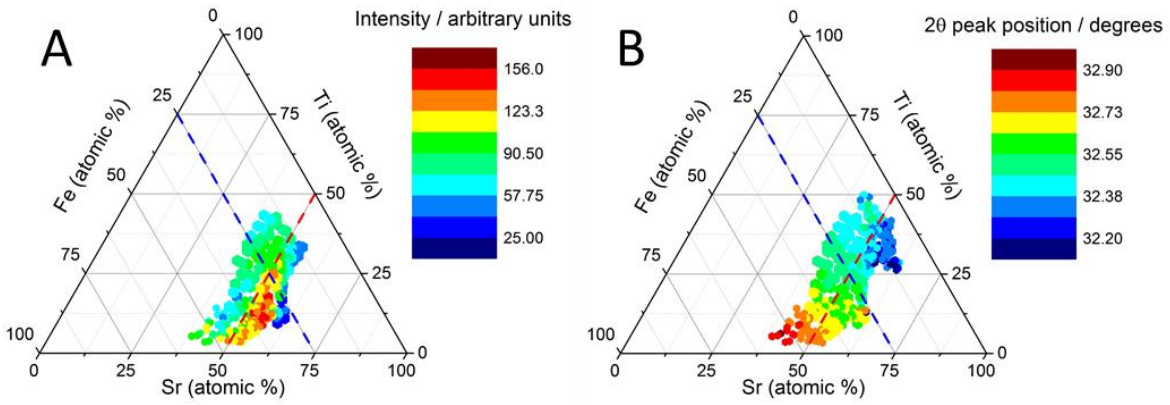

Figure 4-16: Ternary plots showing (A) variation in the intensity of the (110) peak and (B) two theta (110) peak position with composition.

A distinct phase could be identified from the x-ray diffraction data at Sr ≥ 58%, some examples of the diffraction patterns are shown in **Figure 4-17**. A splitting of the (110) diffraction peak is apparent and the crystallinity is greatly decreased compared to the diffraction data obtained for the perovskite phase at Sr contents close to 50%, an example of which is also shown.

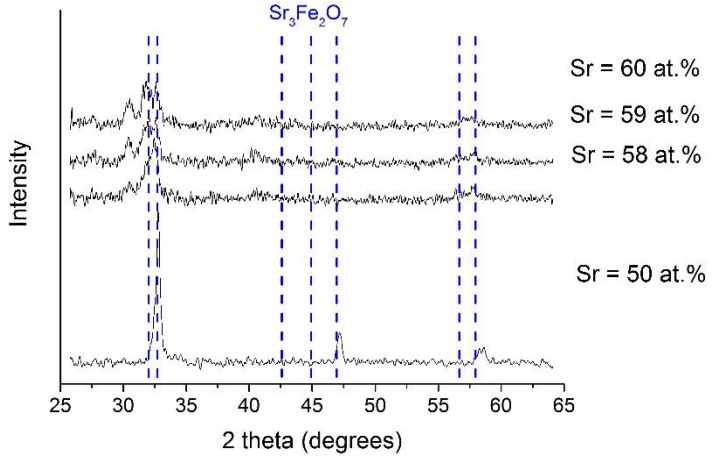

Figure 4-17: XRD data obtained at points with varying Sr concentration. Blue dotted lines show positions of major peaks in the calculated spectrum of Ruddlesden-Popper $Sr_3Fe_2O_7$, a structure in which layers of perovskite structure are interspersed with layers of rock-salt structured SrO.

This phase has been assigned to a Ruddlesden-Popper, $Sr_n(Ti, Fe)_{n-1}O_{3n+1}$, type structure as discussed in **Section 4.1.4.** In these structures the excess Sr forms intergrowth layers of SrO with a rock-salt crystal structure. The ternary diagram in **Figure 4-18** shows the intensity of the diffraction peak at 2θ = 30° which is associated with this phase, showing that it occurs only for Sr compositions above 58%, as indicated by the green dotted line. The n = 3, $Sr_3(Ti, Fe)_2O_7$, phase would therefore seem the most likely candidate. Since the structures decrease in stability with increasing n and n = 3 is considered the limit of stability this would explain the low crystallinity.

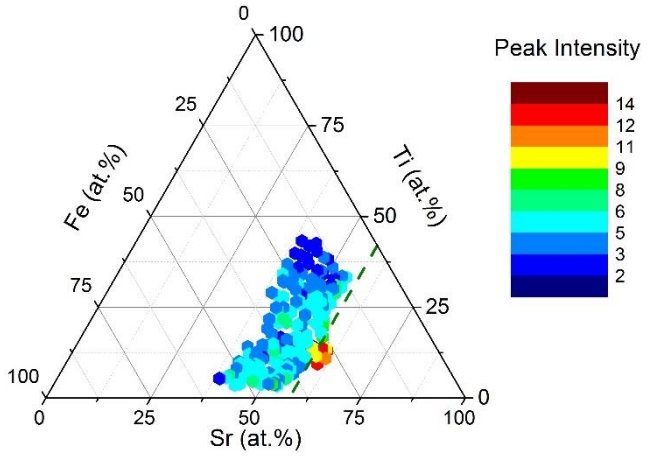

Figure 4-18: Ternary plot showing variation in peak intensity for the two theta = 31 degrees peak in the XRD diffraction pattern of the STFO film deposited at 650 °C under atomic oxygen. The peak appears only at high Sr contents and as such arises from a Sr-rich phase. Green dashed line indicates compositions with Sr = 58%.

4.2.2.3 Determination of lattice parameters

Several studies have been able to observe the effects of oxygen deficiency on the x-ray diffraction data by the Rietveld refinement of the diffractograms to obtain the lattice parameter, a. The replacement of Ti^{4+} ions (r = 0.605 Å) with smaller Fe^{4+} ions (r = 0.585 Å) would be expected to cause a contraction in the crystal lattice and as such a decrease in the lattice parameter. Vegard's law for metallic alloys [135], shown in **Equation** 4-2, states that for a metallic alloy at constant temperature there should be a linear relationship between the lattice constant, a, and the relative concentration of the elements.

$$a_{A_{(1-x)}B_x} = (1-x)a_A + xa_B$$

Equation 4-2

Figure 4-19 shows lattice parameters reported in the literature from studies of $SrTi_{1-x}Fe_xO_{3-y}$ perovskites with increasing Fe content, x. The black dashed line shows the relationship expected between lattice parameter and x for the fully oxidised stoichiometric material if Vergard's law is obeyed. All of the studies showed deviation from Vegard's law assumed to be caused by the presence of larger Fe^{3+} ions in the lattice which leads to a larger than expected lattice parameter.

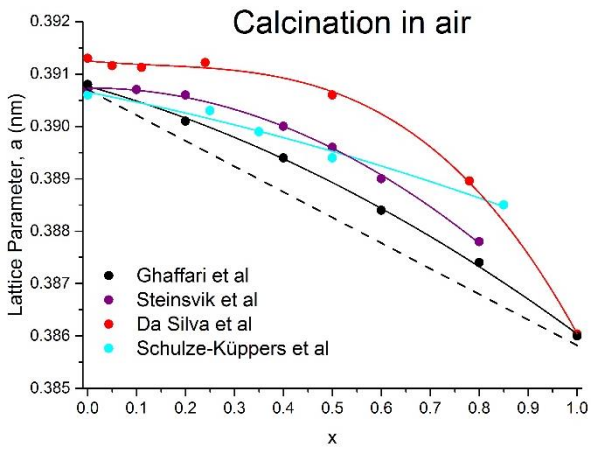

Figure 4-19: Variation in the lattice parameter, a, obtained from previous studies on the $SrTi_{1-x}Fe_xO_{3-y}$ perovskite. Ghaffari *et al.* [102] synthesised STFO by a high temperature solid state reaction involving mechanical mixing of $SrCO_3$, TiO_2 and Fe_2O_3 powders and calcination at 1200 °C in air for a total of 48 h. Steinsvik *et al.* [59], Da Silva *et al.* [103] and Schulze-Küppers *et al.* [93] all used a liquid-mix technique in which Sr, Ti and Fe salts were mixed in citric acid solution with ethylene glycol to form a polymer precursor which was then calcined. Steinsvik *et al.* used a final calcination temperature of 1200 – 1350 °C depending on Fe content in air. Da Silva *et al.* used a final calcination temperature of 750 °C for a total of 2 h. Schulze-Küppers *et al.* used a final calcination temperature of 900 °C for 12 h in air.

The smallest deviation from Vegard's law was obtained by Ghaffari *et al.* [102] who prepared the STFO perovskite by a high temperature solid state reaction which involved mechanical mixing of $SrCO_3$, TiO_2 and Fe_2O_3 powders and calcination at 1200 °C in air for a total of 48 h. The remaining studies used the liquid mix technique described in **Section 1.1.3** with annealing in air at a range of temperatures and durations. There does seem to be a tentative link between annealing temperature and duration and the agreement with Vegard's law. The study by Da Silva *et al.* [103] for which the STFO lattice parameters show a large deviation from Vegard's law calcined the STFO samples twice at 750 °C for 1h in air. This is a much shorter annealing time and lower temperature than used in the other studies.

All of the studies report an overall cubic perovskite structure for the STFO compositions despite the oxygen deficiency in the lattice which demonstrates the robustness of the cubic structure of STFO to the formation of oxygen vacancies. Schulze-Küppers *et al.* [93] did report an orthorhombic perovskite structure for SFO (x = 1) prepared in air and a brownmillerite structure for SFO prepared in Ar. These structures are consistent with those previously reported for $SrFeO_{3-y}$ and were discussed in **Section 4.1.3.2**.

Steinsvik *et al.* [59] also reported transmission electron diffraction data which showed a superstructure with a smallest reproducible cell of 2:2:1 times the perovskite unit cell for the x = 0.6 and x = 0.8 compositions which they assigned to the ordering of oxygen vacancies but this was not apparent in the x-ray diffraction data except in the higher than expected cubic lattice parameter.

Schulze-Küppers *et al.* [93] obtained lattice parameters for materials annealed at 900 °C both in air, shown by the light blue line in **Figure 4-20**, and in Ar, shown by the green line in **Figure 4-20**. The Ar annealed sample showed an increase in the lattice parameter with increasing Fe content and as such it seems likely that this sample contains predominantly Fe^{3+} which causes an expansion of the crystal lattice. A study by Brixner *et al.* [92] however prepared oxygen deficient $SrTi_{1-x}Fe_xO_{3-x/2}$ materials by calcination under Ar for which the oxygen deficiency was confirmed by iodometric titration and found the lattice parameter decreased with increasing Fe content despite the apparent Fe^{3+} oxidation state. The data from this study is also shown in **Figure 4-20.**

One possible explanation for this unusual result would be that the iodometric titration method used for determining the oxygen content is inaccurate, however several studies have shown an agreement between oxygen contents obtained by this method and those obtained by Mossbauer spectroscopy [95, 96]. Also some degree of oxygen deficiency would be expected upon annealing at 1300-1400 °C in an inert atmosphere.

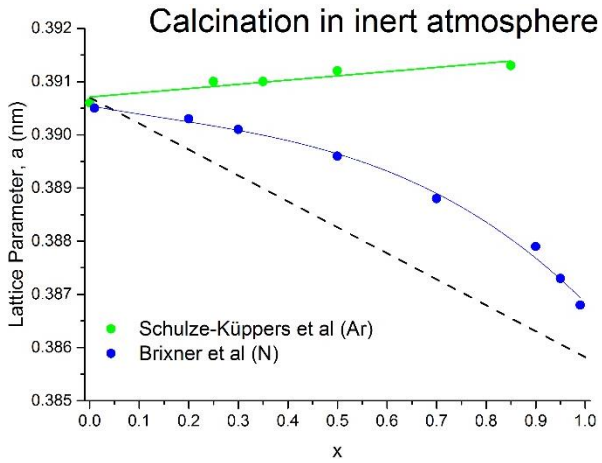

Figure 4-20: Variation in the lattice parameter, a, obtained from previous studies on the $SrTi_{1-x}Fe_xO_{3-y}$ perovskite. Schulze-Küppers *et al.* [93] all used a liquid-mix technique in which Sr, Ti and Fe salts were mixed in citric acid solution with ethylene glycol to form a polymer precursor which was then calcined at a final temperature of 900 °C for 12 h under Ar. Brixner *et al.* [92] synthesised STFO by a high temperature solid state reaction with final calcination at 1300 - 1400 °C under nitrogen for 10-14 h.

The most likely explanation for the disagreement over the trend in lattice parameter for the oxygen deficient materials lies in the difficulty in interpreting the diffraction data of the near-cubic perovskites. Since the materials were obtained at different temperatures, 900 °C for the Schulze-Küppers study [93] and 1300-1400 °C for the Brixner study [92] a difference in the crystal structures of the materials would be entirely possible. In both cases the lattice parameters have been obtained assuming a cubic perovskite structure which may not be realistic.

For the STFO materials in this work a linear relationship was observed between Fe content, x, and both the (110) 2 theta peak position and the calculated lattice parameter as shown in **Figure 4-21** and **Figure 4-22** respectively. This is in accordance with Vegard's law.

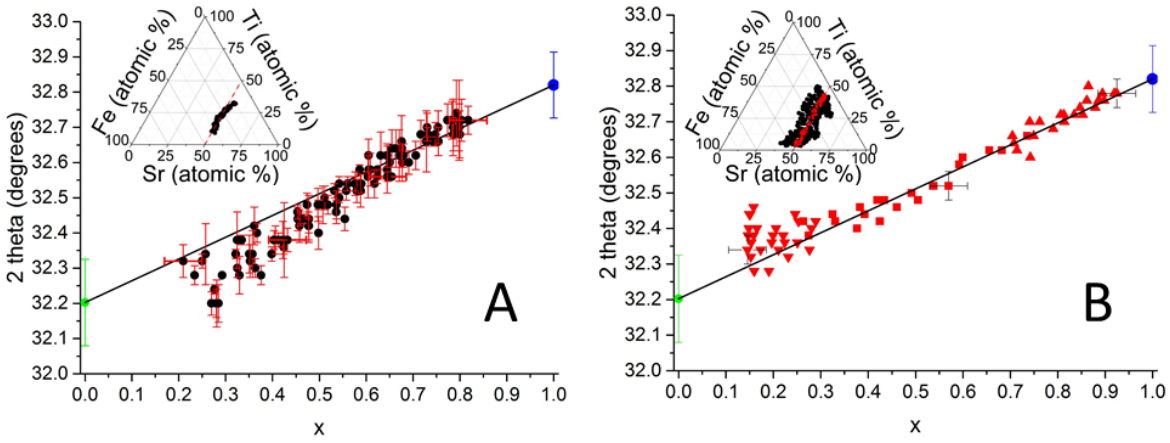

Figure 4-21: Plot to show variation in (110) 2 theta position with Fe content, x, for compositions on the tie-line (Sr content 50 ± 2 at. %). Data shown is from (A) tieline sample with Sr = 50 ± 5 at.% and (B) two Sr graduated samples with Sr (shown by red dots and triangles). Data for $SrTiO_3$ and $SrFeO_3$ is shown in green and blue, respectively. Black line shows Vegard's law calculated from the two end compositions. Horizontal error bars represent error in the compositions of the films obtained by EDX.

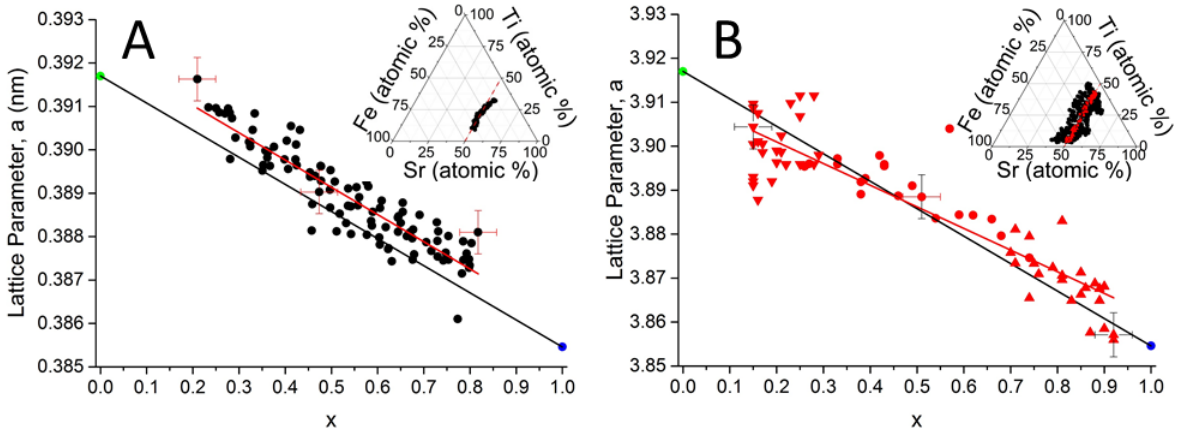

Figure 4-22: Plot to show variation in the lattice parameter, a, with Fe content, x, for compositions on the tie-line (Sr content 50 ± 2 at. %). Data shown is from (A) tieline sample with Sr = 50 ± 5 at.% and (B) two Sr graduated samples with Sr (shown by red dots and triangles). Data for $SrTiO_3$ and $SrFeO_3$ is in green and blue, respectively. Black line shows Vegard's law calculated from the two end compositions. Red line shows linear fit of the data. Horizontal error bars represent error in the compositions of the films obtained by EDX. Vertical error bars were calculated from the error in the linear fit of the data.

4.2.2.4 Effect of preparation conditions

Figure 4-23 shows x-ray diffraction patterns for thin films deposited under molecular oxygen at 650 °C. The crystallinity decreased with increasing Fe content and when the Fe content of the film was above x=0.7 no clear perovskite phase could be identified.

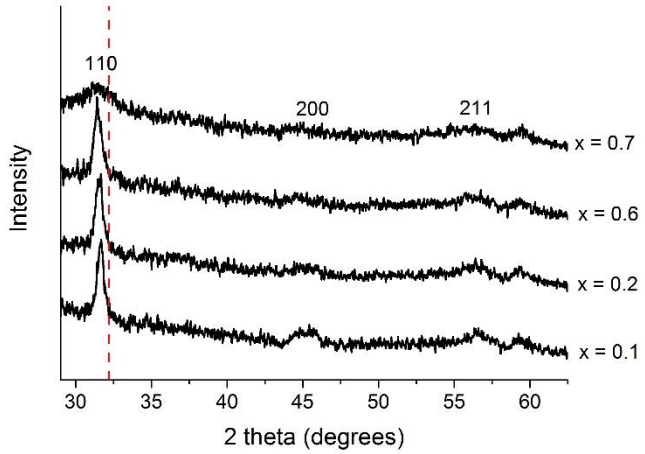

Figure 4-23: X-ray diffraction patterns for a STFO film deposited at 650 °C under molecular oxygen.

The crystallinity of the films could be improved by post-annealing in a tube furnace under O_2 at 650 °C for 6 h. Following this annealing process the cubic perovskite phase could be identified across the compositional range as shown in **Figure 4-24**. The diffraction peaks appear sharper which may be due to an increase in the formation of the perovskite or could simply be an effect of a larger crystallite size.

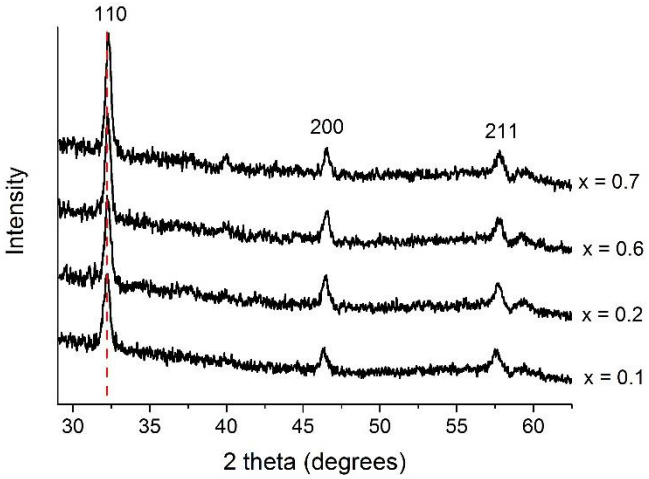

Figure 4-24: X-ray diffraction patterns for a STFO film deposited at 650 °C under molecular oxygen following annealing in a tube furnace under O_2 at 650 °C for 6 h.

The STFO films deposited in molecular oxygen show a large deviation from the expected two theta position of the (110) peak as shown in **Figure 4-25A**. This is likely to be due to the presence of Fe^{3+} (r = 0.645 Å) which has a larger ionic radius than Ti^{4+} (r = 0.605 Å) and Fe^{4+} (r = 0.585 Å) therefore leading to expansion of the crystal lattice. At higher Fe contents the peaks in the diffraction were very weak as shown in **Figure 4-23** so the (110) peak cannot be definitively assigned to the perovskite crystal structure and could arise from another crystal phase.

After annealing the (110) peak positions were in the expected range and similar to those obtained for the films made using the oxygen plasma. However the linear trend of increasing 2 theta position with increasing Fe content, x, is not as apparent as shown in **Figure 4-25B**. One possible explanation for this is that the film is not truly a mixed metallic alloy and contains regions of $SrTiO_3$ and regions of $SrFeO_3$.

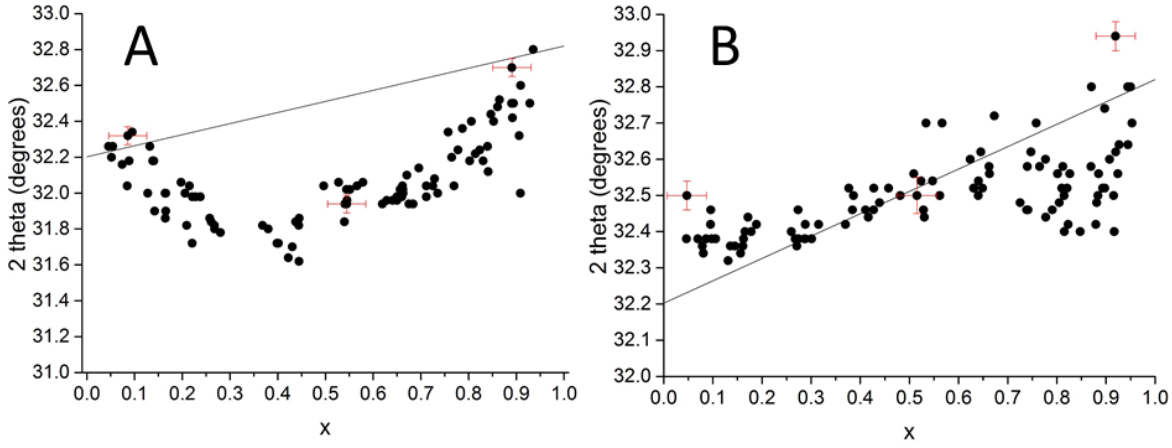

Figure 4-25: Variation in position of the (110) reflection with Fe concentration for a STFO film deposited at 650 °C under molecular oxygen and for the same film following annealing in a tube furnace under O_2 at 650 °C for 6 h. Black line shows Vegard's law calculated from the two end compositions of the films prepared under oxygen plasma. Red line shows linear fit of the data for the films prepared under the oxygen plasma shown in Figure **4-21**.

4.2.3 Raman Spectroscopy

4.2.3.1 $SrTiO_3$ and $SrFeO_3$

All first-order Raman lines are symmetry forbidden for cubic perovskites including $SrTiO_3$ but distortions in the lattice caused by dopants , oxygen vacancies [97] or by the preparation of thin films by pulsed laser deposition [136] have led to symmetry lowering and the observation of Raman active modes in previous studies. **Figure 4-26** shows Raman spectra taken on the uniform films of STO and SFO on SiN, the Raman spectrum of the substrate is also shown. No Raman lines are observed for STO, however, some lines are present in the SFO spectrum which would not be expected for the bulk stoichiometric material.

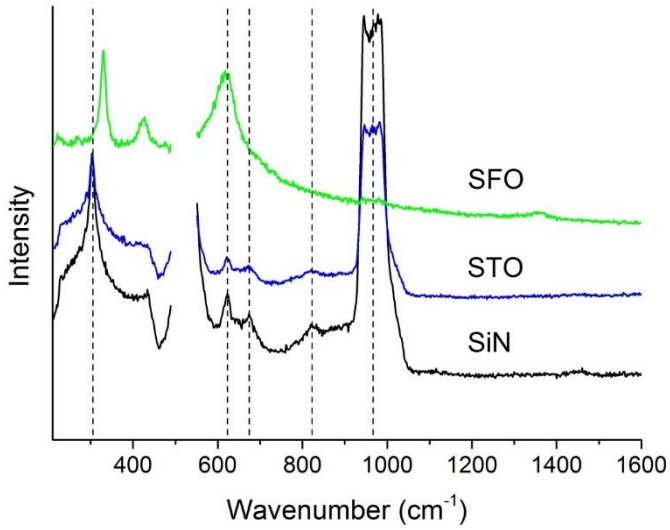

Figure 4-26: Raman spectra taken on uniform films of $SrFeO_3$, $SrTiO_3$ and on the SiN substrate. Data was not collected in the 490 – 550 cm^{-1} region due to an intense first-order SiN line, the dashed lines show the positions of the second-order SiN lines. Spectra have been offset vertically for clarity.

The positions of these lines appear similar to those seen for an oxygen deficient single crystal of composition $SrFeO_{2.85}$ in a previous study [97]. The researchers suggested that these lines were allowed due to symmetry lowering caused by tetragonal distortions to the crystal structure which occur due to the ordering of oxygen vacancies. The substrate peaks are absent in the SFO spectrum which is assumed to be due to greater absorption of the laser beam since the SFO film is much darker in colour than the STO film as was shown in **Section 4.2.1.**

4.2.3.2 $SrTi_xFe_{1-x}O_3$

Figure 4-27 shows Raman spectra for compositions across the STFO film, the feature at 950 – 980 cm^{-1} is second-order scattering from the Si substrate. This line decreases in intensity with increasing iron content due to changes in the material's absorption of the laser radiation which is consistent with the change in colour of the film. There is no evidence to support the presence of the $SrCO_3$ phase which was observed in the XPS data which would be characterised by a line at 1090 cm^{-1} [137] but this does not rule out a thin surface layer.

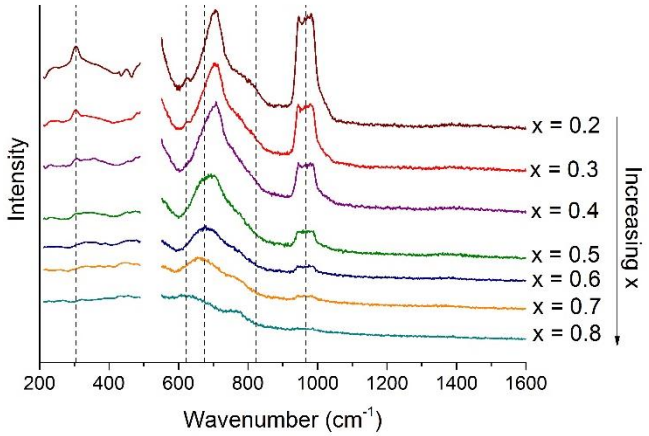

Figure 4-27: Raman spectra for compositions across a STFO film deposited on a SiN substrate. Spectra have been offset vertically for clarity. Data was not collected in the 490 – 550 cm^{-1} region due to an intense first-order SiN line, the dashed vertical lines show the positions of the second-order SiN lines. Spectra have been corrected for varying thickness in the film.

A pronounced peak at around 705 cm^{-1} is present at low Fe content which decreases in intensity and shifts to lower wavenumber as Fe content increases. The line has been observed in previous Raman studies of the bulk $SrTi_{1-x}Fe_xO_3$ material [60, 134, 138] and it has been suggested that the peak corresponds to a O stretching vibration mode [108]. The appearance of the peak is rationalised by a Jahn-Teller distortion which results in an asymmetric relaxation of Fe-O bonds around the iron dopant atom as shown in **Figure 4-28** [139]. This lowers the symmetry from O_h to tetragonal D_{4h}. the O-stretching vibration then results in a change in the polarizability and so the Raman line becomes allowed.

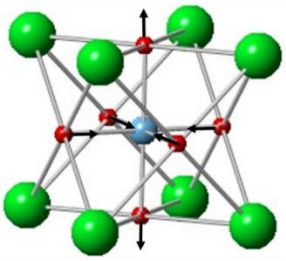

Figure 4-28: Proposed Jahn-Teller distortion around Fe^{4+} ions in $SrTi_{1-x}Fe_xO_3$. The oxygen atoms relax inwards in the xy plane and outwards along the x-axis to lower the symmetry from O_h to D_{4h}. Figure adapted from [139].

The occurrence of a Jahn-Teller distortion for octahedrally co-ordinated Fe(IV) is explained by the presence of a single electron in the e_g orbital which results in an un-symmetrical charge distribution that distorts the geometry of the surrounding ligands. Such an effect however would only be expected in the case where electrons are localised at the ions and not for metallic materials such as $SrFeO_3$.

Vracar *et al.* [60] studied oxidised $SrTi_{1-x}Fe_xO_3$ powder samples with $0.003 < x < 0.5$ and found that the peak due to the O-stretching vibration increased in intensity up to $x = 0.03$ but at higher x the peak intensity decreased. Calculations by Evarestov *et al.* [100] on $SrTi_{1-x}Fe_xO_3$ suggest that $x \approx 0.03$ represents a border between a low Fe dopant concentration where additional electron density was localised at the Fe ions and a high dopant concentration where electronic bands begin to form leading to electronic conductivity. The disappearance of the peak assigned to O-stretching at higher Fe content is therefore consistent with a decreasing Jahn-Teller effect due to the delocalisation of the e_g electron.

In the current study the O-stretching vibration is observed up to much higher Fe contents. This could be a result of the preparation method, reports of thin film preparation of $SrTiO_3$ have reported differences in properties compared to the bulk which have been attributed either to stress due to lattice mismatch with the substrate or the introduction of oxygen vacancies [136]. However an alternative origin for the peak would be a more considerable distortion to the lattice caused by the ordering of either cations or oxygen vacancies which causes variation in the M-O bond lengths and disrupts the symmetry of the MO_6 octahedra, in the same way as was observed for $SrFeO_{3-y}$.

It should also be noted however that the entire spectrum including peaks due to the substrate decreased in intensity with increasing Fe content and so this effect could simply be explained by differences in the material's absorption of the laser radiation. The observation of distinct peaks in the spectrum of SFO in **Figure 4-26** in the absence of any substrate peaks however does speak against this argument.

Figure 4-29 shows how the position of the Raman line assigned to the O-stretching vibration changes across the compositional range. The clearest trend is a shift to lower wavenumber with increasing Fe content consistent with observations based on the spectra shown in **Figure 4-27**.

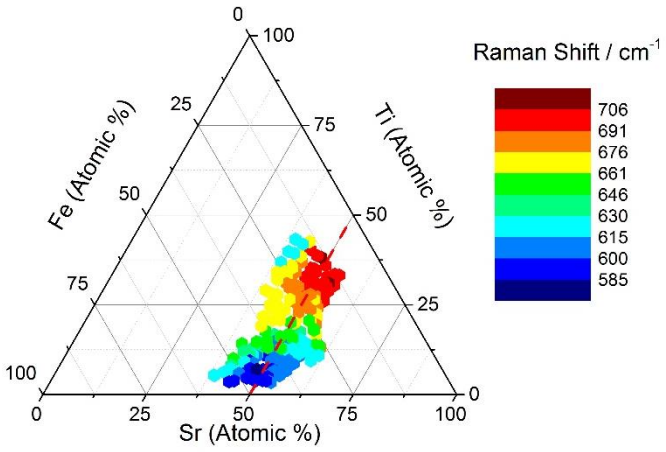

Figure 4-29: Ternary diagram with colour map showing the variation in the shift of the Raman line assigned to the O-stretching vibration with Fe content, x, across the STFO thin films deposited by PVD under atomic oxygen at 650 °C. The clearest trend is a shift to lower wavenumber with increasing Fe content.

Figure 4-30 shows how the position of the Raman line assigned to an O-stretching vibration changes with increasing Fe content, x. Both the sample deposited with tie-line compositions and the Sr-graduated sample show a shift to lower wavenumber with increasing Fe content however whist the data from the Sr-graduated sample shows a relatively smooth decrease, the data from the tie-line sample shows a constant wavenumber for the Raman line for x < 0.5 and a sharp decrease thereafter.

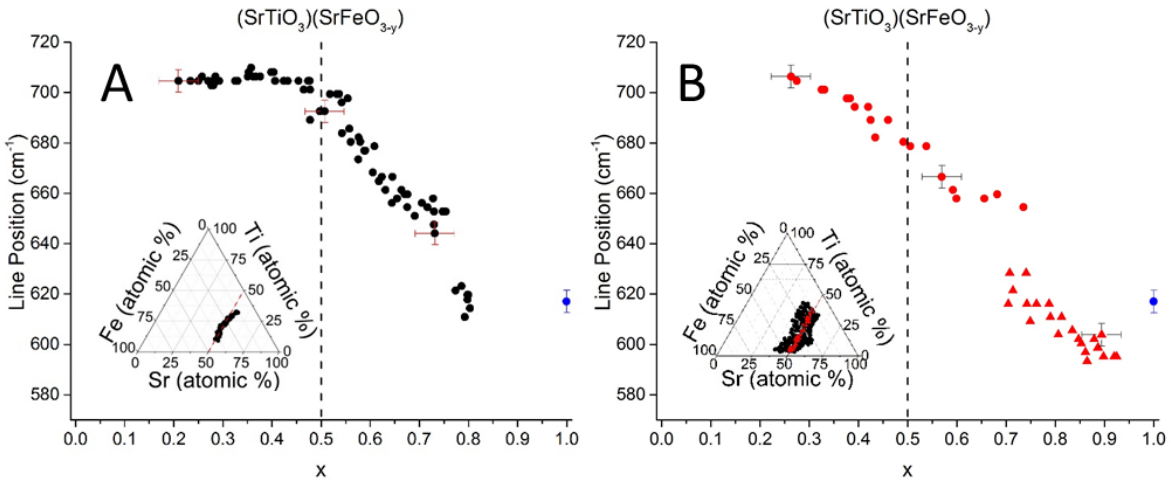

Figure 4-30: Plot to show variation in the position of the Raman line assigned to the O stretching vibration with Fe content, x, for compositions along the $SrTi_{1-x}Fe_xO_3$ tie-line. Data shown is from (A) tieline sample with Sr = 50 ± 5 at.% and (B) two Sr graduated samples with Sr (shown by black dots and triangles, also shown is data from the uniform SFO film (shown by blue dot).

This sharp change in behaviour seen for the tie-line sample could be evidence of a change in the crystal structure for this sample which is supported by the sharp colour change observed by visual inspection of this film in **Section 4.2.1**. By contrast no such sharp colour change was seen for the film deposited over a larger Sr range around the tie-line Sr = 50 ±2 at.%, compositions and so the absence of a sharp transition in the Raman data for this sample is consistent with the visual observation.

The significance of the x=0.5 composition here and in the visual inspection of the films could be evidence of a cation-ordered structure, $(SrTiO_3)_1(SrFeO_{3-y})_n$, where x = 0.5 would represent the double perovskite structure with n = 1 which has alternating planes of $SrTiO_3$ and $SrFeO_{3-y}$.

4.2.3.3 Effect of Preparation Conditions

It may be expected that the introduction of Fe^{3+} ions and oxygen vacancies would lead to a lowering of the symmetry of the cubic perovskite and the observation of Raman lines. However, a study comparing the Raman spectra of fully reduced $SrTi_{1-x}Fe_xO_{3-x/2}$ and fully oxidised $SrTi_{1-x}Fe_xO_3$ powder samples ($x < 0.5$), prepared by solid state techniques, found only broad features for the fully reduced material where pronounced peaks had been observed for the fully oxidised material [60]. Several researchers have concluded that a pronounced peak around 690 cm^{-1} at lower Fe contents of $x < 0.5$ is indicative of the presence of Fe^{4+} [60, 108]. The intensity of this peak in the Raman spectra of the films deposited under molecular oxygen will therefore give an indication of the level of Fe^{4+} and therefore the level of oxidation of the film.

Figure 4-31 shows a comparison of Raman spectra obtained for a point of composition $x = 0.5$ on the thin films deposited by PVD at 650 °C under an oxygen plasma beam, under O_2 and for the O_2 deposited film following post-deposition annealing for 6 hours under O_2 in a tube furnace. The films prepared in molecular oxygen were half as thick as those prepared using the plasma source as shorter deposition times were used. The peaks due to the SiN substrate are therefore more prominent and less intense peaks due to the film are expected.

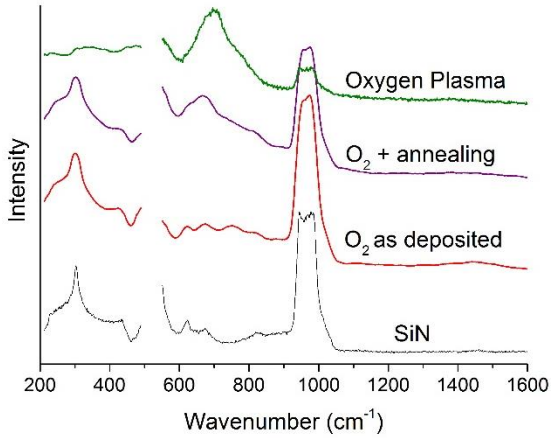

Figure 4-31: Raman spectra for $SrTi_{1-x}Fe_xO_{3-y}$ thin films deposited by PVD at 650 °C using an oxygen plasma source (green), using molecular oxygen (red). Data is also shown for the film deposited under molecular oxygen following a post-deposition anneal of 6 h in a tube furnace under O_2 (purple). The Raman spectrum of the SiN substrate is shown for comparison as Raman lines from the substrate are visible in the spectra from the thin film samples. Spectra have been corrected for varying thickness in the film.

The film deposited in molecular oxygen showed few features prior to annealing although a weak peak at 750 cm^{-1} was noted which is also present in the spectra of the film deposited using the plasma source as a shoulder to the main peak. It is not clear whether the weak peak at 670 cm^{-1} is due to the SiN substrate or the film. These low intensity features would be consistent with a film containing high proportions of Fe^{3+} and oxygen vacancies. Following annealing a peak at 690 cm^{-1} appears in the spectrum, presumably due to an increase in oxidation of the film and the increased presence of Fe^{4+}. Unexpectedly the peak is very low in intensity for compositions lower than x = 0.5 where the peak was observed with highest intensity for the films deposited under the plasma source. The shift in the position of this line with Fe content is much less pronounced however as shown in **Figure 4-32**.

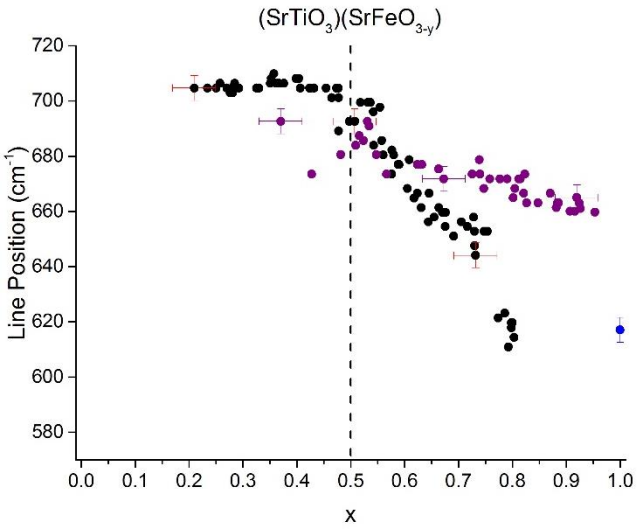

Figure 4-32: Plot to show variation in the position of the Raman line assigned to the O stretching vibration in STFO with Fe content, x, for $SrTi_{1-x}Fe_xO_{3-y}$ films deposited by PVD at 650 °C under an oxygen plasma (points shown by black dots and triangles) and under O_2 following 6 hours of post-deposition annealing in a tube furnace under O_2 (shown by purple dots). Also shown is the position of the Raman line obtain from the spectrum of a uniform film of $SrFeO_{3-y}$ deposited by PVD at 650°C under an oxygen plasma.

4.3 Conclusions

A visual inspection of the films showed a distinct colour change with increasing Fe content which is consistent with the decreased band-gap and increased metallic behaviour noted in previous studies [65]. Particularly interesting however was that the colour change took the form of a sharp transition at x = 0.5 from a light coloured film consistent with the colour of the uniform STO film to a dark metallic film consistent with the uniform SFO film. A more graduated colour change would be expected and this was considered as an indication that there was a significant change in the electronic structure around the x = 0.5 composition. This is somewhat consistent with the conductivity measurements of the films, discussed in **Section 3.2.4**, which appeared to show a significant increase in conductivity at x = 0.45.

X-ray diffraction measurements confirmed a cubic perovskite structure for the thin films of composition $SrTi_{1-x}Fe_xO_{3-y}$ prepared by PVD at 650 °C using an oxygen plasma source for all values of x. Lattice constant refinements confirmed a linear decrease in the lattice constant of the perovskite cell with increasing Fe content from 0.392 ± 0.001 nm for $SrTiO_3$ to 0.386 ± 0.001 nm for $SrFeO_3$. This is in accordance with Vergard's law for metallic alloys and provides evidence that the film is homogeneous and formed from crystallites which contain both Fe and Ti cations. The perovskite structure was found to be robust to changes in the Sr content from $Sr_{0.7}(Ti, Fe)O_{3-y}$ up to $Sr_{1.4}(Ti, Fe)O_{3-y}$. A distinct crystal structure was however observed for more Sr rich compositions for the thin films prepared using the oxygen plasma which was assigned to a Ruddlesen-Popper phase of composition $Sr_4Fe_3O_7$.

Direct evidence of a distortion from the cubic perovskite structure with increasing Fe content was evident in the data from Raman measurement of the samples. No lines were observed in the Raman spectrum of STO in accordance with symmetry rules for a cubic structure. SFO however showed lines which correlated with previous studies on a tetragonally distorted SFO perovskite material. In the case of the compositionally graduated STFO films, an O-stretching vibrational mode was identified which had previously been observed in the literature and assigned to a Jahn-Teller distortion which breaks the symmetry of the BO_6 octahedral by asymmetric relaxation of the B-O bonds [60]. In this case however the Raman line was assigned to a distortion arising from cation ordering in the lattice as discussed in **Section 4.1.3.1**, which leads to differing B-O bond lengths and a break in the symmetry of the BO_6 octahedra.

The adoption of a cation-ordered superstructure of the form $(SrTiO_3)_1(SrFeO_{3-y})_n$ would explain the significance of the x = 0.5 composition since this composition represents a key boundary where the structure moves from alternating planes of $SrTiO_3$ and $SrFeO_{3-y}$ to a structure where Fe ions must be present in adjacent planes which would be expected to cause a significant increase in the mobility of electrons. This is clearly consistent with the increase in conductivity close to this point and also explains the observed colour change. A shift in the Raman line assigned to the O-stretching vibration was also observed to occur sharply at x = 0.5 for the sample deposited at compositions close to the $SrTi_{1-x}Fe_xO_{3-y}$ tieline.

Attempts to prepare the films using molecular oxygen resulted in films with low crystallinity which could not be indexed to the perovskite crystal structure. Subsequent annealing of the films at 650 °C under a flow of oxygen improved the crystallinity of the films but the diffraction data did not show the expected changes with increasing Fe content and it is proposed that these films contain separate domains of $SrTiO_3$ and $SrFeO_3$ crystallites. As such the molecular oxygen method is not recommended as a HT-PVD synthesis route for the preparation of a high-quality homogeneous film.

There was no evidence in the Raman spectra to suggest the presence of carbonates in either the films prepared using the oxygen plasma or the molecular oxygen prepared films. Since the Raman technique is sensitive to detection of (CO_3^{2-}) species this confirms that the carbonates identified in the XPS studies are confined to a thin surface layer and are not a major component of the films.

Chapter 5: Redox electrochemistry

5.1 Introduction

5.1.1 Redox electrochemistry of perovskites

The redox energy of the B-site cation in a perovskite is influenced by the A-O bonding by the inductive effect [140]. The A-site cation, in this case Sr, polarises electrons in the O 2p orbital, drawing electron density away from the B-site cation. Since the valence d-electrons on the B cation form anti-bonding interactions with the O 2p levels this effect results in a stronger B-O bond and consequentially decreases the energy of the redox couple by stabilising the higher oxidation state.

The strength of the inductive effect of the A-site cation depends on the crystal structure and co-ordination of the metal cations and so changes in the potential of the redox couple may provide an indication of changes in the structure of the crystal lattice. This effect has been demonstrated for $Li_x[Mn_2]O_4$ which has the spinel structure. The co-ordination of the Li cation changes from tetrahedral to octahedral as x is increased above 1 and it was found that this resulted in a 1 eV increase in the potential of the Mn^{3+}/Mn^{4+} redox couple.

In the case of STFO, the Pourbaix diagram for $SrTiO_3$ has been calculated by density functional theory and predicts no redox chemistry at pH 13 between -1.5 V, where Ti^{4+} is reduced to Ti^{2+} and 1.5 V where the oxidation of Sr^{2+} to Sr^{4+} is expected [141]. Any redox chemistry observed in this region is likely therefore to be due to the presence of the Fe dopant. Studies on Fe_2O_3 report the Fe^{2+}/Fe^{3+} redox and $Fe^{2+}/Fe(0)$ redox at potentials of approximately 0 V_{RHE} and -0.2 V_{RHE} respectively. Since the Fe^{4+} oxidation state is not common amongst Fe oxides, few examples of this redox couple exist in the literature, however the Fe^{3+}/Fe^{4+} redox has been reported for mixed $Fe(OH)_2$ and $Ni/Fe(OH)_2$ films [142, 143], typically centred around 1.35 V_{RHE}.

Interesting redox chemistry would be predicted for the Fe ions in STFO on the basis that Fe can exist in either the Fe^{4+} or Fe^{3+} oxidation state within the lattice. The redox energy for the interconversion between the Fe^{4+} and Fe^{3+} states should be lowered by the inductive effect of Sr. Additionally since the Fe^{3+} oxidation state can be charge compensated by the formation of oxygen vacancies this presents the possibility of electrochemical oxygen intercalation/de-intercalation accompanying the redox reaction.

5.1.2 Electrochemical oxygen intercalation in perovskites

The reversible electrochemical intercalation and removal of oxygen from the perovskite lattice was first put forward by Kudo *et al.* [144] who proposed the overall reaction shown in **Equation** 5-1, where O_O^x is a neutral lattice oxygen site and $V_{\ddot{O}}$ represents an oxygen vacancy in Kröger-Vink notation [145].

$$V_{\ddot{O}} + 2\,OH^- \rightleftharpoons\ O_O^x + H_2O + 2e^-$$

Equation 5-1

Since then the reversible intercalation of oxygen into the perovskite lattice by electrochemical means has become a well-established concept for perovskites which are able to support oxygen vacancies such as $SrMO_{3-y}$, where M = Fe [95, 96, 146], Co [147-149] or Mn [150]. The complete oxidation/reduction of these materials is given by **Equation** 5-2.

$$SrMO_{2.5} + 0.5\,OH^- \rightleftharpoons SrMO_3 + H_2O + 2e^-$$

Equation 5-2

The electrochemical oxygen intercalation process was first proven for the $SrFeO_{3-y}$ perovskite by Wattiaux *et al.* [96] who were able to prepare cubic $SrFeO_3$ from an oxygen deficient brownmillerite structured $SrFeO_{2.5}$ starting material. The oxygen content of the starting material and products were verified by iodometric titration as well as Mossbauer spectroscopy. The most compelling results however were found in the XRD which showed the conversion of the material from the brownmillerite structure to the cubic perovskite structure.

Nemudry *et al.* [95] repeated this experiment with the use of an in-situ XRD technique and not only confirmed the results obtained by Wattiaux *et al.* but also observed intermediate phases with compositions $SrFeO_{2.75}$ and $SrFeO_{2.87}$ which ex-situ electron diffraction measurements confirmed were consistent with the tetragonal and orthorhombic phases of the material.

Since the large size of the O^{2-} ion would be expected to make the insertion into the lattice difficult it has been proposed that a peroxide-like species is formed from the adsorbed hydroxide ion at the surface according to Equation 5-3 [150].

$$Fe^{3+} - OH^{-} + OH^{-} \rightleftharpoons Fe^{3+} - O^{-} + H_2O + e^{-}$$

Equation 5-3

This species is then able to diffuse through the lattice to oxygen vacancy sites. The formation of the peroxide-like species and their diffusion through the lattice is made possible by the charge transfer reaction shown in **Equation** 5-4. This explains why the observation of oxygen intercalation has generally been limited to perovskites of the type $SrMO_{3-y}$ where M = Fe or Co since these oxides have a high degree of covalency in M-O bonding leading to a small energy barrier for the charge transfer reaction [98].

$$Fe^{3+} + O^{-} \rightleftharpoons Fe^{4+} + O^{2-}$$

Equation 5-4

5.2 Results

5.2.1 $SrTi_{0.5}Fe_{0.5}O_{3-y}$

Cyclic voltammetry obtained at different scan rates for an array electrode of composition $SrTi_{0.5}Fe_{0.5}O_{3-y}$ deposited by PVD under atomic oxygen at 650 °C is presented in Figure **5-1A**. Two redox couples, R1 and R2, were identified, the oxidation and reduction peaks are labelled as A1/C1 and A2/C2. The peak current density of the peaks was proportional to the sweep rate, as shown by Figure **5-1B** which is indicative of the redox process of a surface bound species rather than a species in solution. The oxidation peak, A2, and reduction peak, C2 of the lower potential redox couple, R2, were broad, separated in potential and their positions were dependent on the sweep rate, v, suggesting slow electron transfer kinetics. The oxidation peak A1 was obscured by the onset of the OER and as such the properties of this peak and those of the redox couple R1 are not as apparent.

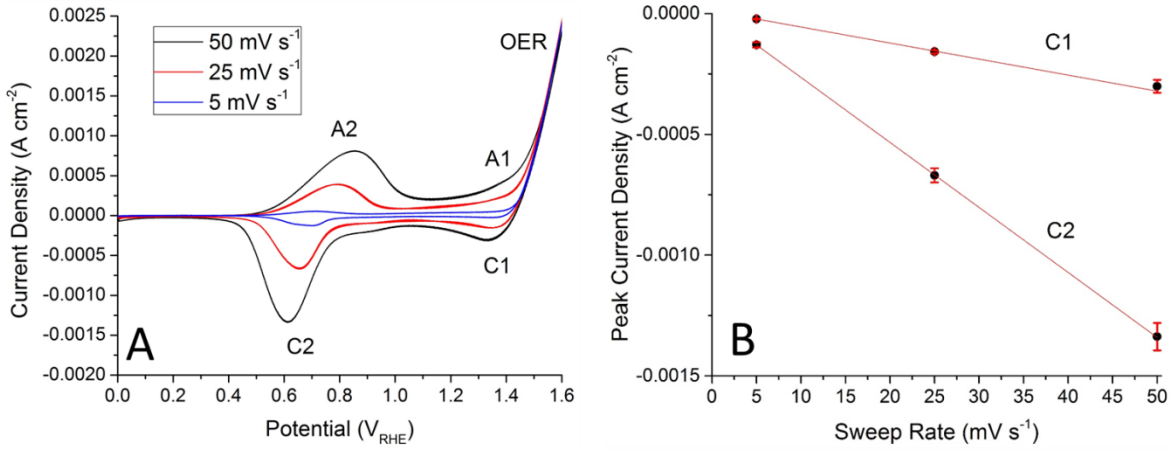

Figure 5-1: (A) Cyclic voltammetry recorded in deoxygenated 0.1 M KOH at sweep rates of 50, 25 and 5 mV s^{-1} on a thin film array electrode with composition $SrTi_{0.5}Fe_{0.5}O_{3-y}$ deposited by PVD at 650 °C under atomic oxygen. Data shown is second cycle. Error bars correspond to data taken from 3 cycles. The voltammetry is dominated by a redox couple for which the potential and peak current of the peaks vary with sweep rate. (B) Plot to show the linear variation in the current density of the reduction peaks with sweep rate, the linear relationship between sweep rate and peak current density suggests that the redox couple arises from a surface bound species.

Both redox reactions are assumed to arise due to the oxidation/reduction of surface Fe ions according to Equation 5-5. In alkaline solution the oxidised surface is highly deprotonated and the reduction of the Fe^{4+} cations by electrons from the external circuit is charge compensated by protonation of the oxygen ligand. The appearance of two distinct sets of redox peaks is rationalised by the presence of Fe ions in distinct chemical environments.

$$Fe^{3+} - OH^- + OH^- \rightleftharpoons Fe^{4+} - O^{2-} + H_2O + e^-$$

Equation 5-5

As discussed above in **Section 5.1.2** the oxide ions formed in this reaction can be intercalated into vacancy sites in the perovskite lattice by diffusion of O^- which forms readily by charge transfer as shown in Equation 5-6.

$$Fe^{4+} + O^{2-} \rightleftharpoons Fe^{3+} + O^-$$

Equation 5-6

The overall equation for the intercalation of oxygen into a vacancy site is given by Equation 5-7. This reaction is accompanied by an increase in the formal oxidation state of the Fe ions from Fe^{3+} to Fe^{4+}.

$$Fe^{3+} - V_{\ddot{O}} - Fe^{3+} + 2OH^- \rightleftharpoons Fe^{4+} - O - Fe^{4+} + H_2O + 4e^-$$

Equation 5-7

Since the redox reaction is not limited to the surface Fe sites and involves bulk Fe the charge associated with this redox is expected to exceed that which would be expected for surface Fe and all of the bulk Fe sites could be involved in the redox reactions. Limitations on the involvement of Fe sites are likely to arise from the stability of oxygen vacancies and the ability of the film to conduct both electrons and oxide ions. This will be discussed further in **Section 5.2.2.1**.

The R1 redox couple has an equilibrium potential close to the reported 1.35 V_{RHE} for the Fe^{3+}/Fe^{4+} redox on mixed $Fe(OH)_2$ and $Ni/Fe(OH)_2$ films [142, 143] whilst the R2 reaction occurs at a lower potential. It seems possible therefore that the R1 redox could arise from the reaction of lower co-ordinated Fe ions in which the Fe^{4+} oxidation state is less well stabilised by the perovskite lattice.

5.2.2 Trends in redox electrochemistry with composition

The trends in the redox electrochemistry of the STFO electrocatalysts will be discussed firstly by consideration of the trends in the charge and potential of the two redox reactions, R1 and R2, with pseudo-ternary composition. The data will be presented in a similar way as in Chapters 3 and 4 with colour-maps to show the variation in a data set over points in the pseudo-ternary diagram shown in **Figure 5-2**.

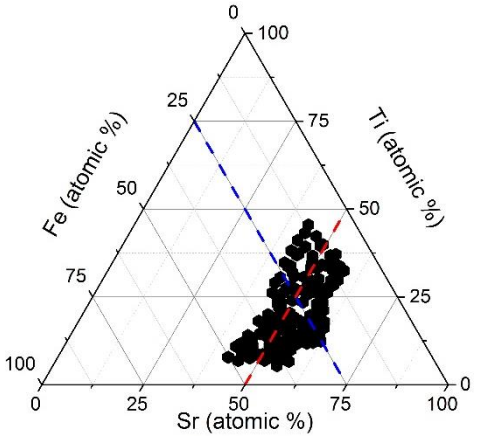

Figure 5-2: Ternary plot showing compositions obtained from SEM-EDX on a $SrTi_{1-x}Fe_xO_{3-y}$ film deposited on ITO at 650 °C under atomic oxygen. Red dashed line indicates position of $SrTi_{1-x}Fe_xO_{3-y}$ tie-line. Blue dashed line indicates position of the $Sr_nTi_{0.75-n}Fe_{0.25}O_{3-y}$ tie-line.

In **Sections 5.2.3** and **5.2.4** two pseudo-binary compositional tie-lines are considered. Firstly, the effect of changing the Ti/Fe ratio at the B-site will be investigated by consideration of data along the $SrTi_{1-x}Fe_xO_{3-y}$ tie-line, shown by the red dashed line in Figure **5-2**, which extends from $SrTiO_3$ with increasing Fe content to $SrFeO_{3-y}$ whilst maintaining a constant Sr content of 50 at.%. Secondly, the $Sr_nTi_{0.75-n}Fe_{0.25}O_{3-y}$ tie-line shown by the blue dashed line in **Figure 5-2**, which consists of compositions with Fe content of 25% will be considered in **Section 5.2.4** to investigate the effect of changing the Sr content as well as altering the ratio of A-site cations and B-site cations from the stoichiometric ABO_3.

5.2.2.1 Peak Charge

The total charge passed, Q, obtained by integrating the current, I, with respect to time, t, is related to the number of moles of reactant consumed according to Equation 5-8 where n is the number of electrons required for the redox reaction and F is the Faraday constant.

$$Q = \int Idt = mnF$$

Equation 5-8

The charge associated with the R1 and R2 redox peaks should provide an indicator as to whether the reactions correspond to a simple redox of surface Fe ions or whether there is oxygen intercalation into the bulk lattice. In the case of the simple surface oxidation with no oxygen intercalation the charge under the redox peak will be limited by the number of moles of Fe at the surface. In the case where oxygen intercalation can occur the charge under the peak will instead be related to the number of sites at which oxygen vacancies can form and would therefore be expected to be much higher.

The ternary diagrams in **Figure 5-3** show how the charge associated with the A2/C2 redox peaks, assigned to a Fe^{3+}/Fe^{4+} redox reaction, changes with the composition of the STFO films. It is apparent that the highest charge is identified at high Fe contents at compositions lying close to the $SrTi_{1-x}Fe_xO_{3-y}$ tie-line shown by the dashed red line. This prominence of the peak at high Fe content and close to the perovskite compositional tie-line lends support to the assignment of these peaks to a Fe^{3+}/Fe^{4+} redox couple in which the Fe^{4+} oxidation state is stabilised.

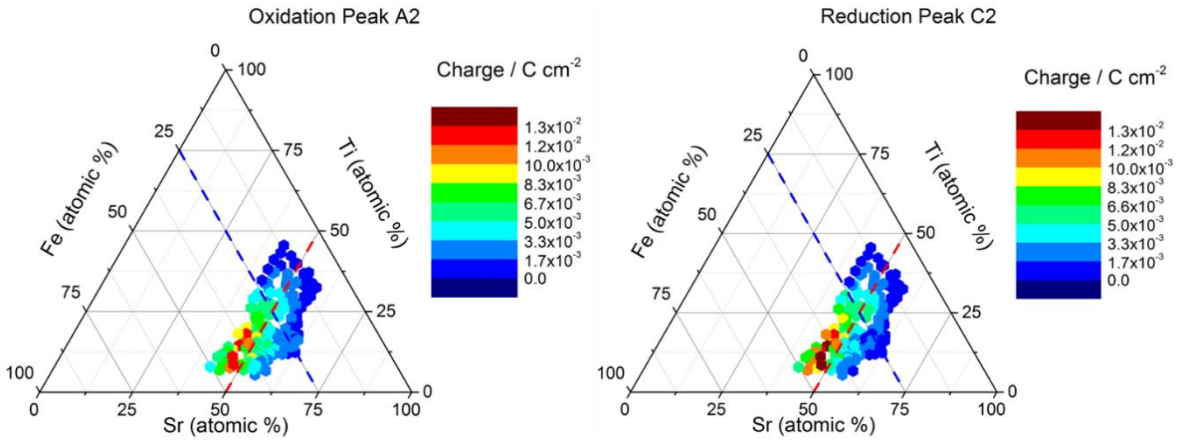

Figure 5-3: Ternary plot with colour map showing the variation in charge under the oxidation peak (A2) and reduction peak (C2). Data obtained from cyclic voltammetry, recorded in deoxygenated 0.1 M KOH, on $SrTi_{1-x}Fe_xO_{3-y}$ model electrocatalysts in the form of thin films deposited by PVD at 650 °C under atomic oxygen. The $SrTi_{1-x}Fe_xO_{3-y}$ and $Sr_nTi_{0.75-n}Fe_{0.25}O_{3-y}$ tie-lines are shown by the red and blue dashed lines, respectively.

The increase in the charge under the A2/C2 redox peaks with increasing proportion of Fe in the film would be consistent with either a simple surface Fe redox or the subsequent intercalation of oxygen into lattice since the formation of oxygen vacancies requires the charge compensating reduction of Fe^{4+} ions to Fe^{3+}. In order to confirm the intercalation of oxygen into the lattice the number of moles of Fe involved in the redox reaction was compared to an estimate of the number of moles of Fe in the surface obtained as described below.

The number of moles of Fe involved in the R2 redox was calculated from the charge under the reduction peak, R2, according to Faraday's Law, shown above in **Equation** 5-8.

The number of moles of Fe in the surface was calculated by first estimating the mass of the surface layer according to **Equation** 5-9, assuming a layer thickness of 0.144 nm equivalent to the radius of the largest ion, O^{2-}. The density was estimated as 5.11 g cm^{-3} which is the literature value for STO since the density of the film is not known. The mass of the surface layer was combined with the wt.% of Fe in the film as obtained from EDX data to give the mass of Fe present in the surface as shown in **Equation** 5-10. The number of moles of Fe in the surface could then be determined using **Equation** 5-11.

$$Mass\ of\ surface\ layer = layer\ thickness \times Electrode\ area \times Density$$

Equation 5-9

$$Mass\ of\ Fe = Mass\ of\ surface\ layer \times Fe\ wt.\%$$

Equation 5-10

$$Moles\ of\ Fe = \frac{Mass\ of\ Fe}{Molecular\ mass\ of\ Fe}$$

Equation 5-11

When the number of moles of Fe involved in the C2 redox process is compared to the number of moles of Fe in the surface, as shown in **Figure 5-4**, it becomes clear the reaction cannot arise solely from Fe ions in the surface without the intercalation of oxygen into the bulk which frees up the surface Fe for further reaction. This analysis does not take into account the surface roughness of the film. If a surface roughness factor of 10 was applied, which is very high, there would still be up to 4 times the expected number of surface moles of Fe involved in the redox.

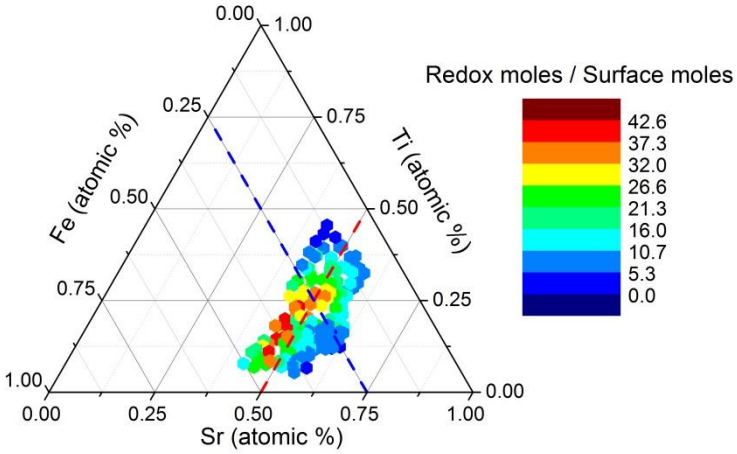

Figure 5-4: Ternary diagram showing the proportion of the Fe surface moles involved in the R2 redox reaction. The number of moles of Fe involved in redox was calculated from the charge under the reduction peak C2 in cyclic voltammetry in 0.1 M KOH at a sweep rate of 50 mVs^{-1}. The number of moles of Fe in the surface was estimated using wt.% Fe obtained by EDX.

The number of moles of Fe involved in the R2 redox was compared to the total number of bulk moles of Fe expected in the film by replacing the layer thickness term in **Equation** 5-9 with the film thickness determined by profilometry measurements which were presented in Chapter 3. The results of this analysis are shown as a colour map on the ternary diagram in **Figure 5-5**. The highest participation of Fe ions in the redox reaction was found for compositions with Fe > 25 at.% and Sr < 50 at.% i.e. to the left of the blue and red dashed lines on the ternary diagram, respectively. In this region up to a third of the Fe ions are active in the R2 redox reaction.

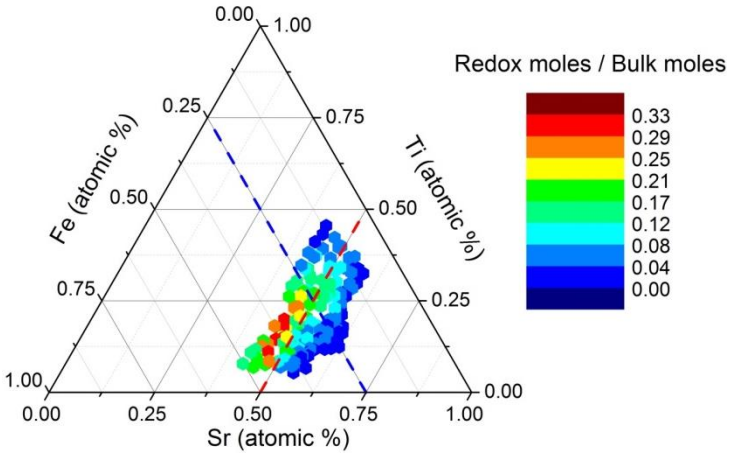

Figure 5-5: Ternary diagram showing the proportion of total Fe bulk moles involved in the R2 redox reaction. The number of moles of Fe involved in redox was calculated from the charge under the reduction peak C2 in cyclic voltammetry in 0.1 M KOH at a sweep rate of 50 mVs^{-1}. The number of moles of Fe in the surface was estimated using wt.% Fe obtained by EDX and profilometry measurements of film thickness.

Since not all Fe ions participate in the R2 redox the reaction must be restricted in some way. Firstly, it seems likely that the reaction will be limited to certain sites since the formation of an oxygen vacancy requires the reduction of two metal ions as shown in **Equation** 5-7. This would be much more likely to occur at Fe-O-Fe sites, where vacancies have been found to be most stable [131] than at Fe-O-Ti sites where the reduction of Ti^{4+} to Ti^{3+} would not be favoured.

Secondly, the oxidation and reduction of bulk metal ions and the corresponding insertion and removal of oxygen ions from the perovskite lattice is assumed to require electronic and oxide ion conductivity respectively. The depth to which Fe ions can participate in the R2 redox reaction may therefore be limited by these factors. The electronic conductivity of the films was discussed in Chapter 3 and confirmed the highest conductivity for high Fe and low Sr compositions which is consistent with the observation of the highest number of ions active in the R2 redox in this region.

Finally in the electrochemical synthesis of stoichiometric cubic $SrFeO_3$ from oxygen deficient brownmillerite structured $SrFeO_{2.5}$ by Wattiaux *et al.* the material was oxidised at a potential of 1.3 V for 3 hours to achieve incorporation of oxygen into the vacancy sites. Whilst a shorter timescale may be expected for a thin film material it seems reasonable to assume that the cycling conducted in this study is unlikely to result in the complete oxidation or reduction of STFO.

Figure 5-6 shows how the charge under the reduction peak C1, provisionally assigned to surface Fe^{4+} reduction, varies with composition. The charge under the oxidation peak A1 has not been investigated as the peak in most cases converges with the onset of the OER. This redox couple was only observed where Sr was present in stoichiometric or above stoichiometric quantities i.e. Sr ≥ 50 at.%.

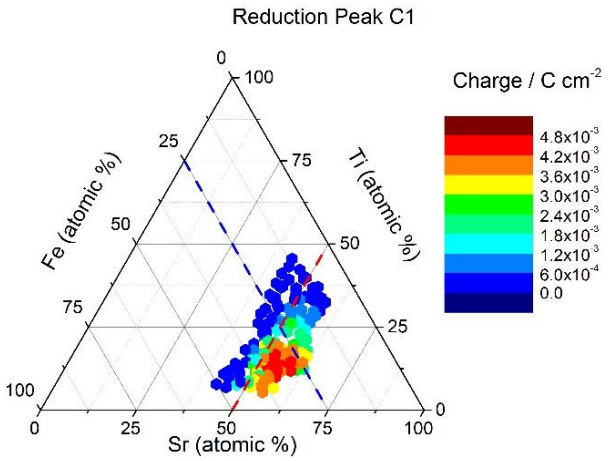

Figure 5-6: Ternary plot with colour map showing the variation in charge under the reduction peak C1 observed for the $SrTi_{1-x}Fe_xO_{3-y}$ film, deposited by PVD at 650 °C under atomic oxygen with composition. The plot shows that this peak is most prominent at high Fe, high Sr contents and indicates a change in the structure of the oxide which destabilises the Fe^{4+} oxidised state.

Several explanations are possible for the increased charge of this redox couple at high Sr contents, firstly, it could arise from a Sr^{2+}/Sr^{4+} redox process which results in the dissolution of Sr. The potential of the observed redox couple is close to the equilibrium potential of this redox which is 1.5 V, however, if this were the case a decrease in the charge under the peak would be expected with repeated cycling and this was not observed. Also there appears to be no explanation why this would not occur for high Sr content films with lower Fe content.

Since the R2 redox reaction was less prominent in this region, as shown in **Figure 5-3**, it seems more likely that the R1 redox process also arises from the Fe^{3+}/Fe^{4+} redox but that the redox couple is increased in energy due to changes in the chemical environment of Fe which relate to the above stoichiometric amount of Sr in the perovskite lattice.

Evidence from XRD measurements presented in **Section 4.2.2** suggested formation of a Ruddlesen-Popper type phase at high Sr contents, > 58 at.%, in which excess Sr formed rock-salt structured SrO intergrowth layers in the perovskite structure. Although such a structure was not confirmed for lower Sr contents this does not rule out the presence of a minor phase. The presence of excess Sr in any form however could explain a disruption in the perovskite lattice leading to lower co-ordination of the Fe ions and a redox potential which is in agreement with those of simple Fe hydroxides [142, 143].

The moles of Fe involved in the R1 redox were calculated from the charge under the C1 reduction peak and compared to the number of moles of Fe in the surface estimated using **Equation** 5-9, **Equation** 5-10 and **Equation** 5-11. The results of this analysis are shown in the ternary diagram in **Figure 5-7**.

Although the participation of Fe sites in the R1 redox is lower than for the R2 redox, at very Sr-rich compositions the number of moles of Fe involved in the redox reaction does start to exceed what could be expected for the Fe surface ions, reaching more than 25 times the estimate for the number of Fe surface ions which is too significant to be accounted for by surface roughness. Oxygen intercalation into the lattice is one possible cause although additional charge from the Sr^{2+}/Sr^{4+} redox is another possibility which would provide an explanation for the "hot-spot" in charge under the peak at high Sr compositions.

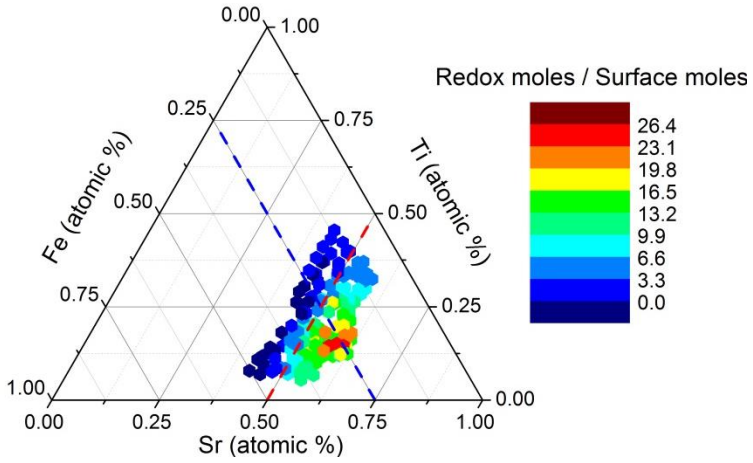

Figure 5-7: Ternary diagram showing the proportion of the Fe surface moles involved in the R1 redox reaction. The number of moles of Fe involved in redox was calculated from the charge under the reduction peak C1 in cyclic voltammetry in 0.1 M KOH at a sweep rate of 50 mVs^{-1}. The number of moles of Fe in the surface was estimated using wt.% Fe obtained by EDX.

The proportion of the total bulk moles of Fe involved in the R1 redox was also calculated in the same way as for the R2 redox above and the results are shown as a colour map on the ternary diagram in **Figure 5-8**.

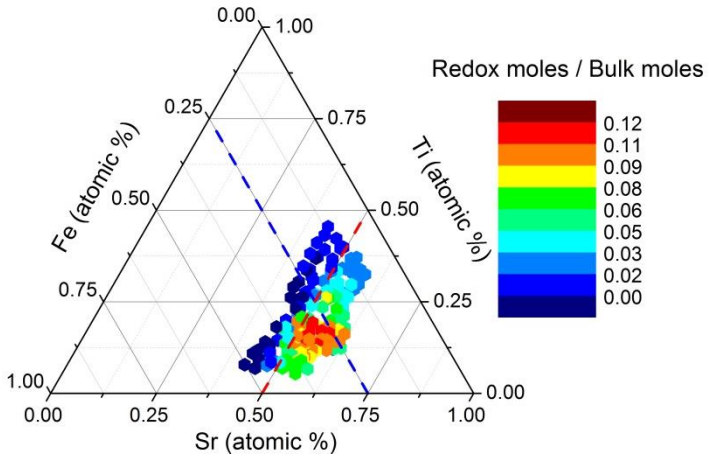

Figure 5-8: Ternary diagram showing the proportion of total Fe bulk moles involved in the R1 redox reaction. The number of moles of Fe involved in redox was calculated from the charge under the reduction peak C1 in cyclic voltammetry in 0.1 M KOH at a sweep rate of 50 mVs^{-1}. The number of moles of Fe in the surface was estimated using wt.% Fe obtained by EDX and profilometry measurements of film thickness.

The lower participation of bulk Fe sites in this redox compared to the R2 redox seems likely to be related to the disruption in the ability of the material to intercalate oxygen. A possible cause for this would be that the lower co-ordinated Fe sites are not able to form the peroxide-like species which are assumed to be necessary to allow diffusion of the oxygen through the lattice. In this case the large O^{2-} ions formed in the surface oxidation would experience a much greater resistance to diffusion through the lattice.

5.2.2.2 Equilibrium Potential

The equilibrium potential of a redox reaction relates to the ease of addition of an electron to the oxidised species or conversely the removal of an electron from the reduced species. A negative shift in the potential of the redox process corresponds to a stabilisation of the oxidised state whilst a positive shift represents stabilisation of the reduced state. The equilibrium potential of the redox couple R2, assigned to the Fe^{3+}/Fe^{4+} redox in the bulk perovskite lattice, varied across the STFO compositional range as shown in **Figure 5-9**.

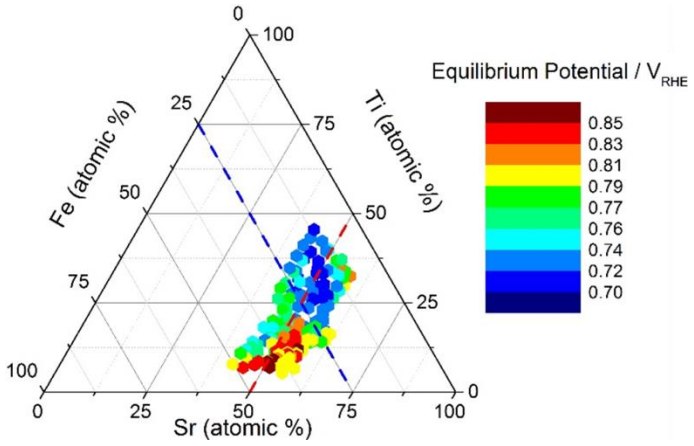

Figure 5-9: Ternary plot with colour map showing the variation in the equilibrium potential of the R2 redox, calculated from $E_{C2} + ((E_{A2}-E_{C2})/2)$. Data obtained from cyclic voltammetry, recorded in deoxygenated 0.1 M KOH, on $SrTi_{1-x}Fe_xO_{3-y}$ model electrocatalysts in the form of thin films deposited by PVD at 650 °C under atomic oxygen.

The major trend was an increase in the equilibrium potential at higher Fe content. This would be consistent with an increase in the electron density in the metal 3d states with increasing Fe/Ti ratio. The metal 3d states form anti-bonding interactions with the O 2p orbitals and so an increase in electron density would be expected to weaken the M-O bonding and stabilise the reduced state. This will be discussed further in **Section 5.2.3** where data along the $SrTi_{1-x}Fe_xO_{3-y}$ tieline will be considered in detail.

Analogous data for the equilibrium potential of the R1 redox is presented in **Figure 5-10**. The data shown in grey represents the compositions where no R1 redox peaks were observed in the voltammetry. Over the remainder of the film the potential of the redox couple appears to depend mainly on the Fe/Ti ratio. However unlike the R2 redox the equilibrium potential decreases with increasing proportion of Fe.

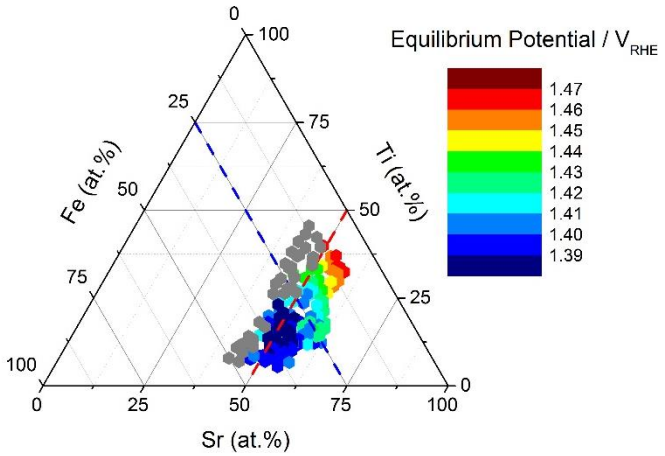

Figure 5-10: Ternary plot with colour map showing the variation in the equilibrium potential of the R1 redox, calculated from $E_{C1} + ((E_{A1}-E_{C2})/2)$. Data obtained from cyclic voltammetry, recorded in deoxygenated 0.1 M KOH, on $SrTi_{1-x}Fe_xO_{3-y}$ model electrocatalysts in the form of thin films deposited by PVD at 650 °C under atomic oxygen. Point shown in grey represent compositions where no R1 redox peaks were observed.

5.2.2.3 Peak Separation

The peak shape of the A2 and C2 redox peaks was shown in cyclic voltammetry of the electrode of composition $SrTi_{0.5}Fe_{0.5}O_{3-y}$ in Figure **5-1A** and which will be presented for other compositions of varying Fe and Sr content in **Sections 5.2.3** and **5.2.4** respectively. The peaks are broad and separated in potential indicating that an over-potential is required to drive the kinetics of the oxidation and reduction reactions.

In the first instance it could be assumed that the poor reaction kinetics arise from poor electron transport and therefore relate to the electronic conductivity of the films. In terms of the trends in the peak separation across the STFO compositions it would, in this case, be expected that the fastest reaction kinetics and therefore the lowest redox peak separation would occur for the most conductive materials. Four point probe measurements identified the high Fe, low Sr compositions to be the most conductive with a decrease in conductivity seen as Fe content decreased and as Sr content increased.

The trend identified from the cyclic voltammetry was however quite different. The separation between the redox peaks appears to be mainly dependent on the Sr content but actually decreases with increasing Sr at.% as shown in **Figure 5-11**. This is indicative of faster reaction kinetics at high Sr contents, the opposite of the trend based purely on the predictions of the conductivity measurements.

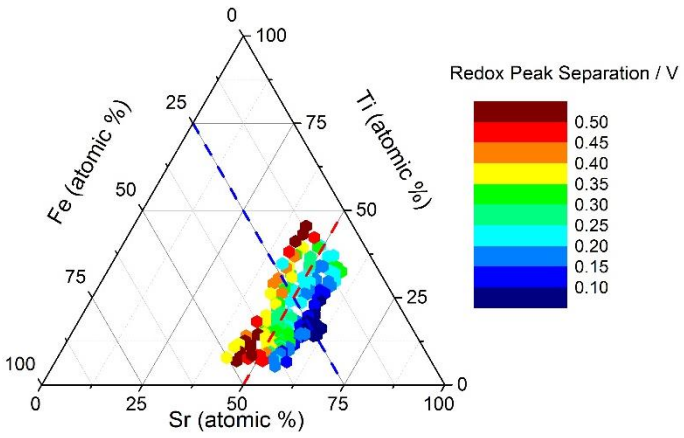

Figure 5-11: Ternary plot with colour map showing the variation in the redox peak separation for the R2 redox reaction calculated from E_{A2}-E_{C2}. Data obtained from cyclic voltammetry, recorded in deoxygenated 0.1 M KOH, on $SrTi_{1-x}Fe_xO_{3-y}$ model electrocatalysts in the form of thin films deposited by PVD at 650 °C under atomic oxygen.

An alternative cause for the slow kinetics is proposed based on the necessity for the oxide ions to move through the lattice to the solution during reduction and back into the lattice from the solution during oxidation. In this case the kinetics could relate to oxide ion conductivity. The observed trend would be consistent with an improvement in oxide ion conductivity with increasing Sr content.

This seems contrary to expectations since the O^- ions require a conduction path though the perovskite lattice which would initially be assumed to consist of the hopping of oxide ions between Fe-O-Fe sites. The presence of additional Sr which could form rock-salt structure SrO would be assumed to disrupt this conduction path. However a study of $SrTiO_3$ and Fe-doped $SrTiO_3$ single crystals after PVD deposition of thin layers of alkaline earth metal oxides including SrO_x reported an improvement in the surface oxygen exchange kinetics [151]. This is assumed to be related to the ability of the rock-salt structure of SrO to accept interstitial oxygen ions [129] which results in quite high oxide ion conductivity for Ruddlesden-Popper structured materials. Surface Sr-enrichment was observed for all compositions in the XPS measurements, which were discussed in **Section 3.2.5**, which is consistent with this proposal.

However in the case where the kinetics of the reaction were limited by oxide ion conductivity the reaction would be limited by the diffusion of oxide ions and the peak current density would be expected to vary linearly with $v^{1/2}$ [15]. On the basis of the linear relationship between the peak current density and v seen in **Figure 5-1** it must therefore be concluded that the slow kinetics of the reactions do arise from slow electron transfer. Since the variation across the film is not consistent with the variation in electronic conductivity it is assumed that the slow electron transfer of the redox process arises from a change in the symmetry of the Fe ions. This is consistent with the intercalation of oxygen which will change the co-ordination number of the Fe ions.

The variation in the redox peak separation across the film seen in **Figure 5-11** is therefore assumed to be due to structural changes in the material with composition discussed in detail in Chapter 4. The co-ordination of the Fe ions will clearly be dependent on the structure adopted and different structures are favoured at different compositions. For example several different ordered oxygen vacancy structures were discussed in **Section 4.1.3.2** in which Fe^{3+} ions adopt tetrahedral or octahedral symmetries and Fe^{4+} ions adopt pentahedral or octahedral symmetries. The more significant the change in symmetry required for the Fe^{3+}/Fe^{4+} redox process the less kinetically favoured such a process will be and a larger separation of the redox peaks will be expected. Since the stability and adoption of these structures is dependent on composition, the variation in the kinetics of the redox process would be an expected result.

Data for the redox peak separation of the R1 redox reaction shows a different trend in which the peak separation increases at higher Fe content. This is considered consistent with the assumption that the slow electron transfer is due to changes in the symmetry of the Fe ions during the redox process since this reaction is assigned to lower co-ordinated Fe ions which experience a different symmetry change than their more fully co-ordinated counterparts.

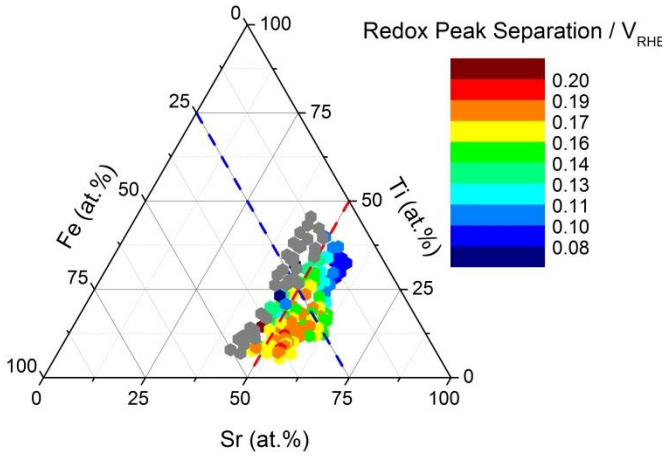

Figure 5-12: Ternary plot with colour map showing the variation in the redox peak separation for the R1 redox reaction calculated from E_{A1}-E_{C1}. Data obtained from cyclic voltammetry, recorded in deoxygenated 0.1 M KOH, on $SrTi_{1-x}Fe_xO_{3-y}$ model electrocatalysts in the form of thin films deposited by PVD at 650 °C under atomic oxygen.

5.2.3 Effect of B-site variation on redox electrochemistry

In order to gain further understanding of the trends in the electrochemistry along the $SrTi_{1-x}Fe_xO_{3-y}$ tie-line additional samples were deposited with compositions close to this tie-line as shown in **Figure 5-15** to provide repeat measurements over this area of interest. Data along this tie line will be plotted in terms of the ratio of Fe to Ti as represented by x in the subsequent analysis.

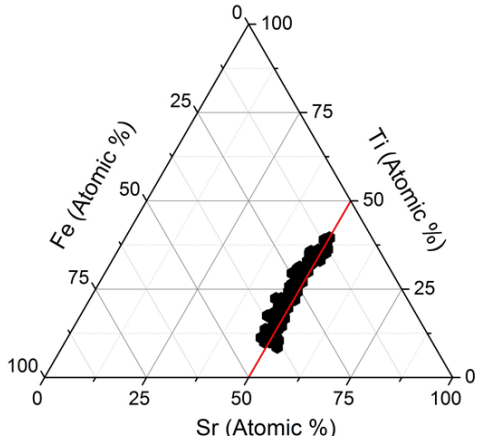

Figure 5-13: Ternary plot showing compositions obtained from SEM-EDX on a $SrTi_{1-x}Fe_xO_{3-y}$ film deposited on ITO at 650 °C under atomic oxygen. Red line indicates position of the $SrTi_{1-x}Fe_xO_{3-y}$ tie-line.

5.2.3.1 Peak Shape

Figure 5-14A shows how the shape of the A2/C2 redox peaks changes as the ratio of Fe to Ti, as denoted by x, increases along the $SrTi_{1-x}Fe_xO_{3-y}$ tie-line. The oxidation peaks are in general broader reaching a lower maximum current than the reduction peaks. At larger values of x the oxidation peak is broader still and shifts to higher potential indicating that the oxidation of Fe^{3+} to Fe^{4+} is more difficult. This could be related to a change in the chemical environment at the Fe sites or a structural change which increases the energy barrier for oxygen intercalation. Moreover it may be that the broad peaks are made up of several overlapping peaks corresponding to different sites with different energy barriers to oxygen intercalation. This may also provide an explanation for the additional reduction peak at 0.9 V.

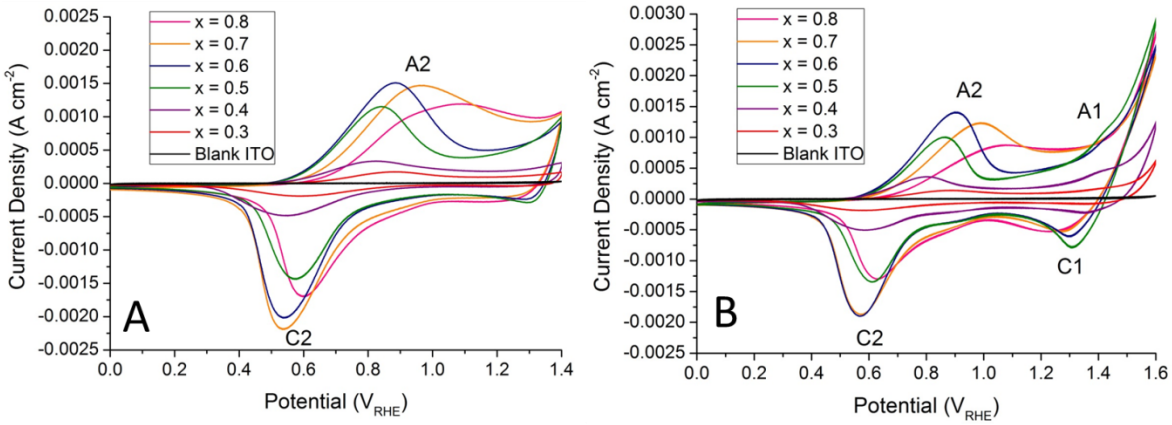

Figure 5-14: Cyclic voltammetry recorded in deoxygenated 0.1 M KOH at a sweep rate of 50 mV s-1 for compositions across a $SrTi_{1-x}Fe_xO_{3-y}$ film deposited under an oxygen plasma, all compositions have Sr content of 50 ± 2 at. %. Cyclic voltammetry for the blank ITO chip under the same conditions is shown by the black line. (A) Shows data with potential limits 0 V < V_{RHE} < 1.4 V whilst B shows data to a higher potential 0 V < V_{RHE} < 1.6 V. Two Fe^{3+}/Fe^{4} redox couples are observed, the redox couple centred at 0.7 V was assigned to Fe ions in the bulk perovskite lattice whilst the redox couple at 1.4 V is thought to arise from Fe ions in a lower co-ordination lattice site.

An alternative cause for the broadening of the oxidation peak would be the presence of more than one type of reduced Fe^{3+} site which may have different symmetries and as such different oxidation potentials. This could be consistent with oxygen-vacancy ordered structures for the reduced materials. The oxidised state by contrast would be expected to contain only octahedral Fe^{4+} which may explain why the reduction peak is sharper.

Figure 5-14B shows how the shape of the cyclic voltammetry changes as the ratio of Fe to Ti, as denoted by x, increases along the $SrTi_{1-x}Fe_xO_{3-y}$ tie-line when the potential window is opened to include the higher redox couple A1/C1 and the onset of the OER. The oxidation peak, A1, is noted to occur immediately prior to the OER suggesting that there could be a relationship between this peak and the OER activity, this will be investigated in the next chapter.

5.2.3.2 Peak Charge

Figure 5-15 shows the peak current density and the charge under the R2 redox peaks for compositions along the $SrTi_{1-x}Fe_xO_{3-y}$ tie-line. At values of $x < 0.66$, the increasing charge under the oxidation and reduction peaks show a clear correlation with increasing Fe content as would be expected for a Fe^{3+}/Fe^{4+} redox process. At values of $x > 0.66$ however there is a slight decrease in the charge under both peaks. This may be related to a decrease in stability of the $SrTi_{1-x}Fe_xO_{3-y}$ films as they approach the $SrFeO_{3-y}$ end composition which is known to be susceptible to anodic dissolution in alkaline electrolyte [152]. The stability of the films is discussed in **Section 5.2.7**.

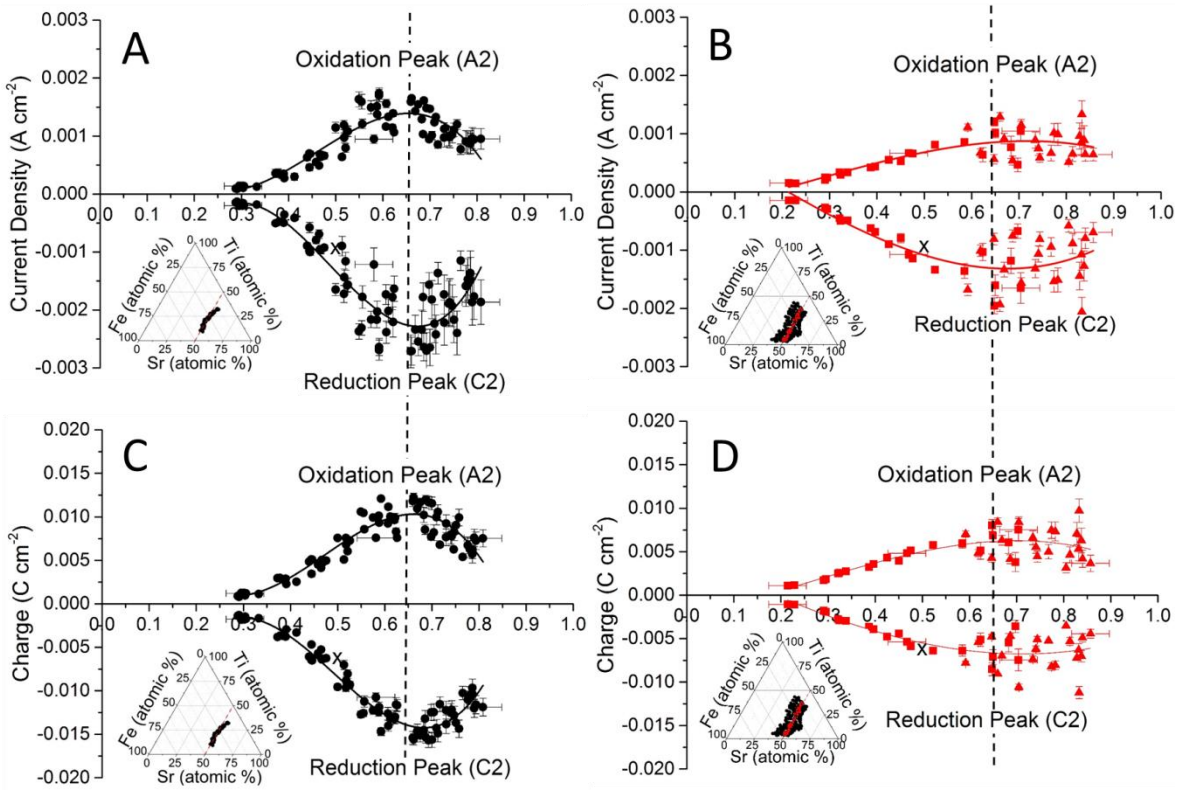

Figure 5-15: Variation of the peak current density (A and B) and charge (C and D) under the oxidation peak A2 and reduction peak C2 with Fe/Ti ratio, x. Data obtained from cyclic voltammetry, recorded in deoxygenated 0.1 M KOH, on $SrTi_{1-x}Fe_xO_{3-y}$ model electrocatalysts in the form of thin films deposited by PVD at 650 °C under atomic oxygen. Plots A and C show data from a sample deposited over small Sr range 45 at.% < Sr < 55 at.%. Plots B and D show data from the tie-line (Sr = 50 ± 2 at.%) of two samples deposited over a larger Sr range 38 at.% < Sr < 62 at.% where square markers indicate data from a sample with compositions $0.2 < x < 0.7$ whilst triangles show data from a sample with compositions $x > 0.6$. Ternary diagrams show sample compositions. The peak current density and charge for both sets of samples increased with increasing x up to a maximum at $x = 0.66$ before decreasing, dotted line at $x = 0.66$ to guide the eye.

Whilst the trend in current density and charge was the same for both samples, the absolute values were much lower for the sample deposited over the larger range of Sr compositions. This was initially assumed to be due to changes in the sample thickness but will be investigated further when the proportion of bulk moles of Fe involved in the redox process is calculated and discussed for each sample.

Figure 5-16 shows the peak current density and the charge under the C1 reduction peak for compositions along the $SrTi_{1-x}Fe_xO_{3-y}$ tie-line. The A1 oxidation peak cannot be considered in this way due to the overlap with the onset of the OER. For the sample deposited over a larger Sr range, shown in B and D, the trend is quite similar to the C2 reduction peak in that there is an increase in the current density and charge with increasing Fe content up to the x = 0.66 composition at which point there is a slight decrease. The increasing scatter in the data supports the theory that the decrease arises due to dissolution of the film.

The sample deposited close to the tie line for which current density and charge data is shown in A and C shows quite a distinct trend however reaching a maximum at x = 0.5 before decreasing quite significantly to x = 0.66 and increasing again. The significance of the x = 0.5 and x = 0.66 compositions was discussed in the previous chapter in relation to possible cation and vacancy ordered structures and this could be further evidence to support the presence of such a structure in this film.

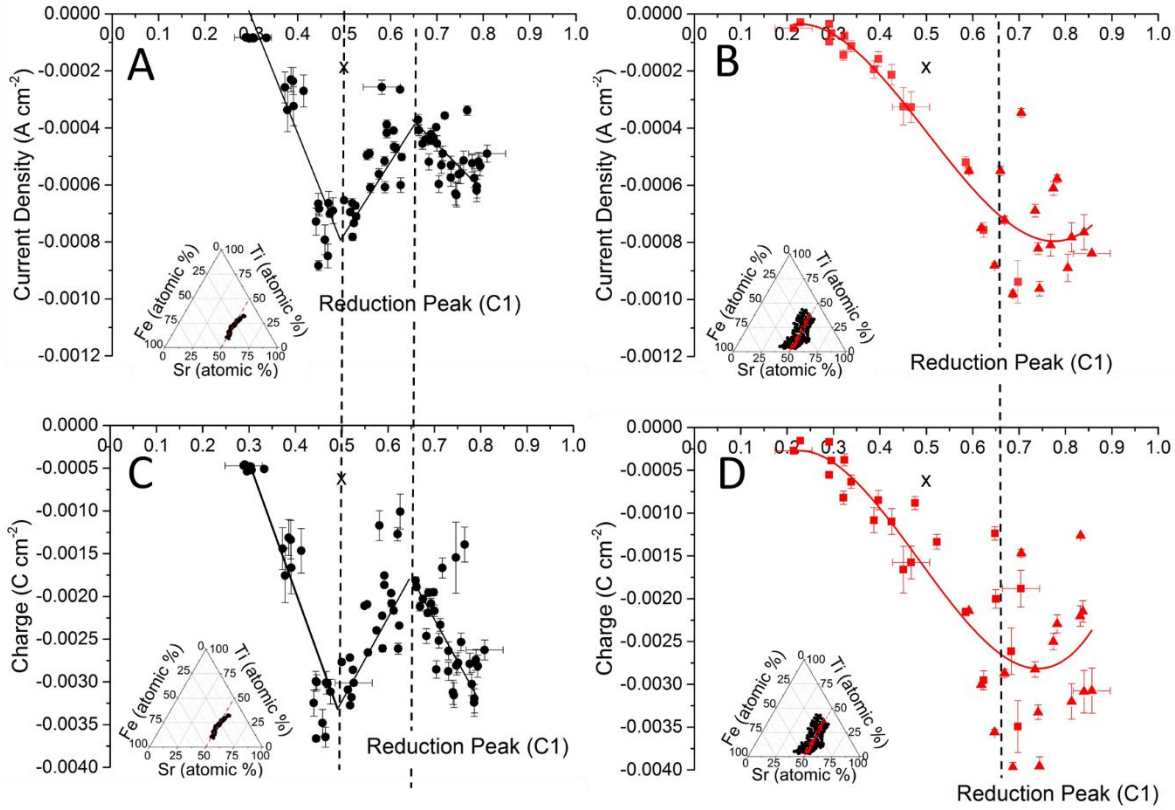

Figure 5-16: Variation of the peak current density (A and B) and charge (C and D) under the reduction peak C1 with Fe/Ti ratio, x. Data obtained from cyclic voltammetry, recorded in deoxygenated 0.1 M KOH, on $SrTi_{1-x}Fe_xO_{3-y}$ model electrocatalysts in the form of thin films deposited by PVD at 650 °C under atomic oxygen. Plots A and C show data from a sample deposited over small Sr range 45 at.% < Sr < 55 at.%. Plots B and D show data from the tie-line (Sr = 50 ± 2 at.%) of two samples deposited over a larger Sr range 38 at.% < Sr < 62 at.% where square markers indicate data from a sample with compositions 0.2 < x < 0.7 whilst triangles show data from a sample with compositions x > 0.6. Ternary diagrams show sample compositions. The peak current density and charge for both sets of samples increased with increasing x up to a maximum at x = 0.66 before decreasing, dotted line at x = 0.66 to guide the eye.

In order to account for changes in the thickness of the film the proportion of bulk moles of Fe involved in each of the R1 and R2 redox reactions was calculated for both electrode arrays according to the method described in **Section 5.2.2.1**. The data is plotted in **Figure 5-17** and confirms a lower participation of Fe ions in the R2 redox process for the sample deposited over the larger Sr range compared to the tie-line sample.

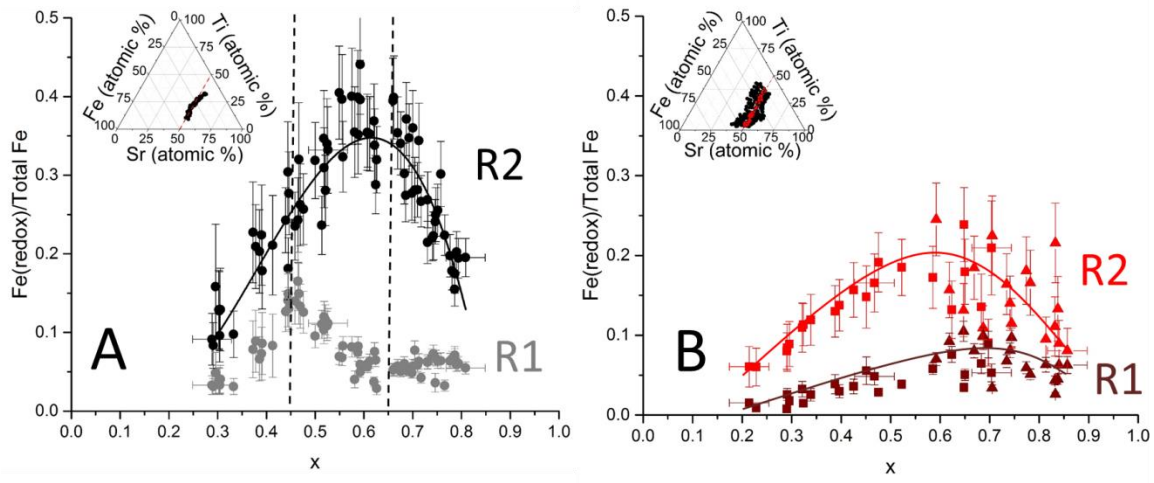

Figure 5-17: Variation of the proportion of total moles of Fe which are involved in the redox reactions, R1 and R2, with x along the $SrTi_{1-x}Fe_xO_{3-y}$ tie-line. Data obtained from cyclic voltammetry, recorded in deoxygenated 0.1 M KOH, on STFO thin film electrode arrays deposited by PVD at 650 °C under atomic oxygen. Plot A shows data from a sample deposited over small Sr range 45 at.% < Sr < 55 at.%. Plot B shows data from the tie-line (Sr = 50 ± 2 at.%) of two samples deposited over a larger Sr range 38 at.% < Sr < 62 at.% where square markers indicate data from a sample with compositions 0.2 < x < 0.7 whilst triangles show data from a sample with compositions x > 0.6. Ternary diagrams show sample compositions.

The difference in the participation of Fe ions in the R2 redox process is assumed to be due either to slight differences in the crystal structure of the STFO material in the two films or a difference in oxygen content. EDX measurements discussed in Chapter 3 identified a slightly lower oxygen content for the Sr graduated sample than for the tie-line sample. Where large numbers of oxygen vacancies exist there is an increased chance that the oxygen vacancies will associate and form an ordered structure. As discussed in Chapter 4 the formation of an oxygen vacancy ordered structure creates inequivalent Fe sites and decreases the ability of oxide ions and electrons to move through the structure which could explain the lower participation in the redox reaction for the more oxygen deficient sample. It should be noted however that no significant difference in the electronic conductivity was observed to support this theory.

The overall trend in the data for the R2 is however the same for both samples and a clear maximum in the proportion of bulk moles of Fe participating in the redox reaction is reached at around x = 0.6. This is close to the composition of x = 0.66 which was highlighted as key in the discussion of the structure of the STFO materials since if cation-ordering occurs in the structure this composition represents the point in which two adjacent layers of $SrFeO_{3-y}$ would be present leading to a greater number of possible oxygen vacancy-ordered structures. The presence of adjacent $SrFeO_3$ layers also introduces new axial Fe-O-Fe oxygen sites which have been found to be the most stable sites for the formation of oxygen vacancies. The downturn in the participation of Fe ions in the R2 redox process above x = 0.6 could therefore be due to the presence of stabilised Fe^{3+} - [V] – Fe^{3+} for which oxidation is not favourable under these conditions.

In terms of the R1 redox process a clear maximum in the participation of the Fe ions in the redox process is reached at a composition of x = 0.45 on the tie-line sample whilst the data from the sample deposited over a larger Sr range shows a very different trend, reaching a maximum at around x = 0.7. This could be related to differing trends identified for the two samples in **Chapter 4** which were assigned to possible differences in the crystal structure or oxygen content. In particular a colour change was observed on the tie-line sample at a composition close to x = 0.5 alongside sharp changes in the position of the Raman mode assigned to the O-stretching vibration. No colour change was observed on the sample deposited over a larger Sr range and the position of the Raman mode decreased gradually with increasing x rather than showing a sharp transition.

5.2.3.3 Equilibrium Potential

Figure 5-18 shows how the equilibrium potential of the R2 redox reaction varies with x along the $SrTi_{1-x}Fe_xO_{3-y}$ tie-line. The data confirms an overall increase in the Fe^{3+}/Fe^{4+} redox potential with increasing x consistent with an increase in electron density in the metal 3d states which form anti-bonding interactions with the O 2p ligands and so destabilise the oxidised Fe^{4+} state and raise the redox energy. The trend in the data shows a decrease in the equilibrium potential of the peak up to x = 0.33 followed by a slight increase to x = 0.66 and finally a larger increase above x = 0.66. These would represent key compositions for a cation ordered structure $(SrTiO_3)_1(SrFeO_3)_n$ with n = 0.5, 1 and 2. The large increase in equilibrium potential at compositions with x > 0.66 could be evidence to support a vacancy ordered state in which the reduced Fe^{3+} ions are stable and oxidation to Fe^{4+} is less favoured.

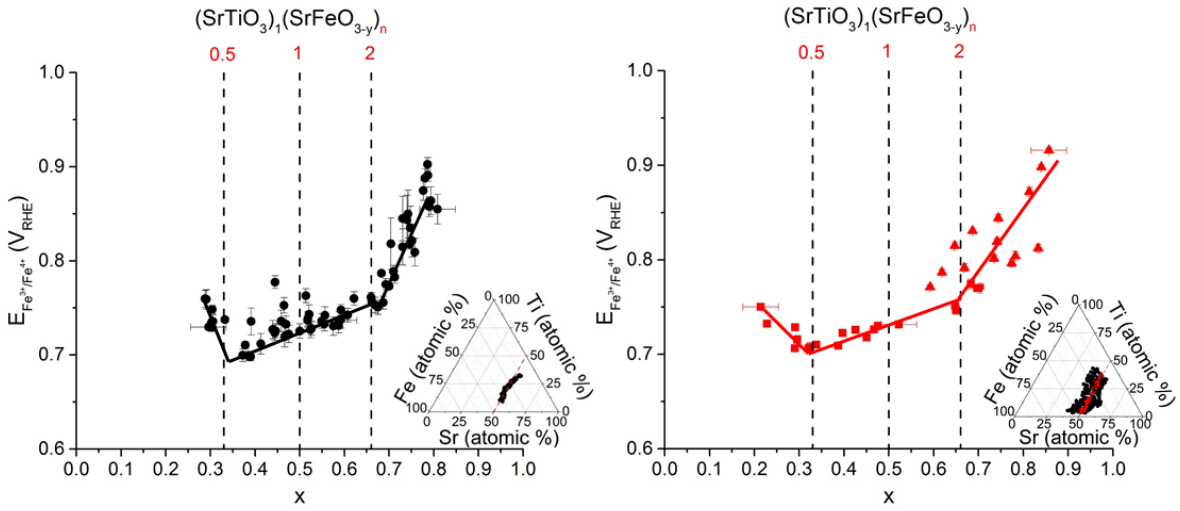

Figure 5-18: Variation of the potential of the equilibrium redox potential of the R2 redox reaction, calculated from $E_{C2} + ((E_{A2}-E_{C2})/2)$, with Fe/Ti ratio, x. Data obtained from cyclic voltammetry, recorded in deoxygenated 0.1 M KOH, on $SrTi_{1-x}Fe_xO_{3-y}$ model electrocatalysts in the form of thin films deposited by PVD at 650 °C under atomic oxygen.

Analogous data for the R1 redox process is shown in **Figure 5-19**, the two samples again show different trends following similar patterns as were observed for the current density and charge under the C1 reduction peak. The equilibrium potential for this redox reaction decreases with increasing Fe content.

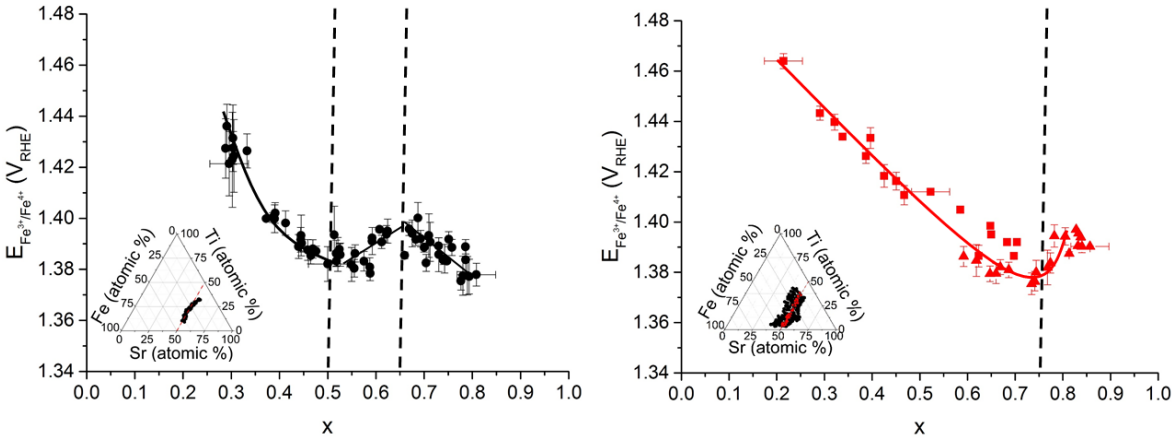

Figure 5-19: Variation of the potential of the equilibrium redox potential of the R1 redox reaction, calculated from $E_{C1} + ((E_{A1}-E_{C1})/2)$, with Fe/Ti ratio, x. Data obtained from cyclic voltammetry, recorded in deoxygenated 0.1 M KOH, on $SrTi_{1-x}Fe_xO_{3-y}$ model electrocatalysts in the form of thin films deposited by PVD at 650 °C under atomic oxygen.

5.2.3.4 Peak Separation

Figure 5-20 shows the separation between the oxidation and reduction peaks of the R2 redox process for compositions on the $SrTi_{1-x}Fe_xO_{3-y}$ tie-line. Both samples show an increase in the redox peak separation above x = 0.5 which suggests slower reaction kinetics.

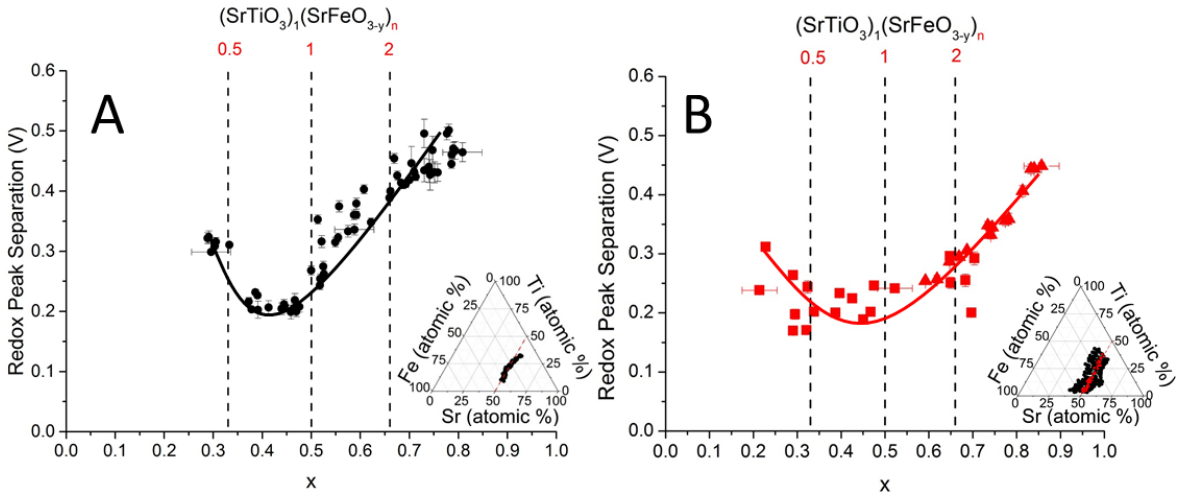

Figure 5-20: Variation in the separation between the oxidation peak A2 and reduction peak C2, calculated from $(E_{A2}-E_{C2})/2$, with Fe/Ti ratio, x. Data obtained from cyclic voltammetry, recorded in deoxygenated 0.1 M KOH, on $SrTi_{1-x}Fe_xO_{3-y}$ model electrocatalysts in the form of thin films deposited by PVD at 650 °C under atomic oxygen. Data shows an increase in redox peak separation with increasing x for x > 0.5.

A similar trend is noted in the peak separation of the R1 redox peaks for the tie-line sample whilst the trend for the Sr graduated sample is unclear as shown in **Figure 5-21**.

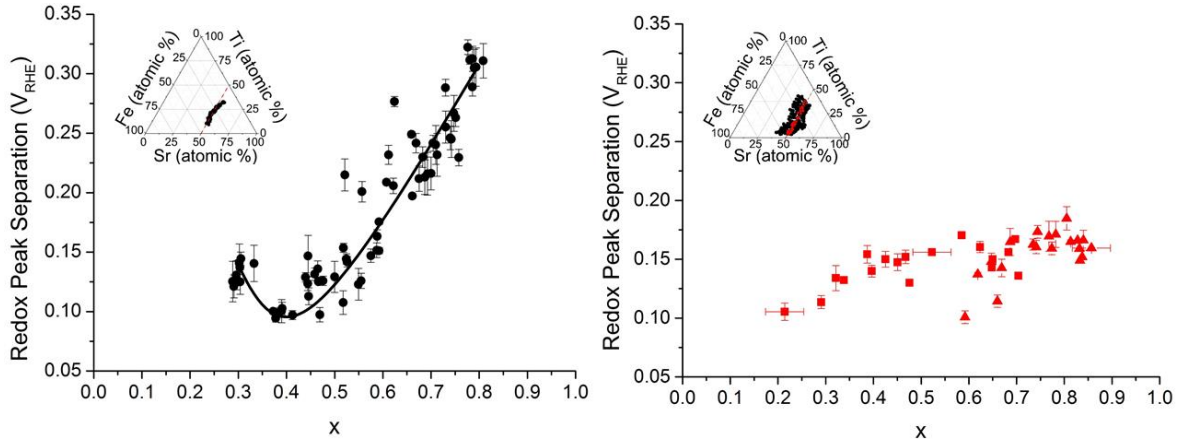

Figure 5-21: Variation in the separation between the oxidation peak A1 and reduction peak C1, calculated from $(E_{A1}-E_{C1})/2$, with Fe/Ti ratio, x. Data obtained from cyclic voltammetry, recorded in deoxygenated 0.1 M KOH, on $SrTi_{1-x}Fe_xO_{3-y}$ model electrocatalysts in the form of thin films deposited by PVD at 650 °C under atomic oxygen. Data shows an increase in redox peak separation with increasing x for x > 0.5.

5.2.4 Effect of A-site variation on redox electrochemistry

No additional samples were deposited to investigate the effect of the Sr content on the electrochemistry of the $SrTi_{1-x}Fe_xO_{3-y}$ model electrocatalysts and data in this section was taken purely from the $Sr_nTi_{0.75-n}Fe_{0.25}O_{3-y}$ tie-line from the Sr graduated samples which is shown by the blue dashed line in **Figure 5-22.**

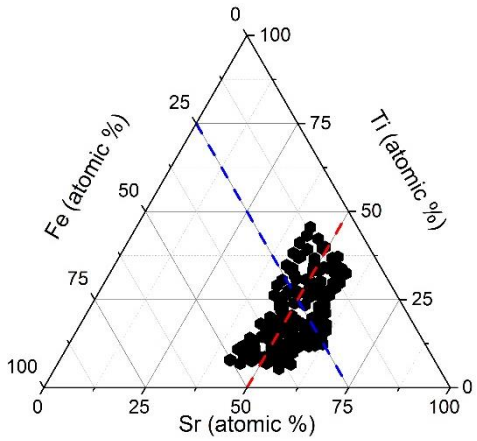

Figure 5-22: Ternary plot showing compositions obtained from SEM-EDX on a $SrTi_{1-x}Fe_xO_{3-y}$ film deposited on ITO at 650 °C under atomic oxygen. Red dashed line indicates position of $SrTi_{1-x}Fe_xO_{3-y}$ tie-line. Blue dashed line indicates position of the $Sr_nTi_{0.75-n}Fe_{0.25}O_{3-y}$ tie-line.

It is expected that away from the $SrTi_{1-x}Fe_xO_{3-y}$ tie line other metal oxide phases will be formed which may affect the electrochemistry and electrocatalytic activity of the $SrTi_{1-x}Fe_xO_{3-y}$ model electrocatalysts. At compositions where Sr is present in excess, i.e. where Sr > (Ti+Fe), the formation of insulating SrO_x phases may also inhibit electrocatalytic activity. Indeed it has been suggested that even at the tie-line compositions, where Sr = (Ti+Fe), Sr may segregate to the surface and that the resulting insulating layer decreases activity for the ORR [110]. The preparation of slightly Sr-deficient films, i.e. where Sr < (Ti+Fe), has been found to decrease the level of Sr segregation and improve electrocatalytic activity for the ORR [111].

5.2.4.1 Peak Shape

Figure 5-23 shows how the shape of the redox peaks changes as the Sr content increases along the $Sr_nTi_{0.5}Fe_{0.5}O_{3-y}$ tie-line. Where Sr is present in stoichiometric amounts at Sr = 50% or is slightly sub-stoichiometric at Sr = 45% the A2/C2 redox couple assigned to Fe in the perovskite lattice is prominent. As Sr content increases above stoichiometry however this peak decreases in intensity and the high potential redox couple A1/C1 becomes more dominant. This could be an indication that at higher Sr contents, above 50 at.%, Fe ions are present in a different chemical environment, possibly due to changes in the crystal structure of the material. This could arise from distortion of the perovskite lattice or the presence of an entirely different crystalline or amorphous phase. One possibility is a Ruddlesden-Popper phase in which the perovskite layers are interspersed with layers of the A-site cation in a rock-salt crystal structure. These phases form when the A-site cation is present in excess and have the composition $A_{n+1}B_nO_{3n+1}$. Some evidence to support the formation of such a phase at Sr > 58% was presented in **Section 4.2.2.2**.

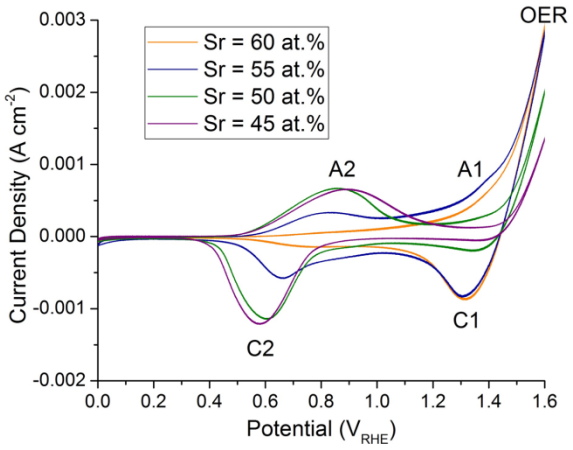

Figure 5-23: Cyclic voltammetry recorded in deoxygenated 0.1 M KOH at a sweep rate of 50 mV s-1 for compositions across a $SrTi_{1-x}Fe_xO_{3-y}$ film deposited under an oxygen plasma, all compositions have Fe content of 25 ± 2 at. %. Cyclic voltammetry for the blank ITO chip under the same conditions is shown by the black line.

5.2.4.2 Peak Charge

Figure 5-24 shows the variation in the peak current density and the charge under the A2/C2 redox couple with increasing Sr at.%. The data shows that for Sr contents below the stoichiometric Sr = 50% composition the peak current density and charge for the redox couple are unaffected by the increase in Sr but where Sr is present in excess both values decrease with increasing Sr content. Since this redox couple is assigned to Fe ions in the perovskite crystal lattice this result suggests that the perovskite phase is formed as the major phase at Sr contents up to Sr = 50 at.% after which point the amount of perovskite phase decreases.

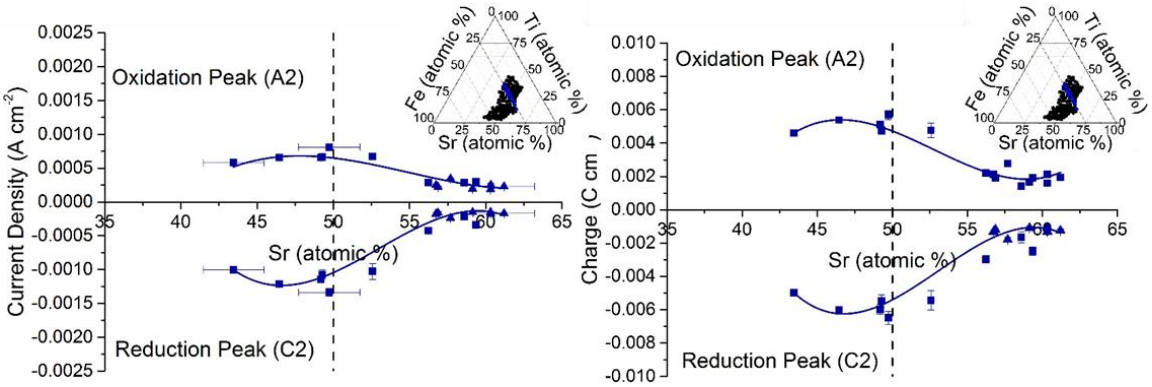

Figure 5-24: Variation of the current density and charge under the oxidation peak (A2) and reduction peak (C2) with Sr at.% along the $Sr_nTi_{0.75-n}Fe_{0.25}O_{3-y}$ tie line where Fe = 25 ± 2 at.%. Data obtained from cyclic voltammetry, recorded in deoxygenated 0.1 M KOH, on $SrTi_{1-x}Fe_xO_{3-y}$ model electrocatalysts in the form of thin films deposited by PVD at 650 °C under atomic oxygen.

Figure 5-25 shows the variation in the peak current density and the charge under the C1 reduction peak with increasing Sr at.%. The data shows an increase in the size of this peak with increasing Sr at.%. It is assumed that this peak arises from the formation of a Sr-rich phase in which the Fe ions are in a distinct chemical environment.

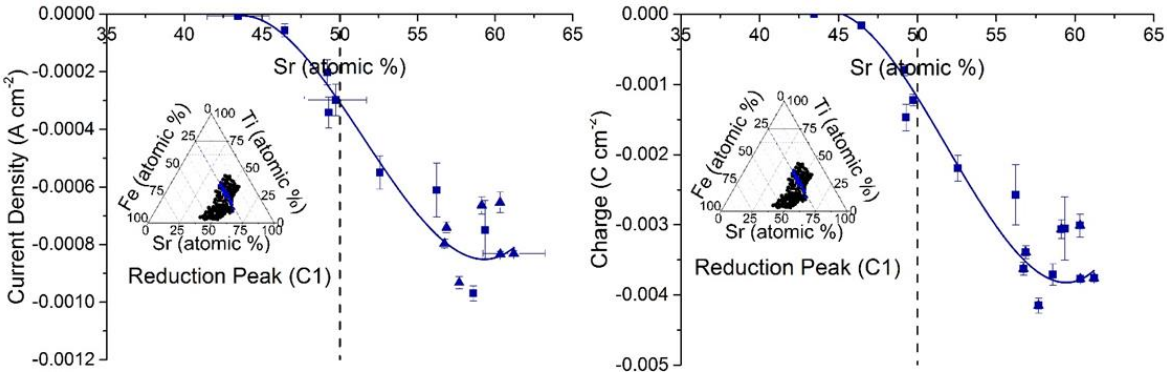

Figure 5-25: Variation of the current density and charge under the reduction peak (C1) with Sr at.%. Data obtained from cyclic voltammetry, recorded in deoxygenated 0.1 M KOH, on $SrTi_{1-x}Fe_xO_{3-y}$ model electrocatalysts in the form of thin films deposited by PVD at 650 °C under atomic oxygen.

The proportion of moles of Fe participating in each of the two redox reactions with increasing Sr content is compared, as shown in **Figure 5-26**. The proportion of Fe ions participating in the R2 redox process, which is assigned to the redox of Fe ions in the perovskite lattice, decreases at Sr > 50 at.% to reach a minimum at x = 60 at.%. There is a corresponding increase in the proportion of Fe ions participating in the R1 redox process which is assigned to lower co-ordinate Fe ions. The switch from the predominance of the R2 redox process to the R1 redox process would be consistent with a change in the chemical environment of the Fe ions at higher Sr content.

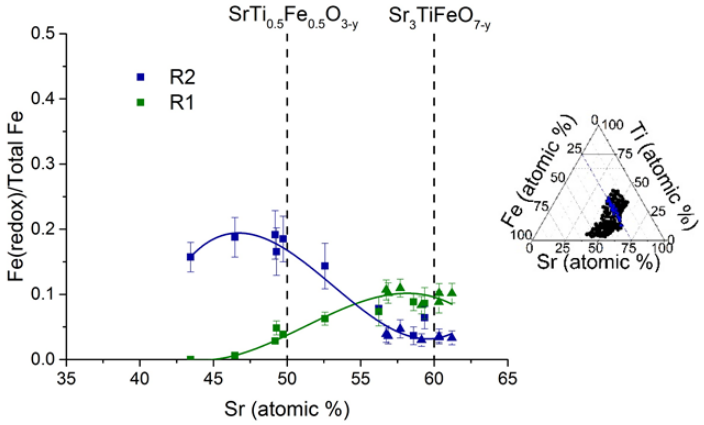

Figure 5-26: Plot to show variation in the ratio of number of moles of Fe atoms involved in redox reactions R1 and R2 with Sr at.%. The number of moles of Fe involved in the redox process is calculated from the charge under the cathodic peaks, C1 and C2 while the total number of moles is estimated using EDX data and thickness data obtained from profilometry measurements.

5.2.4.3 Equilibrium Potential and Peak Separation

Figure 5-27A shows the variation in the equilibrium potential of the R2 redox process. The equilibrium potential reaches a minimum for the Sr = 50 at.% composition which is explained by the stabilisation of the Fe^{4+} oxidation state in the perovskite structure. The A site Sr cation has an inductive effect which draws electron density away from the anti-bonding Fe 3d states, strengthening the Fe – O bond. The increase in the equilibrium potential of the redox reaction above Sr = 50 at.% indicates a change in crystal structure in which this inductive effect is decreased.

Figure 5-27B shows how the separation between the redox peaks changes with Sr content. The separation between the peaks decreases with increasing Sr content with no obvious influence of changes in crystal structure. The decrease in redox peak separation is indicative of faster reaction kinetics with increasing Sr which is assumed to be due to structural changes in the perovskite which favour the electron transfer as was discussed in **Section 5.2.2.3**.

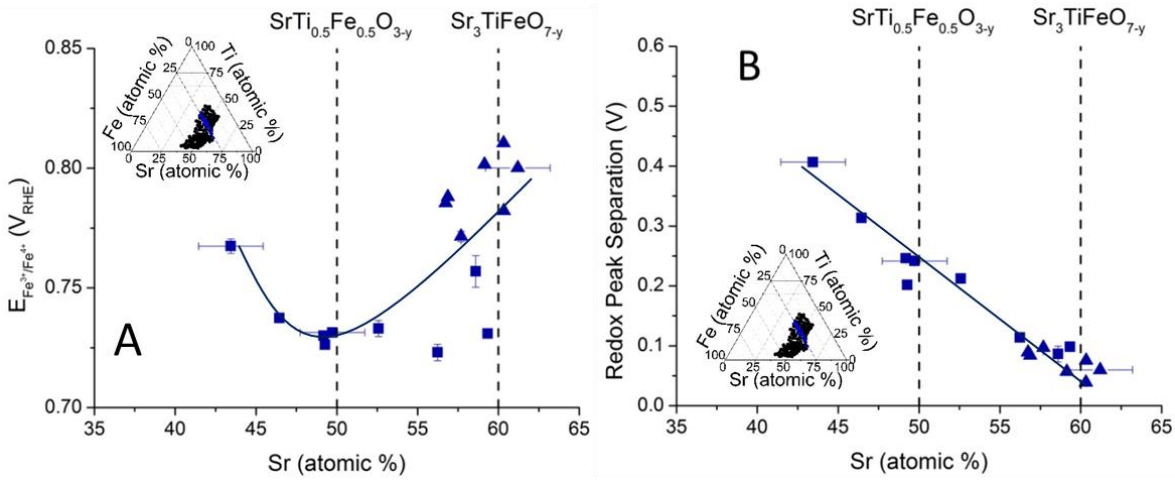

Figure 5-27: Variation in (A) the equilibrium potential of the R2 redox and (B) the separation between the oxidation peak (A2) and reduction peak (C2), calculated from $(E_{A2}-E_{C2})/2$, with Sr at.%. Data obtained from cyclic voltammetry, recorded in deoxygenated 0.1 M KOH, on $SrTi_{1-x}Fe_xO_{3-y}$ model electrocatalysts in the form of thin films deposited by PVD at 650 °C under atomic oxygen.

For the R1 redox reaction the ternary plots in **Figure 5-10** and **Figure 5-12** indicated that the equilibrium potential and redox peak separation respectively depended solely on x and were not affected by Sr composition. The lack of dependence on Sr content is confirmed by **Figure 5-28** using data from the $Sr_nTi_{0.75-n}Fe_{0.25}O_{3-y}$ tie-line.

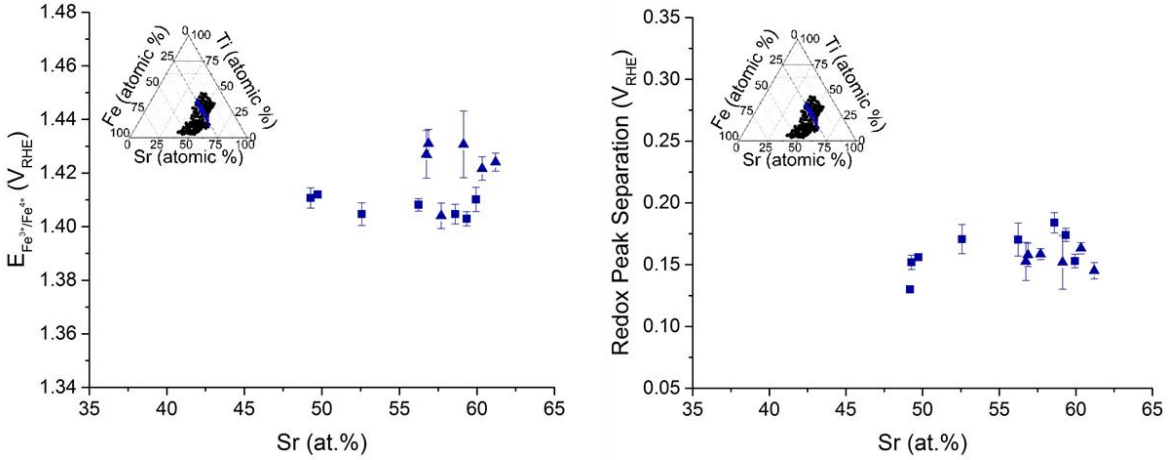

Figure 5-28: Variation of the equilibrium potential and the redox peak separation of the R1 redox reaction along the $Sr_nTi_{0.75-n}Fe_{0.25}O_{3-y}$ tie-line where Fe = 25 ± 2 at.%. Data obtained from cyclic voltammetry, recorded in deoxygenated 0.1 M KOH, on $SrTi_{1-x}Fe_xO_{3-y}$ model electrocatalysts in the form of thin films deposited by PVD at 650 °C under atomic oxygen.

5.2.5 Effect of preparation conditions

A comparison of the cyclic voltammetry obtained for a point of composition $SrTi_{0.5}Fe_{0.5}O_{3-y}$ on films deposited under atomic oxygen and under molecular oxygen before and after annealing is shown in **Figure 5-29**. A set of surface redox peaks presumably due to the Fe^{3+}/Fe^{4+} redox reaction are present in all cases but appear at a higher potential for the films prepared under molecular oxygen compared to the films prepared under atomic oxygen as confirmed by the data in **Table 5-1**. This could be due to a larger number of oxygen vacancies in the film deposited under molecular oxygen, evidence for which was found in the XPS and Raman data. The removal of electron withdrawing oxygen from the perovskite lattice increases the electron density in the Fe 3d states. This leads to a stronger anti-bonding interaction between Fe and O and an increase in the energy of the redox couple.

Alternatively the difference in the cyclic voltammetry could arise from structural differences between the materials since XRD data showed a lower degree of crystallinity for the film deposited in molecular oxygen compared to the film deposited in atomic oxygen. If the film is not fully crystallised in the perovskite structure it would be expected that the inductive effect of the Sr atoms which lead to the lowering of the Fe^{3+}/Fe^{4+} redox energy would be weaker.

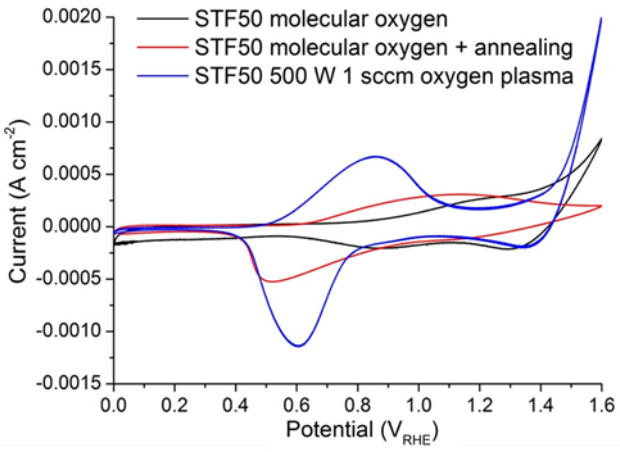

Figure 5-29: Cyclic voltammetry recorded in deoxygenated 0.1 M KOH at a sweep rate of 50 mV s^{-1} for an electrode of composition $SrTi_{0.5}Fe_{0.5}O_{3-y}$ prepared under differing oxygen conditions.

Preparation Method	**E / V_{RHE}**	**ΔE / V_{RHE}**
Oxygen Plasma	0.73 ± 0.03	0.30 ± 0.02
Oxygen Plasma (large Sr range)	0.73 ± 0.03	0.23 ± 0.03
Molecular Oxygen	0.87 ± 0.03	0.30 ± 0.06
Molecular Oxygen (annealed)	0.82 ± 0.02	0.75 ± 0.13

Table 5-1: Data obtained for equilibrium potential, E, and peak separation, ΔE, for Fe^{3+}/Fe^{4+} redox couple from cyclic voltammetry recorded in deoxygenated 0.1 M KOH at a sweep rate of 50 mV s^{-1} for electrodes of composition $SrTi_{0.5}Fe_{0.5}O_{3-y}$ prepared under differing oxygen conditions. Data shown is an average of data from a minimum of 2 electrodes with composition Sr = 50 ± 2 at.% and Fe = 25± 2 at.%.

Cyclic voltammetry for the film deposited in molecular oxygen and subsequently annealed at 650 °C under O_2 in the tube furnace was also shown in **Figure 5-29** and whilst the redox peaks appear larger and slightly closer in potential to those from the oxidised film it is apparent that any activity for oxygen evolution has been lost. The redox potential shifts much closer to that seen for the film prepared using the plasma source but the peak separation is much larger. An explanation for this would be that the annealing process leads to the formation of stable oxygen-vacancy ordered structures which limits the kinetics of the reaction.

5.2.6 Electrochromic behaviour

The oxidation and reduction of the film could be observed visually and videos were recorded during electrochemical cycling to identify changes in the colour of the films. **Figure 5-30** and **Figure 5-31** show stills taken from a video of the electrochemical reduction of a Sr graduated STFO electrode array. The left of the figure shows the appearance of the film prior to the application of electrochemical potential. Upon application of a potential of 0.4 V_{RHE} there is a visible lightening of the colour of the film which continues as the potential is cycled down to 0 V. The observation of a bulk colour change is consistent with a change in the crystal and electronic structure caused by the reversible intercalation of oxygen into the lattice.

Figure 5-30 shows that as a potential of 0.4 V is applied the film takes on a lighter colour and the colour of the film becomes lighter still with a decrease in the potential to 0 V. This colour change corresponds to the reduction of the film which occurs at potentials below 0.7 V_{RHE} as discussed in **Section 5.2.2.2**

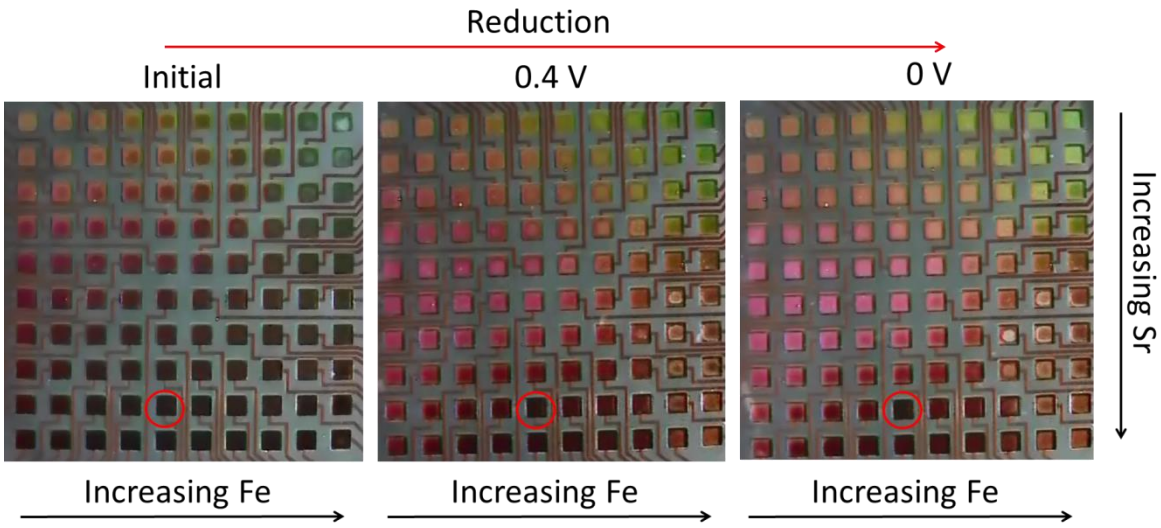

Figure 5-30: Photographs of the STFO electrode arrays prepared at 650 °C using an oxygen plasma before electrochemical reduction, at a potential of 0.4 V and at a potential of 0 V. Red circle indicates a bad electrode in which there is no electrochemical contact.

Photographs of the film upon oxidation by cycling from 0 V to 1.2 V is shown in **Figure 5-31**, the colour change appears to be reversible over most of the film but even after this first cycle it is clear that there is an area of the film at high Sr, high Fe compositions which has been irreversibly changed by the electrochemical cycling.

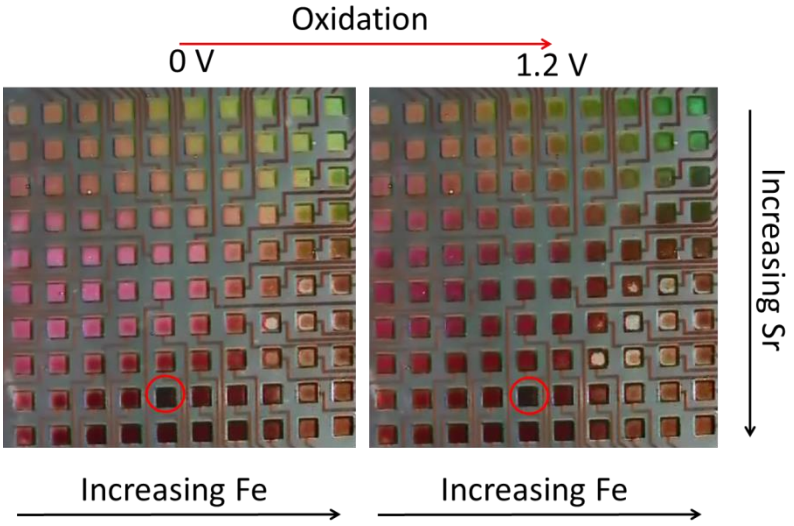

Figure 5-31: Photographs of the $SrTi_{1-x}FexO_{3-y}$ electrode arrays prepared at 650 °C using an oxygen plasma at a potential of 0 V and at a potential of 1.2 V. Red circle indicates a bad electrode in which there is no electrochemical contact.

Photographs taken before and after electrochemical cycling are shown in **Figure 5-32**. There is a clear change in the film at high Sr, high Fe contents which is assumed to be due to the degradation of the film.

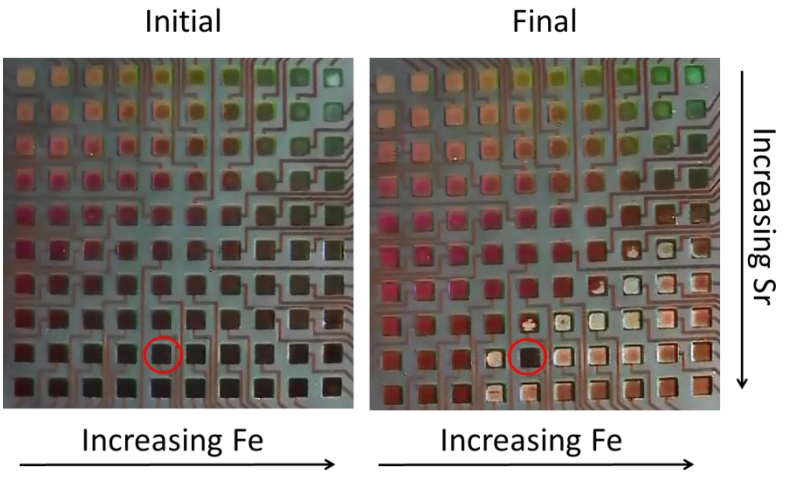

Figure 5-32: Photographs of the STFO electrode arrays prepared at 650 °C using an oxygen plasma before and after repeated electrochemical cycling. Red circle indicates a bad electrode in which there is no electrochemical contact.

The colour change associated with the redox reaction is perhaps more apparent on films deposited with compositions along the $SrTi_{1-x}Fe_xO_{3-y}$ compositional tie line as shown in **Figure 5-33**. Again there is deterioration in the film at high Fe contents even for this tieline composition which shows that it is not just related to an excess of Sr in the films.

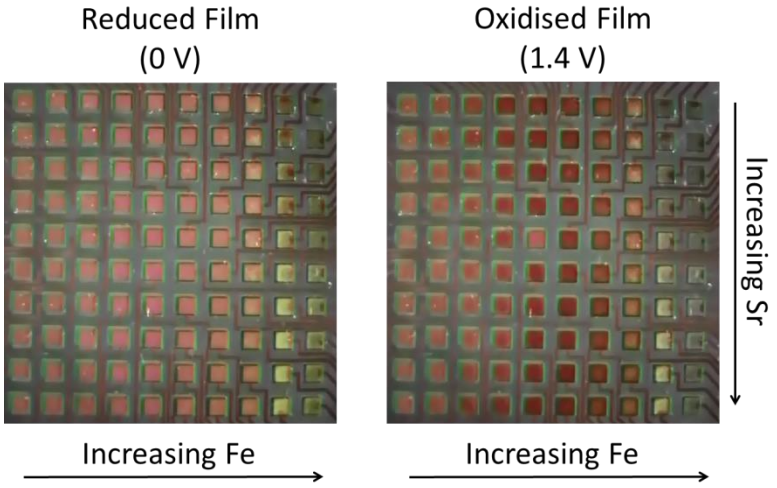

Figure 5-33: Photographs of the STFO electrode arrays prepared at 650 °C using an oxygen plasma before and after electrochemical cycling.

A very clear colour change was also observed for the redox reaction of the STFO films prepared using molecular oxygen as shown in Figure **5-34**. The Fe-rich (left) part of the film takes on a darker colour when oxidised whilst the Ti-rich part of the film (right), for which no redox chemistry was observed, remains unchanged. The colour change was reversible with electrochemical cycling.

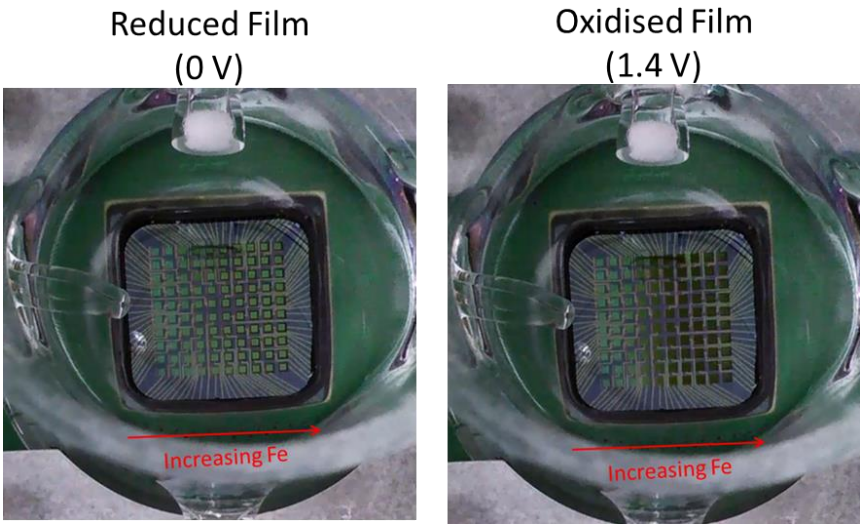

Figure 5-34: Photographs of the STFO electrode arrays prepared at 650 °C using an oxygen plasma taken during electrochemical cycling. The left photograph shows the reduced film whilst the right photograph shows the oxidised film.

5.2.7 Electrochemical stability

In order to investigate the stability of the perovskite electrocatalysts EDX measurements were taken on the samples before and after the electrochemical experiments. Clearly this method cannot determine how much material has been lost but should indicate if there is a preferential loss of any element due to dissolution in the electrolyte. **Figure 5-35** shows the compositions obtained from the EDX measurements prior to electrochemical cycling, A, and after repeated electrochemical cycling, B. The compositions close to the $SrTi_{1-x}Fe_xO_{3-y}$ tie-line, shown in red, appear quite stable although a slightly lower Sr content is noted at the high Fe end of the tie-line.

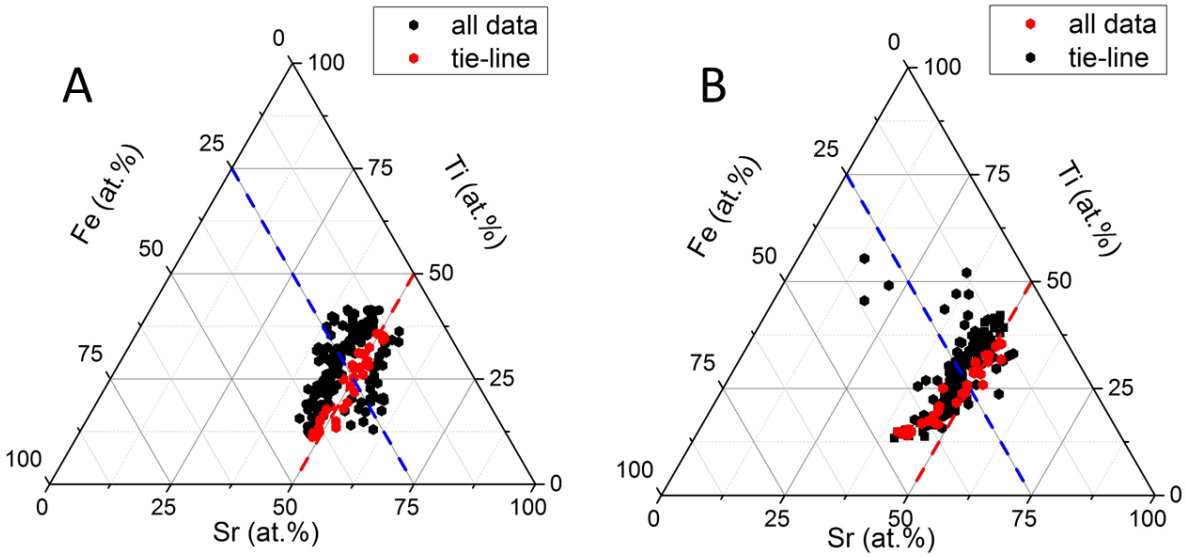

Figure 5-35: Ternary plots showing compositions obtained from SEM-EDX on STFO electrode arrays prepared at 650 °C using an oxygen plasma before (A) and after (B) electrochemical experiments.

Compositions with Sr content in excess of the $SrTi_{1-x}Fe_xO_{3-y}$ tie-line composition however undergo a significant compositional change upon electrochemical cycling particularly when the sample also has high Fe content. This is consistent with the visual observations of the films during the electrochemical cycling.

This observation is confirmed by **Figure 5-36** which uses the ratio of Sr in the sample before and after the electrochemical experiments, labelled Sr and Sr' as a measure of Sr loss and shows how this changes with composition. The ratio is close to one, indicating no loss of Sr across most of the sample but shifts to lower values, indicating a loss of Sr, at high Sr and Fe compositions.

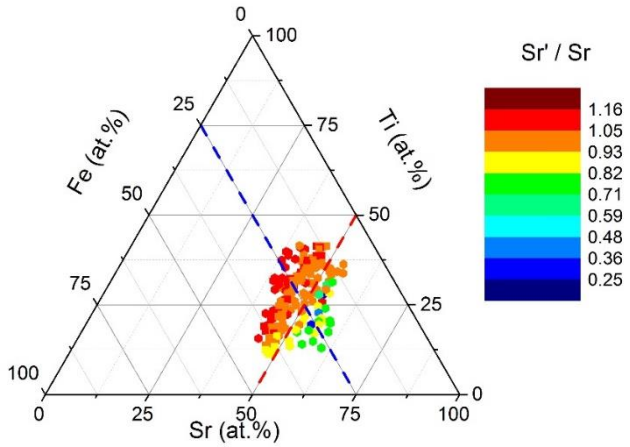

Figure 5-36: Ternary plot showing the composition obtained from SEM-EDX on STFO electrode arrays prepared at 650 °C using an oxygen plasma. Colour map shows the ratio of Sr in the film before and after electrochemical cycling, labelled Sr and Sr' and gives an indication of the stability of the film towards loss of Sr through electrochemical dissolution.

Figure 5-37 shows the same dataset plotted in terms of the Sr content measured by EDX before electrochemical cycling, Sr, against the the Sr content measured after electrochemical cycling, Sr'. This demonstrates quite clearly that at compositions above Sr = 50 at.% , as indicated by the dotted line, there is a loss of Sr with electrochemical cycling.

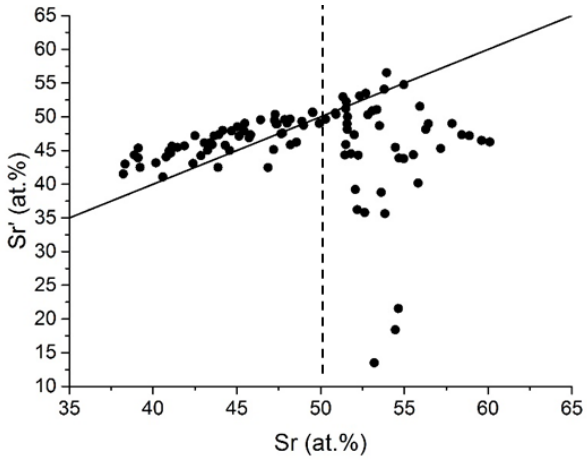

Figure 5-37: Plot to compare the Sr content of STFO electrode arrays prepared at 650 °C using an oxygen plasma measured by EDX before (Sr) and after (Sr') electrochemical cycling.

The change in compositions seems to be limited to loss of Sr from the film and the ratio of Fe to Ti, as described by x, does not change significantly following the electrochemical experiments as shown by **Figure 5-38**. This does not mean that no Ti or Fe is lost from the film and can only confirm that neither Ti nor Fe is preferentially lost from the film.

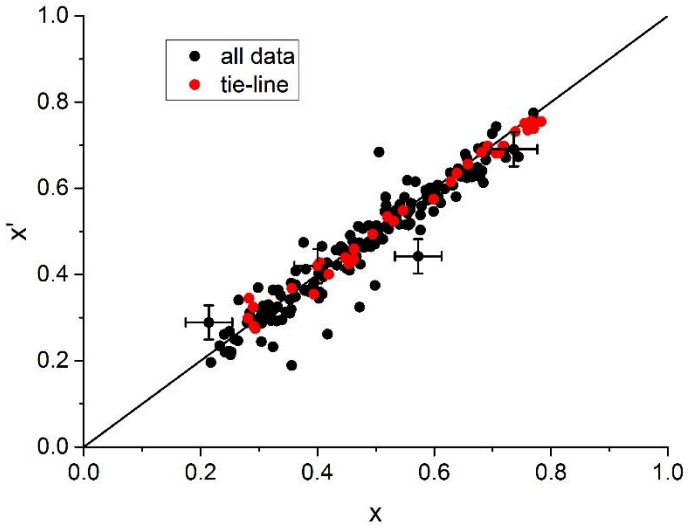

Figure 5-38: Plot showing how the value obtained for x from EDX measurements of $SrTi_{1-x}Fe_xO_{3-y}$ film deposited on ITO at 650 °C under atomic oxygen after electrochemical cycling, labelled as x', changes with x as measured prior to electrochemical cycling. Data shows that the ratio of Fe to Ti does not change significantly during the electrochemical experiments.

A more dramatic change in composition was observed for the films deposited under molecular oxygen as shown in **Figure 5-39** which is indicative of lower stability to electrochemical cycling.

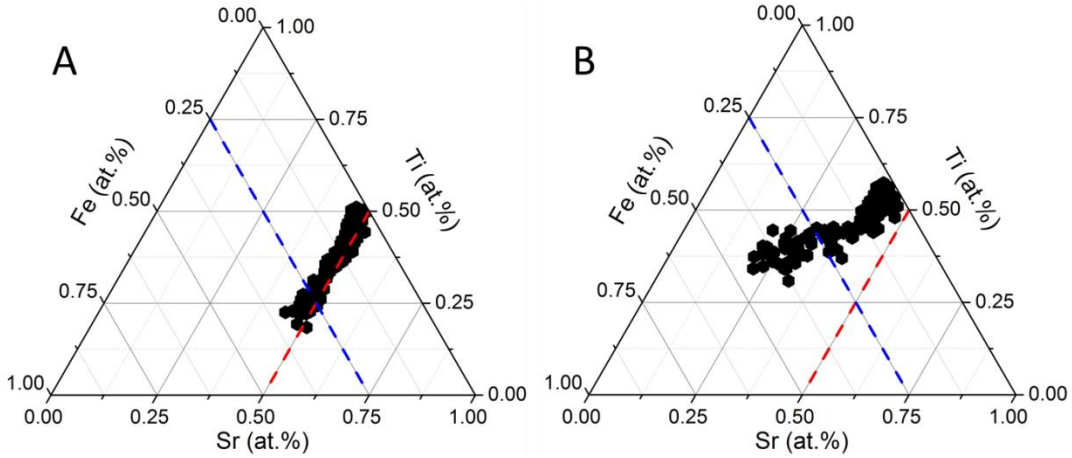

Figure 5-39: Ternary plots showing compositions obtained from SEM-EDX on $SrTi_{1-x}Fe_xO_{3-y}$ films deposited on ITO at 650 °C under molecular oxygen before (A) and after (B) electrochemical experiments.

Additionally there is a clear relationship between the stability of the films and the composition with regard to the proportion of Fe in the film, denoted by x, with films with higher Fe contents showing higher Sr dissolution as confirmed by **Figure 5-40**. At higher Fe contents, over x = 0.5, the proportion of Sr present in the film after electrochemical cycling was found to be about half of the value obtained before the electrochemical experiments. Since x-ray diffraction experiments showed lower crystallinity in this compositional range it is expected that the Sr which undergoes dissolution was present as an amorphous phase not stabilised in the perovskite structure.

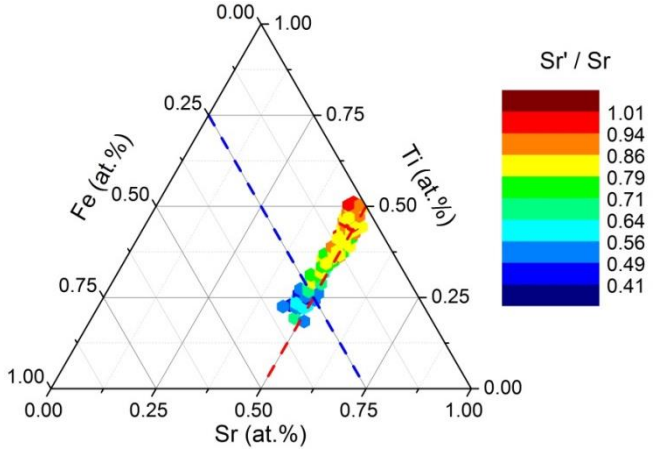

Figure 5-40: Ternary plot showing the composition obtained from SEM-EDX on $SrTi_{1-x}Fe_xO_{3-y}$ film deposited on ITO at 650 °C under molecular oxygen. Colour map shows the ratio of Sr in the film before and after electrochemical cycling, labelled Sr and Sr' and gives an indication of the stability of the film towards loss of Sr through electrochemical dissolution.

When the proportion of Fe retained following electrochemical cycling is compared for electrode arrays prepared in molecular and atomic oxygen, as shown in **Figure 5-41**, it is clear that whilst the films prepared using the oxygen plasma source retain Sr composition up to at least x = 0.5 the films prepared in molecular oxygen begin to preferentially lose Sr at a composition of x = 0.3.

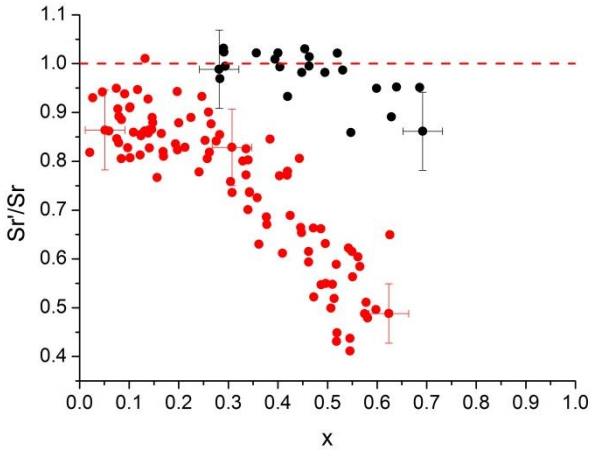

Figure 5-41: Plot to show how Sr loss, defined by the ratio of Sr in the film before and after electrochemical cycling, labelled Sr and Sr', varies with Fe content of the films, defined by x. The STFO film deposited in atomic oxygen retains Sr stoichiometry up to x > 0.5 whilst the film deposited in molecular oxygen loses Sr at x > 0.3.

A difference was also noted in the ratio of Fe to Ti in the films, described by x, obtained before and after electrochemical cycling as shown by **Figure 5-42**. For higher Fe compositions, with higher values of x, the ratio of Fe in the film following electrochemical cycling, labelled x', moves below the line x' = x indicating a loss of Fe relative to Ti. Whilst the change is not dramatic it could indicate some loss of Fe due to electrochemical dissolution.

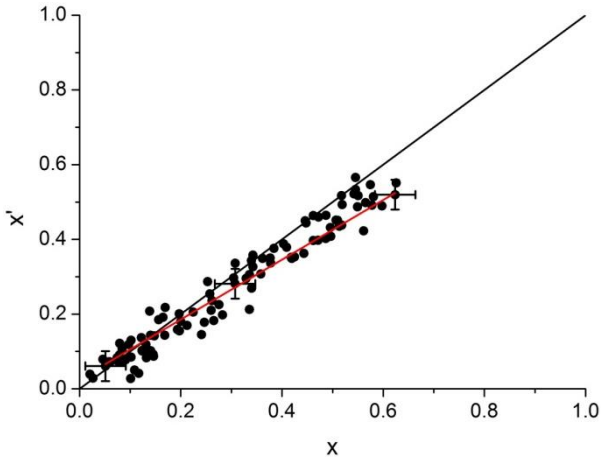

Figure 5-42: Plot showing how the value obtained for x from EDX measurements of $SrTi_{1-x}FexO_{3-y}$ film deposited on ITO at 650 °C under atomic oxygen after electrochemical cycling, labelled as x', changes with x as measured prior to electrochemical cycling. Black line shows x' = x, points on this line show no change in the value of x obtained before and after electrochemical cycling. Red line shows linear fit of data points.

5.3 Conclusions

Cyclic voltammetry of the STFO films revealed two distinct sets of redox peaks which were both assigned to Fe redox reactions. The presence of two sets of peaks is indicative of the presence of different chemical environments for the Fe ions in the lattice. The upper redox reaction, labelled as R1, was assigned to lower co-ordinated Fe ions since the equilibrium potential was closely matched with previous studies on mixed $Fe(OH)_2$ and $Ni/Fe(OH)_2$ films [142, 143]. The redox reaction observed at a lower potential, R2, was assigned to Fe ions fully co-ordinated into the perovskite lattice since the Fe^{4+} oxidation state is stabilised in the perovskite structure by the inductive effect of the Sr cation which has the effect of decreasing the equilibrium redox potential [140].

These assignations were consistent with observed trends in the Faradaic charge under the redox peaks since whilst the Faradaic charge for both redox reactions generally increased with Fe content they showed different trends with increasing Sr content. The Faradaic charge under the R1 redox peaks increased with increasing Fe content whilst the Faradaic charge under the R2 redox peaks was constant up to around Sr = 50 at.% and then decreased. This is significant since at Sr > 50 at.% excess Sr can form SrO layers which intercalate into the perovskite structure to form a Ruddlesden-Popper phase, as discussed in **Section 4.1.4**. The formation of this phase would be expected to result in the introduction of lower co-ordinated Fe ions and a consequent decrease in the number of fully co-ordinated Fe ions.

The number of moles of Fe involved in the redox reaction was calculated from the Faradaic charge under the redox peaks and was found to greatly exceed the number of moles of Fe estimated to be present at the electrode surface. This is explained by the ability of the perovskite lattice to intercalate the surface oxygen into the bulk lattice by diffusion of oxygen to vacancy sites which frees up the surface ions to participate in further reaction. This process was found to be reversible with oxygen also being removed from the lattice upon reduction. This reversible electrochemical intercalation of oxygen has previously been observed for $SrFeO_{3-y}$ [95, 96, 146] but no literature studies on the electrochemical redox processes of the STFO material could be found.

The equilibrium potential of both redox reactions was found to have a dependence on the Fe content, x, of the films. Generally for the R2 redox process, assigned to Fe fully co-ordinated in the perovskite lattice, there was an increase in the equilibrium potential with increasing x which is consistent with weaker M-O bonding and a stabilisation of the reduced Fe^{3+} oxidation state. This is explained by the increase in electron density in the metal 3d states which form anti-bonding interactions with the O 2p states. Conversely for the R1 redox process the equilibrium potential decreases with increasing x. Since the Fe ions are in different environments similar trends would not be expected, however, an explanation for this result is not apparent from the available data.

In general the redox peaks were broad and separated in potential which is indicative of slow electron transfer kinetics. The separation between the redox peaks were also dependent on film composition. For both the R2 and R1 redox reactions the peak separation increased with increasing Fe content, indicating slower reaction kinetics. This is somewhat unexpected since the high Fe content films have the highest conductivity, as discussed in **Section 3.2.4**. Further to this the peak separation decreased with increasing Sr content indicating an improvement in the reaction kinetics despite the low conductivity observed for Sr-rich compositions. It was concluded therefore that the slow kinetics arose not from low electronic conductivity but rather from the change in symmetry of the Fe ions which occurs as oxygen is intercalated into the lattice.

The STFO electrode arrays deposited under molecular oxygen showed redox activity consistent with that observed for the oxygen plasma deposited films in that there were two sets of redox peaks which both appeared to arise from Fe redox reactions. The Faradaic charge was generally lower and the equilibrium potential of the R2 redox process was higher than observed for the oxygen plasma deposited films. It was concluded that both observations arise from a lower crystallinity and a decreased proportion of the perovskite phase relative to other oxide phases consistent with the observations from the XRD studies discussed in **Section 4.2.2.4**. The STFO film which was deposited in molecular oxygen and subsequently annealed also showed redox activity but only one set of redox peaks was observable and there was a very large separation between the peaks. One possible explanation for this would be that stable oxygen-vacancy ordered structures are formed during the annealing which kinetically limits the redox process.

The redox reactions were accompanied by a colour change in the films which is consistent with the change in the bulk electronic structure brought about by the intercalation of oxygen into the lattice. A degradation of the films in the high Fe, high Sr region of composition was also apparent by visual inspection and confirmed by EDX measurements taken before and after electrochemical cycling.

Chapter 6: Electrocatalytic activity of perovskite libraries

6.1 Introduction

6.1.1 Bifunctional Electrocatalysis

The ORR and OER on oxide surfaces have been shown to proceed by an overall 4 e^- multi-step mechanism [153] although the exact reaction pathways have not been determined and it is likely that the reactions occur via several pathways simultaneously at different active sites on the electrode surface. The dominant reaction mechanism will be different for different oxide surfaces depending on the electronic structure and consequent binding strength of the reaction intermediates. A commonly suggested generic reaction pathway for the ORR and OER on oxide surfaces in alkaline media is shown in **Figure 6-1** demonstrating how the two reactions are assumed to share common adsorbed O_2, O, OH and OOH reaction intermediates whilst proceeding in opposite directions. This is important for bi-functional electrocatalysis since the binding interaction between these intermediates and the oxide surface will determine the electrocatalytic activity for both reactions.

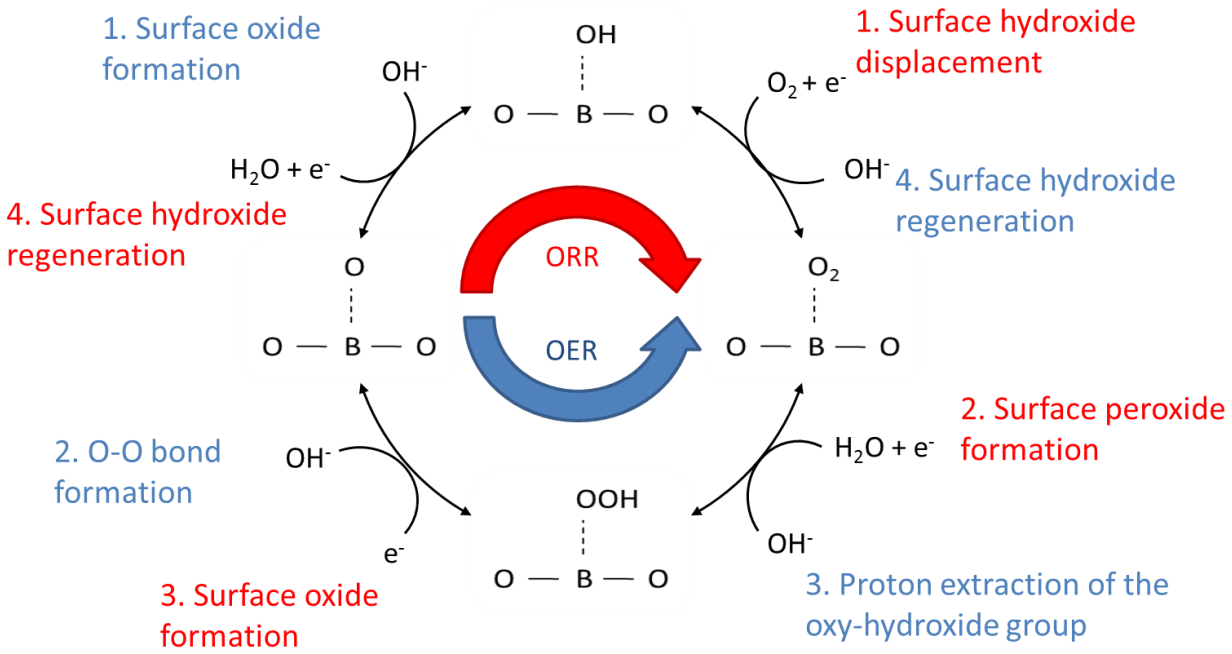

Figure 6-1: Simplified reaction cycle for the ORR/OER on transition metal oxide surfaces in which the charge distribution between the adsorbed species and the metal ion is not considered. ORR mechanism is shown in clockwise direction, descriptions of reaction steps are shown in red. OER mechanism is shown in the anti-clockwise direction, descriptions of reaction steps are shown in blue. Adapted from [46] and [140].

The rate of the reaction is strongly correlated with the binding energy of the oxygen containing intermediates on the electrode surface. Interaction between the surface and the intermediates is a requirement for electrocatalysis but strong binding leads to rate-limiting desorption of products and a passivation of the electrode surface [154]. Although the binding energies for the individual intermediates will differ, they are strongly correlated and a single descriptor of the oxygen binding energy has been found to correlate well with the rate of reaction of both the ORR and OER [155, 156]. This leads to a volcano-shaped relationship between the electrocatalytic activity and the strength of the surface-oxygen bonding where the most active material with optimal oxygen binding energy is found at the peak of the volcano as shown in **Figure 6-2**.

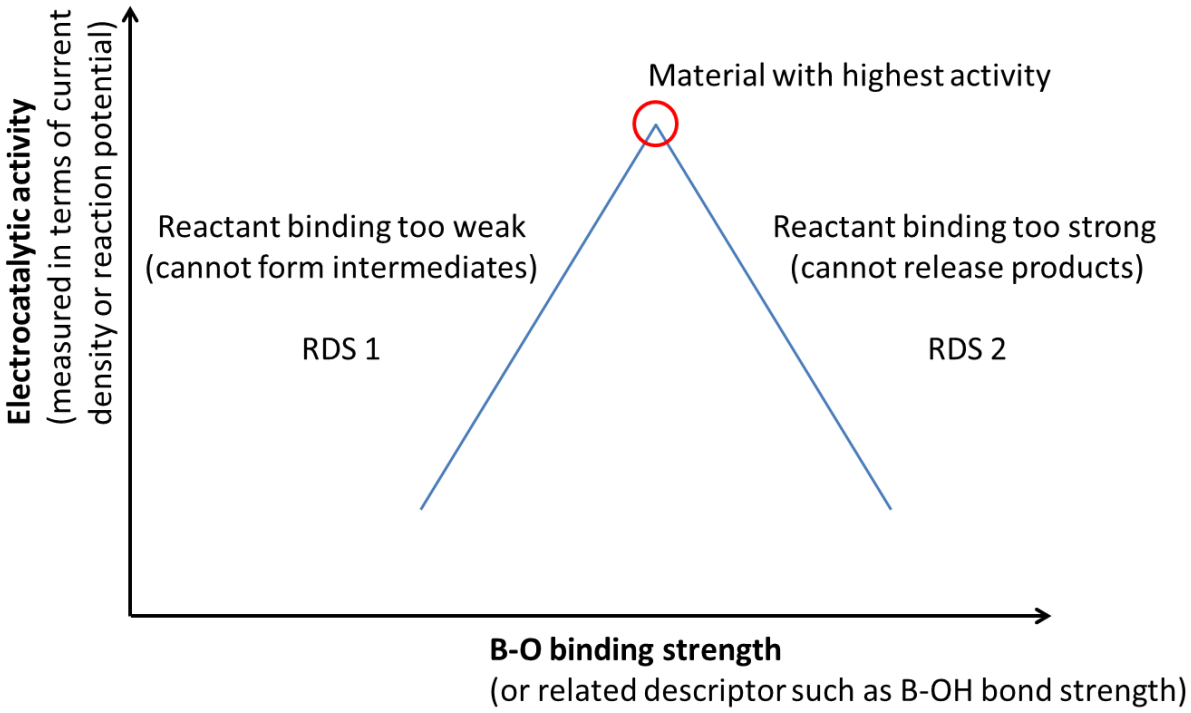

Figure 6-2: Schematic of a volcano plot showing the expected dependence of electrocatalytic activity on a suitable descriptor. On the left hand branch of the plot the interaction between the electrocatalyst and the reactant is too low and the formation of reaction intermediates and products is not favoured. On the right hand branch the interaction between the electrocatalyst and the reactant is too high and the release of the reaction product from the surface is not favoured. The most active material is found at the top of the volcano where these two factors are balanced. The rate determining step may differ for the two branches.

6.1.2 Activity descriptors

Since the oxygen binding energy is not easily measured experimentally a related chemical or physical descriptor which would allow for prediction of active electrocatalyst materials is desirable. Attempts to identify an adequate descriptor for the ORR and OER on transition metal oxides began with experimental studies in which a large number of oxides were screened. This led to the proposal of various chemical descriptors including the potential of the highest redox couple [157, 158], the enthalpy of the transition between the lower and higher redox states [34] and the enthalpy of formation of the transition metal hydroxides [47]. There is a clear relationship between these quantities and the oxygen binding energy as the reactions considered involve the formation of TM-OH bonds. Whilst these descriptors explain the observed electrocatalytic activity they cannot easily be applied for the prediction of new active electrocatalysts since the value of the descriptor may not be easy to obtain theoretically and may require the collection of experimental data.

Improvements in the accuracy of DFT calculations has allowed the oxygen binding energy to be determined theoretically and applied as an ORR/OER descriptor. In addition further calculations have allowed estimates of the theoretical reaction over-potential on a given electrode surface. Rossmeisl *et al.* [155] developed a method for modelling the free energy of adsorption, ΔG_i, of the individual oxygen intermediates as a function of electrode potential which allowed them to construct free energy diagrams for the 4-step mechanism at different over-potentials. Since a negative value of the free energy of the reaction step, ΔG_{rxn}, is required for it to occur at a significant rate, the minimum over-potential required for an individual reaction step could be identified from the potential at which the calculated free energy became negative. The last step to achieve a negative ΔG_{rxn} was assumed to determine the thermodynamic over-potential for the electrocatalysed reaction.

Mann *et al.* [159] applied this approach to a range of perovskite materials for which experimental data was available from earlier studies. The calculated values for over-potential were not directly comparable to their experimental counterparts, partially due to the neglection of activation barriers in the calculation method. However good agreement was found in the reactivity trends and a new activity descriptor was identified which was the difference in adsorption energy of the O and OH intermediates, $\Delta G_{O(ads)} - \Delta G_{HO(ads)}$.

Other theoretical studies have sought to relate electrocatalytic activity to the electronic properties of the electrode surfaces which govern the binding of oxygen adsorbates. The higher metal d-band centre has been confirmed as a good descriptor for ORR activity on metal surfaces since the strength of the interaction with adsorbates increases as the d-states move closer to the Fermi-level. The increase in the strength of the interaction arises from the shifting of anti-bonding states to energies above the Fermi-level where they will be un-occupied whilst bonding states are shifted below the Fermi-level and are occupied [160]. A theoretical study of 3d transition metals, their monoxides and perovskite oxides showed that the calculated oxygen adsorption energy increases with the number of outer electrons of the transition metal [161].

Bockris and Otagawa [47] conducted an experimental screening of 18 different perovskites and found that electrocatalytic activity towards the OER increased with both decreasing B-OH bond strength and an increasing number of valence d-electrons. Despite the relatively large number of materials considered, all would be placed on the right branch of the volcano plot, where the desorption of OH^- is rate limiting. The inverse relationship between B-OH bond strength and number of d-electrons occurs since the interactions between the valence 3d-states on B and the O 2p states are anti-bonding [162].

More recent studies by Suntivich *et al.* found an M shaped relationship between the number of d-electrons and the electrocatalytic activity towards the ORR with peaks in activity for the d^4 and d^7 electronic configurations [61]. This observed trend arises from the splitting of the transition metal d-states into lower energy t_{2g} and higher energy e_g states by the presence of the oxygen ligands, as shown in **Figure 6-3** for the high spin Fe^{4+} ion in $SrFeO_3$. The energy levels are further split for the surface ions where the symmetry of the BO_6 units is broken resulting in a tetragonal distortion. The two maxima in activity at d^4 and d^7 were found to correspond to electronic configurations with an e_g filling of 1, i.e. $t_{2g}^3e_g^1$ (high spin d^4) and $t_{2g}^6e_g^1$ (low-spin d^7). The researchers were therefore able to establish volcano shaped relationships between electrocatalytic activity and the filling of the e_g orbital for both the ORR and the OER determining an ideal e_g occupancy just below one for the ORR [61] and just above one for the OER [46].

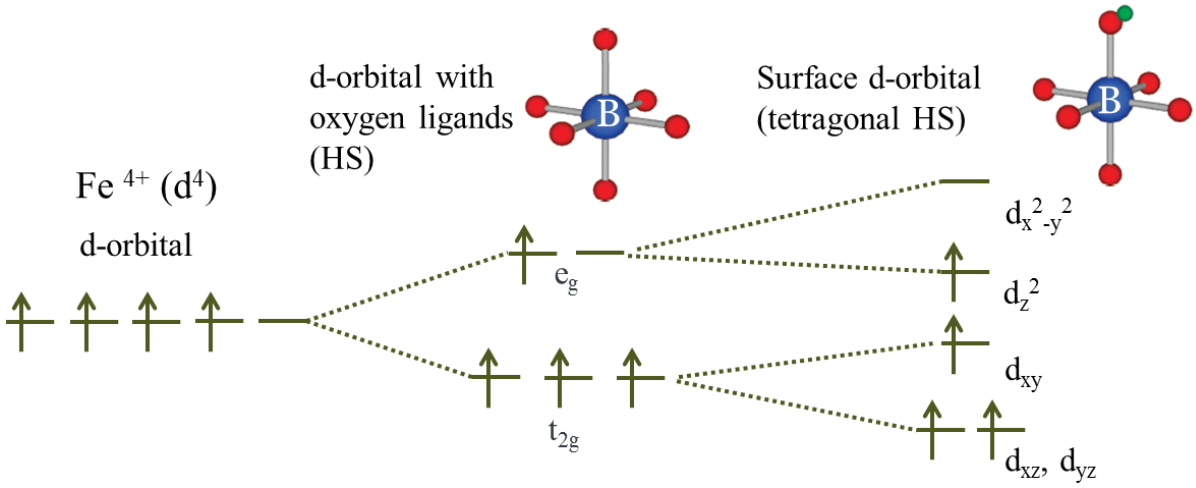

Figure 6-3: Electronic structure of the Fe^{4+} cation in the octahedral B-site of a perovskite lattice. The d-orbital is split into anti-bonding e_g and bonding t_{2g} orbitals by the effects of ligand field splitting. At the surface a tetragonal distortions splits the orbitals further.

The importance of the e_g orbital had been noted in much earlier studies, in particular by Matsumoto *et al.* [163] who investigated transition metal perovskites which exhibit metallic conductivity such as $LaTiO_3$, $SrVO_3$, $SrRuO_3$ and $La_{1-x}Sr_xMnO_3$ in order to establish a link between the nature of the conduction band and catalytic activity for the ORR and OER. They found that materials with a σ* conduction band, formed by the overlap of the e_g orbital of B with the sp_σ orbital of O, showed high activity for both reactions. Materials with π* conduction bands formed from overlap of t_{2g} orbitals of B showed lower activity.

Suntivich *et al.* however rationalised their observations using molecular orbital theory since it has been shown that the electronic band structure observed in bulk transition metal oxides does not extend to the surface and as such the electrons of the surface ions are localised in molecular orbitals [164]. This influence of the e_g orbital occupation on the observed electrocatalytic activity was explained by a larger overlap for the e_g orbitals compared to the t_{2g} orbitals when the O_2 molecule is adsorbed in an end-on configuration [163]. An example of this is shown in **Figure 6-4** which shows the shape and orientation of the d_z^2 orbital which points towards the adsorbed oxygen ligands. It is therefore assumed that the electrons in the e_g orbitals will have the largest influence of the energy of adsorbate binding and therefore electrocatalytic activity.

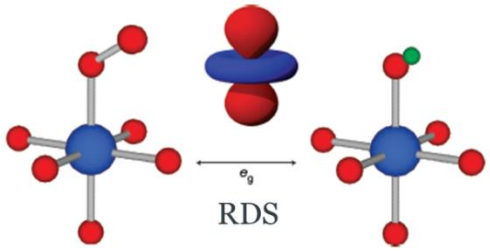

Figure 6-4: Orientation of the d_z^2 with respect to the adsorbed oxygen molecule. The d_z^2orbital points towards the oxygen ligand allowing a large degree of overlap with the oxygen molecular orbitals. Taken from [61].

Their proposed mechanisms for the ORR and OER on perovskites, shown in **Figure 6-5**, were based on earlier suggestions by Goodenough and Cushing [140]. The rate determining step was assumed to change based on the level of e_g filling as indicated. The degree of covalency of the B-O bond was also proposed as a secondary descriptor for the activity of both reactions since increased covalency of this bond leads to improved electron transfer and as such better reaction kinetics.

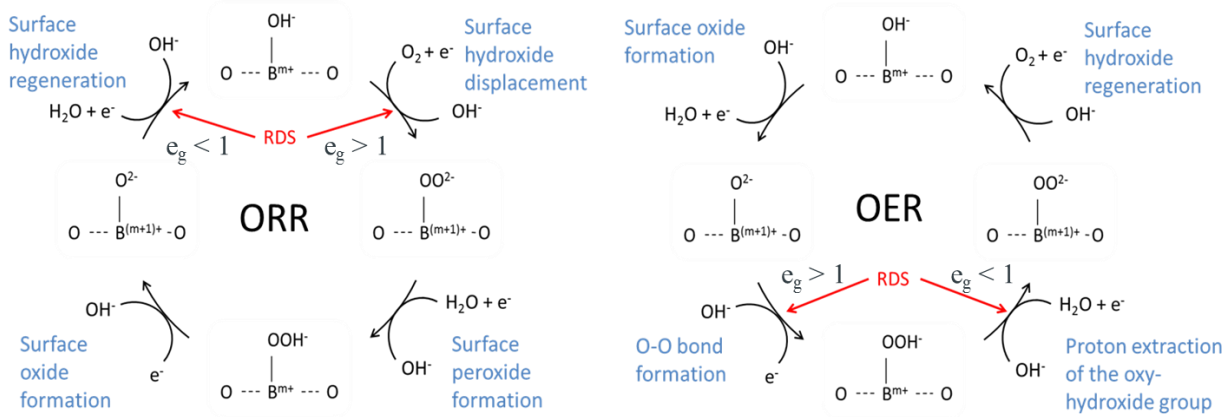

Figure 6-5: Proposed reaction mechanisms for the ORR and OER on ABO_3 perovskites in alkaline solution [46].

A downside of the use of the e_g orbital filling as an activity descriptor is that it is dependent on both the oxidation state and the spin state of the transition metal ion and is therefore not easily measured or computed for some ions with multiple oxidation and spin states. Its usefulness is also disputed on the grounds that a single mechanism and set of rate determining steps cannot be assumed for the entire range of perovskite materials which vary greatly in their structural and electronic properties. Several researchers have proposed alternative mechanisms and it seems likely that the major pathway for both reactions may change depending on the perovskite oxide considered.

It should also be noted that the number e_g orbital filling is a bulk property of the material whereas the electrocatalytic activity will in reality be dependent on the surface electronic structure of the material. A computational study of the $LaMnO_3$ surface [165], a material identified as highly active in the studies by Suntivich *et al.*, investigated the oxygen binding energy at the available surface sites and found a difference in oxygen binding energy for sites of differing co-ordination despite identical e_g-orbital filling. The researchers also challenged the proposed mechanism, suggesting that the binding energy of the B-OO^{2-} intermediate would be too high and that the major pathway for the ORR was more likely to involve the formation of B-OO^- followed by a disproportionation with water to form HO_2^- and OH^-. They suggest that oxygen binding in the form of B-O_2^{2-} would occur at lower co-ordinated sites which are in fact likely to be less electrocatalytically active.

6.1.3 Alternative reaction mechanisms

A further issue raised from the Suntivich *et al.* studies [46, 61], as well as from other studies of perovskite electrocatalyst materials [40, 166, 167], is the role of the conductive carbon additive which was combined with the perovskite materials in order to improve their conductivity and consequentially their electrocatalytic efficiency. It has been suggested [168-171] that the carbon may have a significant role in the ORR mechanism since carbon is known to be active for the electrocatalytic reduction of O_2 to peroxide (HO_2^-), which occurs in alkaline media via the reaction shown in **Equation** 6-1.

$$O_2 + H_2O + 2e^- \rightarrow HO_2^- + OH^-$$

Equation 6-1

Carbon is however not able to catalyse the further reduction of HO_2^- to OH^- which must therefore occur on the perovskite oxide catalyst. Perovskite oxides have been shown to be active catalysts for the electrochemical reduction of HO_2^-, shown in **Equation** 6-2 [172-175], as well as for the chemical decomposition of hydrogen peroxide shown in **Equation** 6-3 [176, 177]. Either reaction may therefore complete the overall 4 e^- reduction.

$$HO_2^- + H_2O + 2e^- \rightarrow 3OH^-$$

Equation 6-2

$$2HO_2^- \rightarrow 2OH^- + O_2$$

Equation 6-3

The potential involvement of the C additive in the ORR mechanism on perovskite/C composite electrodes has been investigated by rotating ring disk electrode (RRDE) experiments [169, 178] and experiments using a channel flow cell [171] both of which have detected the presence of HO_2^- in the electrolyte solution during the ORR. This has led to the proposal of a mechanism whereby the reduction of O_2 to HO_2^- occurs on carbon, the intermediate is desorbed and subsequently reduced by the perovskite oxide electrocatalyst. Support for this theory is found in that the amount of HO_2^- detected decreases with increasing perovskite loading which is explained by the efficient reduction of the intermediate by the perovskite oxide [178]. Additionally in studies of $La_{0.6}Ca_{0.4}CoO_{2-x}$ it was noted that whilst the addition of carbon to perovskite oxides increases ORR activity it has little effect on the OER activity [169]. If the addition of carbon solely increased the electronic conductivity it would be expected to have a similar effect on both reactions.

Poux *et al.* [168] studied the effect of varying the C/oxide ratio on the electrochemical and electrocatalytic properties of two perovskite oxides, $LaCoO_3$ and $La_{0.8}Sr_{0.2}MnO_3$, which had been shown to be active for the ORR in alkaline media in prior studies. In both cases they found that the addition of carbon decreased the separation of anodic and cathodic redox peaks confirming that there was a decrease in the ohmic resistance. They also found that the total capacitance was increased, showing that carbon improved the utilisation of the surface area. An improvement in ORR activity was confirmed by a shift in the onset potential to more positive values and an increase in the ORR current for both perovskites with the addition of carbon but the behaviour of the two materials was not identical with variation of the perovskite loading.

For $LaCoO_3$ which has e_g occupancy of 1, the onset potential for the perovskite/C composite electrodes at all loadings was very similar to that observed on carbon alone and the shape of the ORR curve was not affected significantly by changes in perovskite loading. They concluded from this that the first step of the reduction reaction occurred almost exclusively on the carbon additive with the perovskite only active for the further reduction of H_2O_2 to OH^-. In the case of $La_{0.8}Sr_{0.2}MnO_3$ however the addition of perovskite to carbon resulted in a positive shift in the onset potential and changes in the shape of the ORR curve with perovskite loading indicating that the perovskite oxide contributes significantly to the first reduction step. These results call into question the activity trends observed in studies where the effect of carbon addition is not considered.

Hardin *et al.* employed a similar approach to gain insight into the mechanism of the OER as well as the ORR [179]. They studied $LaNiO_3$, $LaNi_{0.75}Fe_{0.25}O_3$, $LaCoO_3$ and $LaMnO_3$ which all have e_g orbital filling of 1 and which with the exception of $LaNi_{0.75}Fe_{0.25}O_3$ had been included in the study by Suntivich *et al.*. They compared the electrocatalytic activity of the perovskite oxides supported on un-doped C which as discussed above is only active for the first step of O_2 reduction to form HO_2^- with perovskite oxides supported on N-doped carbon which shows additional activity for the chemical disproportionation of peroxide according to Equation 6-3. The addition of the N-doping to the support material improved the mass activity of the catalysts towards both reactions for all materials but to different extents. They were therefore able to demonstrate whether the reaction of the peroxide intermediate was rate determining for each of the materials and were ultimately able to conclude that despite similar e_g occupancy, the rate determining steps in the electrocatalysis of the ORR and OER differed between the materials.

For the $LaMnO_3$ catalyst the mass activity towards the OER increased by 23% when N-doping was added to the carbon support material for $LaCoO_3$ and $LaNi_{0.75}Fe_{0.25}O_3$ the increase in mass activity was 3% and 4% respectively. The authors explained this result using an altered form of the OER reaction cycle as shown in **Figure 6-6**. In this pathway lattice oxygen ions are involved in the potentially rate determining O-O bond formation step. For $LaMnO_3$ step 4 is assumed to be the rate determining step since upon addition of the N-doping to the support material an increase in the activity was observed which was assigned as due to chemical disproportionation of the peroxide intermediate on the support thus by-passing this step. Previous studies on $LaCoO_3$ have suggested that step 1 or 3 would be rate limiting on this material and this is supported by the negligible effect of the addition of the peroxide disproportionation catalyst on the mass activity.

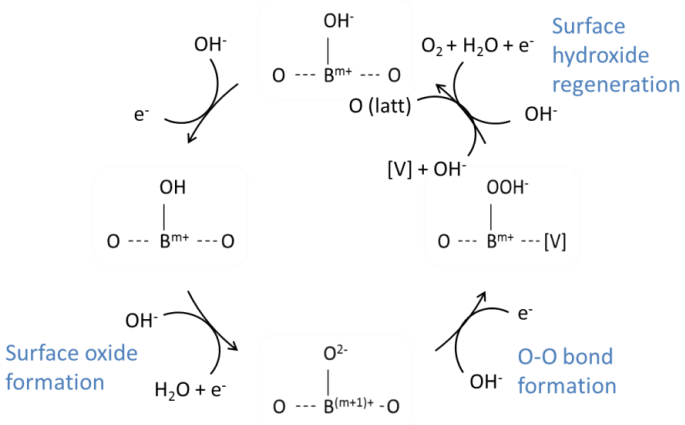

Figure 6-6: Alternative OER mechanism in which lattice oxygen participates in the O-O bond formation step leaving an oxygen vacancy, [V], in the lattice which is subsequently replenished from hydroxide ions in the electrolyte. Adapted from [180].

Support for this proposed OER mechanism includes isotope labelling studies which have proved that lattice oxygen contributes to O_2 evolution at room temperature on certain transition metal oxides including IrO_2 [181] and RuO_2 [182]. It was proposed that for perovskites which readily form oxygen vacancies such as $LaNiO_3$ this mechanism would be favourable and subsequent DFT calculations on the $LaNiO_3$ surface have also lent support to this hypothesis [91]. This mechanism is not expected to occur for all perovskites in fact calculations on the $La_{1-x}Sr_xBO_3$ series of perovskites where B = Mn, Fe, Co and Ni predicted a transition between the "adsorbate" mechanism proposed by Suntivich *et al.* and the "lattice oxygen" mechanism. Further they found that with increasing predominance of the lattice oxygen mechanism, the stability of the electrocatalysts decreased [91].

The results obtained by Hardin *et al.* [179] for the ORR were less conclusive as the mass activities of all the studied perovskite materials were significantly improved upon the addition of N-doping to the support material although the authors suggest that the difference in the observed mass activities were not consistent with the e_g orbital filling providing an adequate descriptor. Additionally they noted that the activity towards the ORR decreased in the order Ni > Co ~ Mn which is consistent with the ease of formation of surface oxygen vacancies suggesting that this may be integral to ORR activity at room temperature.

At high temperature the formation and annihilation of oxygen vacancies is certainly important to the ORR mechanism and the energy of formation of bulk oxygen vacancies has been found to be a good descriptor for ORR activity in the search for electrocatalysts for use in high temperature SOFC applications [183]. Lee *et al.* [183] also computed the O p-band centre relative to the Fermi-level for various perovskite materials commonly used as SOFC cathodes and found a good correlation with surface oxygen exchange coefficient which is a value closely linked to the ORR in SOFCs. They also noted a link between electrocatalytic activity and stability since electrodes with an O p-band centre close to the Fermi level were found to have the highest oxygen exchange rates and were also found to be unstable.

6.1.4 Electrocatalytic activity of STFO

For the $SrTi_{1-x}Fe_xO_{3-y}$ model electrocatalysts considered here the electrocatalytic activity towards the oxygen reduction and oxygen evolution reactions is expected to increase with increasing Fe content, as denoted by x. The Ti^{4+} cation has no d-electrons and as such weak oxygen binding and correspondingly poor electrocatalytic activity is observed for un-doped $SrTiO_3$.

Early theoretical studies assumed a low spin configuration for the Fe^{4+} ion in $SrFeO_3$ [184] but it has since been proven that the Fe^{4+} ion exists in a high-spin state and as such has a $t_{2g}^3e_g^1$ electronic configuration [94] as shown earlier in **Figure 3-5**. According to the theory proposed by Suntivich *et al.* this should make $SrFeO_3$ ideal for bi-functional catalysis of the ORR and OER but whilst good catalytic activity has been reported for $SrFeO_3$ electrodes for the OER, anodic dissolution has also been observed at OER potentials [185]. The addition of Ti and other transition metals has been shown to increase the stability of the material [186] and so this may also have an impact on the trends in activity of the $SrTi_{1-x}Fe_xO_{3-y}$ films towards the OER and ORR as high Fe composition perovskites may not be stable to cycling.

The poor stability of $SrFeO_3$ at OER potentials could be indicative of the involvement of lattice oxygen in the OER mechanism [91]. In this case the "adsorbate" mechanism proposed by Suntivich *et al.* and the related e_g-filling descriptor may not be relevant. The electrocatalysis of the "lattice oxygen" mechanism depends on the ability of the electrode surface to form oxygen vacancies [179]. Both $SrFeO_{3-y}$ and $SrTi_{1-x}Fe_xO_{3-y}$ form oxygen vacancies readily due to the preference of the Fe ion for adopting the Fe^{3+} oxidation state, which has a favourable d^5 electronic configuration rather than the d^4 Fe^{4+} oxidation state. The ability of the $SrTi_{1-x}Fe_xO_{3-y}$ model electrocatalysts to form oxygen vacancies will therefore increase with increasing Fe content but it is expected that this will be accompanied by a decrease in electrode stability.

Oxygen deficient $SrFeO_{3-y}$ and $SrTi_{1-x}Fe_xO_{3-y}$ materials contain Fe^{3+} ions which have the electronic configuration $t_{2g}^3e_g^2$. This higher e_g filling may be expected to decrease the activity towards the ORR and OER due to weak interaction of the electrode surface with the oxygen intermediates since the e_g orbital forms anti-bonding interaction with O $2p^-$. However at the highly oxidising potentials of the OER it would be expected that the material would be fully oxidised and that the Fe ions would be in the Fe^{4+} oxidation state. The situation for the ORR is less certain and the potential of the Fe^{3+}/Fe^{4+} redox process may be important in determining the electrocatalytic activity.

In the case that Fe adopts the formal Fe^{4+} oxidation state there is significant covalent character to the Fe-O bonding and charge transfer occurs from the oxygen ligands to the Fe ion. The ground state is therefore actually dominated by a $d^5\underline{L}$ electronic structure, where $\underline{L}$ represents a ligand hole, rather than the d^4 configuration [94]. The charge fluctuation between the d^4 and $d^5\underline{L}$ states results in delocalised electrons which give rise to metallic conductivity in the material. Since good electronic conductivity is expected to be a requirement for electrocatalysis the oxygen content of the STFO electrocatalysts may be expected to have an impact on the activity towards both the ORR and OER. Four-point probe measurements on the STFO thin films deposited under atomic oxygen showed an increase in conductivity with increasing Fe content. The films deposited under molecular oxygen were highly resistive exceeding the measurement limit of the instrument.

6.2 Results

The experimental set-up for the electrochemical experiments was described in Chapter 2. Measurements of the electrocatalytic activity of the STFO electrode arrays followed the measurement of their redox activity as described in the previous chapter. The electrocatalytic activity of the electrode arrays was assessed by cyclic voltammetry recorded in 0.1 M KOH electrolyte at a sweep rate of 5 mV s^{-1}. The voltammetry was recorded in both de-oxygenated electrolyte, which was bubbled with Ar for 20 minutes prior to the measurements and in oxygenated electrolyte, which was bubbled with O_2 for 20 minutes prior to the measuements.

6.2.1 OER activity

6.2.1.1 Trends in OER activity with composition

The ternary diagrams in **Figure 6-7** show the variation of current density at 1.6 V_{RHE} and onset potential for the OER across ternary compositional space and show that in addition to a dependence of Fe content the Sr content of the film also impacts the activity. For given Fe content, OER activity was highest where Sr content was also high and activity dropped off for the Sr deficient compositions.

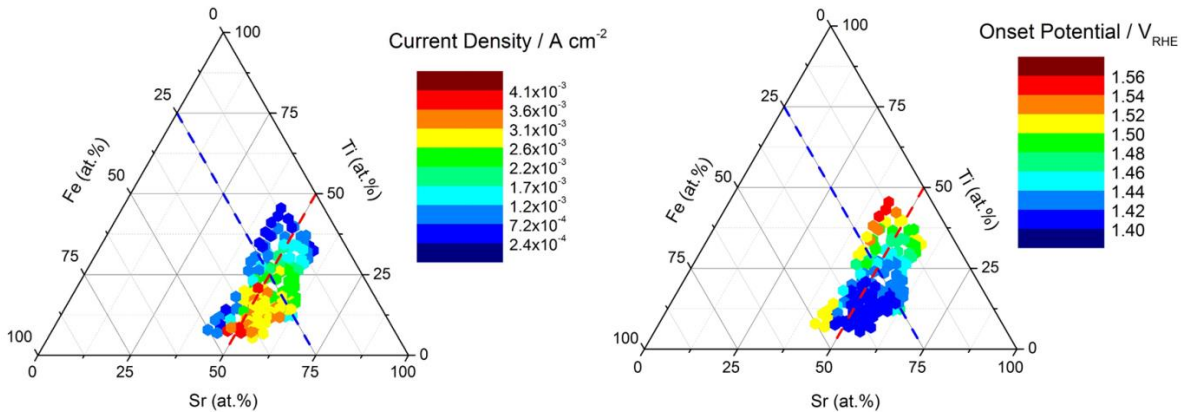

Figure 6-7: Ternary plots with colour maps showing the variation in current density at 1.6 V_{RHE} and onset potential taken at 100 µA. Data obtained from cyclic voltammetry, recorded in deoxygenated 0.1 M KOH at a sweep rate of 5 mV s^{-1}, on $SrTi_{1-x}Fe_xO_{3-y}$ thin film electrodes deposited by PVD at 650 °C under atomic oxygen.

It is noted that in the region of compositional space with favourable OER activity poor electrode stability was also found as discussed in Chapter 5.13. This could point to a mechanism for the OER in which the evolved oxygen originates partially from the lattice since it has been proposed that the adoption of this mechanism leads to higher OER activity coupled with poor electrode stability [91].

6.2.1.2 Effect of B-site variation on OER activity

Figure 6-8 shows the oxygen evolution region of cyclic voltammetry on $SrTi_{1-x}Fe_xO_{3-y}$ thin film electrodes deposited under atomic oxygen. The films showed the expected increase in activity towards the oxygen evolution reaction with increasing x.

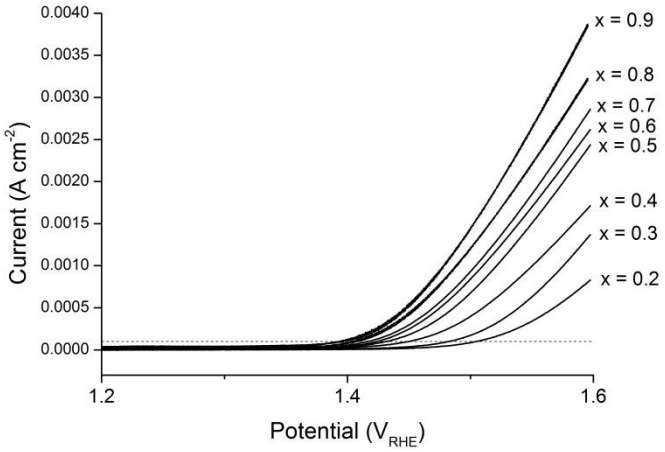

Figure 6-8: Cyclic voltammetry recorded in deoxygenated 0.1 M KOH at a sweep rate of 5 mV s^{-1} for compositions across a $SrTi_{1-x}Fe_xO_{3-y}$ film deposited under an oxygen plasma. Dotted line at 100 µA shows point at which the onset potential was taken.

Figure 6-9 shows how the onset potential for the OER taken at 100 µA varies with x. The onset potential decreases significantly up to a composition where x = 0.5 whilst at higher x there is little further improvement. In fact on the tie-line sample the onset potential actually increases up to x = 0.66 before decreasing again. This trend is not seen on the sample deposited over a larger Sr range for which the OER onset continues to decrease with increasing x at compositions with x > 0.5 but with a shallower gradient.

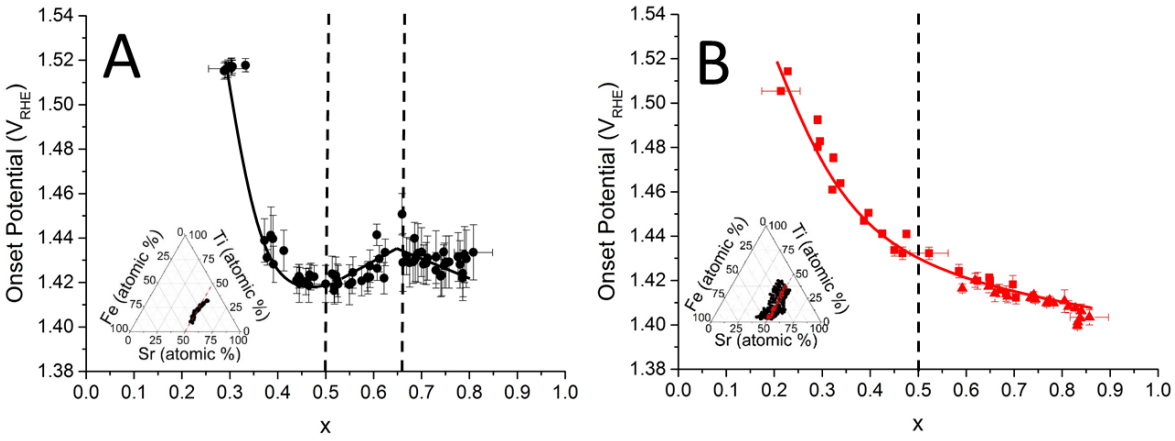

Figure 6-9: Variation in onset potential with varying Fe content, x, of $SrTi_{1-x}Fe_xO_{3-y}$ electrodes deposited by PVD at 650 °C under atomic oxygen.

Figure 6-10 shows how the maximum OER current density taken at 1.6 V changes with increasing x. The current density increases with increasing x up to x = 0.5 but as seen for the onset potential at x > 0.5 the trends differ between the sample deposited with compositions close to the tie-line and the sample deposited over a larger range of Sr compositions. For the tie-line sample the maximum OER current density decreases from x = 0.5 to x =0.66 before increasing again whilst the sample deposited over a larger Sr range continue to increase in current density until x = 0.66 before dropping off slightly and increasing again at x = 0.75.

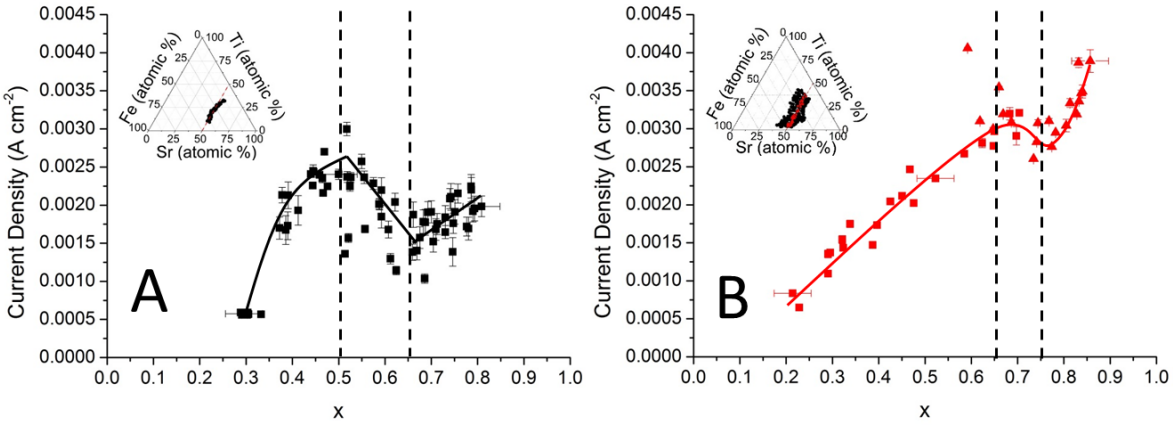

Figure 6-10: Variation in current density with varying Fe content, x, of $SrTi_{1-x}Fe_xO_{3-y}$ electrodes deposited by PVD at 650 °C under atomic oxygen.

6.2.1.3 Effect of A-site variation on OER activity

Figure 6-11 shows the oxygen evolution region of cyclic voltammetry on $Sr_nTi_{0.75-n}Fe_{0.5}O_{3-y}$ thin film electrodes deposited by PVD using an oxygen plasma source for compositions of varying Sr ratio. An increase in the proportion of Sr in the film from 45 at.% to 50 at.% resulted in a decrease in the over-potential for oxygen evolution and an increase in the current density. A further increase up to 55 at.% however showed no further improvement in the OER activity as measured by these factors. In fact increasing the Sr content further still to 60 at.% resulted in an increase in the over-potential for oxygen evolution and a decrease in the current density.

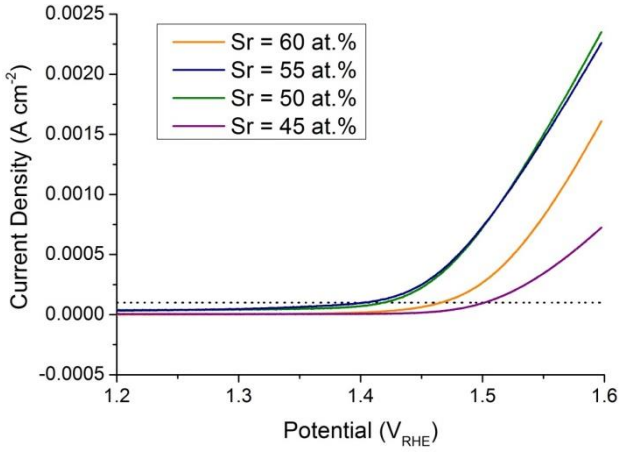

Figure 6-11: Cyclic voltammetry recorded in deoxygenated 0.1 M KOH at a sweep rate of 5 mV s^{-1} for compositions across a $SrTi_{1-x}Fe_xO_{3-y}$ film deposited under an oxygen plasma. Dotted line at 100 µA shows point at which the onset potential was taken.

Figure 6-12 shows the trends in OER onset potential and current density along the $Sr_nTi_{0.75-n}Fe_{0.25}O_{3-y}$ tie-line which was shown by the blue dashed line in **Figure 6-7**. The activity of the electrocatalysts towards the OER increases with increasing Sr content up to Sr = 50% as demonstrated by a decrease in the onset potential and an increase in the current density. It would appear therefore that Sr co-ordination enhances the ability of the Fe active sites to transfer electrons to the oxygen molecule in the OER mechanism. An explanation for this is the inductive effect of the Sr cation which withdraws electron density from anti-bonding 3d states and stabilises the Fe^{4+} oxidation state. Above the stoichiometric $SrTi_{0.5}Fe_{0.5}O_{3-y}$ composition the addition of Sr no longer improves OER activity and any structural distortion or additional phase which results from higher Sr contents does not therefore improve the electrocatalytic activity towards the OER.

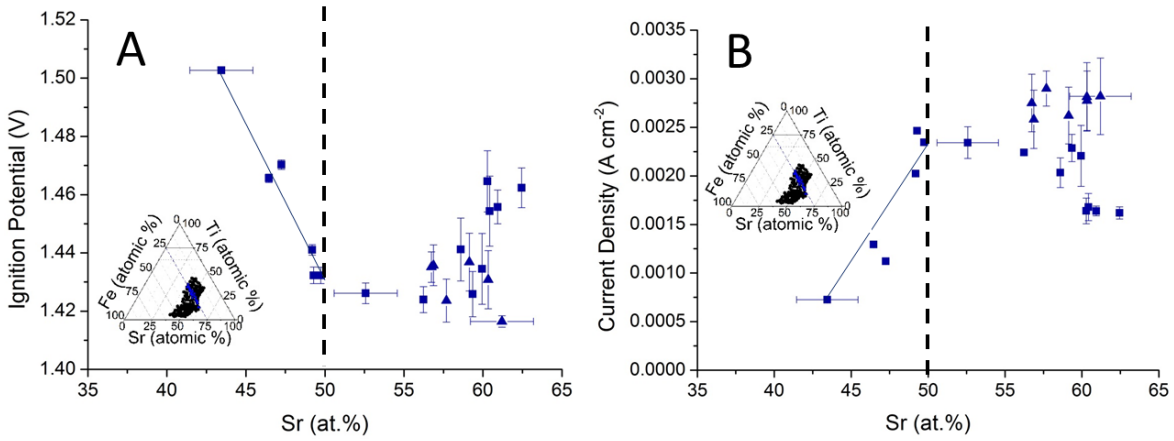

Figure 6-12: Variation in (A) onset potential and (B) current density with Sr at.%. Data obtained from cyclic voltammetry, recorded in deoxygenated 0.1 M KOH, on $SrTi_{1-x}Fe_xO_{3-y}$ electrocatalysts in the form of thin films deposited by PVD at 650 °C under atomic oxygen.

6.2.1.4 Effect of preparation conditions

The oxygen evolution region of cyclic voltammetry obtained for the $SrTi_{1-x}Fe_xO_{3-y}$ thin film electrodes deposited under molecular oxygen is shown for a range of values of x in **Figure 6-13**.

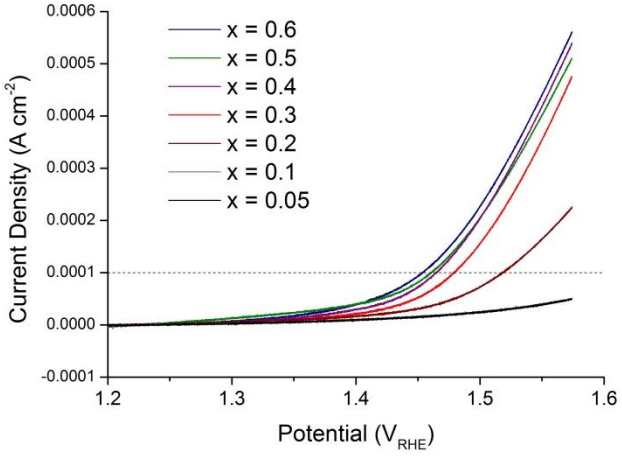

Figure 6-13: Cyclic voltammetry recorded in deoxygenated 0.1 M KOH at a sweep rate of 5 mV s^{-1} for compositions across a $SrTi_{1-x}Fe_xO_{3-y}$ film deposited under molecular oxygen. Dotted line at 100 µA shows point at which the onset potential was taken.

The activity also increases with Fe content, x, as confirmed by the onset potential for the oxygen evolution reaction which followed a similar trend as was seen for the films deposited under the oxygen plasma as shown in **Figure 6-14**. The current density, also shown in **Figure 6-14**, was however much lower for the films than for those deposited under the oxygen plasma which could be related to the poor conductivity observed for the molecular oxygen films.

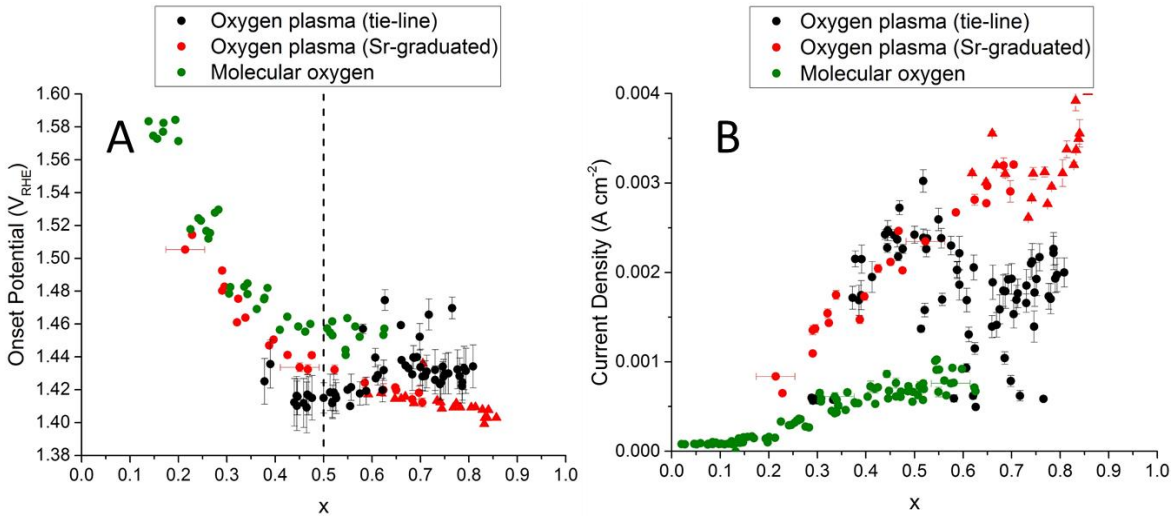

Figure 6-14: Plot to show variation in (A) the onset potential of the OER taken at a current density of 100 µA and (B) the current density taken at a potential of 1.6V with varying Fe content for $SrTi_{1-x}Fe_xO_{3-y}$ films deposited under an oxygen plasma and under molecular oxygen.

6.2.2 ORR activity

Cyclic voltammetry for the $SrTi_{1-x}Fe_xO_{3-y}$ films deposited under atomic oxygen measured in de-oxygenated 0.1 M KOH, shown in black, and oxygenated 0.1 M KOH, shown in red, are shown in **Figure 6-15**. There is evidence of oxygen reduction occurring after the reduction of the film. This is consistent with the proposed mechanisms for oxygen reduction shown in **Figure 6-16** in which the first step of the reaction is the displacement of the surface hydroxide ion by an oxygen molecule. It is assumed therefore that this requires the reduced surface and that the oxygen molecule is not able to displace the O^{2-} ion on the oxidised surface and the reaction cannot occur until after the surface reduction.

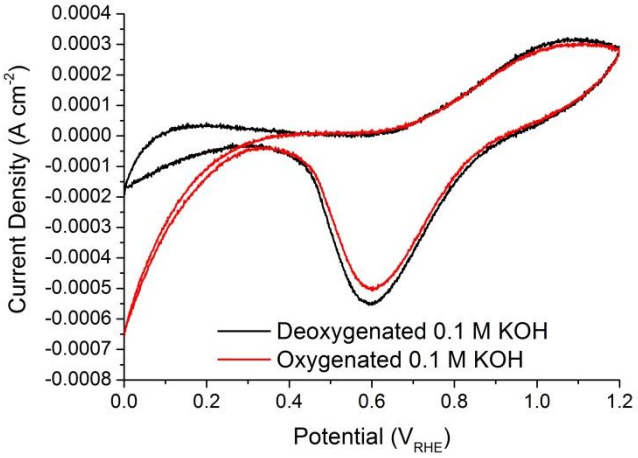

Figure 6-15: Cyclic voltammetry recorded in deoxygenated (black) and oxygenated (red) 0.1 M KOH at a sweep rate of 50 mV s^{-1} for an electrode of composition $SrTi_{0.5}Fe_{0.5}O_{3-y}$ deposited by PVD at 650 °C under atomic oxygen.

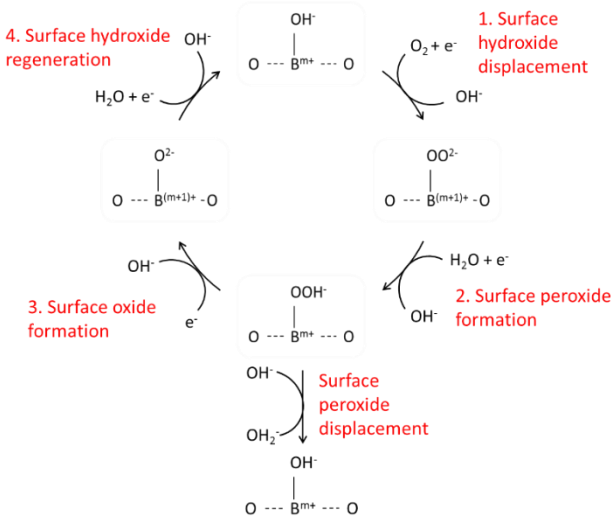

Figure 6-16: Proposed mechanism for the ORR on transition metal oxides with the perovskite structure.

In order to further investigate the mechanism of oxygen reduction on the STFO electrocatalysts the cyclic voltammetry was repeated with 5 mmol of hydrogen peroxide added to the 0.1 M KOH electrolyte. The solution was degassed by bubbling with Ar for 30 mins prior to cycling to remove dissolved oxygen. Despite the absence of oxygen in the solution the cyclic voltammetry was very similar to that observed for the oxygenated solution as shown for the $SrTi_{0.5}Fe_{0.5}O_3$ composition in **Figure 6-17**. This is consistent with the involvement of a peroxide intermediate in the ORR mechanism which is shown in **Figure 6-16** where the reduction of adsorbed peroxide occurs via steps 3 and 4. It is also possible that the surface peroxide could be displaced or desorbed from the surface as shown before re-adsorption and reduction occurs.

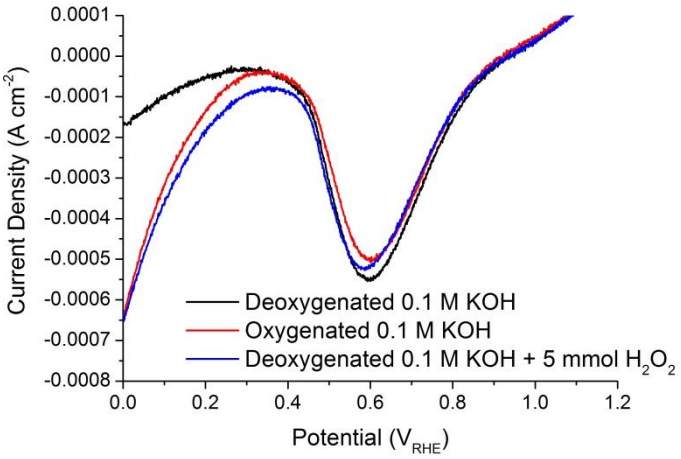

Figure 6-17: Negative sweep from cyclic voltammetry recorded in deoxygenated 0.1 M KOH (black), oxygenated 0.1 M KOH (red) and deoxygenated 0.1 M KOH with 5 mmol H_2O_2 (blue) at a sweep rate of 50 mV s^{-1} for an electrode of composition $SrTi_{0.5}Fe_{0.5}O_{3-y}$ deposited by PVD at 650 °C under atomic oxygen.

The $SrTi_{1-x}Fe_xO_{3-y}$ film deposited under molecular oxygen, which were highly unstable to electrochemical cycling, actually showed better ORR activity although there was still a large overpotential as shown in **Figure 6-18**. This provides further evidence that the ORR requires a reduced surface since the onset of the ORR still follows the surface reduction which occurs at a higher potential than for the films deposited using the oxygen plasma as discussed in **Section 5.2.5**. The reduction of oxygen on the molecular oxygen deposited films appears to occur by two waves, the first of which is assigned to the reduction of oxygen to peroxide (steps 1 and 2 in **Figure 6-16**) and the second of which is assigned to the reduction of the peroxide species (steps 3 and 4 in **Figure 6-16**). The intermediate peroxide may remain on the surface or be desorbed and re-adsorbed as discussed earlier.

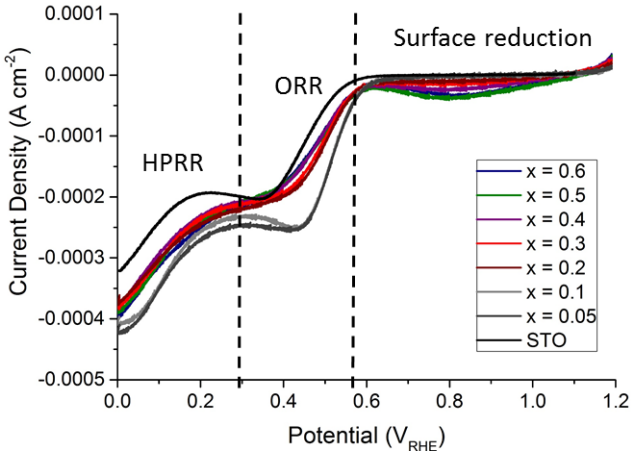

Figure 6-18: Cyclic voltammetry recorded in oxygenated 0.1 M KOH at a sweep rate of 50 mV s^{-1} for compositions across a $SrTi_{1-x}Fe_xO_{3-y}$ film deposited by PVD under molecular oxygen.

All of the STFO compositions show better ORR activity than the un-doped STO film deposited under the same conditions and shown by the black line in **Figure 6-18** as characterised both by a lower over-potential for the reaction and higher maximum current density.

The onset potential for the ORR decreases with increasing x up to x = 0.3 before reaching a plateau, as shown in **Figure 6-19**. This may be due to a decrease in electrode stability with increasing x as was discussed in **Section 5.2.5**

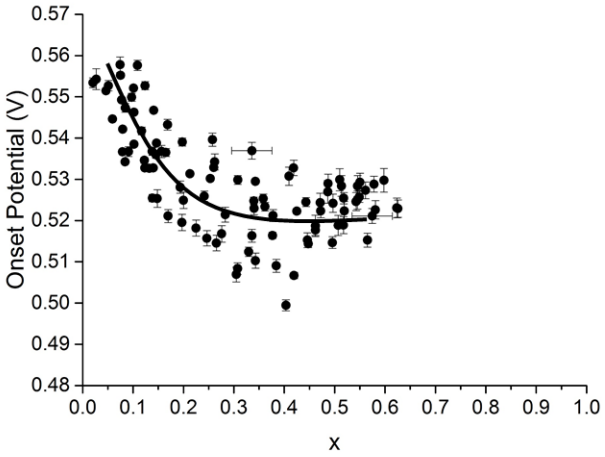

Figure 6-19 Plot showing variation in the onset potential for the ORR taken at a current density of 50 µA with varying Fe content for a $SrTi_{1-x}Fe_xO_{3-y}$ film deposited under molecular oxygen.

6.3 Conclusions

The electrocatalytic activity of the STFO perovskites towards oxygen evolution was found to be tuneable with composition. High OER activity, characterised by over-potentials as low as 0.2 V, was found for compositions with $x > 0.5$ and close to or higher than stoichiometric Sr content (Sr ≥ 50 at.%). The high activity in this region of compositional space was found to correlate strongly with poor stability of the electrode. High OER activity coupled with low electrode stability is considered to be an indicator that the OER proceeds by a mechanism in which the evolved oxygen originates partially from the perovskite lattice, leaving surface oxygen vacancies which are then replenished by hydroxide ions from the solution [48, 91, 179]. The removal and insertion of oxygen from the surface is assumed to weaken the perovskite structure and so cause the electrode dissolution.

The adoption of this mechanism relates to the ability of a material to support oxygen vacancies and has been predicted for $SrFeO_{3-y}$ [91]. The ability of the STFO materials to support oxygen vacancies has been reported in the literature and evidence of the reversible formation and quenching of oxygen vacancies with electrochemical cycling was presented in the previous chapter. For these reasons it seems entirely reasonable to assume that the OER is able to proceed by such a mechanism on the STFO surface.

Since most of the previously proposed activity descriptors for OER activity have been based on an adsorbate evolution mechanism their predictive power is limited in the case of a lattice oxygen participated mechanism. However, **Figure 6-20** shows a correlation between the equilibrium potential of the Fe^{3+}/Fe^{4+} surface redox reaction, discussed in the previous chapter, and the onset potential for the OER which is in agreement with previous reports [34]. The correlation was found with the redox process assigned to lower co-ordinate Fe sites which occurs immediately prior to the OER onset. It may be the case therefore that these sites are the most stable for the formation of the surface oxygen vacancies required for a lattice oxygen participated mechanism and are therefore the most active sites for the OER.

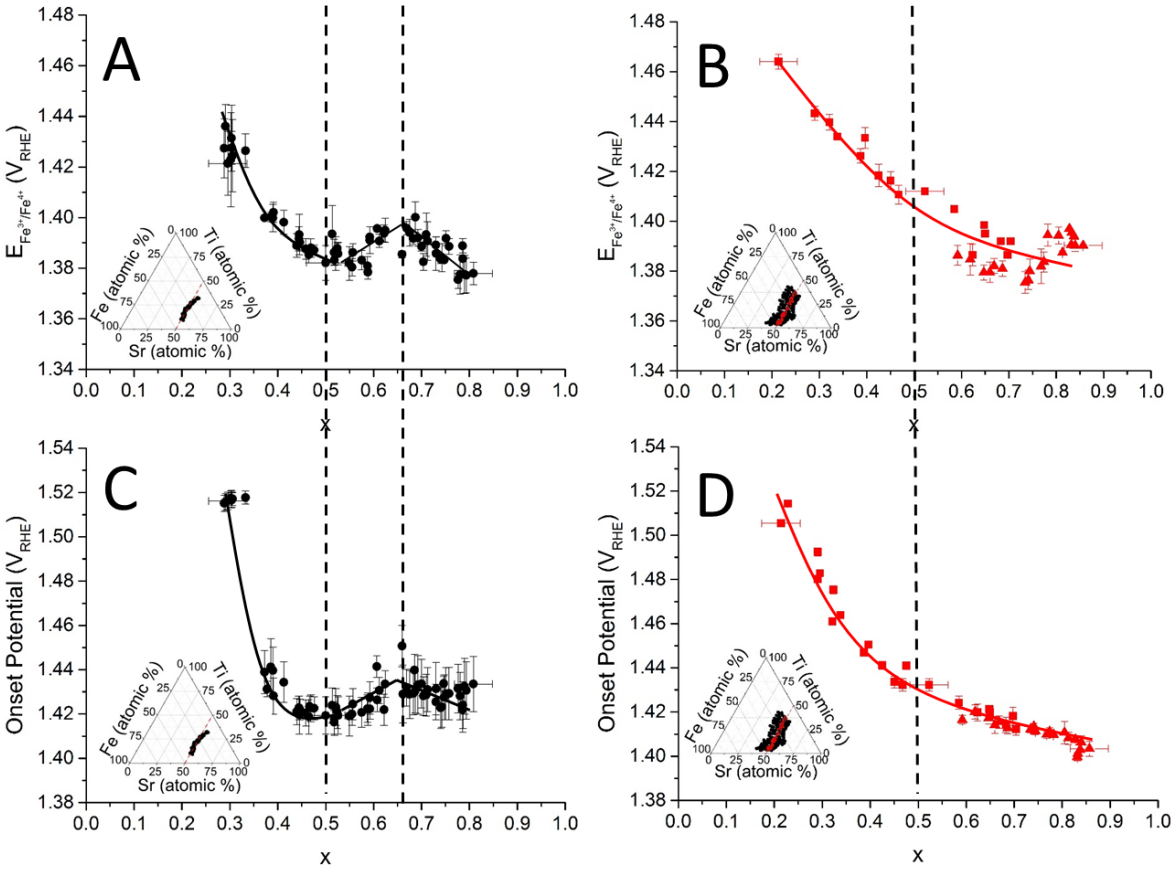

Figure 6-20: Plots showing correlation between the redox potential of the R1 redox reaction assigned to lower co-ordinate Fe sites (A and B) and the onset potential of the OER (C and D). Dashed lines are to guide the eye. Data shown is from (A and C) tieline sample with Sr = 50 ± 5 at.% and (B and D) two Sr graduated samples with Sr (shown by red dots and triangles).

The results are not however inconsistent with the proposed descriptors related to the valence electronic structure of the B-site cation since the Fe sites which are assumed to be the active sites for the OER have a +4 oxidation state under the oxidising conditions of the OER. The Fe^{4+} ions have d^4 valence electronic structure which is split into $t_{2g}^{3}\ e_g^{2}$ by the oxygen ligands. This e_g filling has been proposed to provide optimal B – O bond strength for both the OER and ORR. The increasing OER activity with increasing Fe content, x, along the $SrTi_{1-x}Fe_xO_{3-y}$ tie-line is therefore entirely consistent with this model as the number of active Fe sites is increasing.

The ORR did not occur on the STFO electrocatalysts until after the surface reduction reaction which is assumed to be due to the requirement of a hydroxylated surface in which oxygen is able to displace a hydroxide ion to adsorb at the B cationic site in the first reaction step. The reduced surface contains Fe in the Fe^{3+} oxidation state which has a d^5, $t_{2g}^{3}\ e_g^{1}$ electronic structure which would be predicted by the electronic descriptors to have low oxygen electrocatalytic activity due to weak oxygen binding.

Clearly no activity descriptor can provide absolute accuracy without consideration of other factors. The current work on the STFO system clearly demonstrates however that the chemical state of the reaction surface and in particular the redox electrochemistry is vitally important to the electrocatalytic activity.

For the STFO materials investigated in this work an optimal composition of $SrTi_{0.5}Fe_{0.5}O_{3-y}$ would be recommended as the OER electrocatalytic activity shows no significant increase above this point whilst there is a significant decrease in the electrode stability.

The STFO electrode array deposited in molecular oxygen showed a similar OER onset potential to the samples deposited using the oxygen plasma source, the current density was however much lower which is assumed to be due to the lower conductivity of this sample. The ORR activity of these samples is improved compared to the samples deposited using the oxygen plasma source which is assumed to be due to the greater availability of Fe^{3+} active sites. The sample deposited in molecular oxygen and subsequently annealed in oxygen showed no activity for the OER or ORR. This is consistent with the irreversibility of the Fe^{3+}/Fe^{4+} redox process identified by the large separation between the redox peaks and probably caused by a lack of electronic and oxide ion conductivity.

Chapter 7: Surface Studies on Fe doped STO

7.1 Introduction

Studies on the Fe dosed STO (110) surface by XPS, LEED, LEISS and electrochemical techniques were performed according to the methods described in **Section 2.5**. The aim of these studies was to investigate the mechanism of oxygen electrocatalysis on these surfaces and to identify descriptors for electrocatalytic activity by consideration of surface composition and structure. Studies on well-characterised single crystal surfaces allow for the separation of electronic and geometric factors which both contribute to the electrocatalytic activity.

Single crystal surfaces also act as a useful model system for which reference data for techniques such as XPS can be obtained on a well-characterised material without impurities. The effects of processes such as annealing can also be investigated with a high degree of control over the system. The information gained in these studies can then be used to aid in the analysis of data from the bulk system.

Several ordered reconstructions were obtained for the un-doped STO (110) surface by variation of the surface preparation methods. The composition and structure of these surfaces has been compared and the effects of Ar^+ ion sputtering and annealing have been considered. One STO (110) surface reconstruction was tested electrochemically in order to provide a baseline for the study of the effect of Fe-doping on the surface.

Various methods were attempted for incorporating a dosed layer of Fe into the surface of the STO (110) crystal and these have been discussed and compared with reference to evidence from the XPS and LEIS spectra as well as LEED images. Electrochemical data was obtained for two Fe doped surfaces.

7.1.1 Electrocatalysis on well-defined surfaces

Electrocatalysis can be considered as the influence of the electrode surface on the mechanism and rate of an electrochemical reaction. The electrocatalytic activity of a surface arises from the ability of the surface to adsorb at least one of the reactants or reaction intermediates and in doing so provide a lower energy pathway for the reaction. Often this involves the transfer of electrons between the surface and the adsorbed reactant(s) but electrocatalytic behaviour is not limited to this case. Since electrocatalysis is by definition a surface process, studies on well-characterised surfaces for which the surface structure has been determined can provide highly relevant mechanistic information.

This is especially important since the electrode surface can differ significantly from the bulk material, for example atoms in the surface may be under co-ordinated and there may be terminating groups not present in the bulk, for example –OH groups in the case of oxide materials. The surface of a poly-crystalline material consists of facets with varying crystallographic orientation containing different surface atoms. Each of these surface atoms has a different electronic structure and reactant binding energy determined by its chemical environment.

The electronic structure of the surface atoms is clearly of importance to the binding of reactants and reaction intermediates but the geometry of the surface can play an equal role in electrocatalysis. In some cases reactants adsorb preferentially at bridge sites between two atoms or in a hollow formed from three or more atoms and the presence of these particular atomic arrangements therefore enhances the electrocatalytic activity. Investigation and comparison of the electrocatalytic activity of different well-characterised surfaces of the same material can pin-point such active surface structures. The presence of a particular atomic arrangement may result in optimal binding of the reactants and high activity whilst surfaces which do not contain this arrangement of atoms show poor activity.

The ideal well-defined surface for study is that of a single crystal polished with a high-degree of accuracy to a single crystallographic orientation. However very few materials are commercially available in this form and so for convenience many studies consider thin films grown epitaxially onto single crystal substrates with similar crystal structure. In the case of perovskite oxide materials STO is commercially available and widely used for this purpose.

7.1.2 Perovskite surfaces

Lattice planes representing the three low-index crystallographic orientations of the perovskite crystal structure are shown relative to the cubic unit cell in Figure **7-1.** Investigation of the activity of these three surfaces could shed light onto the mechanism for the ORR and OER on perovskites and the requirements for an active electrode surface.

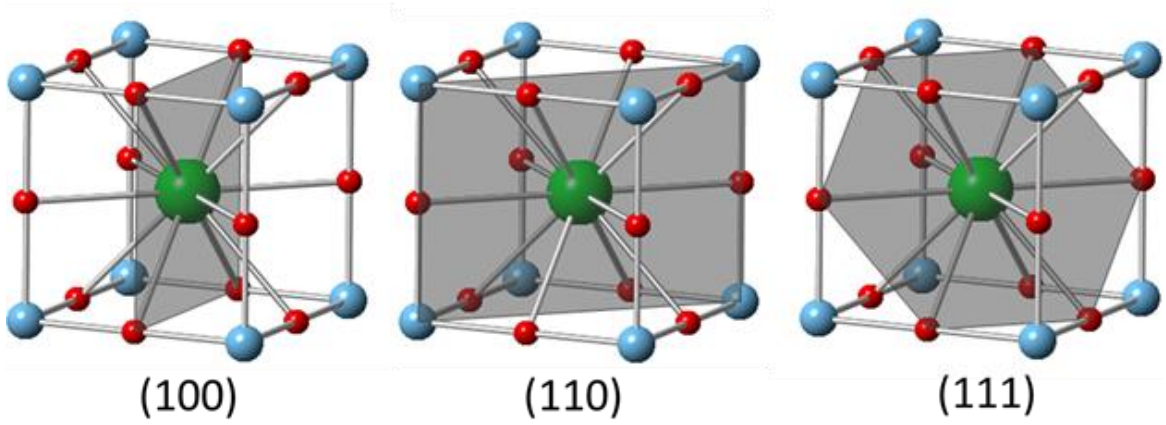

Figure 7-1: Lattice planes of a cubic ABO_3 perovskite such as $SrTiO_3$ drawn using CrystalMaker. The "A" atom is shown in green, the "B" atom in blue and the oxygen atoms in red.

Most studies on perovskite electrocatalysts have focussed on powder materials and there have been very limited studies thus far on the electrocatalytic activity of well-defined perovskite surfaces. Shao-Horn *et al.* [187] investigated (100), (110) and (111) crystallographic orientations of $La_{0.67}Sr_{0.33}MnO_3$ perovskite electrocatalyst films grown epitaxially by PLD on Nb-doped STO substrates. They found that the electrocatalytic activity towards oxygen reduction was comparable for all three surfaces concluding that there was either no surface specificity or that some form of surface reconstruction had rendered all the surfaces equivalent.

A similar study by Komo *et al.* [66] on $La_{0.8}Sr_{0.2}CoO_3$ perovskite epitaxial films grown on STO (100), (110) and (111) substrates by PLD did report a difference in ORR activity between the crystallographic orientations. They also reported an expansion in the crystal lattice as observed by ex-situ XRD following electrochemical cycling. The lattice expansion was assigned to the formation of oxygen vacancies during the ORR and was most apparent on the (110) orientated film which was also the most active for the ORR. A link between the formation of oxygen vacancies and ORR activity was therefore suggested, such a relationship has also been noted for the bulk perovskite materials [179] as discussed in Section 5.1.

Theoretical studies have attempted to determine the active sites for the ORR on $LaMnO_3$ surfaces by calculation of the O_2 binding energies [165]. Optimal binding energies were calculated for MnO_5^{eq} sites which are found only for the (100) surface, oxygen binding at all other sites was calculated to be either too weak or too strong for effective electrocatalysis. These calculations are based on an un-reconstructed surface which given the polarity of the (110) and (111) would be unrealistic in experimental studies especially where the surface has not been carefully prepared as with the aforementioned studies on epitaxial films. Since common reconstructions of the lower index (110) and (111) surfaces usually consist of micro-facetting in the [100] or [010] directions this could explain why these surfaces were active in the experimental studies.

7.1.3 $SrTiO_3$ surfaces

No studies considering the oxygen electrocatalysis of STO surfaces have been reported which is most likely due to the low activity of the stoichiometric un-doped material. Studies investigating oxygen adsorption on STO (100) determined weak physisorption of molecular oxygen onto hollow sites rather than the strong end-on chemisorption predicted for other perovskites including $SrFeO_3$ as well as the La-based perovskite discussed in the previous section. Modification of the STO surface is therefore required in order to strengthen the interaction between the surface and oxygen adsorbates.

STO is an insulator with a band gap of ~3.2 eV [57], it can however become semiconducting by reduction or doping (usually n-type although p-type is known [188]). This is of importance both to the technological application of the material but also to its study since many techniques including Scanning Tunnelling Microscopy (STM), LEED, XPS, Auger Spectroscopy (AES) and Reflection High Energy Electron Diffraction (RHEED) require a conductive sample. A schematic energy level diagram for untreated $SrTiO_3$ is shown in **Figure 7-2**. The Fermi level (E_F) is a thermodynamic quantity describing the total electrochemical potential and therefore expresses the work required to add an electron to the structure (or the work obtained by removing an electron).

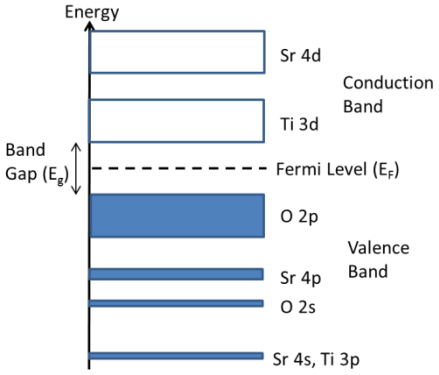

Figure 7-2: Schematic energy level diagram for $SrTiO_3$ showing the position of the band gap (E_g) and Fermi level (E_F).

In the case of untreated STO there are no electronic states close to E_F which would allow for the thermodynamically favoured transfer of electrons required for electrocatalysis.

N-type doping is achieved by substitution of trivalent ions such as Al^{3+} or La^{3+} in to the Sr^{2+} sites or by substitution of pentavalent ions such as Nb^{5+}, V^{5+} or Ta^{5+} into the Ti^{4+} sites [189]. These dopant ions donate electrons to the structure resulting in E_F lying close to the bottom of the conduction band and so providing electronic states for electron transfer. Whilst this results in an increase in the bulk conductivity, the surface layer becomes insulating when exposed to oxygen and requires UHV annealing to restore the conductivity [190].

The STO (100) surface is the most stable and widely studied of these low-index surfaces. When the crystal is viewed along the [100] direction it consists of alternating SrO and TiO_2 planes either of which can form the terminating surface and both of which are non-polar. UHV annealing of the surface was found to result in Sr segregation although the terminating surface is most often reported as TiO_2.

The (110) and (111) surfaces are both polar and much less well characterised in the literature. These surfaces are much more prone to reconstruction than the (100) surface due to the higher surface energy arising from their polarity [191-196].

7.1.4 STO (110) surface

Whilst the non-polar STO (100) surface has been the subject of extensive study, the polar (110) and (111) surfaces have been less well characterised. When viewed in the (110) orientation the structure consists of alternating layers of $(O_2)^{4-}$ and $(SrTiO)^{4+}$ Consequentially two different terminations exist for STO truncated in the (110) plane, these are shown in **Figure 7-3**. Whilst the smallest irreducible unit cell has the same length in the [100] direction for both layers, the length of the unit cell of the O-layer in the [110] direction is half that of the SrTiO layer. Since these surfaces are polar they are prone to reconstruct to more stable configurations and many reconstructions have been reported for both the O and SrTiO layers [191].

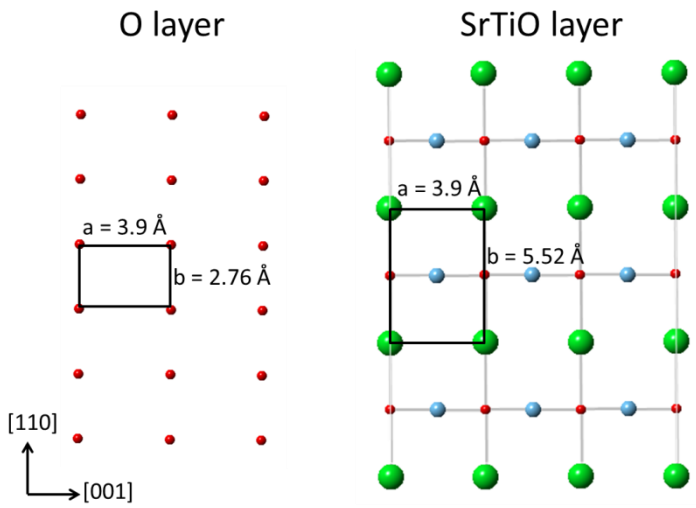

Figure 7-3: Structures of the two possible terminating layers of $SrTiO_3$ (110) [197]. Sr atoms are shown in green, Ti atoms are shown in blue and O atoms are shown in red. The unit cell is overlaid in black.

7.1.4.1 Structure of the STO (110) surface

A variety of reconstructed surfaces have been reported for STO (110) and it has been noted that the methods used for the preparation of particular reconstructions vary considerably between studies [198, 199]. The lack of consensus on the "recipe" for surface preparations is in part due to a lack of standardisation in the sample preparation techniques and in part due to the sensitivity of the surface to reconstruction. The surface preparation methods given in the following sections are therefore unlikely to be reproducible using other equipment.

Reconstructions are generally reported relative to the unit cell of the STO layer as represented in **Figure 7-4**, which is as such defined as the (1x1) cell. The unit cell is represented both in real space and in reciprocal space as observed in LEED experiments.

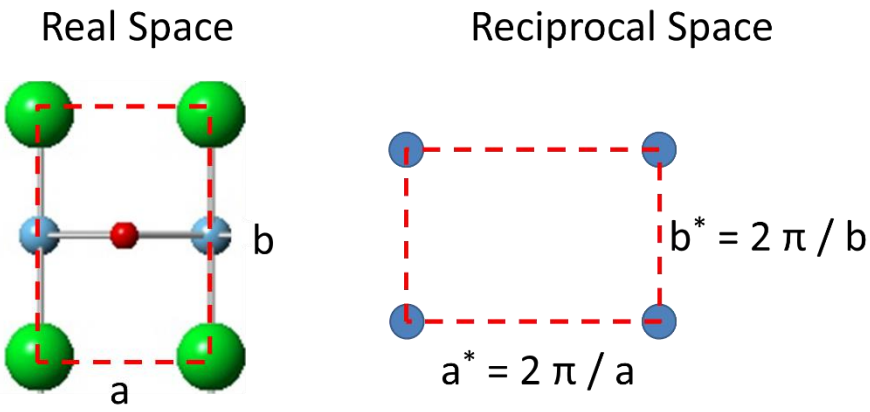

Figure 7-4: Schematic of unit cell of STO (110) in real and reciprocal space. The parameters of the unit cell are labelled a and b in real space and a* and b* in reciprocal space.

Several authors have reported STO (110) - (1x1) surface reconstructions [192, 196, 200] obtained by annealing the surface at 800 – 1000 °C under UHV conditions. STM [196] and atomic force microscopy (AFM) [192] images of the STO (110) – (1x1) surfaces revealed row-like micro-facet structures. Results from metastable impact spectroscopy (MIES) and the XPS data confirm the presence of reduced Ti at the surface and it has therefore been concluded that the surface consists of TiO_2 (100)/ (010) microfaceted planes formed from the loss of Sr from SrTiO. **Figure 7-5** shows how the loss of Sr from the surface does not change the size of the smallest irreducible unit cell and as such the reconstruction is labelled as (1x1). Brunen and Zegenhagen [196] and Gunhold *et al.* [192] however also reported a (1x2) reconstruction which formed at longer annealing times and the authors suggested was due to a further loss of TiO from the surface as shown in **Figure 7-5**. The smallest irreducible unit cell for this surface has the same dimensions in the [001] direction as the underlying STO bulk (110) termination but is twice as large in the [110] direction.

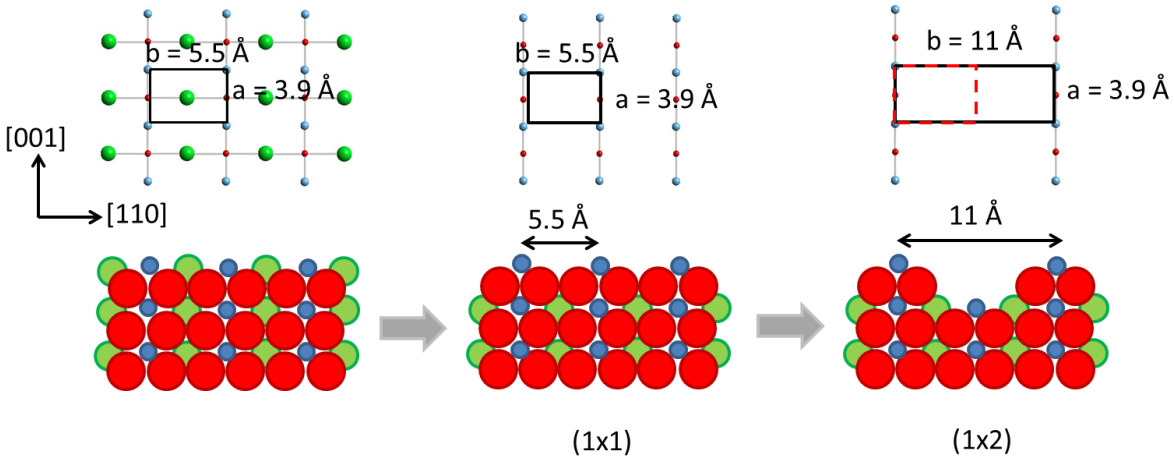

Figure 7-5: Schematic diagram showing the microfaceting of the STO (110) surface during UHV annealing. Sr cations are shown in green, Ti cations in blue and O anions in red. The clean unreconstructed surface is shown on the left, in the centre a slightly reduced surface displaying (1x1) periodicity resulting from loss of Sr is shown and right a fully microfaceted surface displaying (1x2) periodicity is shown.

Further reconstructions of STO (110) have been observed after annealing at higher temperatures or following annealing of Ar^+ sputtered surfaces. These surfaces are less well characterised and many groups have reported different reconstructions under similar annealing conditions. Brunen and Zegenhagen [196] observed (2x5), (3x4), (6x6) and (4x4) reconstructions in LEED experiments following annealing at temperatures between 1175 K and 1395 K for 2-20 h. AES measurements showed that the surface concentration of Sr relative to Ti increased with increasing anneal temperature. They also observed a (6x4) reconstruction following annealing of an Ar^+ sputtered surface. Most of their reported LEED patterns had missing spots and STM evidence suggests co-existing reconstructions.

Russell and Castell [193] observed a series of (nx1) reconstructions of the SrTiO layer ($2 \leq n \leq 6$) in LEED and STM experiments following UHV annealing between 1150 K and 1550 K for 2 h where n increased with annealing temperature. Density functional theory (DFT) calculations showed that these reconstructions were consistent with rings of TiO_4 tetrahedra where the ring size increases from a six membered ring for n = 2 to a 14 membered ring for n = 6 [201]. Cao *et al.* [197] also observed the 4x1 reconstruction of the STO layer albeit using different preparation methods consisting of annealing an Ar^+ sputtered surface at 1750 K for 5 minutes under UHV conditions. They also observed (2x8) and (1x10) reconstructions of the O terminating layer by employing larger sputter doses.

Russell and Castel proposed that the (4x1) microfacets were formed from TiO_2 which diffused from the bulk during annealing.

7.1.4.2 Conductivity of STO (110) surfaces

UHV annealing of STO surfaces has been found to introduce oxygen vacancies which improve the electronic conductivity by donation of electron density to the Ti 3d states. Henrich *et al.* [202] observed the creation of band-gap states in ultraviolet photo-emission and electron energy loss spectroscopy which they attributed to Ti^{3+}-[V], where [V] is an oxygen vacancy. The surface reconstruction has an effect on the electronic properties of the surface. The (1x1) reconstruction discussed above and presented in **Figure 7-5** has been found to exhibit surface metallicity which was attributed to Ti^{2+} electronic states. Further annealing of the surface which led to formation of the (2x1) reconstruction also led to the disappearance of these metallic states although band-gap states attributed to Ti^{3+} remained. It was concluded that the metallic states appeared due to the overlap of the Ti^{2+} electronic states, possible in the (1x1) surface but not possible in the (2x1) surface where the distance between the Ti microfacets is increased preventing the overlap of the Ti^{2+} states.

7.2 Results

7.2.1 XPS studies on the STO (110) surfaces

General observation arising from analysis of the XPS spectra of the STO (110) and Fe doped STO (110) surfaces will be discussed in the following sections. Summaries of the XPS data obtained for specific surfaces reconstructions will be given in **Sections 7.2.3** and **7.2.6**.

Data from XPS measurements on the STO (110) surfaces were fitted according to the same procedures used to fit the data obtained from the STFO thin films discussed in 3.2.5. The data obtained for the Sr 3d, Ti 2p, O 1s and C 1s binding energy regions for the as-received STO (110) crystal is shown in **Figure 7-6** alongside data obtained for the STO film deposited by PVD.

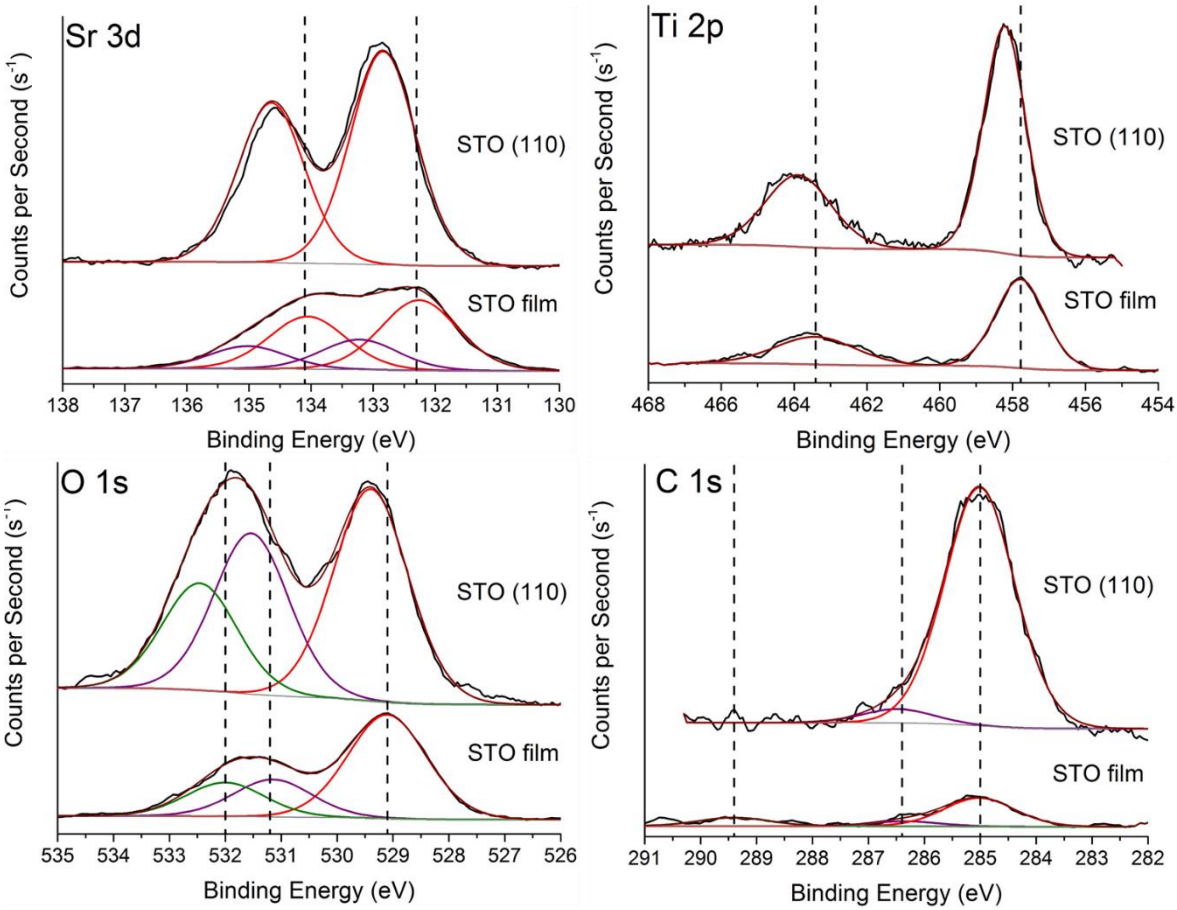

Figure 7-6: Sr 3d, Ti 2p, O 1s and C 1s XPS spectra taken on $SrTiO_3$ surfaces. Plots compare data obtained for the as-received STO (110) crystal with data obtained on STO film deposited by PVD for which the XPS data was discussed in **Section 3.2.5**.

As would be expected there is evidence of adsorbed surface species in the O 1s and C 1s spectra. In the O 1s spectrum the peak shown in red corresponds to oxygen in the perovskite lattice whilst those in purple and green correspond to surface OH and CO respectively. In the C 1s spectrum the peak due to adventitious carbon was observed at the expected binding energy of 285 eV with no charging effects. An additional small peak due to C-O was also present but no carbonate peak. A peak due to carbonates was observed at 289.4 eV for the STO thin film.

The surface composition obtained for the as-received STO (110) crystal was $Sr_{0.26}Ti_{0.18}O_{0.56}$. This composition includes only oxygen in the perovskite lattice, not OH or CO adsorbates. The surface is Sr enriched.

The STO (110) crystal was purchased with 0.5 wt.% Nb dopant in order to ensure the conductivity was high enough for study. As such there was no evidence of any charging effects. As discussed earlier, the data obtained for the thin film showed evidence of charging due to the insulating nature of STO and as such the C 1s peak due to adsorbed carbon which was measured at 287.2 eV was used to charge reference the data by adjustment of the binding energy scale to set the peak at the expected value of 285 eV.

A possible explanation for the binding energy shift seen between the two data sets in the Sr 3d, Ti 2p and O 1s regions in **Figure 7-6** is the error in the charge referencing used for the STO film since this can be affected by differential charging caused by the presence of insulating surface layers. The binding energies of the main peaks in the spectra are summarised in **Table 7-1**, the peak shifts relative to the STO film are included in brackets.

Surface Composition	Binding Energy / eV (BE shift / eV)		
	Sr $3d_{5/2}$	Ti $2p_{3/2}$	O 1s
$Sr_{0.26}Ti_{0.18}O_{0.56}$	132.84 (+ 0.58)	458.22 (+ 0.44)	529.40 (+ 0.39)

Table 7-1: Summary of data from XPS measurement of as-received STO (110). Binding energy shifts shown in brackets are given relative to data for the STO film deposited by PVD.

7.2.1.1 Surface contamination

As discussed earlier XPS measurements on the as-received STO (110) crystal confirmed the presence of surface contaminants. These are particularly apparent in the O 1s region where peaks due to OH and CO were identified and in the C 1s region where peaks due to CO and C were identified. The cleanliness of the prepared STO (110) surfaces was therefore assessed mainly by consideration of these regions. **Figure 7-7** shows the O 1s and C 1s XPS spectra of the as received STO (110) surface and the surface after cleaning by cycles of Ar^+ sputtering using a 3 KeV beam energy and 2 mA beam current and annealing at 650 °C in 1 x 10^{-7} mbar O_2.

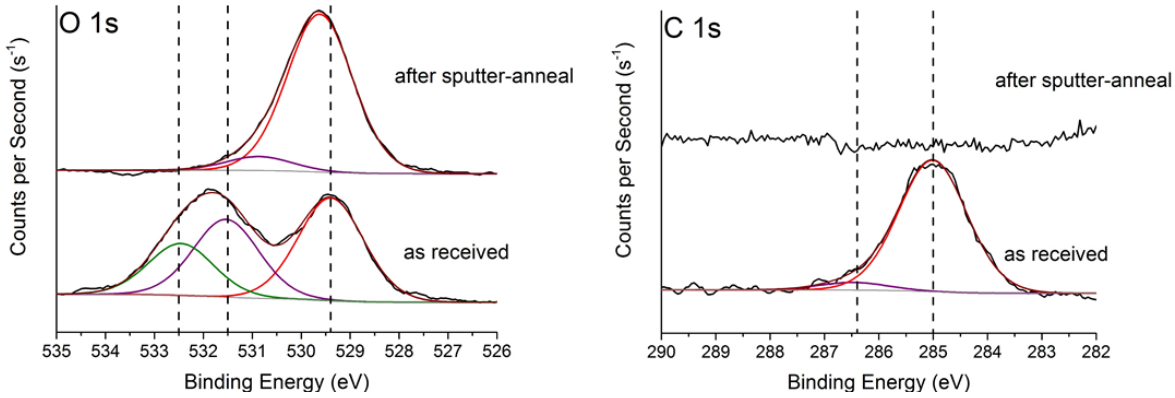

Figure 7-7: C 1s and O 1s XPS spectra taken before and after cleaning of STO (110) crystal by cycles of Ar^+ sputtering using a 3 keV beam energy and 2 mA beam current and annealing at 650 °C in 1 x 10^{-7} mbar O_2.

Following the cleaning procedure the composition of the surface as determined from comparison of the XPS peak intensities corresponded to the stoichiometric $SrTiO_3$. The binding energies of all the major peaks were also shifted positive. Since there was no C 1s peak it is not possible to determine if there are any charging effects which would cause such a positive shift in the peaks however since the Sr 3d peaks are shifted by a larger amount than the Ti 2p and O 1s peaks this is unlikely to be the whole explanation.

Surface Composition	Binding Energy / eV (BE shift / eV)		
	Sr $3d_{5/2}$	Ti $2p_{3/2}$	O 1s
$Sr_{0.20}Ti_{0.20}O_{0.60}$ ($SrTiO_3$)	133.29 (+0.45)	458.44 (+0.22)	529.62 (+ 0.22)

Table 7-2: Summary of data from XPS measurement of as-received STO (110). Binding energy shifts shown in brackets are given relative to data for the STO film deposited by PVD.

LEED indicated that the surface was not well ordered, whilst the 1x1 spots could be identified there were additional diffuse spots and streaking in both the [110] and [100] directions.

7.2.1.2 Effect of Ar^+ ion sputtering

Henrich *et al.* [202] investigated Ar^+ ion sputtering of STO surfaces using ultra-violet photoemission spectroscopy (UPS) and electron-energy loss spectroscopy (EELS). UPS spectra showed additional electronic states in the band-gap which were of d-electron character and as such were assigned to Ti^{3+} - [V] complexes where [V] represents an oxygen vacancy. These states disappeared when the surfaces were exposed to oxygen.

XPS spectra taken immediately following Ar^+ ion sputtering, at 3 KeV beam energy and 2 μA ion current, showed a split in the Sr 3d, Ti 2p and O 1s spectra. The split in the spectra was presumably caused by the two distinct environments created by the presence of both Ti^{3+} and Ti^{4+} ions. In addition a small amount of the Nb dopant was detected at the Ar^+ sputtered surface, whereas no Nb was detected when the surface was prepared by annealing. The removal of oxygen anions results in the donation of electrons to the perovskite lattice which provides additional inter-atomic screening of the core-hole in the final state and causes the slight shift in the spectra to lower binding energy. Electrons from the Nb dopant ions may also contribute to the screening.

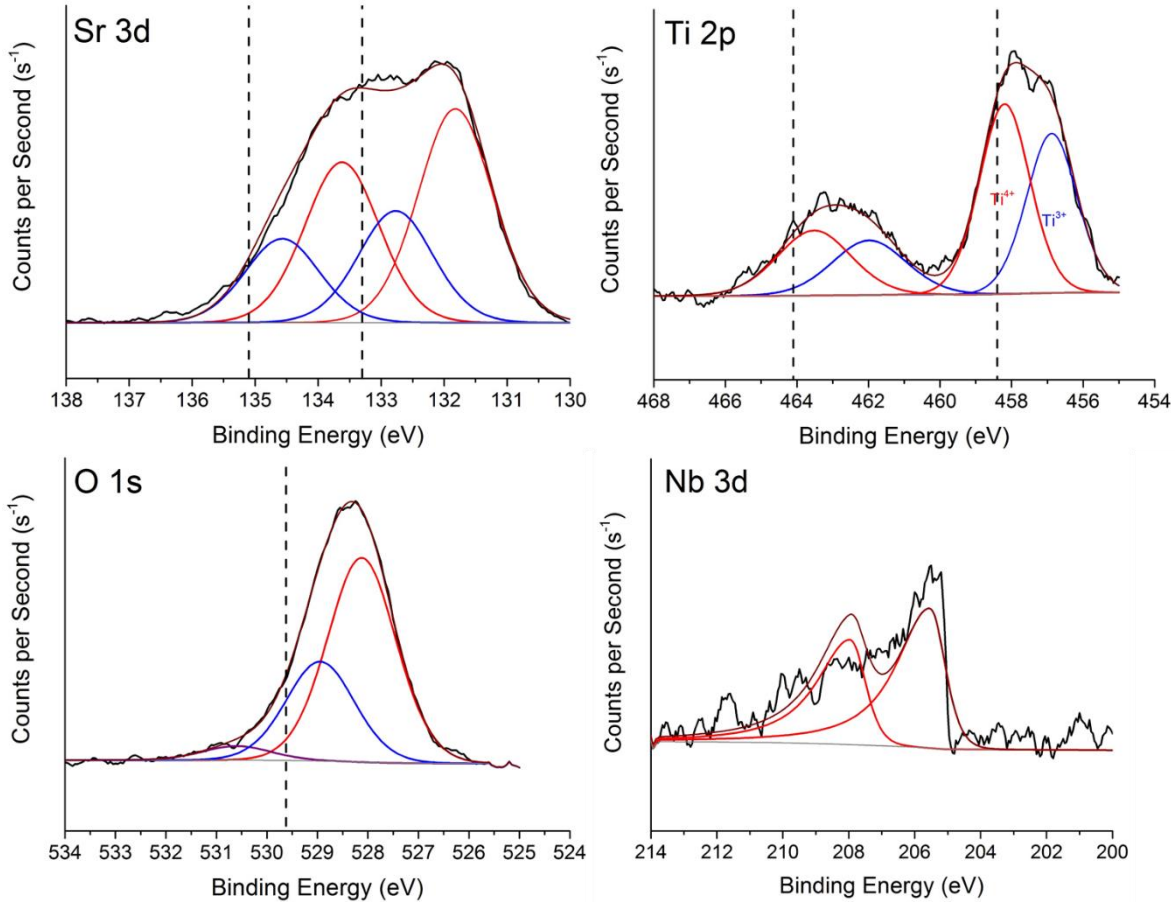

Figure 7-8: Sr 3d, Ti 2p, O 1s and Nb 3d XPS spectra taken on STO (110) following Ar^+ sputtering. Dotted lines show positions of major peaks in the spectra prior to the sputtering process.

The Ti^{3+}states were not stable to annealing and could be quenched both by annealing at 650 °C in 1 x 10^{-7} mbar O_2 and by UHV annealing at 700 °C. It is assumed that during UHV annealing oxygen from the bulk diffuses to replace the lost surface oxygen. Ti^{3+} states are stable at higher annealing temperatures > 800 °C under UHV conditions and this will be discussed in the next section.

7.2.1.3 Effect of annealing

UHV annealing of STO surfaces at ≥ 800 °C is known to lead to the formation of oxygen vacancies which increase the conductivity of the surface. UPS experiments on the annealed surfaces have shown an occupied electronic state in the band gap at 1.1 eV below the Fermi level. This state is mostly Ti 3d in character and has been attributed to Ti^{3+} ions associated with oxygen vacancies [202-205]. This was supported by XPS data which showed the main component of the Ti 2 $p_{3/2}$ peak, assigned to Ti^{4+}, accompanied by an additional peak at 2 eV lower binding energy which was assigned to the presence of Ti^{3+} ions near the surface [196]. UPS experiments on the reduced (110) and (111) STO surfaces [203, 206] also identified a metallic state which was not observed on the non-polar (100) surface. The metallic state was associated with the appearance of another peak in the Ti $2p_{3/2}$ spectrum at 4 eV lower binding energy than the main component which is assigned to the presence of Ti^{2+} near the surface [203].

Figure 7-9 shows XPS taken in the Ti 2p region following various annealing processes. It is assumed that since full oxidation of partially reduced Ti to the Ti^{4+} oxidation state required annealing in 1 x 10^{-5} mbar O_2 that this would be the minimum pressure required to oxidise Fe to Fe^{4+} to create a stoichiometric material.

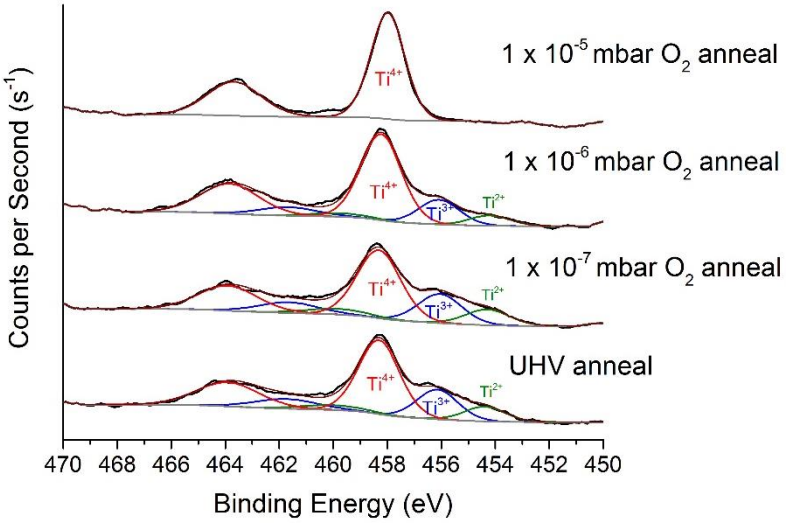

Figure 7-9: Ti 2p XPS spectra taken on the STO (110) surface following annealing at 1000 °C under UHV conditions and following subsequent anneals in 1 x 10^{-5}, 1 x 10^{-6} and 1 x 10^{-5} mbar O_2.

7.2.2 LEISS studies on the STO (110) surfaces

LEISS was also measured on the clean surface. This technique has a higher degree of surface sensitivity than XPS and is limited to only one or two atomic layers. Despite this no evidence of carbon was present and peaks due to Sr, Ti and O could be clearly identified as shown in **Figure 7-10**.

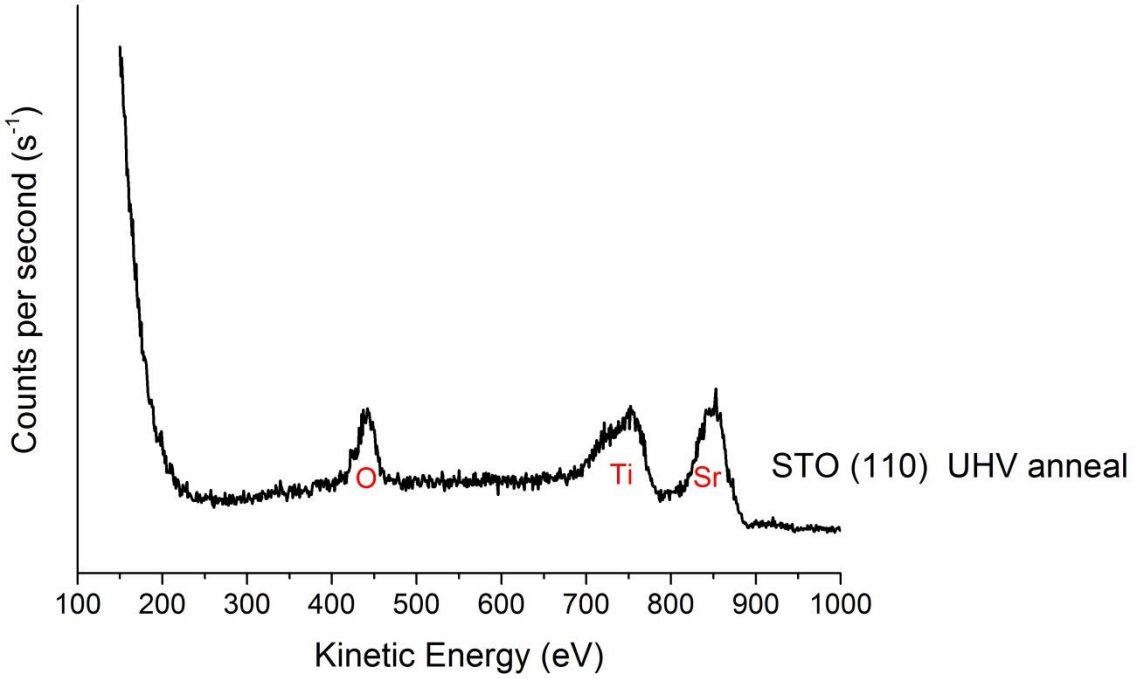

Figure 7-10: LEIS spectra taken after cleaning of STO (110) crystal by cycles of Ar^+ sputtering using a 3 keV beam energy and 2 mA beam current and flash annealing at 650 °C in 1 x 10^{-7} mbar O_2 and at 700 °C in UHV

7.2.3 Reconstructions of the STO (110) surface

Of all the surfaces discussed in the following sections only the STO (110) – (4x1) surface was tested electrochemically.

7.2.3.1 STO (110) – (4x1)

Further preparation of the clean surface, prepared as described in **Section 7.2.1.1**, by cycles of Ar^+ sputtering at 1 kV, 2 mA and annealing at 700 °C in UHV led to the formation of a 4x1 reconstruction, a LEED image of this surface is shown in **Figure 7-11**. The spots are quite diffuse and this may be an indication that the surface was not well-ordered in the reconstruction. The size of the unit cell was estimated from the distance between the spots in the LEED pattern by comparison with the distance between the spots in the LEED pattern of W (100) obtained at the same energy as described in **Section 2.5.5** The resulting lattice parameters were a = 15.4 ± 0.2 Å and b = 5.5 ± 0.2 Å. This compares favourably with the expected lattice parameters for a (4x1) surface based on the dimensions of the (1x1) unit cell reported by Cao *et al.* [197] which are a = 15.60 Å and b = 5.52 Å.

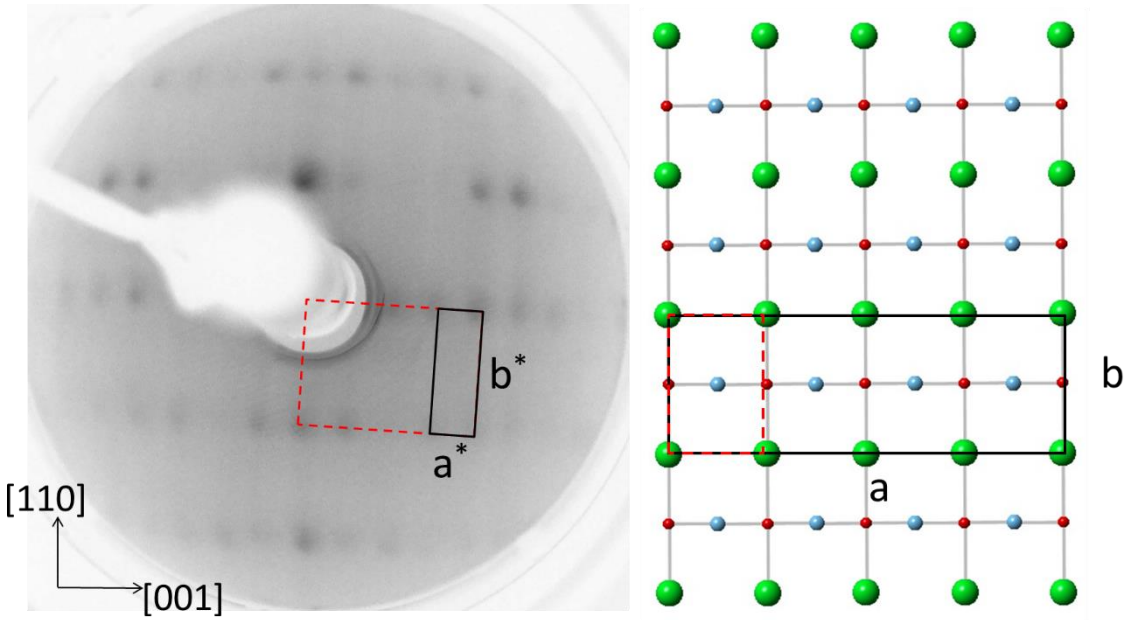

Figure 7-11: LEED image of the STO (110) – (4x1) surface taken at 100 eV shown alongside a schematic of the surface in real space. Black rectangle shows size of irreducible unit cell for this surface in reciprocal space imposed on the LEED image and in real space imposed on the surface schematic, where a and b are the dimensions of the unit cell and a^* and b^* are their reciprocals. Red-dashed box indicates the size of the (1x1) unit cell in both representations.

The 4x1 surface reconstruction was reported by Russell and Castell [193] following annealing between 1100 °C and 1175 °C for 2 hours and also by Cao *et al.* [197] following Ar^+ sputtering for 10 minutes (500 eV, 2 μA) followed by annealing at 1000 °C for 1 h. A higher annealing temperature and longer annealing times may therefore be required to improve the long-range order. However since this surface was clean according to XPS measurement and showed some degree of order it was tested electrochemically. Following the electrochemical testing, the 4x1 reconstruction could be regenerated by repetition of the same procedure of cleaning, as described in **Section 7.2.1.1**, and surface preparation described here.

Data from XPS measurements on the surface, presented in **Table 7-3**, shows the composition of the surface was stoichiometric with no evidence for enrichment of either Sr or Ti. The surface was also stoichiometric in oxygen despite the observation of a Ti^{3+} peak which would be indicative of Ti^{3+} - [V] at the surface. The binding energies of all peaks were shifted negative with respect to the values obtained for the as-received crystal. This would also be consistent with the creation of oxygen vacancies since the removal of oxygen would be expected to donate electrons to the crystal lattice resulting in an increase in screening and so a decrease in binding energy. An alternative explanation could be the removal of an insulating surface oxide layer which would cause charging and an upshift in the binding energy of all the peaks in the spectrum.

Surface Composition	Ti^{3+} / %	Binding Energy / eV (BE shift / eV)		
		Sr $3d_{5/2}$	Ti $2p_{3/2}$	O 1s
$Sr_{0.20}Ti_{0.20}O_{0.60}$	7.1	132.59 (-0.25)	457.77 (-0.43)	528.97 (-0.43)

Table 7-3: Summary of data from XPS measurement of STO (110) – (4x1). Binding energy shifts shown in brackets are given relative to data for the as-received STO (110) surface. The surface composition and proportion of Ti^{3+} were calculated from relative peak intensities.

Cao *et al.* [197] investigated the electronic structure of this surface using UPS and EELS and found no states between the top of the valence band and the Fermi level and low surface metallicity. This would be consistent with widely spaced micro-facets which do not allow for the overlap of Ti^{3+} or Ti^{2+} electronic states to form a band structure.

7.2.3.2 STO (110) – (3x1)

A (3x1) reconstruction of the STO (110) surface was obtained by Ar^+ sputtering at 3 kV, 2 mA and higher temperature annealing at 800 °C under UHV followed by cycles of Ar^+ sputtering at 1 kV, 2 mA and annealing at 700 °C in UHV. The LEED pattern for this surface is shown in **Figure 7-12**. The spots were more distinct than observed for the (4x1) reconstruction described above in 7.2.3.1. The lattice parameters determined from the LEED pattern were a = 12.2 ± 0.2 Å and b = 5.6 ± 0.2 Å. This is in reasonable agreement with the expected lattice parameters for a (3x1) surface based on the dimensions of the (1x1) unit cell reported by Cao *et al.* [197] which are a = 11.70 Å and b = 5.52 Å.

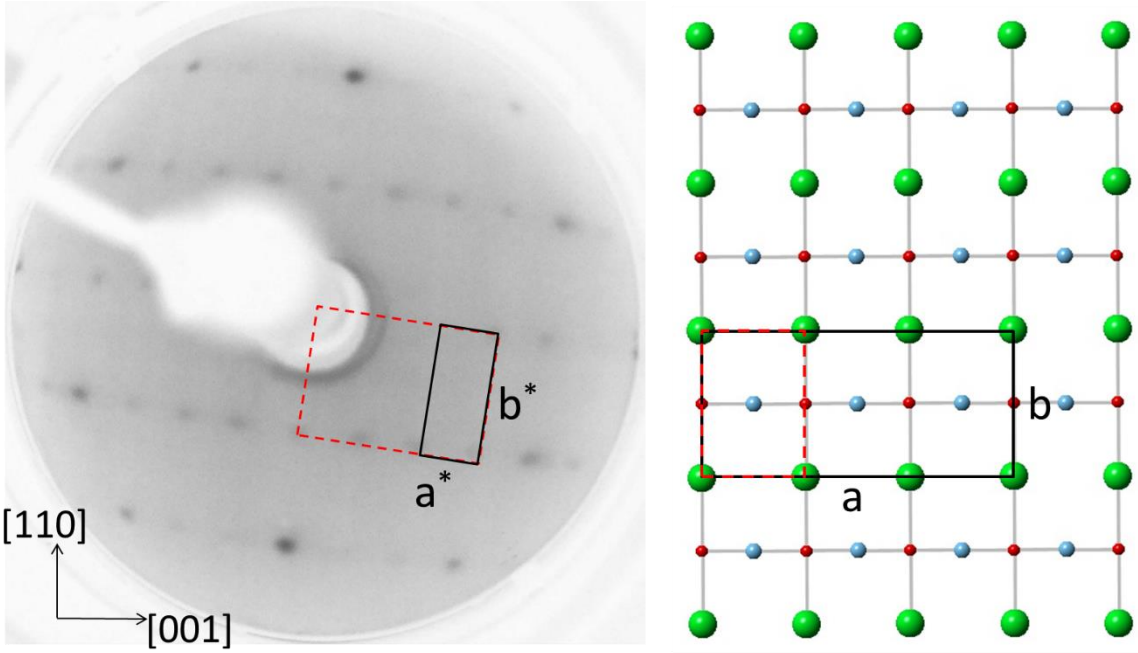

Figure 7-12: LEED image of the STO (110) – (3x1) surface taken at 100 eV shown alongside a schematic of the surface in real space. Black rectangle shows size of irreducible unit cell for this surface in reciprocal space imposed on the LEED image and in real space imposed on the surface schematic, where a and b are the dimensions of the unit cell and a^* and b^* are their reciprocals. Red-dashed box indicates the size of the (1x1) unit cell in both representations.

Russell and Castell [193] reported a 3x1 reconstruction prepared by annealing at 1150 K for 2 hours which when imaged by STM also contained regions of (1x4) reconstruction. None of the spots due to the regions of 1x4 were visible on the LEED images they presented since the STM images indicated that the 1x4 made up only a small proportion of the surface with only a few rows of this reconstruction adjacent to each other.The STO (110) – (3x1) surface was Sr enriched as shown in the summary of XPS data in **Table 7-4**. The microfacet structures observed at the surface of STO are generally assumed to be formed from TiO_2 and it has been suggested that the surface may be Sr enriched but remain TiO_2 terminated.

Surface Composition	Ti^{3+} / %	Binding Energy / eV (BE shift / eV)		
		Sr $3d_{5/2}$	Ti $2p_{3/2}$	O 1s
$Sr_{0.21}Ti_{0.17}O_{0.61}$	8.1	132.81 (-0.03)	458.13 (-0.09)	529.35 (-0.05)

Table 7-4: Summary of data from XPS measurement of STO (110) – (3x1). Binding energy shifts shown in brackets are given relative to data for the as-received STO (110) surface. The surface composition and proportion of Ti^{3+} were calculated from relative peak intensities.

7.2.3.3 STO (110) – (1x4)

A (1x4) reconstruction of the STO (110) surface was obtained by annealing at 800 °C for 2 h followed by a series of short, 2 minute, anneals at a higher temperature of 1000 °C. The LEED image of this surface is shown in **Figure 7-13**. The lattice parameters determined from the LEED pattern were a = 4.1 ± 0.2 Å and b = 21.3 ± 0.2 Å. This agrees with the expected lattice parameters for a (1x4) surface based on the dimensions of the (1x1) unit cell reported by Cao *et al.* [197] which are a = 3.90 Å and b = 22.08 Å.

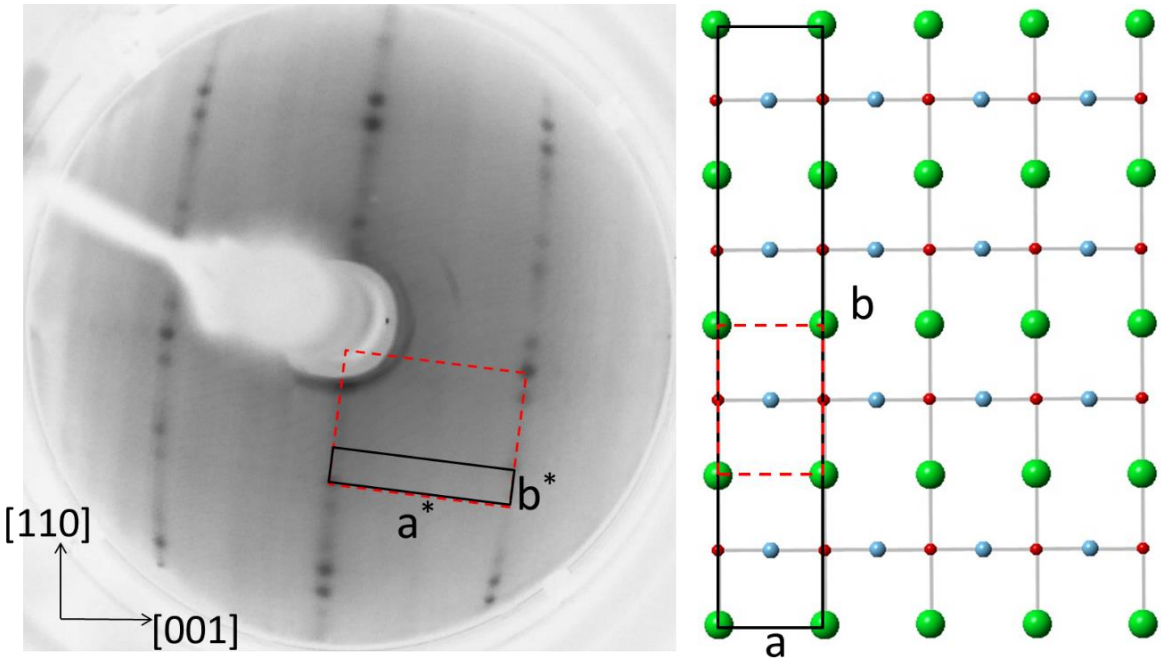

Figure 7-13: LEED image of the STO (110) – (1x4) surface taken at 100 eV shown alongside a schematic of the surface in real space. Black rectangle shows size of irreducible unit cell for this surface in reciprocal space imposed on the LEED image and in real space imposed on the surface schematic, where a and b are the dimensions of the unit cell and a^* and b^* are their reciprocals. Red-dashed box indicates the size of the (1x1) unit cell in both representations.

XPS data for this surface is summarised in **Table 7-5**. The surface composition was approximately stoichiometric and peaks due to both Ti^{3+} and Ti^{2+} were present in the spectra which is consistent with the higher temperature of the UHV anneal. The presence of the Ti^{2+} species in this case would not be expected to result in a metallic surface state since the overlap of the electronic states is prevented by a large separation of the Ti micro-facets as discussed in **Section 7.1.4.2**.

Surface Composition	Ti^{3+} / %	Binding Energy / eV (BE shift / eV)		
		Sr $3d_{5/2}$	Ti $2p_{3/2}$	O 1s
$Sr_{0.20}Ti_{0.21}O_{0.59}$	25.1 (8.9% Ti^{2+})	133.03(+0.19)	458.37 (+0.15)	529.56 (+0.16)

Table 7-5: Summary of data from XPS measurement of STO (110) – (1x4). Binding energy shifts shown in brackets are given relative to data for the as-received STO (110) surface. The surface composition and proportion of Ti^{3+} were calculated from relative peak intensities.

The peaks in the XPS spectra were shifted to higher binding energy than observed for the as-received surface which is contrary to the negative shift in binding energy observed for the (4x1) surface which was assigned to increased electron density in the lattice due to the creation of oxygen vacancies. Since there is an increase in reduced Ti species in this surface compared to the (4x1) surface which should correspond to an increase in oxygen vacancies an explanation is required. The most likely cause would be a decrease in the inter-atomic screening of the nuclear charge in the photo-ionised state caused by the atoms of the surface having fewer neighbouring atoms as a result of the micro-faceting. This was also the case on the (4x1) surface so it could either be considered that this has more of an impact when micro-faceting exists in the [110] direction or that the higher annealing temperature and longer annealing times used to prepare this surface result in a more complete ordering in the reconstruction. The latter seems more likely and is supported by the sharper LEED pattern.

7.2.3.4 STO (110) – (3x1)/(1x4)

The LEED pattern shown in **Figure 7-11** was obtained by annealing the surface at 800 °C for 2 h followed by annealing at 900 °C for 5 minutes. The pattern consists of spots due to both the (3x1) and (1x4) reconstructions discussed in **Section 7.2.3.2** and **Section 7.2.3.3**, respectively. Brunen and Zegenhagen [196] reported a (3x4) reconstructed surface obtained by annealing at 900 °C for 4 hours followed by annealing at 910 °C for 2 hours. It was later proposed by Russell and Castell [193] that this surface was in fact a (3x1)/(1x4) co-reconstruction. They obtained a 3x1 reconstruction by annealing at 875 °C for 2 hours which when imaged by STM contained regions of the (1x4) reconstruction. The LEED pattern obtained in this work appears to agree with this assessment as there are a large number of spots missing from the true (3x4) reconstruction.

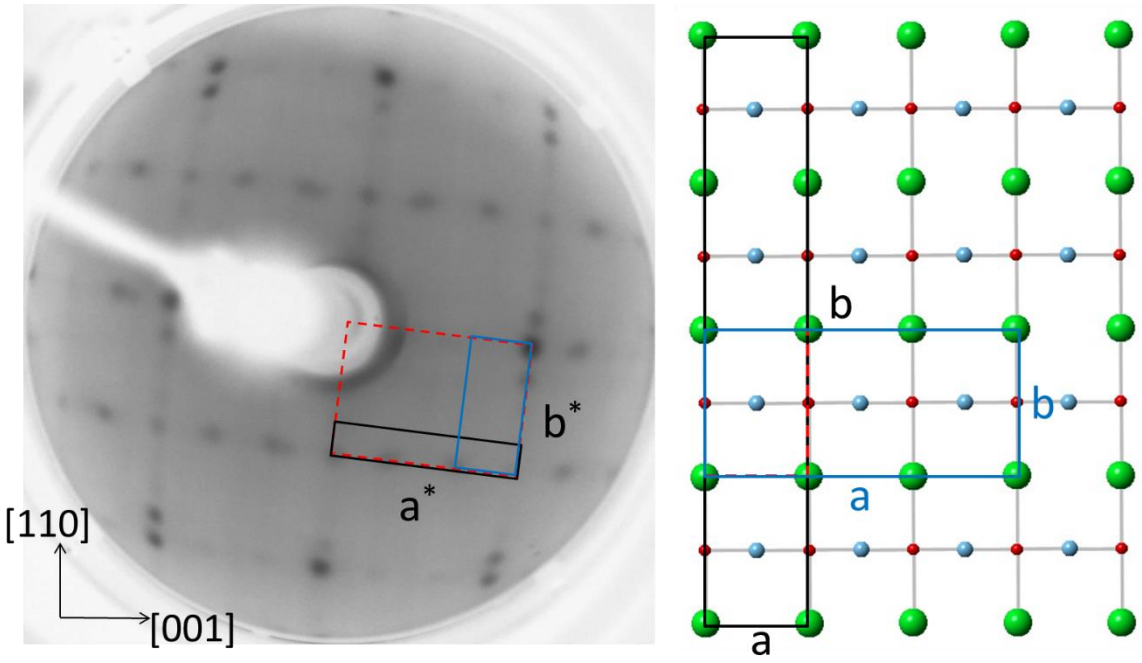

Figure 7-14: LEED image of the STO (110) – (3x1)/(1x4) surface taken at 100 eV shown alongside a schematic of the surface in real space. Blue and black rectangle shows size of irreducible unit cell for the (3x1) and (1x4) reconstructions of this surface, respectively. Unit cells are shown in reciprocal space imposed on the LEED image and in real space imposed on the surface schematic, where a and b are the dimensions of the unit cell and a^* and b^* are their reciprocals. Red-dashed box indicates the size of the (1x1) unit cell in both representations.

The lattice parameters determined from the LEED pattern for the (3x1) reconstruction, the unit cell for which is shown by the blue boxes in **Figure 7-14**, were a = 12 ± 0.2 Å and b = 5.5 ± 0.2 Å. This is in reasonable agreement with the expected lattice parameters for a (3x1) surface based on the dimensions of the (1x1) unit cell reported by Cao *et al.* [197] which are a = 11.70 Å and b = 5.52 Å. For the (1x4) reconstruction, the unit cell for which is shown by the black box in **Figure 7-14**, the determined lattice parameters were a = 3.9 ± 0.2 Å and b = 21.3 ± 0.2 Å. Again, this is in reasonable agreement with the expected lattice parameters for a (1x4) surface based on the dimensions of the (1x1) unit cell reported by Cao *et al.* [197] which are a = 3.90 Å and b = 22.08 Å.

A summary of the XPS data obtained for this surface is presented in **Table 7-6**. The surface was Sr enriched which is consistent with data for the (3x1) reconstruction reported in Section 7.2.3.2. The proportion of Ti^{3+} was between the values reported for the (3x1) and (1x4) reconstructions as would be expected. No peaks due to Ti^{2+} were identified. The shift in binding energy is difficult to interpret since a positive shift was seen for the Sr 3d peaks consistent with that seen for the (1x4) reconstruction whilst the Ti 2p and O 1s peaks were at similar positions as reported for the as-received STO (110) surface.

Surface Composition	Ti^{3+} / %	Binding Energy / eV (BE shift / eV)		
		Sr $3d_{5/2}$	Ti $2p_{3/2}$	O 1s
$Sr_{0.23}Ti_{0.16}O_{0.61}$	13	133.03(+0.19)	458.20 (-0.02)	529.35 (+0.04)

Table 7-6: Summary of data from XPS measurement of STO (110) – (3x4). Binding energy shifts shown in brackets are given relative to data for the as-received STO (110) surface. The surface composition and proportion of Ti^{3+} were calculated from relative peak intensities.

7.2.3.5 STO (110) – (2x1)/(1x4)

All of the aforementioned reconstructions were obtained by a final anneal at at least 700 °C under UHV conditions. Anneals in oxygen between 650 °C and 800 °C were also attempted but usually produced poorly ordered surfaces for which no clear LEED images could be obtained.

One reconstruction which was obtained on an oxygen annealed surface is shown by the LEED image in **Figure 7-15**. This surface was prepared by heating for 1 h in 1 x 10^{-5} mbar O_2 at 600 °C followed by heating in UHV at 400 °C for 2 minutes .The pattern appears to be a combination of the previously observed (1x4) reconstruction with a (2x1) reconstruction. As for the (3x1)/(1x4) reconstruction described in the previous section the number of spots is not sufficient for a (2x4) co-reconstruction and the surface was therefore assigned as a (2x1)/(1x4) reconstruction with regions of the surface reconstructed with each of the (2x1) and (1x4) periodicities. The spots were not bright and many are missing from the pattern indicating that the surface was not highly ordered in either reconstruction.

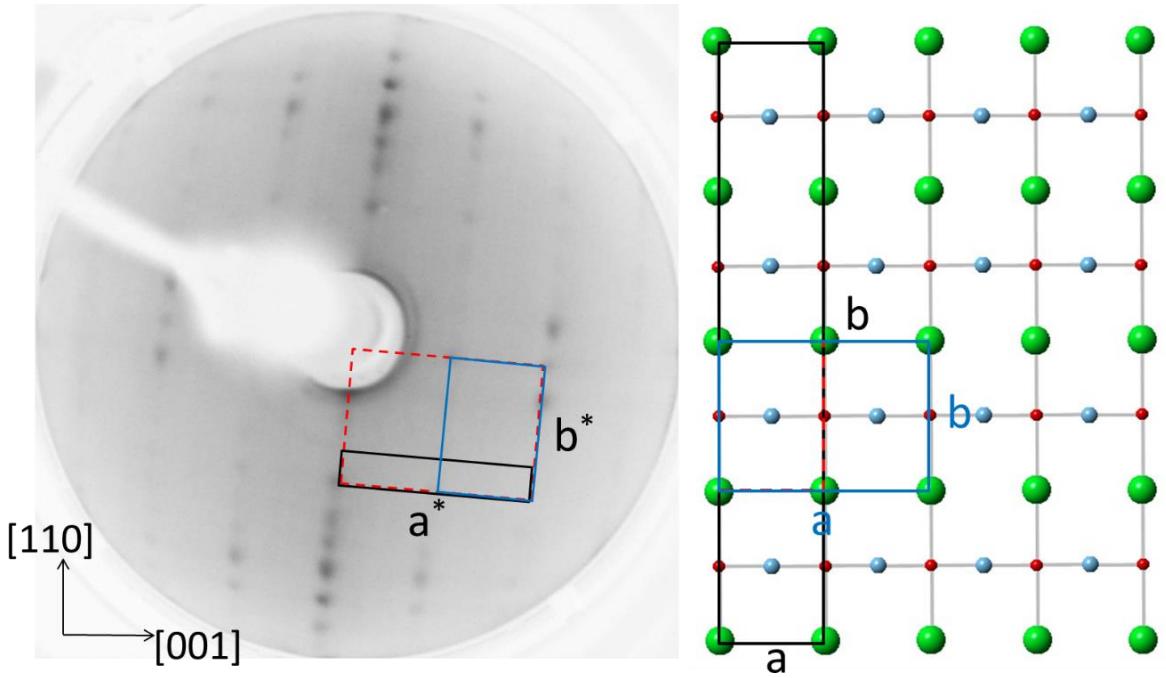

Figure 7-15: LEED image of the STO (110) – (2x1)/(1x4) surface taken at 100 eV shown alongside a schematic of the surface in real space. Blue and black rectangle shows size of irreducible unit cell for the (2x1) and (1x4) reconstructions of this surface, respectively. Unit cells are shown in reciprocal space imposed on the LEED image and in real space imposed on the surface schematic, where a and b are the dimensions of the unit cell and a^* and b^* are their reciprocals. Red-dashed box indicates the size of the (1x1) unit cell in both representations.

The LEED pattern appears similar to one previously reported by Cao *et al.* [197] although they assign the reconstruction to a (2x8) reconstruction of the O-terminating layer, which has a unit cell half the size of the STO layer. Since the true surface termination cannot be determined by these methods this is simply a difference in the chosen reference unit cell. They prepared the surface by Ar^+ ion sputtering followed by UHV annealing at 1475 °C for 5 minutes and argued that the high temperature of this UHV anneal caused diffusion of bulk oxygen to the surface thus forming the reconstructed O terminating layer.

The lattice parameters determined from the LEED pattern for the (2x1) reconstruction, the unit cell for which is shown by the blue boxes in **Figure 7-15**, were a = 7.7 ± 0.2 Å and b = 5.5 ± 0.2 Å. This is in reasonable agreement with the expected lattice parameters for a (2x1) surface based on the dimensions of the (1x1) unit cell reported by Cao *et al.* [197] which are a = 7.80 Å and b = 5.52 Å. For the (1x4) reconstruction the determined lattice parameters were a = 3.9 ± 0.2 Å and b = 21.3 ± 0.2 Å. Again, this is in reasonable agreement with the expected lattice parameters for a (1x4) surface based on the dimensions of the (1x1) unit cell reported by Cao *et al.* [197] which are a = 3.90 Å and b = 22.08 Å.

A summary of the XPS data for this surface is given in **Table 7-7**. The surface was approximately stoichiometric. No peaks due to reduced Ti species were observed which is consistent with annealing in an oxygen environment rather than under UHV conditions. The binding energy shifts are again difficult to interpret. Despite the lack of observation of reduced Ti species there may be a small proportion of oxygen vacancies present at the surface which cause the negative shift in the Ti 2p and O 1s spectra. It is also noted that for this surface and the (3x1)/(4x1) surface described in the previous section the shift in the Sr 3d spectrum differs from that for the Ti 2p and O 1s spectra which could be a result of a distinct inter-atomic screening environment for the TiO_2 micro-facets.

Surface Composition	Ti^{3+} / %	Binding Energy / eV (BE shift / eV)		
		Sr 3d 5/2	Ti 2p 3/2	O 1s
$Sr_{0.20}Ti_{0.21}O_{0.59}$	0	132.90 (+0.06)	458.04 (-0.18)	529.19 (-0.21)

Table 7-7: Summary of data from XPS measurement of STO (110) – (1x4). Binding energy shifts shown in brackets are given relative to data for the as-received STO (110) surface. The surface composition and proportion of Ti^{3+} were calculated from relative peak intensities.

7.2.4 XPS studies on the Fe doped STO (110) surfaces

The Fe dosed surface was measured using XPS and the Fe 2p spectrum is shown in **Figure 7-16**. Also shown is the result of a peak fitting process performed using an asymmetric lorenzian peak profile obtained on a standard metallic Fe sample by Biesinger *et al.* [122]. The binding energy of the $2p_{3/2}$ peak was 705.6 eV which is 1 eV below the value obtained by Biesinger *et al.* for the Fe standard. The reason for this is likely to be an interaction with the underlying STO surface. Since the peak profile was not obtained for a standard on this spectrometer a perfect fit would not be expected, however, the deviation of the spectrum from the expected fit could be evidence of the presence of a small amount of oxidised Fe or could also be an effect of the interaction with the STO surface. The coverage of Fe on the STO surface was estimated to be 5 ± 2 ML.

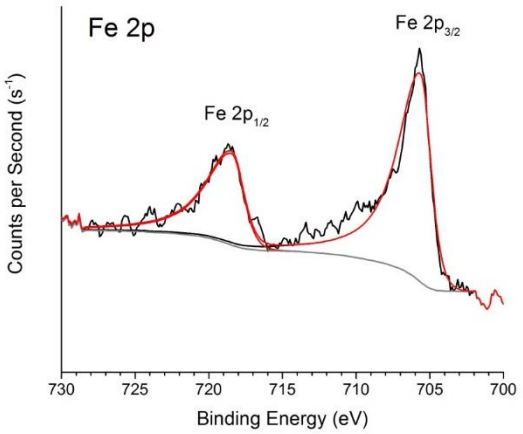

Figure 7-16: Fe 2p XPS spectrum of Fe dosed STO (110) surface. The red line shows the result of a peak fitting process performed using an asymmetric peak profile obtained for metallic Fe by Biesinger [122]

Annealing the Fe dosed STO (110) surface at 700 °C under UHV conditions was found to have no effect on the binding energy or shape of the peaks in the Fe 2p XPS spectra as shown by **Figure 7-7**. The peaks did decrease in intensity which would be consistent with the incorporation of Fe into the surface layers since XPS is a highly surface sensitive technique. It would also however be possible that a proportion of the Fe is simply lost from the surface during the annealing due to evaporation although this would not necessarily be expected at a temperature of 700 °C.

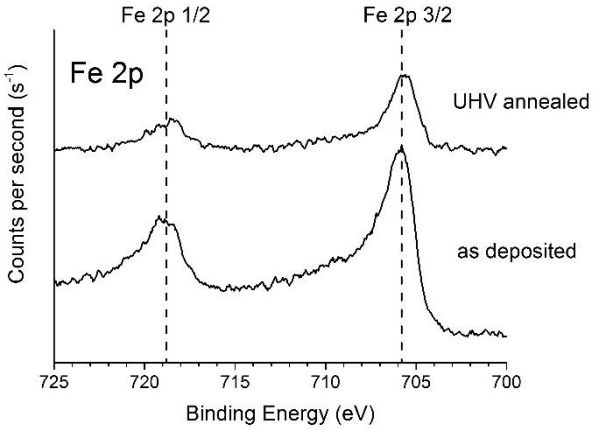

Figure 7-17 Fe 2p XPS spectrum of Fe dosed STO (110) surface as deposited and after annealing under UHV conditions at 700 °C.

Annealing the Fe dosed surfaces under an oxygen atmosphere resulted in the oxidation of the Fe at the surface which could be determined from the Fe 2p XPS spectra, examples of which are shown in **Figure 7-18** for the Fe dosed surface before and after annealing for 30 mins at 700 °C in 1 x 10^{-7} mbar O_2 and 1 x 10^{-5} mbar O_2. The peaks in the spectrum of the STO (110) – Fe surfaces annealed in1 x 10^{-7} mbar and 1 x 10^{-5} mbar O_2 are shifted to a higher binding energies, the Fe $2p_{3/2}$ peak appears at 709 eV and 710 eV respectively. This indicates that the increase in oxygen pressure from 1 x 10^{-7} mbar to 1 x 10^{-5} mbar leads to an increase in the oxidation state of the Fe species.

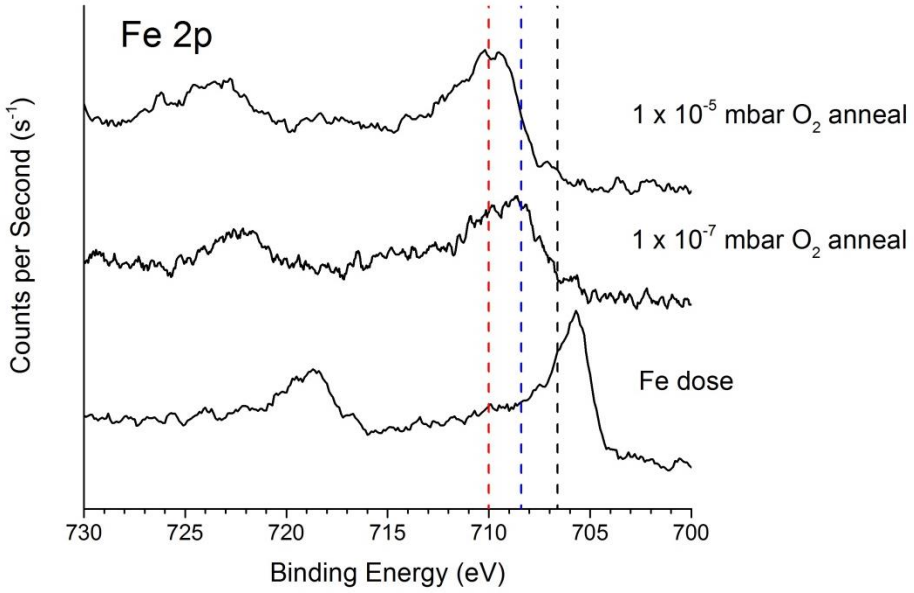

Figure 7-18: Fe 2p XPS spectra taken on Fe dosed STO (110) surfaces. Dotted lines show the positions of Fe $2p_{3/2}$ peaks in Fe metal (black), Fe^{2+} (blue) and Fe^{3+} (red) obtained by Biesinger *et al.* [122].

The Fe 2p XPS spectra of Fe oxides were discussed in detail in **Section 4.4.1.5** in relation to the analysis of the spectra from the STFO films. The binding energy of the Fe $2p_{3/2}$ peak was measured as 710 eV which is in agreement with literature studies on Fe^{3+} oxides but would also be consistent with a Fe^{4+} oxidation state due to the similarity in the electronic ground state of Fe^{4+} in the perovskite lattice. The surface annealed in 1 x 10^{-5} mbar O_2 which showed a binding energy for the Fe $2p_{3/2}$ peak of 710 eV and is therefore assumed to contain Fe in either or both of the Fe^{3+} and Fe^{4+} oxidation states.

The surface annealed in lower oxygen pressure of 1 x 10^{-7} mbar O_2 showed the Fe $2p_{3/2}$ peak at a lower binding energy of 709 eV and may therefore be consistent with Fe in a lower oxidation state, probably a mixture of Fe^{2+} and Fe^{3+} species, since the binding energy for the Fe $2p_{3/2}$ peak in Fe^{2+} oxides has been reported at 708.4 eV [122].

The peaks in both cases are much broader than those seen in the spectrum for the initial Fe dose which is an effect of multiplet splitting of the peak as well as the possible presence of mixed oxidation states as discussed in **Section 4.4.1.5**.

UHV annealing of the oxidised surfaces prepared in 1 x 10^{-5} mbar O_2 resulted in a shift of the Fe 2p XPS peaks to lower binding energy as shown in **Figure 7-19** which is assumed to result from the reduction of the Fe ions from Fe^{4+} or Fe^{3+} to a mixture of Fe^{3+} and Fe^{2+}.

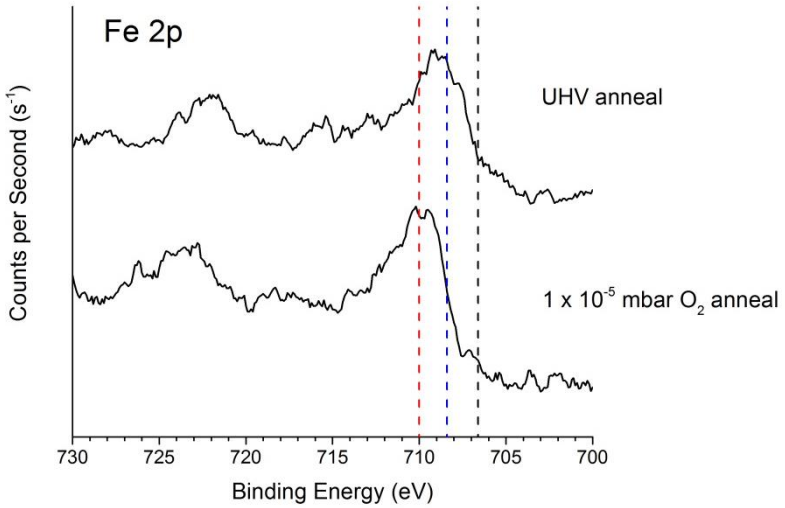

Figure 7-19: Fe 2p XPS spectra taken on Fe dosed STO (110) surfaces. Dotted lines show the positions of Fe $2p_{3/2}$ peaks in Fe metal (black), Fe^{2+} (blue) and Fe^{3+} (red) obtained by Biesinger *et al.* [122].

In the STFO thin film studies discussed in **Chapter 4** the addition of Fe to STO led to a decrease in the observed binding energies of the Sr 3d, Ti 2p and O1s XPS spectra. A similar decrease in binding energy of the major peaks was observed when the dosed Fe was incorporated into the perovskite lattice by oxygen annealing. **Figure 7-20** shows XPS spectra in the Sr 3d, Ti 2p and O 1s regions taken on the oxygen annealed STO (110) surface before Fe dosing, after Fe dosing and annealing in $1x10^{-5}$ mbar O_2 and after a subsequent UHV anneal.

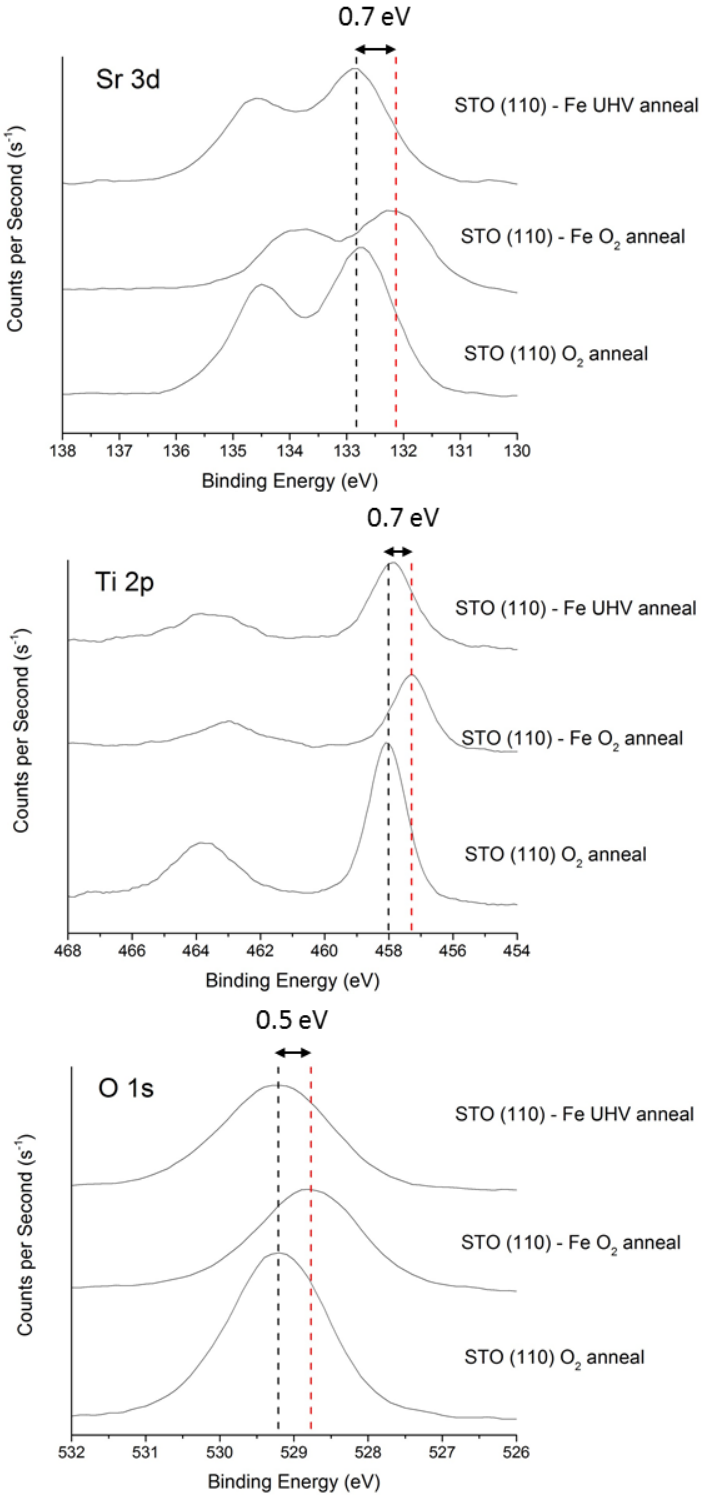

Figure 7-20 XPS spectra in the Sr 3d, Ti 2p and O 1s regions

The binding energy shift observed with Fe addition in the thin film studies was assigned to the addition of delocalised conduction electrons to the perovskite lattice which screen the nuclear charge and reduce the energy of the final photo-ionised state thus lowering the observed binding energy. The delocalised conduction electrons arise from the presence of Fe in the Fe^{4+} oxidation state and a lesser negative shift in binding energy was observed for films assumed to contain Fe^{3+}.

Again similar effects could be produced on the Fe-doped STO (110) crystal. **Figure 7-21** shows data obtained for binding energy shifts in the major peaks of the Sr 3d, Ti 2p and O 1s XPS spectra of Fe-dosed and annealed surfaces with increasing oxygen pressure. The binding energies are given relative to those obtained for the fully oxidised clean STO (110) surface which has been annealed for 30 mins in 1 x 10^{-5} mbar O_2. All annealing times were 30 minutes.

The data for the 1x 10^{-11} oxygen pressure is for surfaces annealed under UHV conditions which was performed after annealing in either 1 x 10^{-7} or 1 x 10^{-5} O_2 to ensure the Fe was incorporated into the surface. Similar binding energies were obtained for the surface annealed in 1 x 10^{-7} mbar O_2 both from annealing the as-deposited Fe-dosed surface and following annealing in 1 x 10^{-5} mbar O_2 and measurements from both experiments were included in the average values given.

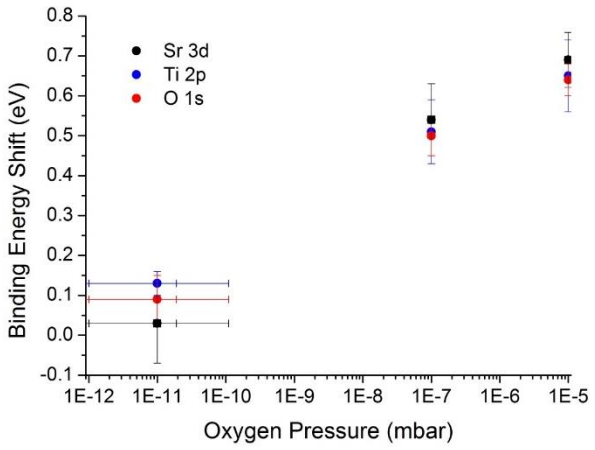

Figure 7-21: Shifts in the binding energy position of the Sr $3d_{3/2}$, Ti $2p_{1/2}$ and O 1s XPS peaks of Fe dosed surfaces following annealing in UHV, 1 x 10^{-7} mbar O_2 and 1 x 10^{-5} mbar O_2 measured relative to the peak positions in the STO surface following annealing in 1 x 10^{-5} mbar O_2. The oxygen pressure for the UHV anneal is an estimate from the mass spectrum and as such is subject to a large degree of error. The UHV anneal data is for a Fe-dosed surfaces which have first been annealed in an oxygen atmosphere (> 1 x 10^{-7} mbar O_2) to incorporate the Fe into the surface.

7.2.5 LEISS studies on Fe doped STO (110) surfaces

Evidence of Fe incorporation into the surface of the STO (110) crystal was also obtained using LEISS. LEISS spectra of the clean surface and Fe-dosed surface before and after annealing in 1 x 10^{-7} mbar O_2 are shown in **Figure 7-22**. The Fe peak can be clearly identified in the spectrum of the Fe-dosed surface and there is a significant decrease in this peak in the oxygen annealed surface. Given the high surface sensitivity of this technique this provides further evidence that the Fe is incorporated into the STO crystal upon annealing in an oxygen environment. Unfortunately no data was available for the UHV annealed surface to confirm the results of the XPS measurements which appeared to show some Fe incorporation.

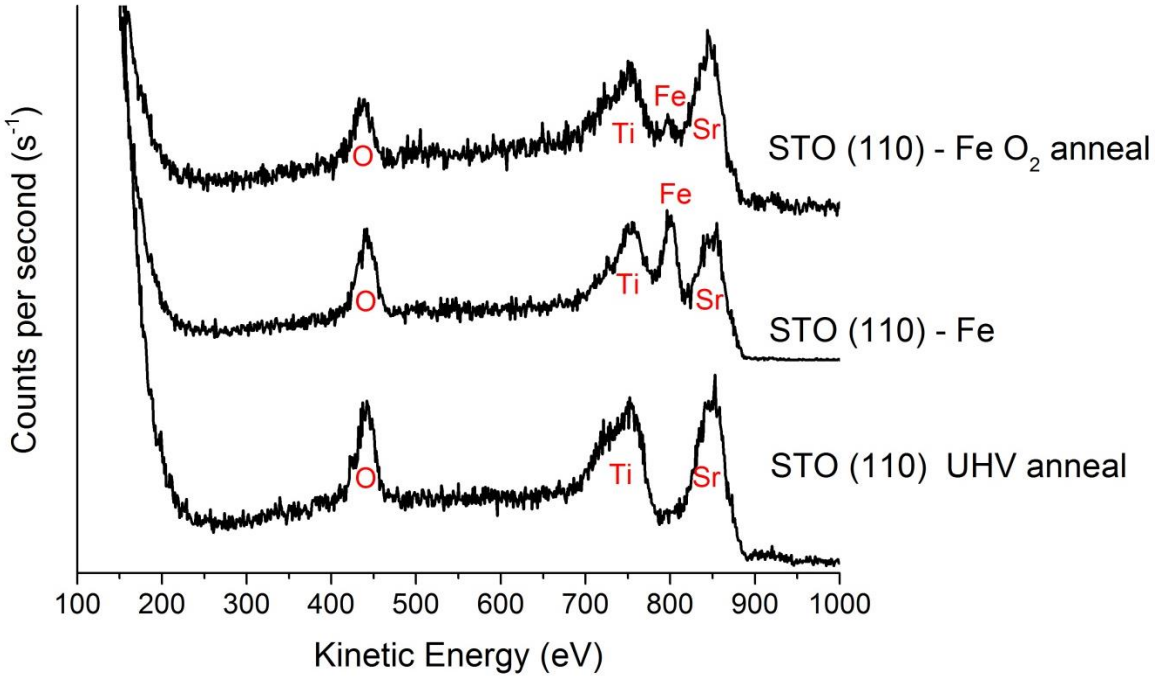

Figure 7-22: LEISS spectra taken on a UHV annealed STO (110) surface before and after deposition of 5 ± 2 ML of Fe and following subsequent annealing of the Fe dosed STO (110) under 1 x 10^{-7} mbar O_2.

7.2.6 Reconstructions of Fe doped STO (110) surface

7.2.6.1 Fe doped STO (110) – (3x1)

The 3x1 surface reconstruction, shown in **Figure 7-23**, was obtained by deposition of Fe onto the 4x1 reconstructed surface, described above in **Section 7.2.3.2**, followed by annealing at 700 °C in UHV for 2 min. The lattice parameters determined from the LEED pattern were a = 11.4 ± 0.2 Å and b = 5.5 ± 0.2 Å. This is in reasonable agreement with the expected lattice parameters for a (3x1) surface based on the dimensions of the (1x1) unit cell reported by Cao *et al.* [197] which are a = 11.70 Å and b = 5.52 Å.

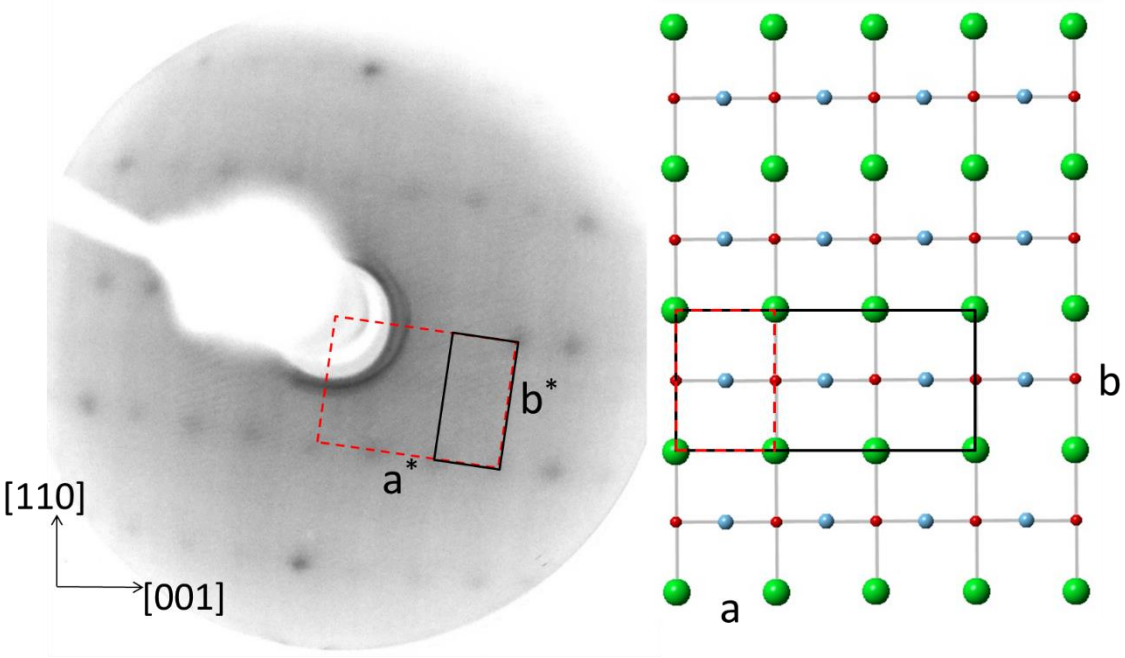

Figure 7-23: LEED image of the Fe doped STO (110) – (3x1) surface taken at 100 eV shown alongside a schematic of the surface in real space. Black rectangle shows size of irreducible unit cell for this surface in reciprocal space imposed on the LEED image and in real space imposed on the surface schematic, where a and b are the dimensions of the unit cell and a^* and b^* are their reciprocals. Red-dashed box indicates the size of the (1x1) unit cell in both representations.

The XPS data obtained for this surface is summarised in **Table** 7-8**.** The binding energy position of the Fe $2p_{3/2}$ peak is consistent with metallic Fe and so the incorporation of Fe into the perovskite lattice seems unlikely.

Surface Composition	Binding Energy / eV (BE shift / eV)			
	Sr $3d_{5/2}$	Ti $2p_{3/2}$	Fe $2p_{3/2}$	O 1s
$Sr_{0.17}Ti_{0.16}Fe_{0.11}O_{0.57}$	132.87 (+0.03)	458.03 (+0.19)	705.46	529.30 (+0.10)

Table 7-8: Summary of data from XPS measurement of Fe doped STO (110) – (3x1). Binding energy shifts shown in brackets are given relative to data for the as-received STO (110) surface. The surface composition was calculated from relative peak intensities.

7.2.6.2 Fe doped STO (110) – (2x1)

The clean 3x1 reconstructed surface described above in **Section 6.4.3** was prepared by Ar^+ sputtering (1 kV, 2mA emission current) before dosing with Fe, annealing at 600 °C in 1 x 10^{-7} mbar O_2 and flash annealing at 700 °C in UHV. The resulting surface reconstruction is shown in **Figure 7-24** and appears to be a (2x1) reconstruction although there are a number of missing spots which indicate that the surface is not well ordered in the reconstruction. The lattice parameters determined from the LEED pattern were a = 7.8 ± 0.2 Å and b = 5.7 ± 0.2 Å. This is in agreement with the expected lattice parameters for a (2x1) surface based on the dimensions of the (1x1) unit cell reported by Cao *et al.* [197] which are a = 7.80 Å and b = 5.52 Å.

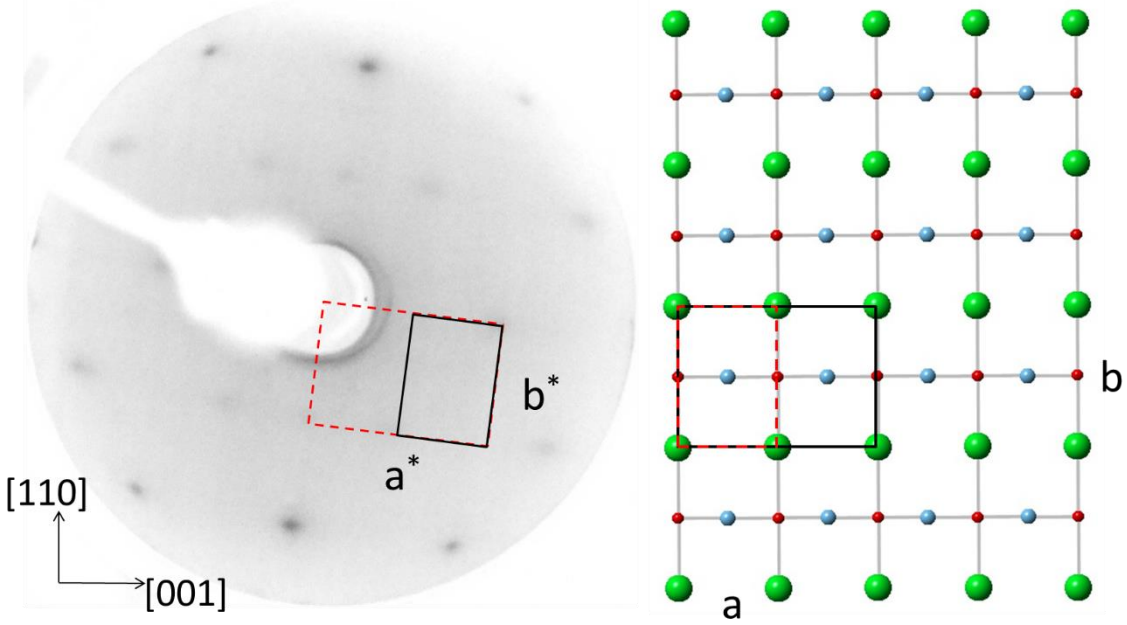

Figure 7-24: LEED image of the Fe doped STO (110) surface taken at 100 eV shown alongside a schematic of the surface in real space. Black rectangle shows size of irreducible unit cell for this surface in reciprocal space imposed on the LEED image and in real space imposed on the surface schematic, where a and b are the dimensions of the unit cell and a^* and b^* are their reciprocals. Red-dashed box indicates the size of the (1x1) unit cell in both representations.

A summary of the XPS data for this surface is given in **Table 7-9**. The position of the Fe $2p_{3/2}$ peak is consistent with oxidised Fe [102, 207]. There is a negative shift in the binding energy which could provide evidence that the Fe is incorporated in to the surface and is able to provide inter-atomic screening as was discussed in **Section 7.2.4**.

Surface Composition	Binding Energy / eV (BE shift / eV)			
	Sr $3d_{5/2}$	Ti $2p_{3/2}$	Fe $2p_{3/2}$	O 1s
$Sr_{0.16}Ti_{0.16}Fe_{0.08}O_{0.59}$	132.74 (-0.10)	457.87 (-0.35)	708.97	529.23 (-0.17)

Table 7-9: Summary of data from XPS measurement of Fe doped STO (110) – (2x1). Binding energy shifts shown in brackets are given relative to data for the as-received STO (110) surface. The surface composition was calculated from relative peak intensities.

7.2.7 Electrochemical Measurements

The methods used to obtain electrochemical data from the prepared STO (110) surfaces were outlined in **Section 2.5.7** Electrochemical data was obtained for a clean STO (110) – (4x1) surface, a STFO (110) – (3x1) surface and a STFO (110) – (2x1) surface.

Limited data is available due to problems with making electrical contact to the single crystal. Two connections to the crystal were available connecting either through a connection to the crystal mount or to the thermocouple connection which was inserted into the hole in the crystal itself. Unfortunately repeated annealing of the crystal particularly in an oxygen environment caused passivation of the components of the crystal mount disrupting the electrical contact.

7.2.7.1 STO (110)

The clean STO surface displaying the 4x1 reconstructions was transferred to the electrochemical chamber (EC) for measurement. **Figure 7-25** shows cyclic voltammetry obtained in Ar purged 0.1 M KOH. There is no evidence of any activity towards oxygen evolution up to 1.6 V_{RHE}. The main feature of the voltammetry was cathodic current at low potential which has no corresponding anodic feature and so is assumed to correspond to the reduction of a species in the solution rather than a reduction of the surface. This could arise from the reduction of H_2O, the reduction of residual oxygen in the solution of the onset of H_2 evolution.

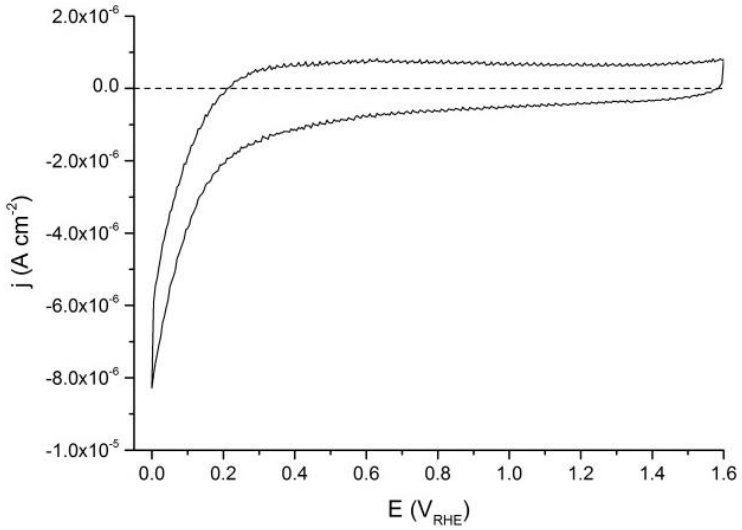

Figure 7-25: Cyclic voltammogram of STO (110)-(4x1) surface in Ar purged 0.1 M KOH using a sweep rate of 50 mV s^{-1}. Second cycle shown.

Figure 7-26 shows a comparison of the cyclic voltammetry of the STO (110) –(4x1) surface with that of the STO thin film prepared by PVD at 650 °C under molecular oxygen. The comparison has been made with the STO film prepared in molecular oxygen since the STO (110) surfaces were also prepared using molecular oxygen. Since the thin film sample will have a larger surface roughness than the single crystal, which has near atomic flatness, a surface roughness factor of 10 has been applied to the geometric current density data from the thin film sample to allow for a more direct comparison.

The CV taken on the STO film electrode showed an anodic peak at high potential, assigned to the onset of the OER, which was not present in the voltammetry taken on the STO (110) – (4x1) sample. The cathodic peak at low potential seen for the STO (110) – (4x1) sample was not present in the voltammetry of the STO film electrode. The small amount of cathodic current could be due to residual oxygen in the solution or a surface reduction at a minority of sites.

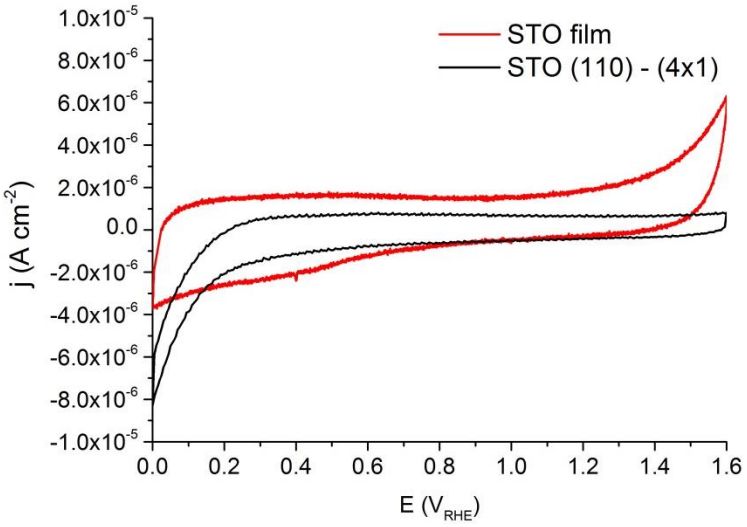

Figure 7-26: Comparison of cyclic voltammograms taken in Ar purged 0.1 M KOH using a sweep rate of 50 mV s^{-1} of STO (110)-(4x1) surface and STO thin film electrode deposited by PVD at 650 °C in molecular oxygen. CVs shown are second cycles.

Cyclic voltammetry taken on the STO (110) – (4x1) surface in oxygenated 0.1 M KOH is shown in **Figure 7-27**. There is a much larger cathodic current which is assigned to the electrocatalysis of oxygen reduction on the surface.

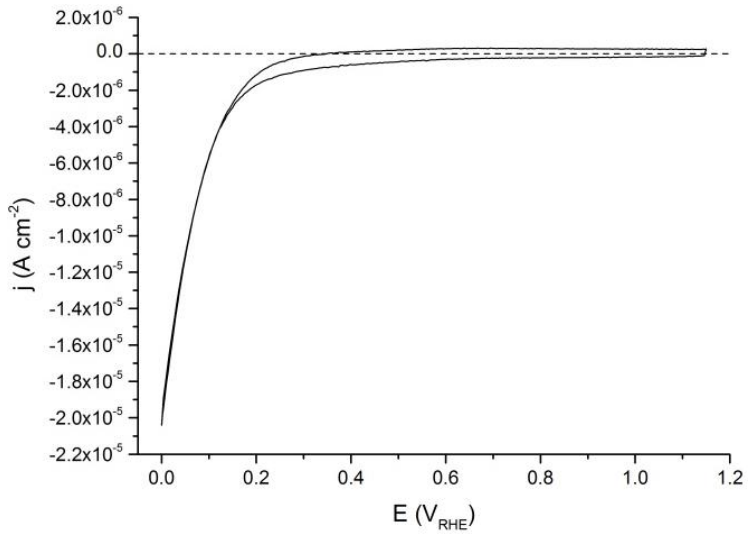

Figure 7-27: Cyclic voltammogram of STO (110)-(4x1) surface in O_2 saturated 0.1 M KOH using a sweep rate of 20 mV s^{-1}. CVs shown are second cycles.

When the voltammetry is compared to that obtained on the STO film prepared in molecular oxygen, as shown in **Figure 7-28**, there is a large difference between the onset of the reduction on the two samples. In addition the onset potential of the reduction on the STO (110) – (4x1) surface appears to coincide with the onset of a second reduction wave in the voltammetry of the STO film.

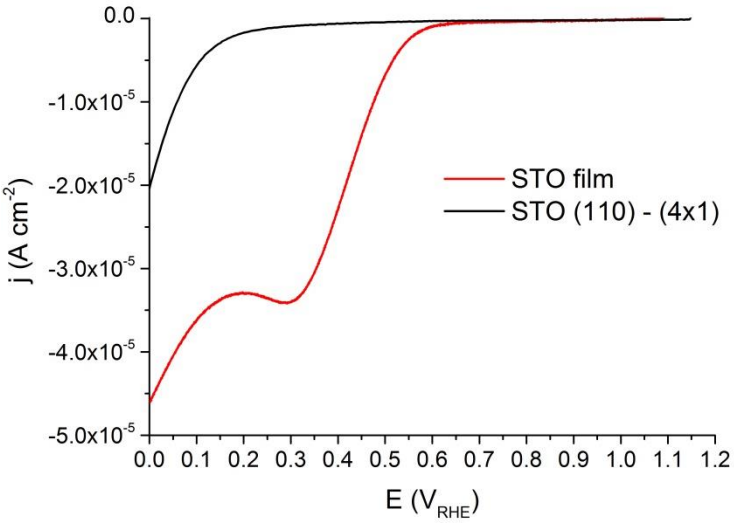

Figure 7-28: Comparison of cyclic voltammograms taken in O_2 purged 0.1 M KOH using a sweep rate of 20 mV s^{-1} of STO (110)-(4x1) surface and STO thin film electrode deposited by PVD at 650 °C in molecular oxygen.

Investigations on the STO film data which were discussed in detail in **Section 6.2.2** suggested that this second reduction wave corresponded to the reduction of hydrogen peroxide. Clearly this would require the preliminary production of hydrogen peroxide for the reaction which for the STO film electrode occurs in the first reduction wave which is assigned to the reduction of oxygen to hydrogen peroxide. Since this reduction is absent in the voltammetry of STO (110) – (4x1) an alternative explanation is required.

A possible explanation is the formation of a surface peroxide species by the interaction of lattice oxygen with oxygen adsorbates. This theory is supported by DFT studies on STO (100) TiO_2 and SrO terminated surfaces which showed that the most favourable sites for oxygen atom adsorption were the metal-oxygen bridge sites with the tendency to from a chemisorbed molecular peroxide, O_{ads} - O_{surf} [208, 209]. The subsequent reduction of this species would lead to a reduction wave at a similar potential to the hydrogen peroxide electrochemical reduction.

The difference in the electrochemistry of the STO film and STO (110) samples is assumed to arise from a difference in the available surface sites. The reduction of oxygen to hydrogen peroxide which is the origin of the first reduction wave with an onset close to 0.6 V_{RHE} is likely to require Ti^{3+} sites since Ti^{4+} has no valence d-electrons to participate in the binding of the oxygen molecule. These Ti^{3+} sites are assumed to be present in the STO film due to the formation of oxygen defects whilst XPS data suggested that no Ti^{3+} was present in the STO (110)-(4x1) surface.

The formation and subsequent reduction of the surface peroxide could however be expected to occur at Sr – O or Ti – O bridge site. The origin of the difference between the cyclic voltammetry in the de-oxygenated solution could now be explained since the cathodic current in the STO film voltammetry would be due to adsorption of OH at the Ti^{3+} sites which is more energetically favourable and occurs at higher potential but since the adsorption is end-on would not result in the formation of surface peroxide. The adsorption of OH on the STO (110) – (4x1) film however does not occur until much lower potential since only the metal-oxygen bridge sites are available.

It may be that the surfaces for which XPS data showed the presence of Ti^{3+} would be more active for the OER and ORR and more closely replicate the activity seen for the STO film electrode however these surface were not tested electrochemically.

7.2.7.2 Fe dosed STO (110)

Cyclic voltammograms obtained for the two Fe dosed STO surfaces and for the clean STO surface are shown in **Figure 7-29**. The incorporation of Fe into the surface should make the surface more conductive and so is expected to improve electron transfer at the surface. Since it is not clear whether the Fe has been incorporated in to the STO surface the increase in current density could also be due to an increase in surface area as the Fe or Fe oxide at the surface may lead to a rougher surface.

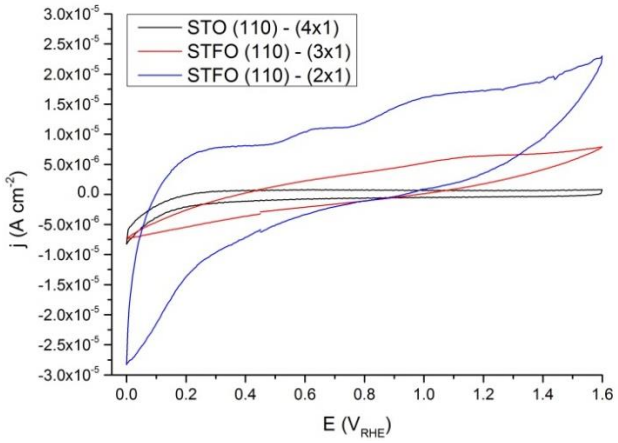

Figure 7-29: Comparison of cyclic voltammetry of STO (110)-(4x1), STFO (110)-(3x1) and STFO (110)-(2x1) surfaces in N_2 purged 0.1 M KOH using a sweep rate of 50 mV s^{-1}.

Figure 7-30 shows the 2nd negative going sweeps from the cyclic voltammetry of the STO (110)-(4x1) reconstruction and the Fe dosed STO (110)-(3x1) reconstruction in O_2 saturated electrolyte. Data could not be obtained for the STFO (110)-(2x1) surface in O_2 saturated electrolyte. The presence of Fe appears to reduce the large overpotential for oxygen reduction and increase current density.

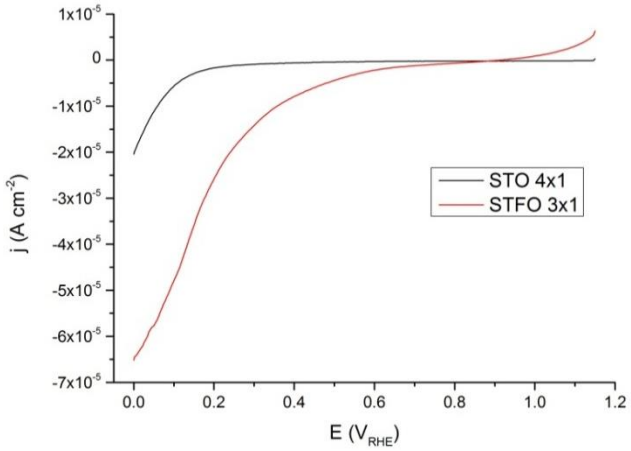

Figure 7-30: Comparison of 2nd negative going sweeps of STO (110)-(4x1) and STFO (110)-(3x1) surfaces in O_2 saturated 0.1 M KOH using a sweep rate of 20 mV s^{-1}.

7.3 Conclusions

Cleaning and preparation of the STO (110) surface was undertaken by a combination of Ar^+ ion sputtering and annealing both in UHV and under an oxygen atmosphere. Carbon impurities which were observable in XPS spectra of the as-received crystal were successfully removed by these methods.

Due to the polarity of the surface the (1x1) unit cell could not be obtained as a starting surface for preparation of the Fe-dosed STO (110) materials. Several surface reconstructions of STO (110) were prepared with unit cells corresponding to (4x1), (3x1) and (1x4) times the unit cell of the STO layer for which the (1x1) cell was defined. In addition surfaces corresponding to domains of different reconstructions were also obtained. Of particular interest was a (3x1)/(1x4) reconstruction which was first reported in the literature as a co-reconstruction but which evidence presented here and in other reports suggests consists of separate domains of the (3x1) and (1x4) reconstructions. A similar (2x1)/(1x4) surface was also obtained.

The preparation methods used for the various surfaces are summarised in **Table 7-10**. It is noted that, for the UHV annealed surfaces, annealing at lower temperatures resulted in reconstruction of the surface in the [001] direction to form (nx1) reconstructions whilst higher temperatures result in reconstruction in the [110] direction to form (1xm) reconstructions. The (3x1)/(1x4) reconstruction was obtained using an annealing temperature intermediate between the annealing temperatures used to obtain the (3x1) and (1x4) reconstructed surfaces.

Reconstruction	Preparation conditions	
	Ar^+ ion sputtering	Annealing
(4x1)	1 kV, 2mA	700 °C , 2 min, UHV
(3x1)	3 kV, 2mA 1 kV, 2 mA	800 °C, 2 h, UHV 700 °C (2 min)
(1x4)	- -	800 °C, 2 h, UHV 1000 °C, 2 min, UHV
(3x1)/(1x4)	-	900 °C, 2 h, UHV
(2x1)/(1x4)	- -	600 °C, 1 h , 1 x 10^{-5} mbar O_2 400 °C, 2 min, UHV

Table 7-10: Summary of conditions used for the preparation of various reconstructions of the STO (110) surface.

These reconstructions of the surface were assumed to be caused by the formation of micro-facets in the [110] and [001] directions. These micro-facets are thought to decrease the overlap of metal 3d states at the surface and as such can lead to surfaces of differing conductivity. Binding energies obtained for the Sr 3d, Ti 2p and O 1s electrons were dependent not only on the composition of the surface and degree of oxidation but also on the surface structure which could be due in part to this effect.

Fe was incorporated into the STO (110) surface by dosing the clean surface with 5 ML of Fe and annealing in oxygen. The successful incorporation of the Fe dopant into the STO (110) surface was confirmed by XPS measurements which showed binding energy shifts in the Sr 3d, Ti 2p and O 1s XPS spectra with the addition of Fe which was consistent with the STFO thin film studies discussed in Section 3.2.5. Additional evidence was provided by LEISS which showed a decrease in the peak assigned to Fe after annealing of the Fe-dosed surface. Since the LEISS technique is highly surface sensitive signal is only obtained from the first few atomic layers with signal greatly decreased below the top layer [87]. The reduction in the signal therefore indicates that the Fe which was present as the top layer after dosing has become incorporated into the surface.

LEED showed ordered (2x1) and (3x1) reconstructions of Fe-doped surfaces which were subsequently tested electrochemically. The preparation methods used are summarised in **Table 7-11**.

Reconstruction	Preparation conditions	
	Ar^+ ion sputtering (Before Fe dose)	Annealing (After Fe dose)
(3x1)	-	700 °C , 2 min, UHV
(2x1)	1 kV, 2 mA	600 °C, 2 min, 1 x 10^{-7} mbar O_2 700 °C (flash)

Table 7-11: Summary of conditions used for the preparation of reconstructions of the Fe doped STO (110) surface.

Unfortunately the experimental method for this system needs refinement as the oxidising environment required to fully incorporate the Fe as Fe^{4+} caused an insulating oxide to form on the connections required to measure the electrochemistry. Initial measurements of less well oxidised surfaces did however show a decrease in the over-potential for the ORR upon addition of Fe for the STFO (110) – (3x1) surface however this surface is unlikely to represent true Fe incorporation into the perovskite lattice. No OER electrocatalytic activity was observed up to 1.6 V_{RHE}.

8. Conclusions and Further Work

The purpose of this work was to assess the activity of $SrTi_{1-x}Fe_xO_{3-y}$ perovskite electrocatalysts towards the oxygen reduction and oxygen evolution reactions and identify structural and electronic factors which contribute to the observed activity trends. High-throughput physical vapour deposition (HT-PVD) was the ideal synthesis method for such a study as compositionally graduated films with compositions across a large portion of the $SrTi_{1-x}Fe_xO_{3-y}$ tie-line could be simultaneously synthesised on a single substrate under identical conditions. When combined with high-throughput screening techniques it was also possible to assess and compare the structural and electronic properties and the electrochemical behaviour of compositions across the range of interest.

Perovskite thin films with compositions $SrTi_{1-x}Fe_xO_{3-y}$ were successfully deposited by HT-PVD at 650 °C using a 500 W oxygen plasma. The use of this reactive oxygen source combined with atomic evaporation sources for deposition of the metallic elements allowed for intimate mixing of the elements and lowered the energy of formation of the crystalline perovskite material. They enabled the use of a lower temperature for synthesis than that required for traditional solid-state synthesis methods.

X-ray diffraction measurements confirmed a cubic perovskite structure for the thin films of composition $SrTi_{1-x}Fe_xO_{3-y}$ for all values of x. Lattice constant refinements confirmed a linear decrease in the lattice constant of the perovskite cell with increasing Fe content from 0.392 ± 0.001 nm for $SrTiO_3$ to 0.386 ± 0.001 nm for $SrFeO_3$. This is in accordance with Vergard's law for metallic alloys and provides evidence that the film constitutes a homogeneous solid solution with crystallites which contain both Fe and Ti cations. The perovskite structure was found to be robust to changes in the Sr content from $Sr_{0.7}(Ti, Fe)O_{3-y}$ up to $Sr_{1.4}(Ti, Fe)O_{3-y}$. However a distinct crystal structure was also observed for more Sr rich compositions which was assigned to a Ruddlesden-Popper phase of composition $Sr_4Fe_3O_7$.

Despite the lack of evidence of a lattice distortion from the diffraction data, except at high Sr content, Raman measurements of the STFO samples were not consistent with a cubic structure in which all lines should be disallowed by symmetry rules. Whilst no lines were observed in the Raman spectrum of STO, in accordance with expectations, measurement of the SFO sample showed lines due to vibrational modes which correlated with previous studies on a tetragonally distorted SFO perovskite material. In the case of the compositionally graduated STFO films, an O-stretching vibrational mode was identified which had previously been observed in the literature and assigned to a Jahn-Teller distortion which breaks they symmetry of the BO_6 octahedral by asymmetric relaxation of the B-O bonds [60].

The Jahn-Teller distortion is thought to arise due to the presence of a single e_g electron in the electronic structure of the Fe^{4+} ion which creates an un-equal charge distribution and is taken as evidence of the presence of the higher oxidation state. This theory does require the localisation of the e_g electron which however should only be the case at low dopant concentrations since at a composition of x = 0.03 the electrons should be delocalised and form electronic bands [108]. Data taken from the $SrTi_{1-x}Fe_xO_{3-y}$ pseudo-binary line showed that the line, which appeared at a wavenumber of 710 cm^{-1} for compositions with low Fe content, decreased in intensity and moved to lower wavenumbers with increasing Fe content. This is consistent with a decreasing Jahn-Teller effect due to the delocalisation of the e_g electron. However the observation of the O-stretching mode up to compositions as high as x = 0.8 suggests another cause and could be evidence of a cation or vacancy ordered superstructure which causes variation in the M-O bond lengths and disrupts the symmetry of the MO_6 octahedra.

Attempts to synthesise the materials under the same conditions but using molecular oxygen rather than the oxygen plasma were less successful. The resulting materials showed poor crystallinity in XRD and evidence from compositional measurements and assessment of the chemical state of the elements using XPS suggested that other oxide phases had been formed. Whilst the crystallinity of the molecular oxygen deposited films could be improved by ex-situ annealing under O_2 to give sharp XRD peaks the lattice parameters obtained from this data showed no dependence on the Fe content. It was concluded that these materials probably consisted of distinct $SrTiO_3$ and $SrFeO_3$ phases rather than a true solid solution. As such the molecular oxygen method is not recommended as a HT-PVD synthesis route for the preparation of a high-quality homogeneous film. This also demonstrates the power of the HT-PVD technique when used in combination with an oxygen plasma source to produce high quality mixed metallic oxides which would be difficult to prepare using solid state methods due to their high thermodynamic formation energies.

Conductivity measurements on the oxygen plasma-prepared thin film samples using the Van der Pauw 4-point probe method showed an increase in conductivity with increasing Fe content consistent with previous studies [59, 65, 92, 101]. The $SrTi_{1-x}Fe_xO_{3-y}$ films were highly resistive at compositions below x = 0.43, exceeding the measurement limit in sheet resistance which corresponded to a conductivity lower than 7×10^{-8} S cm^{-1}. There was a large jump in conductivity at the x = 0.43 composition with conductivity on the order of 3×10^{-5} S cm^{-1} after which point the conductivity increased logarithmically before reaching a plateau at 0.041 ± 0.009 S cm^{-1} for x > 0.75.

Cyclic voltammetry of the STFO films deposited onto electrode arrays revealed redox activity which was strongly correlated with the Fe content of the films and assumed to correspond to the oxidation and reduction of Fe ions which occurs alongside the intercalation of oxygen into oxygen vacancy sites, as shown in **Equation 8-1** . Two distinct sets of redox peaks were identified and assigned to Fe in different chemical environments in the perovskite.

$$Fe^{3+} - V_{\ddot{O}} - \ Fe^{3+} + 2OH^- \rightleftharpoons Fe^{4+} - O - Fe^{4+} + H_2O + 4e^-$$

Equation 8-1

The number of moles of Fe involved in the redox reaction was calculated from the Faradaic charge under the redox peaks and was found to greatly exceed the number of moles of Fe estimated to be present at the electrode surface. This is explained by the ability of the perovskite lattice to intercalate the surface oxygen into the bulk lattice by diffusion of oxygen to vacancy sites which frees up the surface ions to participate in further reaction. This process was found to be reversible with oxygen also being removed from the lattice upon reduction. This reversible electrochemical intercalation of oxygen has previously been observed for $SrFeO_{3-y}$ [95, 96, 146] but no literature studies on the electrochemical redox of the STFO material could be found.

The electrocatalytic activity of the STFO perovskites towards oxygen evolution was found to be tuneable with composition. High OER activity, characterised by over-potentials as low as 0.2 V, was found for compositions with x > 0.5 and close to or higher than stoichiometric Sr content (Sr ≥ 50 at.%). The high OER activity was however found to correlate with low stability of the electrodes towards electrochemical cycling. It is also proposed that the favourable activity in this region of compositional space arises from participation of lattice oxygen in the OER mechanism. The facile exchange of lattice oxygen may also be linked to the catalyst instability.

OER mechanisms involving lattice oxygen have been proposed as an alternative to the usual "adsorbate" mechanism in which all of the oxygen evolved originates from the solution [48, 91, 179]. The adoption of this mechanism relates to the ability of a catalyst to support oxygen vacancies and has been predicted for $SrFeO_{3-y}$ [91]. Whilst the adoption of the lattice oxygen mechanism results in high OER activity there is a clear link with poor electrode stability and so a balancing act between the two factors is required to identify a material with optimal properties for practical application in a fuel cell environment [48, 91].

For the STFO materials investigated in this work an optimal composition of $SrTi_{0.5}Fe_{0.5}O_{3-y}$ would be recommended as the OER activity shows no significant increase with Fe content above this point whilst there is a significant decrease in the electrode stability. Since most of the previously proposed activity descriptors for OER activity have been based on an adsorbate evolution mechanism their predictive power is limited in this case. A correlation was noted between the equilibrium potential of the Fe^{3+}/Fe^{4+} surface redox reaction, shown in Equation 5-5, and the onset potential for the OER. This is in agreement with previous reports [34]. The correlation was found with the redox process assigned to lower co-ordinate Fe sites which occurs immediately prior to the OER onset. It may be the case therefore that these sites are the most stable for the formation of the surface oxygen vacancies required for a lattice oxygen participated mechanism for the OER and are therefore the most active sites for the OER.

The electrocatalytic activity of the STFO perovskites towards oxygen reduction was less impressive as the reaction did not occur on the oxidised surface. It first required the reduction of the surface according to the reverse reaction in Equation 5-5. As such there was a very large over-potential associated with the reaction. It is therefore assumed that for ORR electrocatalysis the reduced protonated surface must be accessible as the bonding in the Fe^{4+}-O^{2-} is too strong for displacement by the oxygen molecule. This highlights the importance of considering the reaction surface when selecting candidates for electrocatalysis, and in particular the equilibrium potential of the redox reactions.

Additional correlations were noted throughout the thin film study between trends in the electrocatalytic activity, electrochemical redox activity, conductivity and Raman measurements which appeared to centre around the x = 0.5 and x=0.66 compositions. It is therefore proposed that ordered superstructures are formed for $SrTi_{1-x}Fe_xO_{3-y}$ perovskites consisting of layered perovskite structures of the formula $(SrTiO_3)_1(SrFeO_{3-y})_n$ where n = 1 or 2 and the oxygen vacancies in the $SrFeO_{3-y}$ layers may also exhibit ordering. The x = 0.5 composition corresponds to a double perovskite structure consisting of alternating planes of $SrTiO_3$ and $SrFeO_{3-y}$.The $SrFeO_{3-y}$ should provide a clear path of conduction of electrons and oxide ions between the Fe cations which may explain the significant increase in conductivity and electrocatalytic activity for compositions close to x = 0.5. The x = 0.66 composition would also be significant as this introduces two adjacent layers of $SrFeO_{3-y}$ which would be able to form a greater number of vacancy ordered structures due to different ordering patterns for the lower-coordinate cations [131].

A complementary surface science study using a commercially available STO (110) single crystal to prepared well-characterised Fe-doped STO surfaces was intended to investigate further the mechanisms of electrocatalysis. Several surface reconstructions of STO (110) were prepared with unit cells corresponding to (4x1), (3x1) and (1x4) times the unit cell of the STO layer for which the (1x1) cell was defined. This was in agreement with previous literature studies. In addition surfaces corresponding to domains of different reconstructions were also obtained. Of particular interest was a (3x1)/(1x4) reconstruction which was first reported in the literature as a co-reconstruction but which evidence presented here and in other reports suggests consists of separate domains of the (3x1) and (1x4) reconstructions. A similar (2x1)/(1x4) surface was also obtained.

XPS and LEISS measurements confirmed that Fe doping was successful in the incorporation of Fe into the STO (110) surface. Binding energy shifts in the XPS spectra provided evidence that the Fe was incorporated into the perovskite structure. LEED showed ordered (2x1) and (3x1) reconstructions of Fe-doped surfaces which were subsequently tested electrochemically.

Unfortunately the experimental method for this system needs refinement as the oxidising environment required to fully incorporate the Fe as Fe^{4+} caused an insulating oxide to form on the connections required to measure the electrochemistry. Initial measurements of less well oxidised surfaces did however show a decrease in the over-potential for the ORR upon incorporation of Fe. No OER electrocatalytic activity was observed within the pH window considered.

The current work on the STFO system has shown the applicability of the high-throughput PVD synthesis and screening of perovskite materials for oxygen electrocatalysis. Future work should be focussed on perovskites shown to have high activity for both reactions such as $LaMnO_3$. This material would also be interesting in surface electrochemical experiments if a suitable single crystal sample could be sourced as results could be compared with calculations on this surface which have indicated that the proposed mechanisms and activity descriptors cannot fully explain the activity [165].

List of References

1. *Global Trends in Renewable Energy Investment 2015*. 2015, Frankfurt School - UNEP Collaborating Centre for Climate and Sustainable Energy Finance.

2. *Digest of UK Energy Statistics 2015*. 2015, Department of Energy and Climate Change.

3. *DIRECTIVE 2009/28/EC OF THE EUROPEAN PARLIAMENT AND OF THE COUNCIL.* Official Journal of the European Union, 2009. **52**: p. 16-62.

4. *Renewables 2015 Global Status Report*. 2015, Renewable Energy Policy Network for the 21st Century (REN21).

5. Dunn, B., H. Kamath, and J.M. Tarascon, *Electrical Energy Storage for the Grid: A Battery of Choices.* Science, 2011. **334**(6058): p. 928-935.

6. Pettersson, J., B. Ramsey, and D. Harrison, *A review of the latest developments in electrodes for unitised regenerative polymer electrolyte fuel cells.* Journal of Power Sources, 2006. **157**(1): p. 28-34.

7. Yang, Z.G., *et al*., *Electrochemical Energy Storage for Green Grid.* Chemical Reviews, 2011. **111**(5): p. 3577-3613.

8. Cheng, F.Y. and J. Chen, *Metal-air batteries: from oxygen reduction electrochemistry to cathode catalysts.* Chemical Society Reviews, 2012. **41**(6): p. 2172-2192.

9. Owen, J.R., *Rechargeable lithium batteries.* Chemical Society Reviews, 1997. **26**(4): p. 259-267.

10. Park, M., *et al*., *Lithium-Air Batteries: Survey on the Current Status and Perspectives Towards Automotive Applications from a Battery Industry Standpoint.* Advanced Energy Materials, 2012. **2**(7): p. 780-800.

11. Girishkumar, G., *et al*., *Lithium - Air Battery: Promise and Challenges.* Journal of Physical Chemistry Letters, 2010. **1**(14): p. 2193-2203.

12. Armand, M. and J.M. Tarascon, *Building better batteries.* Nature, 2008. **451**(7179): p. 652-657.

13. Bockris, J.O.M., *Hydrogen Economy.* Science, 1972. **176**(4041): p. 1323-&.

14. Katsounaros, I., *et al*., *Oxygen Electrochemistry as a Cornerstone for Sustainable Energy Conversion.* Angewandte Chemie-International Edition, 2014. **53**(1): p. 102-121.

15. Pletcher, D., *A First Course in Electrode Processes*. 2nd edition ed. 2009: The Royal Society of Chemistry.

16. Divisek, J. and B. Emonts, *Energy storage via electrolysis/fuel cells*, in *Handbook of Fuel Cells*. 2010, John Wiley & Sons, Ltd.

17. Cifrain, M. and K. Kordesch, *Hydrogen/oxygen (air) fuel cells with alkaline electrolytes*, in *Handbook of Fuel Cells*. 2010, John Wiley & Sons, Ltd.

18. Jorissen, L., *Bifunctional oxygen/air electrodes.* Journal of Power Sources, 2006. **155**(1): p. 23-32.

19. Carmo, M., *et al*., *A comprehensive review on PEM water electrolysis.* International Journal of Hydrogen Energy, 2013. **38**(12): p. 4901-4934.

20. Pletcher, D. and X.H. Li, *Prospects for alkaline zero gap water electrolysers for hydrogen production.* International Journal of Hydrogen Energy, 2011. **36**(23): p. 15089-15104.

21. Nieminen, J., I. Dincer, and G. Naterer, *Comparative performance analysis of PEM and solid oxide steam electrolysers.* International Journal of Hydrogen Energy, 2010. **35**(20): p. 10842-10850.

22. Greeley, J. and N.M. Markovic, *The road from animal electricity to green energy: combining experiment and theory in electrocatalysis.* Energy & Environmental Science, 2012. **5**(11): p. 9246-9256.

23. Bidault, F., *et al*., *Review of gas diffusion cathodes for alkaline fuel cells.* Journal of Power Sources, 2009. **187**(1): p. 39-48.

24. Holtappels, P. and U. Stimming, *Solid oxide fuel cells (SOFC)*, in *Handbook of Fuel Cells*. 2010, John Wiley & Sons, Ltd.

25. Steele, B.C.H. and A. Heinzel, *Materials for fuel-cell technologies.* Nature, 2001. **414**(6861): p. 345-352.

26. Acres, G.J.K., *Recent advances in fuel cell technology and its applications.* Journal of Power Sources, 2001. **100**(1-2): p. 60-66.

27. Yamamoto, O., *Solid oxide fuel cells: fundamental aspects and prospects.* Electrochimica Acta, 2000. **45**(15-16): p. 2423-2435.

28. Ahn, J. and R. Holze, *Bifunctional Electrodes for an Integrated Water-Electrolysis and Hydrogen Oxygen Fuel-Cell with a Solid Polymer Electrolyte.* Journal of Applied Electrochemistry, 1992. **22**(12): p. 1167-1174.

29. Lee, J.S., *et al*., *Metal-Air Batteries with High Energy Density: Li-Air versus Zn-Air.* Advanced Energy Materials, 2011. **1**(1): p. 34-50.

30. Lee, J., B. Jeong, and J.D. Ocon, *Oxygen electrocatalysis in chemical energy conversion and storage technologies.* Current Applied Physics, 2013. **13**(2): p. 309-321.

31. Cheng, Y. and S.P. Jiang, *Advances in electrocatalysts for oxygen evolution reaction of water electrolysis -from metal oxides to carbon nanotubes.* Progress in Natural Science-Materials International, 2015. **25**(6): p. 545-553.

32. Maillard, F., *et al*., *Ru-decorated Pt surfaces as model fuel cell electrocatalysts for CO electrooxidation.* Journal of Physical Chemistry B, 2005. **109**(34): p. 16230-16243.

33. Dau, H., *et al*., *The Mechanism of Water Oxidation: From Electrolysis via Homogeneous to Biological Catalysis.* Chemcatchem, 2010. **2**(7): p. 724-761.

34. Trasatti, S., *Electrocatalysis by Oxides - Attempt at a Unifying Approach.* Journal of Electroanalytical Chemistry, 1980. **111**(1): p. 125-131.

35. Chen, Z.W., *et al*., *A review on non-precious metal electrocatalysts for PEM fuel cells.* Energy & Environmental Science, 2011. **4**(9): p. 3167-3192.

36. Gasteiger, H.A., *et al*., *Activity benchmarks and requirements for Pt, Pt-alloy, and non-Pt oxygen reduction catalysts for PEMFCs.* Applied Catalysis B-Environmental, 2005. **56**(1-2): p. 9-35.

37. Mukerjee, S., *et al*., *Role of Structural and Electronic-Properties of Pt and Pt Alloys on Electrocatalysis of Oxygen Reduction - an in-Situ Xanes and Exafs Investigation.* Journal of the Electrochemical Society, 1995. **142**(5): p. 1409-1422.

38. Toda, T., *et al*., *Enhancement of the electroreduction of oxygen on Pt alloys with Fe, Ni, and Co.* Journal of the Electrochemical Society, 1999. **146**(10): p. 3750-3756.

39. Suntivich, J., *et al*., *Electrocatalytic Measurement Methodology of Oxide Catalysts Using a Thin-Film Rotating Disk Electrode.* Journal of the Electrochemical Society, 2010. **157**(8): p. B1263-B1268.

40. Bursell, M., M. Pirjamali, and Y. Kiros, *La0.6Ca0.4CoO3, La0.1Ca0.9MnO3 and LaNiO3 as bifunctional oxygen electrodes.* Electrochimica Acta, 2002. **47**(10): p. 1651-1660.

41. Roche, I., *et al*., *Carbon-supported manganese oxide nanoparticles as electrocatalysts for the Oxygen Reduction Reaction (ORR) in alkaline medium: Physical characterizations and ORR mechanism.* Journal of Physical Chemistry C, 2007. **111**(3): p. 1434-1443.

42. Hayashi, M., *et al*., *Reverse micelle assisted dispersion of lanthanum manganite on carbon support for oxygen reduction cathode.* Journal of the Electrochemical Society, 2004. **151**(1): p. A158-A163.

43. Liang, Y.Y., *et al*., *Co3O4 nanocrystals on graphene as a synergistic catalyst for oxygen reduction reaction.* Nature Materials, 2011. **10**(10): p. 780-786.

44. Liu, Y., *et al*., *Transition metal oxides as DMFC cathodes without platinum.* Journal of the Electrochemical Society, 2007. **154**(7): p. B664-B669.

45. Matsumoto, Y., H. Manabe, and E. Sato, *Oxygen Evolution on La1-Xsrxcoo3 Electrodes in Alkaline-Solutions.* Journal of the Electrochemical Society, 1980. **127**(4): p. 811-814.

46. Suntivich, J., *et al*., *A Perovskite Oxide Optimized for Oxygen Evolution Catalysis from Molecular Orbital Principles.* Science, 2011. **334**(6061): p. 1383-1385.

47. Bockris, J.O. and T. Otagawa, *The Electrocatalysis of Oxygen Evolution on Perovskites.* Journal of the Electrochemical Society, 1984. **131**(2): p. 290-302.

48. Grimaud, A., *et al*., *Double perovskites as a family of highly active catalysts for oxygen evolution in alkaline solution.* Nature Communications, 2013. **4**.

49. Rios, E., *et al*., *Mixed valency spinel oxides of transition metals and electrocatalysis: case of the MnxCo3-xO4 system.* Electrochimica Acta, 1998. **44**(8-9): p. 1491-1497.

50. Li, N., *et al*., *Electrocatalytic activity of spinel-type oxides LiMn2-XCoXO4 with large specific surface areas for metal-air battery.* Journal of Power Sources, 1998. **74**(2): p. 255-258.

51. Vogt, U.F., *et al*., *Influence of A-Site Variation and B-Site Substitution on the Physical Properties of (La,Sr)FeO3 Based Perovskites.* Fuel Cells, 2009. **9**(6): p. 899-906.

52. Wattiaux, A., *et al*., *Electrolytic Oxygen Evolution in Alkaline-Medium on La1-Xsrxfeo3-Y Perovskite-Related Ferrites .2. Influence of Bulk Properties.* Journal of the Electrochemical Society, 1987. **134**(7): p. 1718-1724.

53. Yuan, C.Z., *et al*., *Mixed Transition-Metal Oxides: Design, Synthesis, and Energy-Related Applications.* Angewandte Chemie-International Edition, 2014. **53**(6): p. 1488-1504.

54. Cao, Y.L., *et al*., *The mechanism of oxygen reduction on MnO2-catalyzed air cathode in alkaline solution.* Journal of Electroanalytical Chemistry, 2003. **557**: p. 127-134.

55. Lima, F.H.B., M.L. Calegaro, and E.A. Ticianelli, *Investigations of the catalytic properties of manganese oxides for the oxygen reduction reaction in alkaline media.* Journal of Electroanalytical Chemistry, 2006. **590**(2): p. 152-160.

56. Raj, I.A. and K.I. Vasu, *Characterization of Electrolytic Mno2-Based Oxygen Electrodes for Alkaline Water Electrolyzer Fuel-Cell Reactions.* International Journal of Hydrogen Energy, 1990. **15**(10): p. 751-756.

57. Cardona, M., *Optical Properties and Band Structure of SrTiO3 and BaTiO3.* Physical Review, 1965. **140**(2A): p. A651-A655.

58. Adler, P. and S. Eriksson, *Structural properties, Mossbauer spectra, and magnetism of perovskite-type oxides SrFe1-xTixO3-y.* Zeitschrift Fur Anorganische Und Allgemeine Chemie, 2000. **626**(1): p. 118-124.

59. Steinsvik, S., *et al*., *The defect structure of SrTi1-xFexO3-y (x=0-0.8) investigated by electrical conductivity measurements and electron energy loss spectroscopy (EELS).* Journal of Physics and Chemistry of Solids, 1997. **58**(6): p. 969-976.

60. Vracar, M., *et al*., *Jahn-Teller distortion around Fe(4+) in Sr(Fe(x)Ti(1-x))O(3-delta) from x-ray absorption spectroscopy, x-ray diffraction, and vibrational spectroscopy.* Physical Review B, 2007. **76**(17).

61. Suntivich, J., *et al*., *Design principles for oxygen-reduction activity on perovskite oxide catalysts for fuel cells and metal-air batteries (vol 3, pg 546, 2011).* Nature Chemistry, 2011. **3**(8): p. 647-647.

62. Tulloch, J. and S.W. Donne, *Activity of perovskite La1-xSrxMnO3 catalysts towards oxygen reduction in alkaline electrolytes.* Journal of Power Sources, 2009. **188**(2): p. 359-366.

63. Villaseca, L., B. Moreno, and E. Chinarro, *Perovskites based on La(Sr)-Mn-O system as electrocatalyst in PEM fuel cell of high temperature.* International Journal of Hydrogen Energy, 2012. **37**(8): p. 7161-7170.

64. Hyodo, T., *et al*., *Catalytic activities of rare-earth manganites for cathodic reduction of oxygen in alkaline solution.* Journal of the Electrochemical Society, 1996. **143**(11): p. L266-L267.

65. Rothschild, A., *et al*., *Electronic structure, defect chemistry, and transport properties of SrTi1-xFexO3-y solid solutions.* Chemistry of Materials, 2006. **18**(16): p. 3651-3659.

66. Komo, M., *et al*., *Oxygen Evolution and Reduction Reactions on La0.8Sr0.2CoO3 (001), (110), and (111) Surfaces in an Alkaline Solution.* Electrochemistry, 2012. **80**(10): p. 834-838.

67. Markovich, M., *et al*., *Epitaxial growth of Nb-doped SrTiO3 films by pulsed laser deposition.* Applied Surface Science, 2012. **258**(23): p. 9496-9500.

68. Lippert, T., *et al*., *Perovskite thin films deposited by pulsed laser ablation as model systems for electrochemical applications.* Progress in Solid State Chemistry, 2007. **35**(2-4): p. 221-231.

69. Tsui, F. and P.A. Ryan, *Combinatorial molecular beam epitaxy synthesis and characterization of magnetic alloys.* Applied Surface Science, 2002. **189**(3-4): p. 333-338.

70. Briceno, G., *et al*., *A Class of Cobalt Oxide Magnetoresistance Materials Discovered with Combinatorial Synthesis.* Science, 1995. **270**(5234): p. 273-275.

71. Xiang, X.D., *et al*., *A Combinatorial Approach to Materials Discovery.* Science, 1995. **268**(5218): p. 1738-1740.

72. Hanak, J.J., *Multiple-Sample-Concept in Materials Research - Synthesis, Compositional Analysis and Testing of Entire Multicomponent Systems.* Journal of Materials Science, 1970. **5**(11): p. 964-&.

73. Koinuma, H., *Quantum functional oxides and combinatorial chemistry.* Solid State Ionics, 1998. **108**(1-4): p. 1-7.

74. Guerin, S. and B.E. Hayden, *Physical vapor deposition method for the high-throughput synthesis of solid-state material libraries.* Journal of Combinatorial Chemistry, 2006. **8**(1): p. 66-73.

75. Anderson, P.S., *et al*., *Synthesis of the ferroelectric solid solution, Pb(Zr1-xTix)O-3 on a single substrate using a modified molecular beam epitaxy technique.* Applied Physics Letters, 2007. **90**(20).

76. Darby, M.S.B., *et al*., *High throughput physical vapour deposition and dielectric and ferroelectric screening of (Bi,Na)TiO3 thin-film libraries.* Journal of Applied Physics, 2013. **113**(1).

77. Canulescu, S., *et al*., *Preparation of epitaxial La0.6Ca0.4Mn1-xFexO3 (x=0, 0.2) thin films: Variation of the oxygen content.* Progress in Solid State Chemistry, 2007. **35**(2-4): p. 241-248.

78. Darby, M.S.B., *et al*., *Synthesis and characterization of Bi-1 (-) xNdxFeO3 thin films deposited using a high throughput physical vapour deposition technique.* Thin Solid Films, 2013. **531**: p. 56-60.

79. Ratner, B.D. and D.G. Castner, *Electron Spectroscopy for Chemical Analysis*, in *Surface Analysis – The Principal Techniques*. 2009, John Wiley & Sons, Ltd. p. 47-112.

80. Bagus, P.S., E.S. Ilton, and C.J. Nelin, *The interpretation of XPS spectra: Insights into materials properties.* Surface Science Reports, 2013. **68**(2): p. 273-304.

81. Wagner, C.D., *et al*., *Empirical Atomic Sensitivity Factors for Quantitative-Analysis by Electron-Spectroscopy for Chemical-Analysis.* Surface and Interface Analysis, 1981. **3**(5): p. 211-225.

82. Briggs, D.a.S., M. P., *Practical Surface Analysis: by auger and x-ray photoelectron spectroscopy*. 1983: Wiley.

83. Riggs, W.M., Davis, L. E., Moulder J. F. and Muilenberg, G. E., *Handbook of X-ray Photoelectron Spectroscopy*. 1979: Perkin-Elmer Corporation.

84. Banwell, C.N.a.M., E. M., *Fundamentals of Molecular Spectroscopy*. Fourth ed. 1994.

85. Van Der Pauw, L.J., *A method of measuring specific resistivity and Hall effects of discs of arbitrary shape.* Philips Research Reports, 1958. **13**: p. 1-9.

86. Guerin, S., *et al*., *Combinatorial electrochemical screening of fuel cell electrocatalysts.* Journal of Combinatorial Chemistry, 2004. **6**(1): p. 149-158.

87. Woodruff, D.P., Delchar, T.A, *Modern Techniques of Surface Science*. 1986, Cambridge: Cambridge University Press.

88. Feldman, L.C.a.M., J. W, *Fundamentals of Surface and Thin Film Analysis*. 1986: Elsevier.

89. Palmer, N.R. and D.A. King, *Ion-Scattering Spectroscopy of Beta-N and Beta-3-Co (Square-Root 2xsquare-Root 2) R45-Degrees Structures on W(100).* Physica Scripta, 1983. **T4**: p. 122-125.

90. Richter, J., *et al*., *Materials design for perovskite SOFC cathodes.* Monatshefte Fur Chemie, 2009. **140**(9): p. 985-999.

91. Rong, X., J. Parolin, and A.M. Kolpak, *A Fundamental Relationship between Reaction Mechanism and Stability in Metal Oxide Catalysts for Oxygen Evolution.* Acs Catalysis, 2016. **6**(2): p. 1153-1158.

92. Brixner, L.H., *Preparation and properties of the SrTi1−xFexO3−x2/Ox2 system.* Materials Research Bulletin, 1968. **3**(4): p. 299-308.

93. Schulze-Küppers, F., *et al*., *Structural and functional properties of SrTi1−xFexO3−δ (0 ⩽ x ⩽ 1) for the use as oxygen transport membrane.* Separation and Purification Technology, 2015. **147**: p. 414-421.

94. Bocquet, A.E., *et al*., *Electronic-Structure of Srfe4+O3 and Related Fe Perovskite Oxides.* Physical Review B, 1992. **45**(4): p. 1561-1570.

95. Nemudry, A., *et al*., *Room temperature electrochemical redox reactions of the defect perovskite SrFeO2.5+x.* Chemistry of Materials, 1998. **10**(9): p. 2403-2411.

96. Wattiaux, A., *et al*., *A Novel Preparation Method of the Srfeo3 Cubic Perovskite by Electrochemical Means.* Solid State Communications, 1991. **77**(7): p. 489-493.

97. Adler, P., *et al*., *Magnetoresistance effects in SrFeO3-delta: Dependence on phase composition and relation to magnetic and charge order.* Physical Review B, 2006. **73**(9).

98. Torrance, J.B., *et al*., *Simple and Perovskite Oxides of Transition-Metals - Why Some Are Metallic, While Most Are Insulating.* Journal of Solid State Chemistry, 1991. **90**(1): p. 168-172.

99. Takeda, Y., *et al*., *Properties of Srmo3-Delta (M=Fe,Co) as Oxygen Electrodes in Alkaline-Solution.* Journal of Applied Electrochemistry, 1982. **12**(3): p. 275-280.

100. Evarestov, R.A., *et al*., *Single impurities in insulators: Ab initio study of Fe-doped SrTiO3.* Physical Review B, 2003. **67**(6).

101. da Silva, L.F., *et al*., *Insight into the Effects of Fe Addition on the Local Structure and Electronic Properties of SrTiO3.* Journal of Physical Chemistry C, 2014. **118**(9): p. 4930-4940.

102. Ghaffari, M., *et al*., *Preparation, surface state and band structure studies of SrTi(1 (-) x)Fe(x)O(3 (-) (delta)) (x=0-1) perovskite-type nano structure by X-ray and ultraviolet photoelectron spectroscopy.* Surface Science, 2012. **606**(5-6): p. 670-677.

103. da Silva, L.F., *et al*., *Synthesis and thermal decomposition of SrTi1-x Fe (x) O-3 (0.0 a parts per thousand currency sign x a parts per thousand currency sign 0.1) powders obtained by the polymeric precursor method.* Journal of Thermal Analysis and Calorimetry, 2009. **97**(1): p. 173-177.

104. Hodges, J.P., *et al*., *Evolution of Oxygen-Vacancy Ordered Crystal Structures in the Perovskite Series SrnFenO3n−1 (n=2, 4, 8, and ∞), and the Relationship to Electronic and Magnetic Properties.* Journal of Solid State Chemistry, 2000. **151**(2): p. 190-209.

105. Yu, Z.W., *et al*., *Structural and electrical properties of SrFexTi1-xO3 (x=0.001, 0.005 and 0.01) thin films prepared by pulsed laser depositions.* Ceramics International, 2015. **41**: p. S223-S227.

106. Jung, W. and H.L. Tuller, *Investigation of cathode behavior of model thin-film SrTi(1-x)Fe(x)O(3-delta) (x=0.35 and 0.5) mixed ionic-electronic conducting electrodes.* Journal of the Electrochemical Society, 2008. **155**(11): p. B1194-B1201.

107. Morin, F.J. and J.R. Oliver, *Energy-Levels of Iron and Aluminum in Srtio3.* Physical Review B, 1973. **8**(12): p. 5847-5854.

108. Evarestov, R., *et al*., *Jahn-Teller effect in the phonon properties of defective SrTiO3 from first principles.* Physical Review B, 2012. **85**(17).

109. Falcon, H., *et al*., *SrFeO3-delta perovskite oxides: Chemical features and performance for methane combustion.* Chemistry of Materials, 2002. **14**(5): p. 2325-2333.

110. Chen, Y., *et al*., *Impact of Sr segregation on the electronic structure and oxygen reduction activity of SrTi1-xFexO3 surfaces.* Energy & Environmental Science, 2012. **5**(7): p. 7979-7988.

111. Jung, W. and H.L. Tuller, *Investigation of surface Sr segregation in model thin film solid oxide fuel cell perovskite electrodes.* Energy & Environmental Science, 2012. **5**(1): p. 5370-5378.

112. van der Heide, P.A.W., *et al*., *X-ray photoelectron spectroscopic and ion scattering study of the SrTiO3(001) surface.* Surface Science, 2001. **473**(1-2): p. 59-70.

113. van der Heide, P.A.W., *Surface core level shifts in photo-electron spectra from the Ca, Sr and Ba titanates.* Surface Science, 2001. **490**(3): p. L619-L626.

114. Bocquet, A.E., *et al*., *Electronic structure of early 3d-transition-metal oxides by analysis of the 2p core-level photoemission spectra.* Physical Review B, 1996. **53**(3): p. 1161-1170.

115. Okada, K., T. Uozumi, and A. Kotani, *Split-Off State Formation in the Final-State of Photoemission in Ti Compounds.* Journal of the Physical Society of Japan, 1994. **63**(8): p. 3176-3184.

116. Zaanen, J. and G.A. Sawatzky, *Strong Interference between Decay Channels and Valence-Electron Rearrangements in Core-Hole Spectroscopy.* Physical Review B, 1986. **33**(12): p. 8074-8083.

117. Xiao, G., *et al*., *Synthesis and characterization of Mo-doped SrFeO3−δ as cathode materials for solid oxide fuel cells.* Journal of Power Sources, 2012. **202**(0): p. 63-69.

118. Al-Rawas, A.D., *et al*., *The formation and structure of mechano-synthesized nanocrystalline Sr3Fe2O6.4: XRD Rietveld, Mössabuer and XPS analyses.* Materials Research Bulletin, 2015. **65**(0): p. 142-148.

119. Gupta, R.P. and S.K. Sen, *Calculation of Multiplet Structure of Core Para-Vacancy Levels.* Physical Review B, 1974. **10**(1): p. 71-77.

120. Grosvenor, A.P., *et al*., *Investigation of multiplet splitting of Fe 2p XPS spectra and bonding in iron compounds.* Surface and Interface Analysis, 2004. **36**(12): p. 1564-1574.

121. Mcintyre, N.S. and D.G. Zetaruk, *X-Ray Photoelectron Spectroscopic Studies of Iron-Oxides.* Analytical Chemistry, 1977. **49**(11): p. 1521-1529.

122. Biesinger, M.C., *et al*., *Resolving surface chemical states in XPS analysis of first row transition metals, oxides and hydroxides: Cr, Mn, Fe, Co and Ni.* Applied Surface Science, 2011. **257**(7): p. 2717-2730.

123. Dulli, H., *et al*., *Surface segregation and restructuring of colossal-magnetoresistant manganese perovskites La0.65Sr0.35MnO3.* Physical Review B, 2000. **62**(22): p. 14629-14632.

124. Szot, K. and W. Speier, *Surfaces of reduced and oxidized SrTiO3 from atomic force microscopy.* Physical Review B, 1999. **60**(8): p. 5909-5926.

125. Tsujimoto, Y., *et al*., *Infinite-layer iron oxide with a square-planar coordination.* Nature, 2007. **450**(7172): p. 1062-U8.

126. Sleight, A.W., J.L. Gillson, and P.E. Bierstedt, *High-Temperature Superconductivity in Bapb1-Xbixo3 System.* Solid State Communications, 1975. **17**(1): p. 27-28.

127. Kwon, S., *et al*., *Effects of cation stoichiometry on the dielectric properties of CaCu3Ti4O12.* Journal of Alloys and Compounds, 2009. **473**(1-2): p. 433-436.

128. Subramanian, M.A., *et al*., *High dielectric constant in ACu(3)Ti(4)O(12) and ACu(3)Ti(3)FeO(12) phases.* Journal of Solid State Chemistry, 2000. **151**(2): p. 323-325.

129. Goodenough, J.B., *Electronic and ionic transport properties and other physical aspects of perovskites.* Reports on Progress in Physics, 2004. **67**(11): p. 1915.

130. Hodges, J.P., *et al*., *Evolution of oxygen-vacancy ordered crystal structures in the perovskite series SrnFenO3n-1 (n=2, 4, 8, and infinity), and the relationship to electronic and magnetic properties.* Journal of Solid State Chemistry, 2000. **151**(2): p. 190-209.

131. Berger, R.F., D.P. Broberg, and J.B. Neaton, *Tuning the electronic structure of SrTiO3/SrFeO3−x superlattices via composition and vacancy control.* APL Mater., 2014. **2**(4): p. 046101.

132. Wrighton, M.S., *et al*., *Strontium titanate photoelectrodes. Efficient photoassisted electrolysis of water at zero applied potential.* Journal of the American Chemical Society, 1976. **98**(10): p. 2774-2779.

133. Chroneos, A., *et al*., *Oxygen transport in perovskite and related oxides: A brief review.* Journal of Alloys and Compounds, 2010. **494**(1-2): p. 190-195.

134. Nguyen, V.M. and T.T.P. Doan, *SrTi1-xFexO3 nanoparticle: a study of structural, optical, impedance and magnetic properties.* Journal of Experimental Nanoscience, 2011. **6**(3): p. 226-237.

135. Vegard, L., *Die Konstitution der Mischkristalle und die Raumfüllung der Atome.* Zeitschrift für Physik, 1921. **5**(1): p. 17-26.

136. Sirenko, A.A., *et al*., *Observation of the first-order Raman scattering in SrTiO3 thin films.* Physical Review Letters, 1999. **82**(22): p. 4500-4503.

137. Ni, S., X. Yang, and T. Li, *Hydrothermal synthesis and photoluminescence properties of SrCO3.* Materials Letters, 2011. **65**(4): p. 766-768.

138. Lenser, C., *et al*., *Spectroscopic study of the electric field induced valence change of Fe-defect centers in SrTiO3.* Physical Chemistry Chemical Physics, 2011. **13**(46): p. 20779-20786.

139. Alexandrov, V.E., J. Maier, and R.A. Evarestov, *Ab initio study of SrFexTi1-xO3: Jahn-Teller distortion and electronic structure.* Physical Review B, 2008. **77**(7).

140. Goodenough, J.B. and B.L. Cushing, *Oxide-Based ORR catalysts*, in *Handbook of Fuel Cells - Fundamentals, Technology and Applications*, W. Vielstich, Gasteiger, H. A., Lamm, A. and Yokokawa, H., Editor. 2010, John Wiley & Sons

141. Castelli, I.E., K.S. Thygesen, and K.W. Jacobsen, *Calculated Pourbaix Diagrams of Cubic Perovskites for Water Splitting: Stability Against Corrosion.* Topics in Catalysis, 2014. **57**(1-4): p. 265-272.

142. Li, X.H., F.C. Walsh, and D. Pletcher, *Nickel based electrocatalysts for oxygen evolution in high current density, alkaline water electrolysers.* Physical Chemistry Chemical Physics, 2011. **13**(3): p. 1162-1167.

143. Chen, J.Y.C., *et al*., *Operando Analysis of NiFe and Fe Oxyhydroxide Electrocatalysts for Water Oxidation: Detection of Fe4+ by Mossbauer Spectroscopy.* Journal of the American Chemical Society, 2015. **137**(48): p. 15090-15093.

144. Kudo, T., H. Obayashi, and T. Gejo, *Electrochemical Behavior of Perovskite-Type Nd1-Xsrxcoo3 in an Aqueous Alkaline-Solution.* Journal of the Electrochemical Society, 1975. **122**(2): p. 159-163.

145. Kröger, F.A. and H.J. Vink, *Relations between the Concentrations of Imperfections in Crystalline Solids*, in *Solid State Physics*, S. Frederick and T. David, Editors. 1956, Academic Press. p. 307-435.

146. Piovano, A., *et al*., *Time Resolved in Situ XAFS Study of the Electrochemical Oxygen Intercalation in SrFeO2.5 Brownmillerite Structure: Comparison with the Homologous SrCoO2.5 System.* Journal of Physical Chemistry C, 2011. **115**(4): p. 1311-1322.

147. Nemudry, A., P. Rudolf, and R. Schollhorn, *Topotactic electrochemical redox reactions of the defect perovskite SrCoO2.5+x.* Chemistry of Materials, 1996. **8**(9): p. 2232-2238.

148. Karvonen, L., *et al*., *O-K and Co-L XANES Study on Oxygen Intercalation in Perovskite SrCoO3-delta.* Chemistry of Materials, 2010. **22**(1): p. 70-76.

149. Le Toquin, R., *et al*., *Time-resolved in situ studies of oxygen intercalation into SrCoO2.5, performed by neutron diffraction and X-ray absorption spectroscopy.* Journal of the American Chemical Society, 2006. **128**(40): p. 13161-13174.

150. Mefford, J.T., *et al*., *Anion charge storage through oxygen intercalation in LaMnO3 perovskite pseudocapacitor electrodes.* Nature Materials, 2014. **13**(7): p. 726-732.

151. Wagner, S.F., *et al*., *Enhancement of oxygen surface kinetics of SrTiO3 by alkaline earth metal oxides.* Solid State Ionics, 2006. **177**(19-25): p. 1607-1612.

152. Matsumoto, Y. and E. Sato, *Oxygen Evolution on Srfeo3 Electrode.* Abstracts of Papers of the American Chemical Society, 1979(Apr): p. 255-&.

153. Sunarso, J., *et al*., *Oxygen Reduction Reaction Activity of La-Based Perovskite Oxides in Alkaline Medium: A Thin-Film Rotating Ring-Disk Electrode Study.* Journal of Physical Chemistry C, 2012. **116**(9): p. 5827-5834.

154. Norskov, J.K., *et al*., *Origin of the overpotential for oxygen reduction at a fuel-cell cathode.* Journal of Physical Chemistry B, 2004. **108**(46): p. 17886-17892.

155. Rossmeisl, J., *et al*., *Electrolysis of water on oxide surfaces.* Journal of Electroanalytical Chemistry, 2007. **607**(1-2): p. 83-89.

156. Rossmeisl, J., A. Logadottir, and J.K. Norskov, *Electrolysis of water on (oxidized) metal surfaces.* Chemical Physics, 2005. **319**(1-3): p. 178-184.

157. Vijh, A.K., *Relationship between Band Gaps of Oxides and Standard Electrode Potentials of Oxide Electrodes.* Electrochimica Acta, 1972. **17**(1): p. 91-&.

158. Tseung, A.C.C. and S. Jasem, *Oxygen Evolution on Semiconducting Oxides.* Electrochimica Acta, 1977. **22**(1): p. 31-34.

159. Man, I.C., *et al*., *Universality in Oxygen Evolution Electrocatalysis on Oxide Surfaces.* Chemcatchem, 2011. **3**(7): p. 1159-1165.

160. Norskov, J.K., *et al*., *Towards the computational design of solid catalysts.* Nature Chemistry, 2009. **1**(1): p. 37-46.

161. Calle-Vallejo, F., *et al*., *Number of outer electrons as descriptor for adsorption processes on transition metals and their oxides.* Chemical Science, 2013. **4**(3): p. 1245-1249.

162. Goodenough, J.B., *Covalency Criterion for Localized vs Collective Electrons in Oxides with the Perovskite Structure.* Journal of Applied Physics, 1966. **37**(3): p. 1415-1422.

163. Matsumoto, Y., H. Yoneyama, and H. Tamura, *Influence of Nature of Conduction-Band of Transition-Metal Oxides on Catalytic Activity for Oxygen Reduction.* Journal of Electroanalytical Chemistry, 1977. **83**(2): p. 237-243.

164. Morin, F.J. and T. Wolfram, *Surface States and Catalysis on D-Band Perovskites.* Physical Review Letters, 1973. **30**(24): p. 1214-1217.

165. Ahmad, E.A., *et al*., *Optimizing Oxygen Reduction Catalyst Morphologies from First Principles.* Journal of Physical Chemistry C, 2015. **119**(29): p. 16804-16810.

166. Lee, C.K., *et al*., *Thermal treatment of La0.6Ca0.4CoO3 perovskites for bifunctional air electrodes.* Journal of the Electrochemical Society, 1997. **144**(11): p. 3801-3806.

167. Muller, S., K. Striebel, and O. Haas, *La0.6ca0.4coo3 - a Stable and Powerful Catalyst for Bifunctional Air Electrodes.* Electrochimica Acta, 1994. **39**(11-12): p. 1661-1668.

168. Poux, T., *et al*., *Dual role of carbon in the catalytic layers of perovskite/carbon composites for the electrocatalytic oxygen reduction reaction.* Catalysis Today, 2012. **189**(1): p. 83-92.

169. Malkhandi, S., *et al*., *Electrocatalytic Activity of Transition Metal Oxide-Carbon Composites for Oxygen Reduction in Alkaline Batteries and Fuel Cells.* Journal of the Electrochemical Society, 2013. **160**(9): p. F943-F952.

170. Li, X.X., *et al*., *Electrocatalytic Activities of La0.6Ca0.4CoO3 and La0.6Ca0.4CoO3-Carbon Composites Toward the Oxygen Reduction Reaction in Concentrated Alkaline Electrolytes.* Journal of the Electrochemical Society, 2011. **158**(5): p. A597-A604.

171. Hermann, V., *et al*., *Mechanistic studies of oxygen reduction at La0.6Ca0.4CoO3-activated carbon electrodes in a channel flow cell.* Electrochimica Acta, 2000. **46**(2-3): p. 365-372.

172. Poux, T., *et al*., *Electrocatalysis of hydrogen peroxide reactions on perovskite oxides: experiment versus kinetic modeling.* Physical Chemistry Chemical Physics, 2014. **16**(27): p. 13595-13600.

173. Wang, G.L., *et al*., *Electrocatalytic activity of perovskite La1-xSrxMnO3 towards hydrogen peroxide reduction in alkaline medium.* Journal of Power Sources, 2010. **195**(19): p. 6463-6467.

174. Matsumoto, Y., H. Yoneyama, and H. Tamura, *Mechanism of Oxygen Reduction at a Lanio3 Electrode.* Bulletin of the Chemical Society of Japan, 1978. **51**(7): p. 1927-1930.

175. Zhuang, S.X., *et al*., *Electrocatalytic Activity of Nanoporous Perovskite La1-xCaxCoO3 Towards Hydrogen Peroxide Reduction in Alkaline Medium.* International Journal of Electrochemical Science, 2012. **7**(1): p. 338-344.

176. Ariafard, A., H.R. Aghabozorg, and F. Salehirad, *Hydrogen peroxide decomposition over La0.9Sr0.1Ni1-xCrxO3 perovskites.* Catalysis Communications, 2003. **4**(11): p. 561-566.

177. Falcon, H., R.E. Carbonio, and J.L.G. Fierro, *Correlation of oxidation states in LaFexNi1-xO3+delta oxides with catalytic activity for H2O2 decomposition.* Journal of Catalysis, 2001. **203**(2): p. 264-272.

178. Poux, T., *et al*., *Electrocatalytic Oxygen Reduction Reaction on Perovskite Oxides: Series versus Direct Pathway.* ChemPhysChem, 2014: p. n/a-n/a.

179. Hardin, W.G., *et al*., *Tuning the Electrocatalytic Activity of Perovskites through Active Site Variation and Support Interactions.* Chemistry of Materials, 2014. **26**(11): p. 3368-3376.

180. Hardin, W.G., *et al*., *Highly Active, Nonprecious Metal Perovskite Electrocatalysts for Bifunctional Metal-Air Battery Electrodes.* Journal of Physical Chemistry Letters, 2013. **4**(8): p. 1254-1259.

181. Fierro, S., *et al*., *Investigation of the oxygen evolution reaction on Ti/IrO2 electrodes using isotope labelling and on-line mass spectrometryle.* Electrochemistry Communications, 2007. **9**(8): p. 1969-1974.

182. Wohlfahrtmehrens, M. and J. Heitbaum, *Oxygen Evolution on Ru and Ruo2 Electrodes Studied Using Isotope Labeling and Online Mass-Spectrometry.* Journal of Electroanalytical Chemistry, 1987. **237**(2): p. 251-260.

183. Lee, Y.L., *et al*., *Prediction of solid oxide fuel cell cathode activity with first-principles descriptors.* Energy & Environmental Science, 2011. **4**(10): p. 3966-3970.

184. Mehandru, S.P. and A.B. Anderson, *Oxygen Evolution on a Srfeo3 Anode - Mechanistic Considerations from Molecular-Orbital Theory.* Journal of the Electrochemical Society, 1989. **136**(1): p. 158-166.

185. Matsumoto, Y., J. Kurimoto, and E. Sato, *Oxygen Evolution on Srfeo3 Electrode.* Journal of Electroanalytical Chemistry, 1979. **102**(1): p. 77-83.

186. Matsumoto, Y., J. Kurimoto, and E. Sato, *Anodic Characteristics of Srfe0.9m0.1o3(M-Ni, Co, Ti, Mn) Electrodes.* Electrochimica Acta, 1980. **25**(5): p. 539-543.

187. Stoerzinger, K.A., *et al*., *Highly Active Epitaxial La(1-x)SrxMnO3 Surfaces for the Oxygen Reduction Reaction: Role of Charge Transfer.* Journal of Physical Chemistry Letters, 2015. **6**(8): p. 1435-1440.

188. Higuchi, T., *et al*., *Electronic structure of p-type SrTiO3 by photoemission spectroscopy.* Physical Review B, 1998. **57**(12): p. 6978-6983.

189. Baniecki, J.D., *et al*., *Density functional theory and experimental study of the electronic structure and transport properties of La, V, Nb, and Ta doped SrTiO3.* Journal of Applied Physics, 2013. **113**(1).

190. Rodenbucher, C., *et al*., *Insulator-to-metal transition of SrTiO3:Nb single crystal surfaces induced by Ar+ bombardment.* Applied Physics Letters, 2013. **102**(10).

191. Deak, D.S., *Strontium titanate surfaces (vol 23, pg 127, 2007).* Materials Science and Technology, 2007. **23**(5): p. 630-630.

192. Gunhold, A., *et al*., *Changes in the surface topography and electronic structure of SrTiO3(110) single crystals heated under oxidizing and reducing conditions.* Surface Science, 2004. **566**: p. 105-110.

193. Russell, B.C. and M.R. Castell, *Reconstructions on the polar SrTiO(3) (110) surface: Analysis using STM, LEED, and AES.* Physical Review B, 2008. **77**(24).

194. Russell, B.C. and M.R. Castell, *(root 13X root 13)R13.9 degrees and (root 7X root 7)R19.1 degrees reconstructions of the polar SrTiO3 (111) surface.* Physical Review B, 2007. **75**(15).

195. Tanaka, H. and T. Kawai, *Surface structure of reduced SrTiO3(111) observed by scanning tunneling microscopy.* Surface Science, 1996. **365**(2): p. 437-442.

196. Brunen, J. and J. Zegenhagen, *Investigation of the SrTiO3 (110) surface by means of LEED, scanning tunneling microscopy and Auger spectroscopy.* Surface Science, 1997. **389**(1-3): p. 349-365.

197. Cao, Y.W., *et al*., *Electronic structures of the SrTiO3(110) surface in different reconstructions.* Journal of Chemical Physics, 2012. **137**(4).

198. Bonnell, D.A., *Local structure and properties of oxide surfaces: Scanning probe analyses of ceramics.* Journal of the American Ceramic Society, 1998. **81**(12): p. 3049-3070.

199. Deak, D.S., *Strontium titanate surfaces.* Materials Science and Technology, 2007. **23**(2): p. 127-136.

200. Bando, H., *et al*., *Structure and Electronic States on Reduced Srtio3(110) Surface Observed by Scanning-Tunneling-Microscopy and Spectroscopy.* Journal of Vacuum Science & Technology B, 1995. **13**(3): p. 1150-1154.

201. Enterkin, J.A., *et al*., *A homologous series of structures on the surface of SrTiO3(110).* Nature Materials, 2010. **9**(3): p. 245-248.

202. Henrich, V.E., G. Dresselhaus, and H.J. Zeiger, *Surface Defects and Electronic-Structure of Srtio3 Surfaces.* Physical Review B, 1978. **17**(12): p. 4908-4921.

203. Haruyama, Y., *et al*., *Annealing temperature dependence on the electronic structure of the reduced SrTiO3 (111) surface.* Journal of Electron Spectroscopy and Related Phenomena, 1998. **88**: p. 695-699.

204. Aiura, Y., *et al*., *Effects of Surface Oxygen Vacancies on Electronic States of Tio2(110), Tio2(001) and Srtio3(001) Surfaces.* Physica B, 1994. **194**: p. 1215-1216.

205. Courths, R., B. Cord, and H. Saalfeld, *Bulk and Surface Ti3d Valence and Defect States in Srtio3(001) from Resonant Photoemission.* Solid State Communications, 1989. **70**(11): p. 1047-1051.

206. Aiura, Y., *et al*., *Effect of Surface Oxygen Vacancies on Electronic States of Reduced Srtio3(110) Surface.* Physica C, 1994. **235**: p. 1009-1010.

207. Mills, P. and J.L. Sullivan, *A Study of the Core Level Electrons in Iron and Its 3 Oxides by Means of X-Ray Photoelectron-Spectroscopy.* Journal of Physics D-Applied Physics, 1983. **16**(5): p. 723-732.

208. Alexandrov, V., *et al*., *First-Principles Modeling of Oxygen Interaction with SrTiO3(001) Surface: Comparative Density-Functional LCAO and Plane-Wave Study.* Integrated Ferroelectrics, 2011. **123**: p. 10-17.

209. Guhl, H., W. Miller, and K. Reuter, *Oxygen adatoms at SrTiO3(001): A density-functional theory study.* Surface Science, 2010. **604**(3-4): p. 372-376.